

OPEN ACCESS

# Technical Design Report for the Upgrade of the ALICE Inner Tracking System

To cite this article: B Abelev et al and The ALICE Collaboration 2014 *J. Phys. G: Nucl. Part. Phys.* **41** 087002

View the [article online](#) for updates and enhancements.

## Related content

- [Photoconduction in Polyimide \(Kapton H\)](#)  
Yoshiaki Takai, Mal-Mun Kim, Atsuhiko Kurachi et al.
- [Surface Modification of Polyimide Film by Dielectric Barrier Discharge at Atmospheric Pressure](#)  
Peng Shi, Li Lingjun, Li Wei et al.
- [Effect of Molecular Order on Photoconduction of Polyimide](#)  
Kazuo Iida, Misao Waki, Shuhei Nakamura et al.

## Recent citations

- [Performance and luminosity models for heavy-ion operation at the CERN Large Hadron Collider](#)  
R. Bruce *et al*
- [Production of pions, kaons, \(anti-\)protons and  \$\phi\$  mesons in Xe–Xe collisions at  \$\sqrt{s\_{\mathrm{NN}}} = 5.44\$  TeV](#)  
S. Acharya *et al*
- [Nirbhay Kumar Behera](#)



ALICE-TDR-017



CERN-LHCC-2013-024  
02 December 2013

# Technical Design Report

## for the

### Upgrade of the

# ALICE Inner Tracking System

The ALICE Collaboration



## The ALICE collaboration

B. Abelev<sup>75</sup>, J. Adam<sup>39</sup>, D. Adamová<sup>83</sup>, M.M. Aggarwal<sup>87</sup>, G. Aglieri Rinella<sup>34</sup>,  
M. Agnello<sup>93,111</sup>, A. Agostinelli<sup>26</sup>, N. Agrawal<sup>46</sup>, Z. Ahammed<sup>131</sup>, N. Ahmad<sup>18</sup>,  
A. Ahmad Masoodi<sup>18</sup>, I. Ahmed<sup>15</sup>, S.U. Ahn<sup>68</sup>, S.A. Ahn<sup>68</sup>, I. Aimo<sup>93,111</sup>, S. Aiola<sup>136</sup>,  
M. Ajaz<sup>15</sup>, A. Akindinov<sup>58</sup>, D. Aleksandrov<sup>99</sup>, B. Alessandro<sup>111</sup>, D. Alexandre<sup>102</sup>,  
A. Alici<sup>105,12</sup>, A. Alkin<sup>3</sup>, J. Alme<sup>37</sup>, T. Alt<sup>41</sup>, V. Altini<sup>31</sup>, S. Altinpinar<sup>17</sup>,  
I. Altsybeev<sup>130</sup>, C. Alves Garcia Prado<sup>120</sup>, E.C. Anderssen<sup>74</sup>, C. Andrei<sup>78</sup>,  
A. Andronic<sup>96</sup>, V. Anguelov<sup>92</sup>, J. Anielski<sup>53</sup>, T. Antičić<sup>97</sup>, F. Antinori<sup>108</sup>, P. Antonioli<sup>105</sup>,  
L. Aphecetche<sup>112</sup>, H. Appelshäuser<sup>51</sup>, N. Arbor<sup>71</sup>, S. Arcelli<sup>26</sup>, N. Armesto<sup>16</sup>,  
R. Arnaldi<sup>111</sup>, T. Aronsson<sup>136</sup>, I.C. Arsene<sup>21,96</sup>, M. Arslanodok<sup>51</sup>, A. Augustinus<sup>34</sup>,  
R. Averbeck<sup>96</sup>, T.C. Awes<sup>84</sup>, M.D. Azmi<sup>18,89</sup>, M. Bach<sup>41</sup>, A. Badalà<sup>107</sup>, Y.W. Baek<sup>42,70</sup>,  
S. Bagnasco<sup>111</sup>, R. Bailhache<sup>51</sup>, V. Bairathi<sup>91</sup>, R. Bala<sup>90</sup>, A. Baldissari<sup>14</sup>,  
F. Baltasar Dos Santos Pedrosa<sup>34</sup>, J. Bán<sup>59</sup>, R.C. Baral<sup>61</sup>, R. Barbera<sup>27</sup>, F. Barile<sup>31</sup>,  
G.G. Barnaföldi<sup>135</sup>, L.S. Barnby<sup>102</sup>, V. Barret<sup>70</sup>, J. Bartke<sup>116</sup>, M. Basile<sup>26</sup>,  
J. Bastian Van Beelen<sup>34</sup>, N. Bastid<sup>70</sup>, S. Basu<sup>131</sup>, B. Bathen<sup>53</sup>, G. Batigne<sup>112</sup>,  
M. Battistini<sup>34</sup>, B. Batyunya<sup>66</sup>, P.C. Batzing<sup>21</sup>, J. Baudot<sup>54</sup>, C. Baumann<sup>51</sup>,  
I.G. Bearden<sup>80</sup>, H. Beck<sup>51</sup>, C. Bedda<sup>93</sup>, N.K. Behera<sup>46</sup>, I. Belikov<sup>54</sup>, F. Bellini<sup>26</sup>,  
R. Bellwied<sup>122</sup>, E. Belmont-Moreno<sup>64</sup>, G. Bencedi<sup>135</sup>, M. Benettoni<sup>108</sup>, F. Benotto<sup>111</sup>,  
S. Beole<sup>25</sup>, I. Berceanu<sup>78</sup>, A. Bercuci<sup>78</sup>, Y. Berdnikov<sup>11,85</sup>, D. Berenyi<sup>135</sup>, M.E. Berger<sup>115</sup>,  
R.A. Bertens<sup>57</sup>, D. Berzano<sup>25</sup>, A. Besson<sup>54</sup>, L. Betev<sup>34</sup>, A. Bhasin<sup>90</sup>, A.K. Bhati<sup>87</sup>,  
A. Bhatti<sup>15</sup>, B. Bhattacharjee<sup>43</sup>, J. Bhom<sup>127</sup>, L. Bianchi<sup>25</sup>, N. Bianchi<sup>72</sup>, C. Bianchin<sup>57</sup>,  
J. Bielčik<sup>39</sup>, J. Bielčíková<sup>83</sup>, A. Bilandžić<sup>80</sup>, S. Bjelogrić<sup>57</sup>, F. Blanco<sup>10</sup>, D. Blau<sup>99</sup>,  
C. Blume<sup>51</sup>, F. Bock<sup>92,74</sup>, F.V. Boehmer<sup>115</sup>, A. Bogdanov<sup>76</sup>, H. Bøggild<sup>80</sup>,  
M. Bogolyubsky<sup>55</sup>, L. Boldizsár<sup>135</sup>, M. Bombara<sup>40</sup>, J. Book<sup>51</sup>, H. Borel<sup>14</sup>,  
A. Borisov<sup>134,95</sup>, J. Bornschein<sup>41</sup>, V.N. Borshchov<sup>3</sup>, C. Bortolin<sup>34</sup>, F. Bossú<sup>65</sup>,  
M. Botje<sup>81</sup>, E. Botta<sup>25</sup>, S. Böttger<sup>50</sup>, P. Braun-Munzinger<sup>96</sup>, T. Breitner<sup>50</sup>,  
T.A. Broker<sup>51</sup>, T.A. Browning<sup>94</sup>, M. Broz<sup>38</sup>, E. Bruna<sup>111</sup>, G.E. Bruno<sup>31</sup>, D. Budnikov<sup>98</sup>,  
H. Buesching<sup>51</sup>, S. Bufalino<sup>111</sup>, P. Buncic<sup>34</sup>, O. Busch<sup>92</sup>, Z. Buthelezi<sup>65</sup>, D. Caffarri<sup>28</sup>,  
X. Cai<sup>7</sup>, H. Caines<sup>136</sup>, A. Caliva<sup>57</sup>, E. Calvo Villar<sup>103</sup>, P. Camerini<sup>24</sup>,  
V. Canoa Roman<sup>34</sup>, F. Carena<sup>34</sup>, W. Carena<sup>34</sup>, P. Cariola<sup>104</sup>,  
F. Carminati<sup>34</sup>, A. Casanova Diaz<sup>72</sup>, J. Castillo Castellanos<sup>14</sup>, E.A.R. Casula<sup>23</sup>,  
V. Catanesu<sup>78</sup>, T. Caudron<sup>34</sup>, C. Cavicchioli<sup>34</sup>, C. Ceballos Sanchez<sup>9</sup>, J. Cepila<sup>39</sup>,  
P. Cerello<sup>111</sup>, B. Chang<sup>123</sup>, S. Chapeland<sup>34</sup>, J.L. Charvet<sup>14</sup>, S. Chattopadhyay<sup>131</sup>,  
S. Chattopadhyay<sup>101</sup>, M. Cherney<sup>86</sup>, C. Cheshkov<sup>129</sup>, B. Cheynis<sup>129</sup>,  
V. Chibante Barroso<sup>34</sup>, D.D. Chinellato<sup>122,121</sup>, P. Chochula<sup>34</sup>, M. Chojnacki<sup>80</sup>,  
S. Choudhury<sup>131</sup>, P. Christakoglou<sup>81</sup>, C.H. Christensen<sup>80</sup>, P. Christiansen<sup>32</sup>, T. Chujo<sup>127</sup>,  
S.U. Chung<sup>95</sup>, C. Cicalo<sup>106</sup>, L. Cifarelli<sup>12,26</sup>, F. Cindolo<sup>105</sup>, G. Claus<sup>54</sup>, J. Cleymans<sup>89</sup>,  
F. Colamaria<sup>31</sup>, D. Colella<sup>31</sup>, S. Coli<sup>111</sup>, C. Colledani<sup>54</sup>, A. Collu<sup>23</sup>, M. Colocci<sup>26</sup>,  
G. Conesa Balbastre<sup>71</sup>, Z. Conesa del Valle<sup>49,34</sup>, M.E. Connors<sup>136</sup>, G. Contin<sup>24</sup>,  
J.G. Contreras<sup>11</sup>, T.M. Cormier<sup>84,134</sup>, Y. Corrales Morales<sup>25</sup>, P. Cortese<sup>30</sup>,  
I. Cortés Maldonado<sup>2</sup>, M.R. Cosentino<sup>74,120</sup>, F. Costa<sup>34</sup>, P. Crochet<sup>70</sup>, R. Cruz Albino<sup>11</sup>,  
E. Cuautle<sup>63</sup>, L. Cunqueiro<sup>72,34</sup>, A. Dainese<sup>108</sup>, R. Dang<sup>7</sup>, A. Danu<sup>62</sup>, E. Da Riva<sup>34</sup>,  
D. Das<sup>101</sup>, I. Das<sup>49</sup>, K. Das<sup>101</sup>, S. Das<sup>4</sup>, A. Dash<sup>121</sup>, S. Dash<sup>46</sup>, S. De<sup>131</sup>, C. Decosse<sup>34</sup>,  
H. Delagrangé<sup>1,112</sup>, A. Deloff<sup>77</sup>, E. Dénes<sup>135</sup>, G. D'Erasmus<sup>31</sup>, G.O.V. de Barros<sup>120</sup>,  
A. De Caro<sup>12,29</sup>, G. de Cataldo<sup>104</sup>, J. de Cuveland<sup>41</sup>, A. De Falco<sup>23</sup>, D. De Gruttola<sup>29,12</sup>,



Content from this work may be used under the terms of the [Creative Commons Attribution 3.0 licence](https://creativecommons.org/licenses/by/3.0/). Any further distribution of this work must maintain attribution to the author(s) and the title of the work, journal citation and DOI.

N. De Marco<sup>111</sup>, S. De Pasquale<sup>29</sup>, G. De Robertis<sup>104</sup>, K. De Roo<sup>81</sup>, R. de Rooij<sup>57</sup>, M.A. Diaz Corchero<sup>10</sup>, T. Dietel<sup>53,89</sup>, R. Divià<sup>34</sup>, D. Di Bari<sup>31</sup>, S. Di Liberto<sup>109</sup>, A. Di Mauro<sup>34</sup>, P. Di Nezza<sup>72</sup>, Ø. Djuvsland<sup>17</sup>, A. Dobrin<sup>57</sup>, T. Dobrowolski<sup>77</sup>, D. Domenicis Gimenez<sup>120</sup>, B. Dönigus<sup>51</sup>, O. Dordic<sup>21</sup>, S. Dorheim<sup>115</sup>, A. Dorokhov<sup>54</sup>, G. Doziere<sup>54</sup>, A.K. Dubey<sup>131</sup>, A. Dubla<sup>57</sup>, L. Ducroux<sup>129</sup>, W. Dulinski<sup>54</sup>, P. Dupieux<sup>70</sup>, A.K. Dutta Majumdar<sup>101</sup>, R.J. Ehlers III<sup>136</sup>, D. Elia<sup>104</sup>, H. Engel<sup>50</sup>, B. Erasmus<sup>34,112</sup>, H.A. Erdal<sup>37</sup>, D. Eschweiler<sup>41</sup>, B. Espagnon<sup>49</sup>, M. Estienne<sup>112</sup>, S. Esumi<sup>127</sup>, D. Evans<sup>102</sup>, S. Evdokimov<sup>55</sup>, G. Eyyubova<sup>21</sup>, D. Fabris<sup>108</sup>, J. Faivre<sup>71</sup>, D. Falchieri<sup>26</sup>, A. Fantoni<sup>72</sup>, M. Fasel<sup>92</sup>, D. Fehlker<sup>17</sup>, L. Feldkamp<sup>53</sup>, D. Felea<sup>62</sup>, A. Feliciello<sup>111</sup>, G. Feofilov<sup>130</sup>, J. Ferencei<sup>83</sup>, A. Fernández Téllez<sup>2</sup>, E.G. Ferreira<sup>16</sup>, A. Ferretti<sup>25</sup>, A. Festanti<sup>28</sup>, J. Figiel<sup>116</sup>, M.A.S. Figueredo<sup>120,124</sup>, S. Filchagin<sup>98</sup>, D. Finogeev<sup>56</sup>, F.M. Fionda<sup>31</sup>, E.M. Fiore<sup>31</sup>, G. Fiorenza<sup>104</sup>, E. Floratos<sup>88</sup>, M. Floris<sup>34</sup>, S. Foertsch<sup>65</sup>, P. Foka<sup>96</sup>, S. Fokin<sup>99</sup>, E. Fragiaco<sup>110</sup>, A. Francescon<sup>28,34</sup>, M. Franco<sup>104</sup>, U. Frankenfeld<sup>96</sup>, U. Fuchs<sup>34</sup>, C. Furget<sup>71</sup>, M. Fusco Girard<sup>29</sup>, J.J. Gaardhøje<sup>80</sup>, M. Gagliardi<sup>25</sup>, D. Gajanana<sup>81</sup>, M. Gallio<sup>25</sup>, D.R. Gangadharan<sup>19,74</sup>, P. Ganoti<sup>84,88</sup>, C. Garabatos<sup>96</sup>, E. Garcia-Solis<sup>13</sup>, C. Gargiulo<sup>34</sup>, I. Garishvili<sup>75</sup>, J. Gerhard<sup>41</sup>, M. Germain<sup>112</sup>, A. Gheata<sup>34</sup>, M. Gheata<sup>34,62</sup>, B. Ghidini<sup>31</sup>, P. Ghosh<sup>131</sup>, S.K. Ghosh<sup>4</sup>, P. Gianotti<sup>72</sup>, P. Giubileo<sup>28</sup>, P. Giubellino<sup>34</sup>, E. Gladysz-Dziadus<sup>116</sup>, P. Gläsel<sup>92</sup>, R. Gomez<sup>11</sup>, M. Gomez Marzoa<sup>34</sup>, P. González-Zamora<sup>10</sup>, S. Gorbunov<sup>41</sup>, L. Görlich<sup>116</sup>, S. Gotovac<sup>114</sup>, L.K. Graczykowski<sup>133</sup>, R. Grajcarek<sup>92</sup>, L.C. Greiner<sup>74</sup>, A. Grelli<sup>57</sup>, A. Grigoras<sup>34</sup>, C. Grigoras<sup>34</sup>, V. Grigoriev<sup>76</sup>, A. Grigoryan<sup>1</sup>, S. Grigoryan<sup>66</sup>, B. Grinyov<sup>3</sup>, N. Grion<sup>110</sup>, D. Grondin<sup>71</sup>, J.F. Grosse-Oetringhaus<sup>34</sup>, J.-Y. Grossiord<sup>129</sup>, R. Grosso<sup>34</sup>, F. Guber<sup>56</sup>, R. Guernane<sup>71</sup>, B. Guerzoni<sup>26</sup>, M. Guilbaud<sup>129</sup>, K. Gulbrandsen<sup>80</sup>, H. Gulkanyan<sup>1</sup>, T. Gunji<sup>126</sup>, A. Gupta<sup>90</sup>, R. Gupta<sup>90</sup>, K. H. Khan<sup>15</sup>, R. Haake<sup>53</sup>, Ø. Haaland<sup>17</sup>, C. Hadjidakis<sup>49</sup>, M. Haiduc<sup>62</sup>, H. Hamagaki<sup>126</sup>, G. Hamar<sup>135</sup>, L.D. Hanratty<sup>102</sup>, A. Hansen<sup>80</sup>, J.W. Harris<sup>136</sup>, H. Hartmann<sup>41</sup>, A. Harton<sup>13</sup>, D. Hatzifotiadiou<sup>105</sup>, S. Hayashi<sup>126</sup>, S.T. Heckel<sup>51</sup>, M. Heide<sup>53</sup>, H. Helstrup<sup>37</sup>, E. Hennes<sup>81</sup>, A. Herghelegiu<sup>78</sup>, G. Herrera Corral<sup>11</sup>, B.A. Hess<sup>33</sup>, K.F. Hetland<sup>37</sup>, B. Hicks<sup>136</sup>, H. Hillemanns<sup>34</sup>, A. Himmi<sup>54</sup>, B. Hippolyte<sup>54</sup>, J. Hladky<sup>60</sup>, P. Hristov<sup>34</sup>, M. Huang<sup>17</sup>, C. Hu-Guo<sup>54</sup>, T.J. Humanic<sup>19</sup>, D. Hutter<sup>41</sup>, D.S. Hwang<sup>20</sup>, S. Igoilkin<sup>34</sup>, P. Ijzermans<sup>34</sup>, R. Ilkaev<sup>98</sup>, I. Ilkiv<sup>77</sup>, M. Inaba<sup>127</sup>, E. Incani<sup>23</sup>, G.M. Innocenti<sup>25</sup>, C. Ionita<sup>34</sup>, M. Ippolitov<sup>99</sup>, M. Irfan<sup>18</sup>, M. Ivanov<sup>96</sup>, V. Ivanov<sup>85</sup>, O. Ivanytskyi<sup>3</sup>, A. Jacholkowski<sup>27</sup>, J. Jadlovsky<sup>36</sup>, C. Jahnke<sup>120</sup>, H.J. Jang<sup>68</sup>, M.A. Janik<sup>133</sup>, P.H.S.Y. Jayarathna<sup>122</sup>, S. Jena<sup>46,122</sup>, R.T. Jimenez Bustamante<sup>63</sup>, P.G. Jones<sup>102</sup>, H. Jung<sup>42</sup>, A. Junique<sup>34</sup>, A. Jusko<sup>102</sup>, S. Kalcher<sup>41</sup>, P. Kalinak<sup>59</sup>, A. Kalweit<sup>34</sup>, J. Kamin<sup>51</sup>, J.H. Kang<sup>137</sup>, V. Kaplin<sup>76</sup>, S. Kar<sup>131</sup>, A. Karasu Uysal<sup>69</sup>, O. Karavichev<sup>56</sup>, T. Karavicheva<sup>56</sup>, E. Karpechev<sup>56</sup>, U. Kebschull<sup>50</sup>, R. Keidel<sup>138</sup>, M. Keil<sup>34</sup>, B. Ketzer<sup>115,35</sup>, M. Mohisin. Khan<sup>III,18</sup>, P. Khan<sup>101</sup>, S.A. Khan<sup>131</sup>, A. Khanzadeev<sup>85</sup>, Y. Kharlov<sup>55</sup>, B. Kileng<sup>37</sup>, B. Kim<sup>137</sup>, D. Kim<sup>137</sup>, D.W. Kim<sup>68,42</sup>, D.J. Kim<sup>123</sup>, J.S. Kim<sup>42</sup>, M. Kim<sup>42</sup>, M. Kim<sup>137</sup>, S. Kim<sup>20</sup>, T. Kim<sup>137</sup>, S. Kirsch<sup>41</sup>, I. Kisel<sup>41</sup>, S. Kiselev<sup>58</sup>, A. Kisiel<sup>133</sup>, G. Kiss<sup>135</sup>, J.L. Klay<sup>6</sup>, J. Klein<sup>92</sup>, C. Klein-Bösing<sup>53</sup>, A. Kluge<sup>34</sup>, M.L. Knichel<sup>96</sup>, A.G. Knospe<sup>117</sup>, C. Kobdaj<sup>34,113</sup>, M. Kofarago<sup>34,81</sup>, M.K. Köhler<sup>96</sup>, T. Kollegger<sup>41</sup>, A. Kolojvari<sup>130</sup>, V. Kondratiev<sup>130</sup>, N. Kondratyeva<sup>76</sup>, A. Konevskikh<sup>56</sup>, V. Kovalenko<sup>130</sup>, M. Kowalski<sup>34,116</sup>, S. Kox<sup>71</sup>, G. Koyithatta Meethalevedu<sup>46</sup>, J. Kral<sup>123</sup>, I. Králik<sup>59</sup>, F. Kramer<sup>51</sup>, A. Kravčáková<sup>40</sup>, M. Krelina<sup>39</sup>, M. Kretz<sup>41</sup>, M. Krivda<sup>102,59</sup>, F. Krizek<sup>83,44</sup>, M. Krus<sup>39</sup>, E.B. Krymov<sup>130</sup>, E. Kryshen<sup>85,34</sup>, M. Krzewicki<sup>96</sup>, V. Kučera<sup>83</sup>, Y. Kucheriaev<sup>99</sup>, T. Kugathasan<sup>34</sup>, C. Kuhn<sup>54</sup>, P.G. Kuijer<sup>81</sup>, I. Kulakov<sup>51</sup>, J. Kumar<sup>46</sup>, P. Kurashvili<sup>77</sup>, A. Kurepin<sup>56</sup>, A.B. Kurepin<sup>56</sup>, A. Kuryakin<sup>98</sup>, S. Kushpil<sup>83</sup>, V. Kushpil<sup>83</sup>, M.J. Kweon<sup>92,48</sup>, Y. Kwon<sup>137</sup>, P. Ladron de Guevara<sup>63</sup>, C. Lagana Fernandes<sup>120</sup>, I. Lakomov<sup>49</sup>, R. Langoy<sup>132</sup>, C. Lara<sup>50</sup>, A. Lardeux<sup>112</sup>, A. Lattuca<sup>25</sup>, S.L. La Pointe<sup>111,57</sup>,

P. La Rocca<sup>27</sup>, R. Lea<sup>24</sup>, G.R. Lee<sup>102</sup>, I. Legrand<sup>34</sup>, J. Lehnert<sup>51</sup>, R.C. Lemmon<sup>82</sup>,  
M. Lenhardt<sup>96</sup>, V. Lenti<sup>104</sup>, E. Leogrande<sup>57</sup>, M. Leoncino<sup>25</sup>, I. León Monzón<sup>119</sup>,  
Y. Lesenechal<sup>34</sup>, P. Lévai<sup>135</sup>, S. Li<sup>7,70</sup>, J. Lien<sup>132</sup>, R. Lietava<sup>102</sup>, S. Lindal<sup>21</sup>,  
V. Lindenstruth<sup>41</sup>, C. Lippmann<sup>96</sup>, M.A. Lisa<sup>19</sup>, O.M. Listratenko<sup>3</sup>, H.M. Ljunggren<sup>32</sup>,  
D.F. Lodato<sup>57</sup>, F. Loddio<sup>104</sup>, P.I. Loenne<sup>17</sup>, V.R. Loggins<sup>134</sup>, V. Loginov<sup>76</sup>, D. Lohner<sup>92</sup>,  
C. Loizides<sup>74</sup>, X. Lopez<sup>70</sup>, E. López Torres<sup>9</sup>, X.-G. Lu<sup>92</sup>, P. Luettig<sup>51</sup>, M. Lunardon<sup>28</sup>,  
J. Luo<sup>7</sup>, G. Luparello<sup>57</sup>, C. Luzzi<sup>34</sup>, A. M. Gago<sup>103</sup>, P. M. Jacobs<sup>74</sup>, R. Ma<sup>136</sup>,  
A. Maevskaya<sup>56</sup>, M. Mager<sup>34</sup>, D.P. Mahapatra<sup>61</sup>, A. Maire<sup>54,92</sup>, M. Malaev<sup>85</sup>,  
I. Maldonado Cervantes<sup>63</sup>, L. Malinina<sup>IV,66</sup>, D. Mal'Kevich<sup>58</sup>, N.A. Maltsev<sup>130</sup>,  
P. Malzacher<sup>96</sup>, A. Mamonov<sup>98</sup>, L. Manceau<sup>111</sup>, V. Manko<sup>99</sup>, F. Manso<sup>70</sup>,  
V. Manzari<sup>34,104</sup>, A. Mapelli<sup>34</sup>, M. Marchisone<sup>25,70</sup>, J. Mares<sup>60</sup>, G.V. Margagliotti<sup>24</sup>,  
A. Margotti<sup>105</sup>, A. Marín<sup>96</sup>, C.A. Marin Tobon<sup>34</sup>, C. Markert<sup>117,34</sup>, M. Marquard<sup>51</sup>,  
D. Marras<sup>106</sup>, I. Martashvili<sup>125</sup>, N.A. Martin<sup>96</sup>, P. Martinengo<sup>34</sup>, M.I. Martínez<sup>2</sup>,  
G. Martínez García<sup>112</sup>, J. Martin Blanco<sup>112</sup>, Y. Martynov<sup>3</sup>, A. Mas<sup>112</sup>, S. Masciocchi<sup>96</sup>,  
M. Maserà<sup>25</sup>, M. Maslov<sup>118</sup>, A. Masoni<sup>106</sup>, L. Massacrier<sup>112</sup>, A. Mastroserio<sup>31</sup>,  
S. Mattiazzi<sup>108</sup>, A. Matyja<sup>116</sup>, C. Mayer<sup>116</sup>, J. Mazer<sup>125</sup>, R. Mazumder<sup>47</sup>, G. Mazza<sup>111</sup>,  
M.A. Mazzoni<sup>109</sup>, F. Meddi<sup>22</sup>, A. Menchaca-Rocha<sup>64</sup>, J. Mercado Pérez<sup>92</sup>, M. Meres<sup>38</sup>,  
Y. Miake<sup>127</sup>, K. Mikhaylov<sup>66,58</sup>, L. Milano<sup>34</sup>, J. Milosevic<sup>V,21</sup>, A. Mischke<sup>57</sup>,  
A.N. Mishra<sup>47</sup>, D. Miśkowiec<sup>96</sup>, C.M. Mitu<sup>62</sup>, J. Mlynarz<sup>134</sup>, B. Mohanty<sup>79,131</sup>,  
L. Molnar<sup>54</sup>, M. Mongelli<sup>104</sup>, L. Montaña Zetina<sup>11</sup>, E. Montes<sup>10</sup>, M. Morando<sup>28</sup>,  
D.A. Moreira De Godoy<sup>120</sup>, F. Morel<sup>54</sup>, S. Moretto<sup>28</sup>, A. Morreale<sup>123,112</sup>, A. Morsch<sup>34</sup>,  
V. Muccifora<sup>72</sup>, E. Mudnic<sup>114</sup>, F. Muhammad Bhopal<sup>15</sup>, S. Muhuri<sup>131</sup>, M. Mukherjee<sup>131</sup>,  
H. Müller<sup>34</sup>, M.G. Munhoz<sup>120</sup>, S. Murray<sup>89</sup>, L. Musa<sup>34</sup>, J. Musinsky<sup>59</sup>, B.K. Nandi<sup>46</sup>,  
R. Nania<sup>105</sup>, E. Nappi<sup>104</sup>, C. Nattrass<sup>125</sup>, T.K. Nayak<sup>131</sup>, S. Nazarenko<sup>98</sup>,  
A. Nedosekin<sup>58</sup>, M. Nicassio<sup>96</sup>, M. Niculescu<sup>34,62</sup>, B.S. Nielsen<sup>80</sup>, S. Nikolaev<sup>99</sup>,  
S. Nikulin<sup>99</sup>, V. Nikulin<sup>85</sup>, B.S. Nilsen<sup>86</sup>, F. Noferini<sup>105,12</sup>, P. Nomokonov<sup>66</sup>,  
G. Nooren<sup>57</sup>, A. Nyanin<sup>99</sup>, J. Nystrand<sup>17</sup>, H. Oeschler<sup>92,52</sup>, S. Oh<sup>136</sup>, S.K. Oh<sup>VI,67,42</sup>,  
A. Okatan<sup>69</sup>, L. Oláh<sup>135</sup>, J. Oleniacz<sup>133</sup>, A.C. Oliveira Da Silva<sup>120</sup>, J. Onderwaater<sup>96</sup>,  
C. Oppedisano<sup>111</sup>, A. Ortiz Velasquez<sup>32</sup>, A. Oskarsson<sup>32</sup>, J. Otwinowski<sup>96</sup>, K. Oyama<sup>92</sup>,  
Y. Pachmayer<sup>92</sup>, M. Pachr<sup>39</sup>, P. Pagano<sup>29</sup>, G. Paic<sup>63</sup>, F. Painke<sup>41</sup>, C. Pajares<sup>16</sup>,  
S.K. Pal<sup>131</sup>, A. Palmeri<sup>107</sup>, S. Panati<sup>111</sup>, D. Pant<sup>46</sup>, D. Pantano<sup>108</sup>, V. Papikyan<sup>1</sup>,  
G.S. Pappalardo<sup>107</sup>, W.J. Park<sup>96</sup>, A. Passfeld<sup>53</sup>, C. Pastore<sup>104</sup>, D.I. Patalakha<sup>55</sup>,  
V. Paticchio<sup>104</sup>, B. Paul<sup>101</sup>, T. Pawlak<sup>133</sup>, T. Peitzmann<sup>57</sup>, H. Pereira Da Costa<sup>14</sup>,  
E. Pereira De Oliveira Filho<sup>120</sup>, D. Peresunko<sup>99</sup>, C.E. Pérez Lara<sup>81</sup>, W. Peryt<sup>I,133</sup>,  
A. Pesci<sup>105</sup>, Y. Pestov<sup>5</sup>, P. Petagna<sup>34</sup>, V. Petráček<sup>39</sup>, M. Petran<sup>39</sup>, M. Petris<sup>78</sup>,  
M. Petrovici<sup>78</sup>, C. Petta<sup>27</sup>, H. Pham<sup>54</sup>, S. Piano<sup>110</sup>, M. Pikna<sup>38</sup>, P. Pillot<sup>112</sup>,  
O. Pinazza<sup>34,105</sup>, L. Pinsky<sup>122</sup>, D.B. Piyarathna<sup>122</sup>, M. Płoskoń<sup>74</sup>, M. Planinic<sup>97,128</sup>,  
J. Pluta<sup>133</sup>, S. Pochybova<sup>135</sup>, P.L.M. Podesta-Lerma<sup>119</sup>, M.G. Poghosyan<sup>34,86</sup>,  
E.H.O. Pohjoisaho<sup>44</sup>, B. Polichtchouk<sup>55</sup>, N. Poljak<sup>97,128</sup>, A. Pop<sup>78</sup>,  
S. Porteboeuf-Houssais<sup>70</sup>, J. Porter<sup>74</sup>, V. Pospisil<sup>39</sup>, B. Potukuchi<sup>90</sup>, S.K. Prasad<sup>4,134</sup>,  
R. Preghenella<sup>105,12</sup>, F. Prino<sup>111</sup>, M.A. Protsenko<sup>3</sup>, C.A. Pruneau<sup>134</sup>, I. Pshenichnov<sup>56</sup>,  
G. Puddu<sup>23</sup>, C. Puggioni<sup>106</sup>, V. Punin<sup>98</sup>, J. Putschke<sup>134</sup>, H. Qvigstad<sup>21</sup>, A. Rachevski<sup>110</sup>,  
S. Raha<sup>4</sup>, J. Rak<sup>123</sup>, A. Rakotozafindrabe<sup>14</sup>, L. Ramello<sup>30</sup>, R. Raniwala<sup>91</sup>, S. Raniwala<sup>91</sup>,  
S.S. Räsänen<sup>44</sup>, B.T. Rascanu<sup>51</sup>, J.E. Rasson<sup>74</sup>, D. Rathee<sup>87</sup>, A.W. Rauf<sup>15</sup>, V. Razazi<sup>23</sup>,  
K.F. Read<sup>125</sup>, J.S. Real<sup>71</sup>, K. Redlich<sup>VII,77</sup>, R.J. Reed<sup>136</sup>, A. Rehman<sup>17</sup>, P. Reichelt<sup>51</sup>,  
M. Reicher<sup>57</sup>, F. Reidt<sup>34,92</sup>, R. Renfordt<sup>51</sup>, A.R. Reolon<sup>72</sup>, A. Reshetin<sup>56</sup>, F. Rettig<sup>41</sup>,  
J.-P. Revol<sup>34</sup>, K. Reygers<sup>92</sup>, V. Riabov<sup>85</sup>, R.A. Ricci<sup>73</sup>, T. Richert<sup>32</sup>, M. Richter<sup>21</sup>,  
P. Riedler<sup>34</sup>, W. Riegler<sup>34</sup>, F. Riggi<sup>27</sup>, A. Rivetti<sup>111</sup>, E. Rocco<sup>57</sup>,  
M. Rodríguez Cahuantzi<sup>2</sup>, A. Rodríguez Manso<sup>81</sup>, K. Røed<sup>21</sup>, E. Rogochaya<sup>66</sup>,  
S. Rohni<sup>90</sup>, D. Rohr<sup>41</sup>, D. Röhrich<sup>17</sup>, R. Romita<sup>124,82</sup>, F. Ronchetti<sup>72</sup>, L. Ronflette<sup>112</sup>,  
P. Rosnet<sup>70</sup>, S. Rossegger<sup>34</sup>, M.J. Rossewicz<sup>81</sup>, A. Rossi<sup>34</sup>, S. Roudier<sup>71</sup>, J. Rousset<sup>34</sup>,

A. Roy<sup>47</sup>, C. Roy<sup>54</sup>, P. Roy<sup>101</sup>, A.J. Rubio Montero<sup>10</sup>, R. Rui<sup>24</sup>, R. Russo<sup>25</sup>,  
E. Ryabinkin<sup>99</sup>, Y. Ryabov<sup>85</sup>, A. Rybicki<sup>116</sup>, M. Sacchetti<sup>104</sup>, S. Sadovsky<sup>55</sup>,  
K. Šafařík<sup>34</sup>, B. Sahlmuller<sup>51</sup>, R. Sahoo<sup>47</sup>, P.K. Sahu<sup>61</sup>, J. Saini<sup>131</sup>, C.A. Salgado<sup>16</sup>,  
J. Salzwedel<sup>19</sup>, S. Sambyal<sup>90</sup>, V. Samsonov<sup>85</sup>, X. Sanchez Castro<sup>54,63</sup>,  
F.J. Sánchez Rodríguez<sup>119</sup>, L. Šándor<sup>59</sup>, A. Sandoval<sup>64</sup>, M. Sano<sup>127</sup>, G. Santagati<sup>27</sup>,  
R. Santoro<sup>34</sup>, D. Sarkar<sup>131</sup>, E. Scapparone<sup>105</sup>, F. Scarlassara<sup>28</sup>, R.P. Scharenberg<sup>94</sup>,  
C. Schiaua<sup>78</sup>, R. Schicker<sup>92</sup>, J.D. Schipper<sup>81</sup>, C. Schmidt<sup>96</sup>, H.R. Schmidt<sup>33</sup>,  
S. Schuchmann<sup>51</sup>, J. Schukraft<sup>34</sup>, M. Schulc<sup>39</sup>, T. Schuster<sup>136</sup>, Y. Schutz<sup>34,112</sup>,  
K. Schwarz<sup>96</sup>, K. Schweda<sup>96</sup>, G. Scioli<sup>26</sup>, E. Scomparin<sup>111</sup>, P.A. Scott<sup>102</sup>, R. Scott<sup>125</sup>,  
G. Segato<sup>28</sup>, J.E. Seger<sup>86</sup>, I. Selyuzhenkov<sup>96</sup>, S. Senyukhov<sup>54</sup>, J. Seo<sup>95</sup>, E. Serradilla<sup>10,64</sup>,  
A. Sevcenco<sup>62</sup>, I. Sgura<sup>104</sup>, A. Shabetai<sup>112</sup>, G. Shabratova<sup>66</sup>, R. Shahoyan<sup>34</sup>,  
A. Shangaraev<sup>55</sup>, N. Sharma<sup>125,61</sup>, S. Sharma<sup>90</sup>, K. Shigaki<sup>45</sup>, K. Shtejer<sup>25</sup>, Y. Sibiriyak<sup>99</sup>,  
S. Siddhanta<sup>106</sup>, T. Siemiarczuk<sup>77</sup>, D. Silvermyr<sup>84</sup>, C. Silvestre<sup>71</sup>, G. Simatovic<sup>128</sup>,  
R. Singaraju<sup>131</sup>, R. Singh<sup>90</sup>, S. Singha<sup>79,131</sup>, V. Singhal<sup>131</sup>, B.C. Sinha<sup>131</sup>, T. Sinha<sup>101</sup>,  
B. Sitar<sup>38</sup>, M. Sitta<sup>30</sup>, T.B. Skaali<sup>21</sup>, K. Skjerdal<sup>17</sup>, R. Smakal<sup>39</sup>, N. Smirnov<sup>136</sup>,  
R.J.M. Snellings<sup>57</sup>, W. Snoeys<sup>34</sup>, C. Søgaard<sup>32</sup>, R. Soltz<sup>75</sup>, J. Song<sup>95</sup>, M. Song<sup>137</sup>,  
V. Sooden<sup>100</sup>, F. Soramel<sup>28</sup>, S. Sorensen<sup>125</sup>, M. Spacek<sup>39</sup>, J. Špalek<sup>59</sup>, E. Spiriti<sup>72</sup>,  
I. Sputowska<sup>116</sup>, M. Spyropoulou-Stassinaki<sup>88</sup>, B.K. Srivastava<sup>94</sup>, J. Stachel<sup>92</sup>, I. Stan<sup>62</sup>,  
G. Stefanek<sup>77</sup>, M. Steinpreis<sup>19</sup>, E. Stenlund<sup>32</sup>, G. Steyn<sup>65</sup>, J.H. Stiller<sup>92</sup>, D. Stocco<sup>112</sup>,  
M. Stolpovskiy<sup>55</sup>, P. Strmen<sup>38</sup>, A.A.P. Suaide<sup>120</sup>, M.A. Subieta Vasquez<sup>25</sup>, T. Sugitate<sup>45</sup>,  
C. Suire<sup>49</sup>, M. Suleymanov<sup>15</sup>, M. Šuljić<sup>24</sup>, R. Sultanov<sup>58</sup>, M. Šumbera<sup>83</sup>, X. Sun<sup>7</sup>,  
T. Susa<sup>97</sup>, T.J.M. Symons<sup>74</sup>, A. Szanto de Toledo<sup>120</sup>, I. Szarka<sup>38</sup>, A. Szczepankiewicz<sup>34</sup>,  
M. Szymanski<sup>133</sup>, J. Takahashi<sup>121</sup>, M.A. Tangaro<sup>31</sup>, J.D. Tapia Takaki<sup>VIII,49</sup>,  
A. Tarantola Peloni<sup>51</sup>, A. Tarazona Martinez<sup>34</sup>, A. Tauro<sup>34</sup>, G. Tejeda Muñoz<sup>2</sup>,  
A. Telesca<sup>34</sup>, C. Terrevoli<sup>31</sup>, A. Ter Minasyan<sup>76</sup>, J. Thäder<sup>96</sup>, D. Thomas<sup>57</sup>,  
R. Tieulent<sup>129</sup>, A.R. Timmins<sup>122</sup>, A. Toia<sup>51,108</sup>, H. Torii<sup>126</sup>, V. Trubnikov<sup>3</sup>,  
W.H. Trzaska<sup>123</sup>, T. Tsuji<sup>126</sup>, A. Tumkin<sup>98</sup>, R. Turchetta<sup>100</sup>, R. Turrisi<sup>108</sup>, T.S. Tveter<sup>21</sup>,  
I.T. Tymchuk<sup>3</sup>, J. Ulery<sup>51</sup>, K. Ullaland<sup>17</sup>, A. Uras<sup>129</sup>, G.L. Usai<sup>23</sup>, M. Vajzer<sup>83</sup>,  
M. Vala<sup>66,59</sup>, L. Valencia Palomo<sup>49,70</sup>, V. Valentino<sup>104</sup>, I. Valin<sup>54</sup>, S. Vallerio<sup>25,92</sup>,  
P. Vande Vyvre<sup>34</sup>, L. Vannucci<sup>73</sup>, J. Van Der Maarel<sup>57</sup>, J.W. Van Hoorne<sup>34</sup>,  
M. van Leeuwen<sup>57</sup>, A. Vargas<sup>2</sup>, R. Varma<sup>46</sup>, M. Vasileiou<sup>88</sup>, A. Vasiliev<sup>99</sup>, P. Vasta<sup>104</sup>,  
V. Vechernin<sup>130</sup>, M. Veldhoen<sup>57</sup>, A. Velure<sup>17</sup>, M. Venaruzzo<sup>24</sup>, E. Vercellin<sup>25</sup>, S. Vergara  
Limón<sup>2</sup>, B. Verlaet<sup>81</sup>, R. Vernet<sup>8</sup>, M. Verweij<sup>134</sup>, L. Vickovic<sup>114</sup>, G. Viesti<sup>28</sup>,  
J. Viinikainen<sup>123</sup>, Z. Vilakazi<sup>65</sup>, O. Villalobos Baillie<sup>102</sup>, A. Vinogradov<sup>99</sup>,  
L. Vinogradov<sup>130</sup>, Y. Vinogradov<sup>98</sup>, T. Virgili<sup>29</sup>, Y.P. Viyogi<sup>131</sup>, A. Vodopyanov<sup>66</sup>,  
M.A. Völkl<sup>92</sup>, K. Voloshin<sup>58</sup>, S.A. Voloshin<sup>134</sup>, G. Volpe<sup>34</sup>, B. von Haller<sup>34</sup>,  
I. Vorobyev<sup>130</sup>, D. Vranic<sup>96,34</sup>, J. Vrláková<sup>40</sup>, B. Vulpescu<sup>70</sup>, A. Vyushin<sup>98</sup>, B. Wagner<sup>17</sup>,  
J. Wagner<sup>96</sup>, V. Wagner<sup>39</sup>, M. Wang<sup>7,112</sup>, Y. Wang<sup>92</sup>, D. Watanabe<sup>127</sup>, M. Weber<sup>122</sup>,  
J.P. Wessels<sup>53</sup>, U. Westerhoff<sup>53</sup>, J. Wiechula<sup>33</sup>, J. Wikne<sup>21</sup>, M. Wilde<sup>53</sup>, G. Wilk<sup>77</sup>,  
J. Wilkinson<sup>92</sup>, M.C.S. Williams<sup>105</sup>, B. Windelband<sup>92</sup>, M. Winn<sup>92</sup>, M. Winter<sup>54</sup>,  
C. Xiang<sup>7</sup>, C.G. Yaldo<sup>134</sup>, Y. Yamaguchi<sup>126</sup>, H. Yang<sup>57</sup>, P. Yang<sup>7</sup>, S. Yang<sup>17</sup>, S. Yano<sup>45</sup>,  
S. Yasnopolskiy<sup>99</sup>, J. Yi<sup>95</sup>, Z. Yin<sup>7</sup>, I.-K. Yoo<sup>95</sup>, I. Yushmanov<sup>99</sup>, V. Zaccaro<sup>80</sup>, C. Zach<sup>39</sup>,  
A. Zaman<sup>15</sup>, C. Zampolli<sup>105</sup>, S. Zaporozhets<sup>66</sup>, A. Zarochentsev<sup>130</sup>, P. Závada<sup>60</sup>,  
N. Zaviyalov<sup>98</sup>, H. Zbroszczyk<sup>133</sup>, I.S. Zgura<sup>62</sup>, M. Zhalov<sup>85</sup>, F. Zhang<sup>7</sup>, H. Zhang<sup>7</sup>,  
X. Zhang<sup>70,7,74</sup>, Y. Zhang<sup>7</sup>, C. Zhao<sup>21</sup>, V.I. Zherebchevsky<sup>130</sup>, D. Zhou<sup>7</sup>, F. Zhou<sup>7</sup>,  
Y. Zhou<sup>57</sup>, H. Zhu<sup>7</sup>, J. Zhu<sup>7</sup>, J. Zhu<sup>7</sup>, X. Zhu<sup>7</sup>, A. Zichichi<sup>12,26</sup>, A. Zimmermann<sup>92</sup>,  
M.B. Zimmermann<sup>34,53</sup>, G. Zinovjev<sup>3</sup>, Y. Zoccarato<sup>129</sup>, M. Zynovyev<sup>3</sup>, M. Zyzak<sup>51</sup>

## Affiliation Notes

<sup>I</sup> Deceased

<sup>II</sup> Also at: St-Petersburg State Polytechnical University

<sup>III</sup> Also at: Department of Applied Physics, Aligarh Muslim University, Aligarh, India

<sup>IV</sup> Also at: M.V. Lomonosov Moscow State University, D.V. Skobeltsyn Institute of Nuclear Physics, Moscow, Russia

<sup>V</sup> Also at: University of Belgrade, Faculty of Physics and "Vinča" Institute of Nuclear Sciences, Belgrade, Serbia

<sup>VI</sup> Permanent Address: Konkuk University, Seoul, Korea

<sup>VII</sup> Also at: Institute of Theoretical Physics, University of Wrocław, Wrocław, Poland

<sup>VIII</sup> Also at: University of Kansas, Lawrence, KS, United States

## Collaboration Institutes

<sup>1</sup> A.I. Alikhanyan National Science Laboratory (Yerevan Physics Institute) Foundation, Yerevan, Armenia

<sup>2</sup> Benemérita Universidad Autónoma de Puebla, Puebla, Mexico

<sup>3</sup> Bogolyubov Institute for Theoretical Physics, Kiev, Ukraine

<sup>4</sup> Bose Institute, Department of Physics and Centre for Astroparticle Physics and Space Science (CAPSS), Kolkata, India

<sup>5</sup> Budker Institute for Nuclear Physics, Novosibirsk, Russia

<sup>6</sup> California Polytechnic State University, San Luis Obispo, CA, United States

<sup>7</sup> Central China Normal University, Wuhan, China

<sup>8</sup> Centre de Calcul de l'IN2P3, Villeurbanne, France

<sup>9</sup> Centro de Aplicaciones Tecnológicas y Desarrollo Nuclear (CEADEN), Havana, Cuba

<sup>10</sup> Centro de Investigaciones Energéticas Medioambientales y Tecnológicas (CIEMAT), Madrid, Spain

<sup>11</sup> Centro de Investigación y de Estudios Avanzados (CINVESTAV), Mexico City and Mérida, Mexico

<sup>12</sup> Centro Fermi - Museo Storico della Fisica e Centro Studi e Ricerche "Enrico Fermi", Rome, Italy

<sup>13</sup> Chicago State University, Chicago, USA

<sup>14</sup> Commissariat à l'Energie Atomique, IRFU, Saclay, France

<sup>15</sup> COMSATS Institute of Information Technology (CIIT), Islamabad, Pakistan

<sup>16</sup> Departamento de Física de Partículas and IGFAE, Universidad de Santiago de Compostela, Santiago de Compostela, Spain

<sup>17</sup> Department of Physics and Technology, University of Bergen, Bergen, Norway

<sup>18</sup> Department of Physics, Aligarh Muslim University, Aligarh, India

<sup>19</sup> Department of Physics, Ohio State University, Columbus, OH, United States

<sup>20</sup> Department of Physics, Sejong University, Seoul, South Korea

<sup>21</sup> Department of Physics, University of Oslo, Oslo, Norway

<sup>22</sup> Dipartimento di Fisica dell'Università 'La Sapienza' and Sezione INFN Rome

<sup>23</sup> Dipartimento di Fisica dell'Università and Sezione INFN, Cagliari, Italy

<sup>24</sup> Dipartimento di Fisica dell'Università and Sezione INFN, Trieste, Italy

<sup>25</sup> Dipartimento di Fisica dell'Università and Sezione INFN, Turin, Italy

<sup>26</sup> Dipartimento di Fisica e Astronomia dell'Università and Sezione INFN, Bologna, Italy

<sup>27</sup> Dipartimento di Fisica e Astronomia dell'Università and Sezione INFN, Catania, Italy

<sup>28</sup> Dipartimento di Fisica e Astronomia dell'Università and Sezione INFN, Padova, Italy

<sup>29</sup> Dipartimento di Fisica 'E.R. Caianiello' dell'Università and Gruppo Collegato INFN, Salerno, Italy



- <sup>30</sup> Dipartimento di Scienze e Innovazione Tecnologica dell'Università del Piemonte Orientale and Gruppo Collegato INFN, Alessandria, Italy
- <sup>31</sup> Dipartimento Interateneo di Fisica 'M. Merlin' and Sezione INFN, Bari, Italy
- <sup>32</sup> Division of Experimental High Energy Physics, University of Lund, Lund, Sweden
- <sup>33</sup> Eberhard Karls Universität Tübingen, Tübingen, Germany
- <sup>34</sup> European Organization for Nuclear Research (CERN), Geneva, Switzerland
- <sup>35</sup> Excellence Cluster Universe, Technische Universität München, Munich, Germany
- <sup>36</sup> Faculty of Electrical Engineering and Informatics, Technical University, Košice, Slovakia
- <sup>37</sup> Faculty of Engineering, Bergen University College, Bergen, Norway
- <sup>38</sup> Faculty of Mathematics, Physics and Informatics, Comenius University, Bratislava, Slovakia
- <sup>39</sup> Faculty of Nuclear Sciences and Physical Engineering, Czech Technical University in Prague, Prague, Czech Republic
- <sup>40</sup> Faculty of Science, P.J. Šafárik University, Košice, Slovakia
- <sup>41</sup> Frankfurt Institute for Advanced Studies, Johann Wolfgang Goethe-Universität Frankfurt, Frankfurt, Germany
- <sup>42</sup> Gangneung-Wonju National University, Gangneung, South Korea
- <sup>43</sup> Gauhati University, Department of Physics, Guwahati, India
- <sup>44</sup> Helsinki Institute of Physics (HIP), Helsinki, Finland
- <sup>45</sup> Hiroshima University, Hiroshima, Japan
- <sup>46</sup> Indian Institute of Technology Bombay (IIT), Mumbai, India
- <sup>47</sup> Indian Institute of Technology Indore, Indore (IITI), India
- <sup>48</sup> Inha University, College of Natural Sciences
- <sup>49</sup> Institut de Physique Nucleaire d'Orsay (IPNO), Universite Paris-Sud, CNRS-IN2P3, Orsay, France
- <sup>50</sup> Institut für Informatik, Johann Wolfgang Goethe-Universität Frankfurt, Frankfurt, Germany
- <sup>51</sup> Institut für Kernphysik, Johann Wolfgang Goethe-Universität Frankfurt, Frankfurt, Germany
- <sup>52</sup> Institut für Kernphysik, Technische Universität Darmstadt, Darmstadt, Germany
- <sup>53</sup> Institut für Kernphysik, Westfälische Wilhelms-Universität Münster, Münster, Germany
- <sup>54</sup> Institut Pluridisciplinaire Hubert Curien (IPHC), Université de Strasbourg, CNRS-IN2P3, Strasbourg, France
- <sup>55</sup> Institute for High Energy Physics, Protvino, Russia
- <sup>56</sup> Institute for Nuclear Research, Academy of Sciences, Moscow, Russia
- <sup>57</sup> Institute for Subatomic Physics of Utrecht University, Utrecht, Netherlands
- <sup>58</sup> Institute for Theoretical and Experimental Physics, Moscow, Russia
- <sup>59</sup> Institute of Experimental Physics, Slovak Academy of Sciences, Košice, Slovakia
- <sup>60</sup> Institute of Physics, Academy of Sciences of the Czech Republic, Prague, Czech Republic
- <sup>61</sup> Institute of Physics, Bhubaneswar, India
- <sup>62</sup> Institute of Space Science (ISS), Bucharest, Romania
- <sup>63</sup> Instituto de Ciencias Nucleares, Universidad Nacional Autónoma de México, Mexico City, Mexico
- <sup>64</sup> Instituto de Física, Universidad Nacional Autónoma de México, Mexico City, Mexico
- <sup>65</sup> iThemba LABS, National Research Foundation, Somerset West, South Africa
- <sup>66</sup> Joint Institute for Nuclear Research (JINR), Dubna, Russia
- <sup>67</sup> Konkuk University, Seoul, South Korea
- <sup>68</sup> Korea Institute of Science and Technology Information, Daejeon, South Korea

- <sup>69</sup> KTO Karatay University, Konya, Turkey
- <sup>70</sup> Laboratoire de Physique Corpusculaire (LPC), Clermont Université, Université Blaise Pascal, CNRS-IN2P3, Clermont-Ferrand, France
- <sup>71</sup> Laboratoire de Physique Subatomique et de Cosmologie (LPSC), Université Joseph Fourier, CNRS-IN2P3, Institut Polytechnique de Grenoble, Grenoble, France
- <sup>72</sup> Laboratori Nazionali di Frascati, INFN, Frascati, Italy
- <sup>73</sup> Laboratori Nazionali di Legnaro, INFN, Legnaro, Italy
- <sup>74</sup> Lawrence Berkeley National Laboratory, Berkeley, CA, United States
- <sup>75</sup> Lawrence Livermore National Laboratory, Livermore, CA, United States
- <sup>76</sup> Moscow Engineering Physics Institute, Moscow, Russia
- <sup>77</sup> National Centre for Nuclear Studies, Warsaw, Poland
- <sup>78</sup> National Institute for Physics and Nuclear Engineering, Bucharest, Romania
- <sup>79</sup> National Institute of Science Education and Research, Bhubaneswar, India
- <sup>80</sup> Niels Bohr Institute, University of Copenhagen, Copenhagen, Denmark
- <sup>81</sup> Nikhef, National Institute for Subatomic Physics, Amsterdam, Netherlands
- <sup>82</sup> Nuclear Physics Group, STFC Daresbury Laboratory, Daresbury, United Kingdom
- <sup>83</sup> Nuclear Physics Institute, Academy of Sciences of the Czech Republic, Řež u Prahy, Czech Republic
- <sup>84</sup> Oak Ridge National Laboratory, Oak Ridge, TN, United States
- <sup>85</sup> Petersburg Nuclear Physics Institute, Gatchina, Russia
- <sup>86</sup> Physics Department, Creighton University, Omaha, NE, United States
- <sup>87</sup> Physics Department, Panjab University, Chandigarh, India
- <sup>88</sup> Physics Department, University of Athens, Athens, Greece
- <sup>89</sup> Physics Department, University of Cape Town, Cape Town, South Africa
- <sup>90</sup> Physics Department, University of Jammu, Jammu, India
- <sup>91</sup> Physics Department, University of Rajasthan, Jaipur, India
- <sup>92</sup> Physikalisches Institut, Ruprecht-Karls-Universität Heidelberg, Heidelberg, Germany
- <sup>93</sup> Politecnico di Torino, Turin, Italy
- <sup>94</sup> Purdue University, West Lafayette, IN, United States
- <sup>95</sup> Pusan National University, Pusan, South Korea
- <sup>96</sup> Research Division and ExtreMe Matter Institute EMMI, GSI Helmholtzzentrum für Schwerionenforschung, Darmstadt, Germany
- <sup>97</sup> Rudjer Bošković Institute, Zagreb, Croatia
- <sup>98</sup> Russian Federal Nuclear Center (VNIIEF), Sarov, Russia
- <sup>99</sup> Russian Research Centre Kurchatov Institute, Moscow, Russia
- <sup>100</sup> Rutherford Appleton Laboratory, Chilton, United Kingdom
- <sup>101</sup> Saha Institute of Nuclear Physics, Kolkata, India
- <sup>102</sup> School of Physics and Astronomy, University of Birmingham, Birmingham, United Kingdom
- <sup>103</sup> Sección Física, Departamento de Ciencias, Pontificia Universidad Católica del Perú, Lima, Peru
- <sup>104</sup> Sezione INFN, Bari, Italy
- <sup>105</sup> Sezione INFN, Bologna, Italy
- <sup>106</sup> Sezione INFN, Cagliari, Italy
- <sup>107</sup> Sezione INFN, Catania, Italy
- <sup>108</sup> Sezione INFN, Padova, Italy
- <sup>109</sup> Sezione INFN, Rome, Italy
- <sup>110</sup> Sezione INFN, Trieste, Italy
- <sup>111</sup> Sezione INFN, Turin, Italy
- <sup>112</sup> SUBATECH, Ecole des Mines de Nantes, Université de Nantes, CNRS-IN2P3, Nantes, France

- <sup>113</sup> Suranaree University of Technology, Nakhon Ratchasima, Thailand
- <sup>114</sup> Technical University of Split FESB, Split, Croatia
- <sup>115</sup> Technische Universität München, Munich, Germany
- <sup>116</sup> The Henryk Niewodniczanski Institute of Nuclear Physics, Polish Academy of Sciences, Cracow, Poland
- <sup>117</sup> The University of Texas at Austin, Physics Department, Austin, TX, USA
- <sup>118</sup> Ukrainian Academy of Sciences (KIPT-KFTI), Kharkov, Ukraine
- <sup>119</sup> Universidad Autónoma de Sinaloa, Culiacán, Mexico
- <sup>120</sup> Universidade de São Paulo (USP), São Paulo, Brazil
- <sup>121</sup> Universidade Estadual de Campinas (UNICAMP), Campinas, Brazil
- <sup>122</sup> University of Houston, Houston, TX, United States
- <sup>123</sup> University of Jyväskylä, Jyväskylä, Finland
- <sup>124</sup> University of Liverpool, Liverpool, United Kingdom
- <sup>125</sup> University of Tennessee, Knoxville, TN, United States
- <sup>126</sup> University of Tokyo, Tokyo, Japan
- <sup>127</sup> University of Tsukuba, Tsukuba, Japan
- <sup>128</sup> University of Zagreb, Zagreb, Croatia
- <sup>129</sup> Université de Lyon, Université Lyon 1, CNRS/IN2P3, IPN-Lyon, Villeurbanne, France
- <sup>130</sup> V. Fock Institute for Physics, St. Petersburg State University, St. Petersburg, Russia
- <sup>131</sup> Variable Energy Cyclotron Centre, Kolkata, India
- <sup>132</sup> Vestfold University College, Tonsberg, Norway
- <sup>133</sup> Warsaw University of Technology, Warsaw, Poland
- <sup>134</sup> Wayne State University, Detroit, MI, United States
- <sup>135</sup> Wigner Research Centre for Physics, Hungarian Academy of Sciences, Budapest, Hungary
- <sup>136</sup> Yale University, New Haven, CT, United States
- <sup>137</sup> Yonsei University, Seoul, South Korea
- <sup>138</sup> Zentrum für Technologietransfer und Telekommunikation (ZTT), Fachhochschule Worms, Worms, Germany

# Contents

<b>The ALICE collaboration</b>	<b>iii</b>
<b>1 Introduction</b>	<b>1</b>
1.1 Physics objectives . . . . .	2
1.2 Current detector performance and limitations . . . . .	4
1.3 Upgrade overview . . . . .	5
1.3.1 Upgrade concept . . . . .	5
1.3.2 Detector layout overview . . . . .	6
1.3.3 Experimental conditions . . . . .	8
1.3.4 Document summary . . . . .	10
<b>2 Pixel Chip</b>	<b>11</b>
2.1 Detector technology . . . . .	12
2.2 Principle of operation . . . . .	13
2.2.1 Particle detection . . . . .	13
2.2.2 Read-out . . . . .	15
2.3 General requirements . . . . .	16
2.4 STAR pixel detector . . . . .	18
2.5 ALICE developments . . . . .	18
2.5.1 MISTRAL . . . . .	19
2.5.2 ASTRAL . . . . .	20
2.5.3 CHERWELL . . . . .	21
2.5.4 ALPIDE . . . . .	22
2.6 Prototype circuits and experimental results . . . . .	23
2.6.1 Common characteristics and methods . . . . .	24
2.6.2 MIMOSA . . . . .	25
2.6.3 CHERWELL-1 . . . . .	30
2.6.4 Explorer-0, Explorer-1 . . . . .	32
2.6.5 pALPIDE . . . . .	35
2.7 Radiation hardness . . . . .	37
2.7.1 Radiation effects . . . . .	37
2.7.2 Test set-ups and test structures . . . . .	37
2.7.3 Single device test . . . . .	38
2.7.4 Tests of prototype structures . . . . .	38
2.7.5 Single event effects . . . . .	40
2.8 Summary and plans . . . . .	41
<b>3 Pixel Chip mass production, testing and quality assurance</b>	<b>43</b>
3.1 Wafers for CMOS production . . . . .	43
3.1.1 Different wafer starting material during the R&D phase . . . . .	44
3.1.2 Quality assurance tests of wafer starting material . . . . .	45
3.2 Thinning and dicing . . . . .	46
3.2.1 Thinning tests carried out in the R&D phase . . . . .	47

3.3	Single chip test . . . . .	48
3.3.1	Visual and metrological inspection . . . . .	49
3.3.2	Electrical and functional test . . . . .	50
3.4	Wafer post-processing . . . . .	51
<b>4</b>	<b>Detector Staves</b>	<b>53</b>
4.1	Stave design . . . . .	53
4.1.1	Inner Barrel Stave . . . . .	54
4.1.2	Outer Barrel Stave . . . . .	55
4.2	Mechanical support structure and cooling . . . . .	58
4.2.1	Materials and production processes . . . . .	59
4.2.2	Thermal characterisation . . . . .	61
4.2.3	Structural characterisation . . . . .	64
4.3	Flex Printed Circuit . . . . .	66
4.3.1	Inner Barrel . . . . .	66
4.3.2	Outer Barrel . . . . .	67
4.4	Pixel Chip to FPC connection . . . . .	68
4.4.1	Laser soldering . . . . .	69
4.4.2	SpTAB interconnection . . . . .	70
4.5	Assembly procedures . . . . .	71
4.5.1	Inner Barrel Stave . . . . .	72
4.5.2	Outer Barrel Stave . . . . .	73
4.5.3	Stave test and characterisation . . . . .	76
<b>5</b>	<b>Global support structure, services and integration</b>	<b>79</b>
5.1	General requirements . . . . .	79
5.2	Detector support structure . . . . .	80
5.3	Services . . . . .	82
5.3.1	Cooling . . . . .	82
5.3.2	Cabling . . . . .	85
5.3.3	Service support structure . . . . .	86
5.4	Beam pipe . . . . .	87
5.4.1	Beam pipe radius and wall thickness . . . . .	88
5.4.2	Beam pipe supports . . . . .	88
5.4.3	Beam pipe bake-out . . . . .	89
5.5	Installation and removal . . . . .	89
5.5.1	Sequence . . . . .	90
5.5.2	Muon Forward Tracker installation . . . . .	91
5.5.3	Detector cage . . . . .	93
5.6	Survey and mechanical alignment . . . . .	94
<b>6</b>	<b>Read-out electronics</b>	<b>97</b>
6.1	General layout . . . . .	97
6.2	Pixel Chip read-out architectures . . . . .	98
6.2.1	ALPIDE architecture . . . . .	98
6.2.2	Rolling-shutter architecture . . . . .	99
6.2.3	Data transmission . . . . .	100
6.3	Staves layout . . . . .	102
6.3.1	Inner Layers . . . . .	103
6.3.2	Middle and Outer Layers . . . . .	104
6.3.3	Modules interconnection topology . . . . .	104

6.4	Data transmission lines . . . . .	106
6.4.1	Long cables . . . . .	106
6.5	Power distribution and regulation . . . . .	107
6.5.1	DC-DC conversion . . . . .	108
<b>7</b>	<b>Detector performance</b>	<b>109</b>
7.1	Experimental conditions . . . . .	109
7.2	Requirements . . . . .	110
7.3	Detector specifications . . . . .	110
7.4	Simulation tools and models . . . . .	113
7.4.1	Fast estimation tools . . . . .	113
7.4.2	Detailed Monte Carlo simulations . . . . .	114
7.5	Reconstruction tools . . . . .	117
7.5.1	Cluster finding . . . . .	117
7.5.2	Track finding . . . . .	118
7.5.3	Vertex finding and track-to-vertex association . . . . .	120
7.6	Track and vertex reconstruction performance . . . . .	121
7.7	Particle identification . . . . .	123
7.7.1	Simulation tool and truncated mean method . . . . .	124
7.7.2	PID efficiency and contamination . . . . .	125
7.7.3	Heavily ionizing particles . . . . .	127
7.8	Performance for improved or degraded sensor parameters . . . . .	128
7.8.1	Tracking efficiency vs. layer detection efficiency and redundancy . . . . .	130
<b>8</b>	<b>Physics performance</b>	<b>133</b>
8.1	Simulation methods and conditions . . . . .	133
8.1.1	Hybrid simulation method . . . . .	133
8.1.2	Simulation conditions . . . . .	134
8.2	Heavy flavour . . . . .	134
8.2.1	Motivation . . . . .	134
8.2.2	Expected yields . . . . .	135
8.2.3	D mesons . . . . .	136
8.2.4	Beauty . . . . .	141
8.2.5	Heavy-flavour baryons . . . . .	146
8.2.6	Heavy flavour $R_{AA}$ and $v_2$ . . . . .	151
8.2.7	D meson fragmentation function in jets . . . . .	154
8.3	Low-mass dielectrons . . . . .	155
8.3.1	Motivation . . . . .	155
8.3.2	Experimental aspects and simulation inputs . . . . .	155
8.3.3	Electron reconstruction and background rejection . . . . .	156
8.3.4	Results on physics performance . . . . .	158
8.4	Hypernuclei . . . . .	158
8.5	Summary of the physics reach . . . . .	162
<b>A</b>	<b>Explorer measurement summary</b>	<b>163</b>
<b>B</b>	<b>Alternative Stave implementation options</b>	<b>167</b>
B.1	Microchannel cooling systems . . . . .	167
B.1.1	Polyimide microchannels . . . . .	167
B.1.2	Evaporative cooling with silicon microchannels . . . . .	169
B.2	Chips embedding in flex . . . . .	170
B.3	Serial powering . . . . .	171

<b>Bibliography</b>	<b>173</b>
<b>Glossary</b>	<b>179</b>

# 1 Introduction

ALICE (A Large Ion Collider Experiment) is designed to address the physics of strongly interacting matter, and in particular the properties of the Quark-Gluon Plasma (QGP), using proton–proton, proton–nucleus and nucleus–nucleus collisions at the CERN LHC.

The ALICE apparatus consists of a central barrel, a forward muon spectrometer, and a set of small detectors for triggering and event characterisation. The apparatus allows for a comprehensive study of hadrons, electrons, muons, photons and jets produced in heavy-ion collisions. The Pb–Pb programme is accompanied by precision measurements from pp and p–Pb collisions to provide a quantitative base for comparison with results from Pb–Pb collisions. The ALICE scientific plans and organisation for the approved programme are defined in the ALICE Physics Performance Report Vol. I [1] (scientific programme) and Memorandum of Understanding [2] (the sharing of resources and responsibilities). An updated description of the ALICE detector can be found in [3].

Prior to the start-up of the LHC heavy-ion programme, the nature of the QGP as an almost-perfect liquid emerged from the experimental investigations at CERN SPS and at BNL RHIC. ALICE has confirmed this basic picture, observing the creation of hot hadronic matter at unprecedented values of temperatures, densities and volumes, and exceeding the precision and kinematic reach of all significant probes of the QGP that had been measured over the past decade. These physics results have been achieved by ALICE after only two years of Pb–Pb running and one p–Pb run, demonstrating its excellent capabilities to measure high-energy nuclear collisions at the LHC.

Despite this success there are several frontiers, including high precision measurements of rare probes over a broad range of transverse momenta, for which the current experimental setup is not yet fully optimised. The detector upgrades, combined with a significant increase of luminosity, will enhance the physics capabilities of ALICE enormously. ALICE is therefore preparing a major upgrade of its apparatus, planned for installation in the second long LHC shutdown (LS2) in the years 2018–2019. The ALICE long-term physics goals, its experimental strategy and the upgrade plans are discussed in the ALICE Upgrade Letter of Intent [4]. The main physics topics addressed, which will be briefly discussed in Sec. 1.1, require the measurement of heavy-flavour hadrons, quarkonia, and low-mass dileptons at low transverse momenta, together with novel measurements of jets and their constituents. Many of these measurements in Pb–Pb collisions are characterised by a very small signal-over-background ratio, which calls for large statistics with un-triggered running (“minimum-bias” data). For these measurements, the upgrade will provide an increase of statistics of about two orders of magnitude with respect to the initial programme until LS2. For the measurements that are currently based on rare triggers, the increase in statistics will be of one order of magnitude. All of these measurements require also a significant improvement in vertexing and tracking efficiency at low transverse momentum.

The upgrade strategy is based on the LHC plans to increase the luminosity of Pb–Pb collisions progressively after LS2, eventually reaching an interaction rate of about 50 kHz, i.e. instantaneous luminosity of  $\mathcal{L} = 6 \times 10^{27} \text{ cm}^{-2} \text{ s}^{-1}$ . In the proposed plan, the ALICE detector will be upgraded to enable the read-out of all interactions and accumulate more than  $10 \text{ nb}^{-1}$  of Pb–Pb collisions following LS2, corresponding to about  $10^{11}$  interactions.



The upgrades include:

- A new beampipe with smaller diameter;
- A new, high-resolution, low-material Inner Tracking System (ITS);
- Upgrade of the Time Projection Chamber (TPC), consisting of the replacement of the wire chambers with Gas Electron Multiplier (GEM) detectors and new pipelined read-out electronics;
- Upgrade of the read-out electronics of Transition Radiation Detector (TRD), Time Of Flight detector (TOF), and Muon Spectrometer for high rate operation;
- Upgrade of the forward trigger detectors;
- Upgrade on the online systems and offline reconstruction and analysis framework.

These plans are presented in the ALICE Upgrade Letter of Intent. A new detector, the Muon Forward Telescope (MFT), was recently proposed to add vertexing capabilities to the current Muon Spectrometer. This proposal is contained in the Addendum to the ALICE Upgrade Letter of Intent [5]. The MFT consists of five planes of silicon pixel detectors placed in front of the hadronic absorber, covering the acceptance of the Muon Spectrometer. The detector technology envisaged for the MFT is the same as that proposed for the ITS.

This paper presents the upgrade of the Inner Tracking System. The primary focus of the ITS upgrade is on improving the performance for detection of heavy-flavour hadrons, and of the thermal photons and low-mass dileptons emitted by the QGP. It will be shown that the new ITS will greatly improve the distance of closest approach to the primary vertex, tracking efficiency at low transverse momenta, and read-out capabilities. This document presents the detector specifications and layout, the R&D activities and technical implementation of the main components, and detector and physics performance.

This chapter gives an overview of the physics objectives (Sec. 1.1); current ITS performance and limitations (Sec. 1.2); and the design objectives and layout of the new ITS (Sec. 1.3).

## 1.1 Physics objectives

The goal of the ALICE experiment is the study of the Quark-Gluon Plasma (QGP) state of matter. Properties of the QGP that are accessible to experimental measurement include initial temperature and transport coefficients. Measuring such characteristics would go a long way towards a better understanding of QCD as a genuine multi-particle theory. To achieve this goal, high statistics measurements are required, as these will give access to the very rare physics channels needed to understand the dynamics of this condensed phase of QCD.

The ALICE upgrade addresses the challenge of expected Pb–Pb interaction rates of up to 50 kHz. A key requirement of the upgrade is to develop methods by which 50 kHz Pb–Pb collisions can be inspected with the least possible bias. This implies shipping all data to the online systems either continuously or utilising a minimum bias trigger. Full online calibration, event reconstruction and event data reduction will allow for writing all events on tape, with an overall online data reduction factor of about 20. Such an upgrade would provide an accumulated sample in the order of  $10 \text{ nb}^{-1}$ , which is the minimum needed for the proposed physics programme. The upgrade physics programme is discussed in detail in [4].

Heavy-flavour measurements are the primary scope of a new ITS with largely improved tracking and read-out rate capabilities. The two main open questions concerning heavy-flavour interactions with the QGP medium—along with the corresponding experimental handles—are:

- Thermalisation and hadronisation of heavy quarks in the medium, which can be studied by measuring the heavy-flavour baryon/meson ratio, the strange/non-strange ratio for charm, the azimuthal anisotropy  $v_2$  for charm and beauty mesons, and the possible in-medium thermal production of charm quarks.
- Heavy-quark in-medium energy loss and its mass dependence, which can be addressed by measuring the nuclear modification factors  $R_{AA}$  of the  $p_T$  distributions of D and B mesons separately in a wide momentum range, as well as heavy flavour production associated with jets.

The new measurements that will become possible with the ITS upgrade and  $10\text{ nb}^{-1}$  include:

- D meson  $R_{AA}$  and  $v_2$  down to zero  $p_T$ ;
- $D_s$  meson  $R_{AA}$  and  $v_2$  down to at least  $2\text{ GeV}/c$ ;
- $\Lambda_c$  baryon  $R_{AA}$  and  $v_2$  down to  $2\text{ GeV}/c$  and  $3\text{ GeV}/c$ , respectively;
- baryon/meson ratio for charm ( $\Lambda_c/D$ ) down to  $2\text{ GeV}/c$ ;
- B meson  $R_{AA}$  and  $v_2$  via non-prompt  $D^0$  measurement down to  $2\text{ GeV}/c$ ;
- B meson  $R_{AA}$  and  $v_2$  via non-prompt  $J/\psi$  measurement down to  $1\text{ GeV}/c$ ;
- B meson fully-reconstructed decays ( $B^+ \rightarrow \bar{D}^0 \pi^+$ ) down to  $2\text{ GeV}/c$ ;
- $\Lambda_b$  baryon reconstruction for  $p_T > 7\text{ GeV}/c$ ;
- D meson production within jets, both leading and sub-leading, and D meson fragmentation function over a broad momentum range.

In addition, the reduced material thickness and the improved tracking precision and efficiency of the new ITS provide an essential contribution for a detailed measurement of low-mass dielectrons. This measurement gives access to:

- Thermal radiation from the QGP, via real and virtual photons detected as dielectrons.
- In-medium modifications of hadronic spectral functions related to chiral symmetry restoration, in particular for the  $\rho$  meson in its  $e^+e^-$  decay mode.

The production measurement of hypernuclear states, like  ${}^3_\Lambda\text{H} \rightarrow {}^3\text{He} + \pi^-$ , will also largely benefit from the improved tracking resolution and the high envisaged integrated luminosity.

In summary, the design goals that are instrumental for the physics programme are:

1. Highly efficient tracking, both in association with the TPC and in standalone mode, over an extended momentum range, with special emphasis on very low momenta.
2. Very precise reconstruction of secondary vertices from decaying charm and beauty hadrons.

## 1.2 Current detector performance and limitations

The present ALICE ITS consists of six cylindrical layers of silicon detectors placed coaxially around the beam pipe. The layers are located at radii between 39 mm and 430 mm and cover the pseudo-rapidity range  $|\eta| < 0.9$  for vertices located within  $z = \pm 60$  mm with respect to the nominal interaction point (i.e.  $\pm 1\sigma$  of the luminous region). Within the boundaries set by technological limitations and available funds, the number, position and segmentation of the layers were optimised to achieve a high precision in the determination of the charged particle distance of closest approach to the primary vertex and efficient track finding in combination with the TPC. Therefore, the inner radius is the minimum allowed by the radius of the beam pipe. The outer radius is determined by the necessity to match tracks with those from the TPC. The first layer has a more extended pseudo-rapidity coverage ( $|\eta| < 1.98$ ) which, together with the Forward Multiplicity Detectors (FMD), provides continuous coverage for the measurement of charged particle multiplicity. As will be illustrated in Chap. 7 optimising the detector geometry to achieve the highest standalone tracking efficiency would lead to an alternative configuration including a larger number of layers and different radii.

As a result of the high particle density (the current system is designed for up to 100 particles per  $\text{cm}^2$  for Pb–Pb collisions at  $\sqrt{s_{NN}} = 5.5$  TeV), and in order to achieve the required accuracy in the measurement of the track distance of closest approach, the first two layers of the ITS are made of Silicon Pixel Detectors (SPD), while the two middle layers are made of Silicon Drift Detectors (SDD). The two outer layers, where the track density has fallen to one particle per  $\text{cm}^2$ , are equipped with double-sided Silicon micro-Strip Detectors (SSD). The four outer layers have analogue read-out and therefore can be used for particle identification (PID) via  $dE/dx$  measurement in the non-relativistic ( $1/\beta^2$ ) region. All detector elements were carefully optimised to minimise their radiation length, achieving 1.1 %  $X_0$  per layer, the lowest value among all the current LHC experiments.

The performance of the present ITS for tracking and identifying charged particles in pp and Pb–Pb collisions will be discussed in Chap. 7. The capabilities for heavy flavour detection will be reviewed in Chap. 8. The precision of the present ITS in the determination of the track distance of closest approach is adequate to study the production of charm mesons in exclusive decay channels (e.g.  $D^0 \rightarrow K\pi$  and  $D^+ \rightarrow K\pi\pi$ ) at values of transverse momentum above 1 GeV/c. At lower transverse momenta, however, the statistical significance of the measurement is insufficient for currently achievable datasets.

The challenge is even greater for charm baryons. The most abundantly produced charm baryon ( $\Lambda_c$ ) has a proper decay length ( $c\tau$ ) of only 60  $\mu\text{m}$ . This is lower than the impact parameter resolution of the present ITS in the transverse momentum range of the majority of  $\Lambda_c$  daughter particles. Therefore, charm baryons are presently not measurable by ALICE in central Pb–Pb collisions. For the same reasons as outlined above, the study of beauty mesons, beauty baryons, and of hadrons with more than one heavy quark are also beyond the capability of the current detector.

A crucial limitation of the present ITS detector is given by its limited read-out rate capabilities. The ITS can run at a maximum rate of 1 kHz (with dead time close to 100 %), irrespective of the detector occupancy. For all physics channels that cannot be selected by a trigger, this rate limitation restricts ALICE to use only a small fraction of the full Pb–Pb collision rate of 8 kHz that the LHC presently can deliver and prevents the collection of required reference data in pp collisions. Clearly the present ITS is inadequate to fulfil the required rate capabilities envisaged for the ALICE long-term plans discussed in the previous section.

Finally, the impossibility to access the present ITS detector for maintenance and repair interventions during the yearly LHC shutdowns represents a major limitation in sustaining

high data quality. Rapid accessibility to the detector is a key priority in the design of the upgraded ITS.

### 1.3 Upgrade overview

#### 1.3.1 Upgrade concept

In this section, the key features of the ITS upgrade will be discussed and compared to the present ITS, following the considerations presented in Sec. 1.1 and Sec. 1.2.

- **First detection layer closer to the beam line:** the reduction of the beampipe diameter in the centre of the ALICE detector is one of the main ingredients to improve the measurement of the impact parameter resolution. As will be discussed in detail in Sec. 5.4.1, current studies indicate that it should be possible to arrive at a beampipe inner radius of 17.2 mm, to be compared to the present value of 29 mm. However, in this TDR a conservative number of 19.2 mm for the beampipe inner radius is assumed. The wall thickness of the central Beryllium beampipe section is assumed to be 0.8 mm. Using a smaller value of 0.5 mm is challenging due to possible issues with gas tightness and mechanical stability.
- **Reduction of material budget:** reducing the material budget of the first detection layer is particularly important for improving the impact parameter resolution. In general, reducing the overall material budget will allow the tracking performance and momentum resolution to be significantly improved. As will be shown in Chap. 4, the use of Monolithic Active Pixel Sensors (MAPS) will allow the silicon material budget per layer to be reduced by a factor of seven in comparison to the present ITS (50  $\mu\text{m}$  instead of 350  $\mu\text{m}$ ). A careful optimisation of the analogue front-end timing specifications and read-out architecture will allow the power density to be reduced by a factor of at least two. At the same time this will increase the pixel density by a factor of 50.

The lower power consumption and a highly optimised scheme for the distribution of the electrical power and signals will allow the material budget of the electrical power and signal cables to be reduced by a factor of five. Mechanics, cooling and other detector elements can also be slightly improved when compared to the present ITS design. Combining all these new elements together, it should be possible to build a detector with a radiation length of 0.3%  $X_0$  per layer or better for the three Inner Layers.

An example of the feasibility of such a design is represented by the STAR HFT detector [6]. Achieving such a low material budget is particularly critical for the first detection layer, since it affects strongly the impact parameter resolution at low  $p_T$  where the resolution is mainly determined by multiple Coulomb scattering.

- **Geometry and segmentation:** the studies presented in this document are based on a detector consisting of seven concentric cylindrical layers covering a radial extension from 22 mm to 430 mm with respect to the beamline. The physics studies of the benchmark channels presented in Chap. 8 are based on the assumption that all layers are segmented in pixels with dimensions of 20  $\mu\text{m} \times 20 \mu\text{m}$ . However, as will be illustrated in Chap. 7, the detector performance in terms of impact parameter resolution and standalone momentum does not change significantly, if the cell size for the inner layers would increase to 30  $\mu\text{m} \times 30 \mu\text{m}$  and the outermost four layers would have a much lower granularity, for example 50  $\mu\text{m} \times 50 \mu\text{m}$ .

- **Measurement of energy loss:** the new detector will not measure the ionisation in the silicon layers. As will be shown in detail in Chap. 8, in order to assess the benefit of PID capabilities, studies have been carried out on benchmark measurements of the ALICE upgrade programme that should be most sensitive to low-momentum PID, namely the low-mass di-electron analysis and the  $\Lambda_c \rightarrow pK\pi$  reconstruction. These studies have shown that if the new ITS would preserve the same PID capabilities as the current one, the benefit on the benchmark channels considered would be marginal. Therefore, on this basis it is proposed to have a new ITS with binary read-out without information on the charge signal amplitude. It is assumed that all measurements that are being performed with the current detector using the ITS PID (identified charged hadron spectra, flow and correlations) will have been completed by the end of the LHC second run, before the ALICE upgrade scheduled for LS2. Moreover, the possibility to use the information of the cluster size to identify light hyper-nuclei is being studied (see Chap. 8).
- **Read-out time:** as mentioned in Sec. 1.2, the present ITS features a maximum read-out rate of 1 kHz. The new detector is designed to be able to read the data related to each individual interaction up to a rate of 100 kHz for Pb–Pb collisions and 400 kHz for pp collisions, a factor two higher than the ALICE upgrade requirements. The read-out architectures that allows such rates to be achieved are presented in Chap. 6.

On the basis of the above considerations, the baseline solution for the layout of the ITS upgrade is to replace the existing ITS detector in its entirety with seven concentric layers of pixel detectors. Monolithic Active Pixel Sensors (MAPS) implemented using the 0.18  $\mu\text{m}$  CMOS technology of TowerJazz have been selected as the technology for all layers. The basic MAPS element is the Pixel Chip. It consists of a single silicon die of about 15 mm  $\times$  30 mm, which incorporates a high-resistivity silicon epitaxial layer (sensor active volume), a matrix of charge collection diodes (pixels) with a pitch of the order of 30  $\mu\text{m}$ , and the electronics that perform signal amplification, digitisation and zero-suppression. Only the information on whether or not a particle was crossing a pixel is read out. The main functional elements of the new ITS are introduced in the following section, while its main geometrical parameters are listed in Tab. 1.1.

As will be shown in Chap. 7, a new silicon tracker featuring the characteristics listed above will enable the track position resolution at the primary vertex to be improved by a factor of three or greater. The standalone tracking efficiency would be comparable to what can be presently achieved by combining the information of the ITS and the TPC, but extended to much lower values of transverse momentum. The relative momentum resolution of the silicon tracker standalone would be about 4 % up to 2 GeV/ $c$  and remain below 6 % up to 20 GeV/ $c$ .

### 1.3.2 Detector layout overview

The geometry and requirements of the new ITS provide a natural grouping of the seven layers in two separate barrels (Inner Barrel and Outer Barrel), each with different specifications, as shown in Figs. 1.1 and 1.2. The Inner Barrel consists of the three innermost layers, also referred to as Inner Layers (Layers 0 to 2), while the Outer Barrel contains the four outermost layers, also referred as Outer Layers (Layers 3 to 6). The ITS layers are azimuthally segmented in units named Staves, which are mechanically independent. Staves are fixed to a support structure, half-wheel shaped, to form the Half-Layers. The term Stave will be used to refer to the complete detector element. It consists of the following main components:

**Table 1.1:** Geometrical parameters of the upgraded ITS.

	Inner Barrel			Outer Barrel			
	Inner Layers			Middle Layers		Outer Layers	
	Layer 0	Layer 1	Layer 2	Layer 3	Layer 4	Layer 5	Layer 6
Radial position (min.) (mm)	22.4	30.1	37.8	194.4	243.9	342.3	391.8
Radial position (max.) (mm)	26.7	34.6	42.1	197.7	247.0	345.4	394.9
Length (sensitive area) (mm)	271	271	271	843	843	1475	1475
Pseudo-rapidity coverage <sup>a</sup>	$\pm 2.5$	$\pm 2.3$	$\pm 2.0$	$\pm 1.5$	$\pm 1.4$	$\pm 1.4$	$\pm 1.3$
Active area (cm <sup>2</sup> )	421	562	702	10 483	13 104	32 105	36 691
Pixel Chip dimensions (mm <sup>2</sup> )				15 $\times$ 30			
Nr. Pixel Chips	108	144	180	2688	3360	8232	9408
Nr. Staves	12	16	20	24	30	42	48
Staves overlap in $r\phi$ (mm)	2.23	2.22	2.30	4.3	4.3	4.3	4.3
Gap between chips in $z$ ( $\mu$ m)				100			
Chip dead area in $r\phi$ (mm)				2			
Pixel size ( $\mu$ m <sup>2</sup> )	(20 – 30) $\times$ (20 – 30)			(20 – 50) $\times$ (20 – 50)			

<sup>a</sup> The pseudorapidity coverage of the detector layers refers to tracks originating from a collision at the nominal interaction point ( $z = 0$ ).

- **Space Frame:** truss-like lightweight mechanical support structure for the single stave based on composite material (carbon fiber).
- **Cold Plate:** carbon ply that embeds the cooling pipes.
- **Hybrid Integrated Circuit:** assembly consisting of the polyimide flexible printed circuit (FPC) on which the Pixel Chips ( $2 \times 7$ ) and some passive components are bonded.
- **Half-Stave:** the Stave of the Outer Barrel is further segmented in azimuth in two halves, named Half-Stave. Each Half-Stave consists of a number of modules glued on a common cooling unit.
- **Module:** The Staves of the Outer Barrel are further segmented longitudinally to Modules. Each Module consists of a Hybrid Integrated Circuit that is glued onto a carbon plate (Module Plate).

The Staves for the Inner Barrel and the Outer Barrel are illustrated schematically in Fig. 1.3.

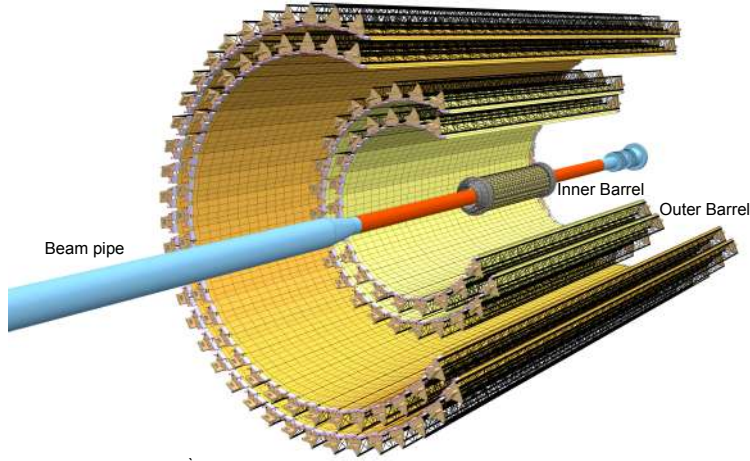


**Figure 1.1:** Layout of the new ITS detector.

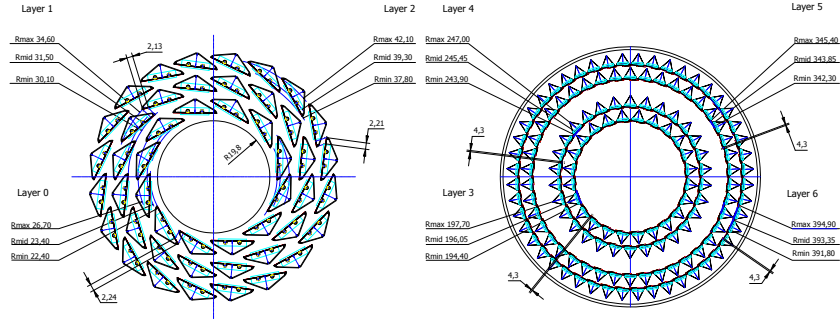


**Figure 1.2:** Schematic view of the cross section of the Inner Barrel (left) and Outer Barrel (right).

### 1.3.3 Experimental conditions

The experimental conditions in terms of interaction rates and particle multiplicity, which have been used as basis for the definition of the detector specifications and simulation of its performance, are presented below.

Table 1.2 summarises the expected maximum hit densities for primary and secondary charged particles. An additional contribution to the overall particle load comes from  $e^+e^-$  pairs generated in the electromagnetic interaction of the crossing ion bunches. These will be referred to as QED electrons. The latter contribution depends on the detector integration time.

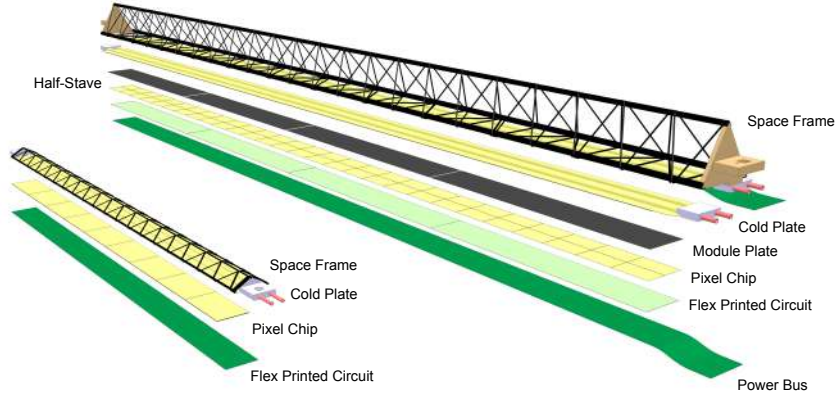


**Figure 1.3:** Schematic drawing of the Inner Barrel (left) and Outer Barrel (right) Staves.

**Table 1.2:** Expected maximum hit densities and radiation levels (see text for details).

Layer	Radius (mm)	Particle fluxes		Radiation doses	
		Prim. & sec. particles <sup>a</sup> (cm <sup>-2</sup> )	QED electrons <sup>b</sup> (cm <sup>-2</sup> )	NIEL <sup>c</sup> (1 MeV n <sub>eq</sub> /cm <sup>2</sup> )	TID <sup>c</sup> (krad)
0	23	30.4	6.02	$9.2 \times 10^{12}$	646
1	32	20.4	3.49	$6.0 \times 10^{12}$	380
2	39	14.9	2.35	$3.8 \times 10^{12}$	216
3	196	1.0	$2.1 \times 10^{-2}$	$5.4 \times 10^{11}$	15
4	245	0.7	$9.0 \times 10^{-3}$	$5.0 \times 10^{11}$	10
5	344	0.3	$1.3 \times 10^{-3}$	$4.8 \times 10^{11}$	8
6	393	0.3	$4.0 \times 10^{-4}$	$4.6 \times 10^{11}$	6

<sup>a</sup> maximum hit densities in central Pb–Pb collisions (including secondaries produced in material)

<sup>b</sup> for an integration time of 10  $\mu$ s, an interaction rate of 50 kHz, a magnetic field of 0.2 T and  $p_T > 0.3$  MeV/c; a magnetic field of 0.2 T, which is planned for a run dedicated to the measurement of low-mass di-electrons, corresponds to the worst case scenario in terms of detector occupancy

<sup>c</sup> including a safety factor of ten

The expected radiation doses and hadron fluences for the upgraded ITS detector are computed for the following integrated luminosities, which correspond to the target statistics needed for the proposed physics studies:

- $8 \times 10^{10}$  Pb–Pb inelastic collisions;
- $1 \times 10^{11}$  p–Pb inelastic collisions;
- $4 \times 10^{11}$  pp inelastic collisions.

A conservative safety factor of ten is further applied to take into account uncertainties on the beam background, possible beam losses, inefficiency in data taking and data quality requirements. The expected radiation levels are summarised in Tab. 1.2. As will be explained in Chap. 2, the technology adopted for the new ITS Pixel Chip shows no significant performance degradation when exposed to these radiation levels even when operated at room temperature.



### 1.3.4 Document summary

Chapter 2 deals with the R&D activities on the Pixel Chip. It first covers the most relevant characteristics of the CMOS technology adopted for the implementation of the Pixel Chip and the principle of operation of MAPS. The main requirements of the Pixel Chip for the new ITS are then introduced and compared with the specifications of the pixel chip recently developed for the STAR HFT detector. The design and experimental characterisation of several prototype circuits, which were developed to optimise the different parts of the final Pixel Chip, are presented in detail. The chapter concludes with an outlook on the R&D needed to complete the development of the Pixel Chip.

Chapter 3 covers several aspects related to the Pixel Chip production testing and quality assurance. The procurement and qualification of the silicon wafers used for the fabrication of the Pixel Chip, with special focus on the aspects related to the thickness and resistivity of the epitaxial layer, the R&D on thinning and dicing and first ideas on the Pixel Chip series test are presented.

Chapter 4 presents the design and characterisation of the full-scale prototypes of the Staves for the Inner Barrel and Outer Barrel. The prototypes developed so far are equipped with dummy silicon chips, and their characterisation covers only the mechanical and thermal aspects.

The detector's overall layout and services, and its integration in the ALICE central barrel are discussed in Chap. 5. This chapter deals also with the aspects related to the precision and stability with which the relative position of the detector modules can be defined, and with the alignment of the overall detector with respect to the beampipe and the other ALICE detectors.

The complete read-out chain, from the Pixel Chip to the ALICE DAQ system, is discussed in Chap. 6.

The detector performance and physics studies, which are based on Monte Carlo simulations that include the transport of particles in a detailed model of the new detector, are presented in Chap. 7 and 8 respectively.

Finally, Chap. ?? presents the project time schedule, organisation, cost estimate and preliminary sharing of responsibilities among the participating institutes.

## 2 Pixel Chip

The particle sensors and the associated read-out electronics to be used for vertexing and tracking detection systems in particle physics experiments have very demanding requirements in terms of granularity, material thickness, read-out speed, power consumption and radiation hardness. The development of sensors based on silicon (Si) semiconductor technology and of read-out electronics based on CMOS technology (application-specific integrated circuits, ASICs) in the 1980s revolutionised the implementation of such detection systems. This technology can be used to match the majority of the above requirements. Given this, Si microstrip and pixel sensors are at the heart of the majority of particle tracking systems used in particle physics experiments today. Nevertheless, compromises exist in the implementation of this technology. Perhaps the most significant is the interface between the sensor and the read-out electronics, i.e. they are typically separate components. For example, the state-of-the-art Si pixel detectors used in the innermost layers of the LHC experiments ATLAS, CMS, LHCb and ALICE all consist of Si pixel sensors bump-bonded to CMOS read-out electronics. This technology can be optimised by thinning both sensor and read-out ASIC as well as reducing the bump-bonding pitch as much as possible. Nevertheless there are technical limitations and these are close to being reached with the present detectors. To go beyond these limitations and construct detection systems with, for example higher granularity and less material thickness, requires the development of new technology. The optimal way to achieve this is to integrate both sensor and read-out electronics to create a single detection device. This is the approach taken with CMOS Monolithic Active Pixels Sensors (MAPS).

Over the last 15 years, extensive R&D has been carried out on MAPS. This has brought the technology to the level where it is now, a viable option for vertexing and tracking detection systems in particle and nuclear physics. The technology can meet the majority of the requirements of such systems. There are limitations, however; most significantly its limited radiation tolerance and moderate read-out time. It is, however, a very promising technology for heavy-ion experiments such as ALICE, which have less stringent radiation tolerance and read-out time requirements. It is also in such experiments, where measurements at low transverse momentum are crucial, that the advantages of MAPS technology are readily seen. The first large scale application of MAPS technology in a collider experiment is to the STAR PXL detector, currently under construction as an upgrade to the STAR detector at RHIC. The first three sectors have recently been successfully installed and the full PXL detector will be commissioned in early 2014.

Unfortunately the technology used for STAR (the ULTIMATE sensor developed by the IPHC PICSEL group in 0.35  $\mu\text{m}$  technology) does not meet the specifications for the ALICE ITS upgrade, particularly in terms of read-out time. In principle, this limitation can be overcome by using the 0.18  $\mu\text{m}$  technology of TowerJazz as described below.

We have addressed the radiation hardness of the sensors implemented using the TowerJazz technology, the design of optimised pixel cells and of low-power read-out architectures using several existing and new prototypes. New ALICE prototype sensors incorporating four different architectures have been designed and fabricated, and first tests performed. In this chapter, we shall first describe the most relevant features of the CMOS technology selected for the implementation of the Pixel Chip (Sec. 2.1) and explain the principle of operation of such a sensor (Sec. 2.2). We shall then discuss the requirements for the

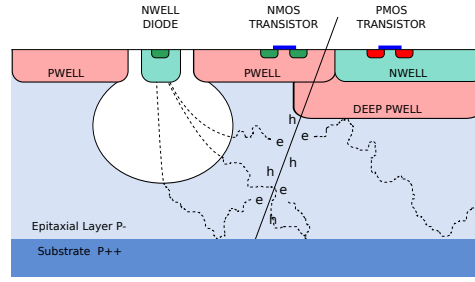


**Figure 2.1:** Schematic cross section of a MAPS pixel in the TowerJazz 0.18  $\mu\text{m}$  imaging CMOS with the deep p-well feature.

ALICE ITS Pixel Chip (Sec. 2.3) and briefly present the specifications of the STAR pixel detector, which is the first large-scale application of CMOS sensors in a HEP experiment (Sec. 2.4). It will be shown that the state-of-the-art MAPS do not fulfil the ALICE ITS requirements, which motivates the development of new architectures (Sec. 2.5). Several prototypes have been developed to optimise the different parts of the Pixel Chip. The prototypes and their characterisation are presented in Sec. 2.6. All aspects related to the radiation hardness of the technology and the specific circuits implemented in the ALICE Pixel Chip are discussed in Sec. 2.7. The chapter concludes with a summary (Sec. 2.8), giving the prospect for the development of the final chip.

## 2.1 Detector technology

The 0.18  $\mu\text{m}$  CMOS technology by TowerJazz has been selected for the implementation of the Pixel Chip for all layers of the new ITS. Figure 2.1 shows a schematic cross section of a pixel in this technology. In the following section, we discuss the main features that make this technology suitable, and in some respect unique, for the implementation of the ITS Pixel Chip.

- Due to the transistor feature size of 0.18  $\mu\text{m}$  and a gate oxide thickness below 4 nm, it is expected that the CMOS process is substantially more robust to the total ionising dose than other technologies (such as 0.35  $\mu\text{m}$ ) employed up to now as the baseline for the production of CMOS sensors in particle physics applications.
- The feature size and the number of metal layers available (up to six) are adequate to implement high density and low power digital circuits. This is essential since a large part of the digital circuitry (e.g. memories) will be located at the periphery of the pixel matrix and its area must be minimised to reduce the insensitive area as much as possible.
- It is possible to produce the chips on wafers with an epitaxial layer of up to 40  $\mu\text{m}$  thickness and with a resistivity between 1  $\text{k}\Omega\text{cm}$  and 6  $\text{k}\Omega\text{cm}$ . With such a resistivity, a sizeable part of the epitaxial layer can be depleted. This increases the signal-to-noise ratio and may improve the resistance to non-ionising irradiation effects.
- The access to a stitching technology allows the production of sensors with dimensions exceeding those of a reticle and enables the manufacturing of die sizes up to a single die per 200 mm diameter wafer. As a result, insensitive gaps between neighbouring chips disappear and the alignment of sensors on a Stave is facilitated. This option

has not yet been exploited by the prototypes, but is foreseen as an option for future large-scale chips.

- The availability of a deep p-well option allows the production of pixel structures with significantly enhanced functionality.

The last point is a unique feature of this process and can be key to enable low-power read-out architectures. In standard implementations, the sensing diode is an n-well normally used as the substrate of PMOS transistors. As a consequence, only NMOS transistors can be used in the pixel area. In fact, any PMOS transistor requires an additional n-well that competes with the sensing diode in collecting the signal charge. The front-end electronics located in the pixel must fully rely on NMOS devices, so only simple, low-gain amplifiers or source followers can be implemented. Hit discrimination, which requires more sophisticated signal processing, cannot be performed at the pixel level and the full matrix must be scanned during the read-out phase. A few alternatives have been proposed to allow the use of PMOS in the pixel, like the use of deep n-well and of high voltage CMOS technologies. However, both options lead to a significant increase of the capacitance of the sensing electrode. Therefore, the power consumption in the front-end must be increased accordingly to preserve an adequate signal-to-noise ratio. The use of a deep p-well in the region where the front-end electronics is foreseen circumvents this problem (cf. Fig. 2.1). The n-wells that accommodate the PMOS transistors are fabricated on top of the deep p-well. The signal electrons are reflected by the electric potential at the junction between the epitaxial layer and the deep p-well and can be collected only by the sensing diode. Its size can then be tailored to optimise the charge collection efficiency and the signal-to-noise ratio, while full CMOS front-end electronics can be put in the pixel. The effectiveness of the deep p-well approach has already been demonstrated and circuits with complex front ends similar to those used for hybrid sensors read-out have already been produced. The focus of the ALICE R&D is on assessing the radiation hardness and on studying the deep p-well approach in order to design circuits that minimise power consumption and integration time.

## 2.2 Principle of operation

### 2.2.1 Particle detection

As indicated in Fig. 2.1, when a charged particle traverses the silicon sensor's active volume, it liberates charge carriers (electrons and holes) in the semiconductor material. The released charge is then collected by electrodes that reveal not only the presence of a particle but also—due to a fine segmentation—its impinging point onto the sensor. The nature and quantitative behaviour of the charge collection mechanism are functions of the material properties (resistivity or doping level/profile) and geometry (thickness of sensitive material, pixel pitch, electrode shape) as well as the electric field configuration (electrode potential and geometry) of the sensor. The amount of deposited charge depends on the particle species and its momentum (Bethe-Bloch). Minimum ionising particles (MIPs, e.g. 0.5 GeV/c pions), which define the requirement on the minimal detectable charge, typically release some 60 electrons per 1  $\mu\text{m}$  path length in thin silicon layers [7].

An extensive R&D program is carried out to optimise the charge generation, collection and its transformation into an electrical signal. Different substrate materials have been considered. They consist of an epitaxial layer grown on top of a low-resistivity silicon wafer used for standard CMOS manufacturing. The resistivity and thickness of the epitaxial layer range from 1 k $\Omega$  cm to 6 k $\Omega$  cm and from 18  $\mu\text{m}$  to 40  $\mu\text{m}$ , respectively. The possibility of using high-resistivity Czochralski wafers, with a resistivity larger than 1 k $\Omega$  cm, is also

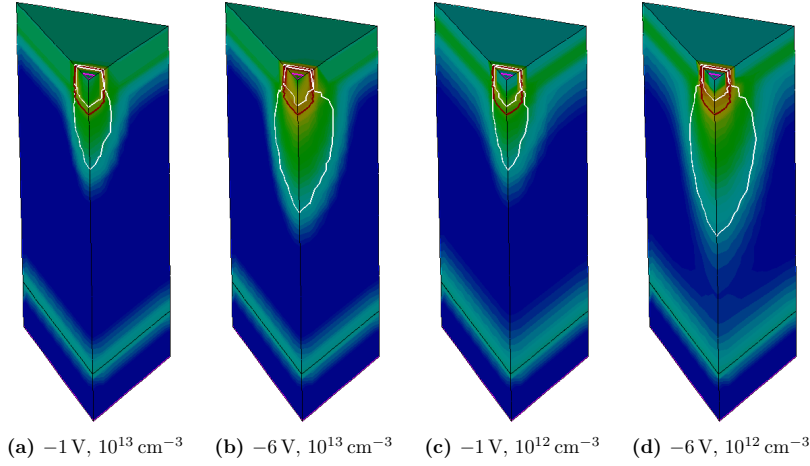


**Figure 2.2:** Semiconductor device simulations of the different settings of total diode reverse bias and epitaxial layer doping. The diode is made of a  $3\text{ }\mu\text{m} \times 3\text{ }\mu\text{m}$  square n-well, which has a  $0.5\text{ }\mu\text{m}$  spacing to the surrounding p-well. Shown is one eighth of the total pixel. The colour code shows logarithmically the absolute value of the electrical field, and the white line indicates boundaries of the depletion region.

being studied. More details on the properties of the substrate materials used for the manufacturing of the CMOS Pixel Chips are given in Sec. 3.1. For the optimisation of the pixel layout an extensive set of different structures with different read-out circuits were developed and characterised, namely the MIMOSA-32/-34 (Sec. 2.6.2), CHERWELL-1 (Sec. 2.6.3) and Explorer (Sec. 2.6.4) families. The latter is designed to allow reverse bias on the substrate, increasing the reverse voltage on the collection diode up to  $-8\text{ V}$  with respect to the typical values of  $-0.8\text{ V}$  to  $-1.6\text{ V}$  used in this technology.

The influence of the different geometries and starting materials has been studied by semiconductor device simulations. While a quantitative prediction is very difficult to achieve since it depends on the precise knowledge of doping profiles, it gives some qualitative insights. Figure 2.2 shows the depleted volume inside the pixel cell for different configurations.

Another important aspect of the detection circuitry is the noise originating mainly from the input capacitance ( $kTC$  noise) and the small input transistor (in particular random telegraph signal noise, RTS noise).  $kTC$  noise is created by resetting the collection electrode, i.e. by recharging the diode capacitance. One way to mitigate this noise contribution is to measure the voltage signal on the diode twice and subtract the value of the first measurement from the second one (correlated double sampling, CDS). The RTS noise is known to depend on the transistor geometries and type (NMOS or PMOS) and different layouts are under study to identify the best performing one. RTS noise typically diminishes when increasing the size, which however also increases the capacitance; some trade-off between gain and noise needs to be made. Additional so-called shot noise is caused by the leakage of the collection node. Its magnitude is proportional to the square root of the number of leaked electrons and hence does not only depend on the electrode geometry but also on the integration time.

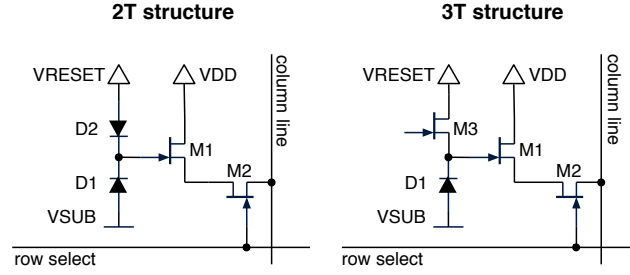


**Figure 2.3:** Simplified schematic drawing of the 2T and 3T pixel structures, as used in the rolling-shutter read-out scheme.

### 2.2.2 Read-out

The traditional MAPS in-pixel circuits are the so called 2T and 3T structures (Fig. 2.3). The pixel electrode is connected to a source follower (M1) that buffers the analogue voltage signal. A second transistor (M2) is used as a switch to select the output of the buffer and make it available to the corresponding column line, such that it can be read out at the end of column circuitry. A variation of this circuit is the so-called 3T structure that includes an extra transistor (M3) to actively reset the pixel. The way such an arrangement is read out is called a rolling-shutter read-out (cf. Fig. 2.4): rows are read out one after the other by selecting the row switches (M2) and—in case of 3T—applying the reset pulse shortly after. In this way each row integrates the signal between two consecutive passings of the row-select signal (the shutter) and each row is essentially continuously sensitive. The biggest advantages of this architecture are the very small number of transistors needed within each pixel and that it can be implemented with transistors of the same polarity, which is a requirement in standard CMOS imaging processes.

In the scope of the ALICE ITS upgrade, the only information of relevance is whether or not a particle is crossing a pixel. This information is obtained by applying a threshold to the analogue signal of a collection node. Where and how this is done is where the proposed architectures differ the most.

The most common way to get the binary information is to use the rolling-shutter architecture and place a comparator at the end of column. This technique is followed by MISTRAL (Sec. 2.5.1) which, however, takes advantage of the smaller feature size and reads out two rows at once, speeding up the read-out process by a factor of two and halving the integration time. Due to the small feature sizes, a variation to this arrangement becomes available: one may place the comparator inside the free area of several pixels (as done by CHERWELL, Sec. 2.5.3). One may even place a single comparator within each pixel (as done by ASTRAL, Sec. 2.5.2). The big advantage of the last structure is that the analogue signal is propagated over a short distance, reducing the capacitive load on the line drivers, hence reducing the power consumption and increasing the read-out speed. ASTRAL is still using a rolling shutter to read out the fired pixels, but the column drivers now drive digital signals, which requires less power.

When the digital information is available in the pixel itself, one may consider other read-out schemes as well. One prominent example is a data-driven read-out in which the digital outputs of the pixels are fed into an encoder circuit that generates directly the address of a hit pixel. This can, in turn, be used to reset this pixel and go to the next valid one; the procedure is iterated until all pixels are read out. The big advantage, in addition to

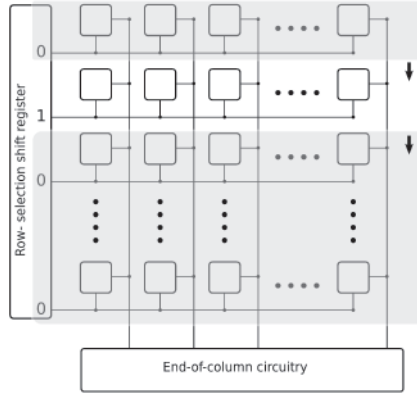


**Figure 2.4:** Principle of the rolling-shutter read-out scheme.

the low power consumption, is the fast read-out time. This approach is followed by the ALPIDE development (Sec. 2.5.4).

It is important to note that the way the read-out is performed in the rolling-shutter architecture implies that the sensor is always integrating for a full shutter period, which typically ranges between  $30\ \mu\text{s}$  (MISTRAL, CHERWELL) and  $20\ \mu\text{s}$  (ASTRAL). Signals from all events within this time are integrated, which leads to pile-up in case of large bunch-crossing rates. A certain amount of pile-up can be tolerated since the global ALICE tracking can separate hits from tracks belonging to different events based on the information of other detectors (studied in Chap. 7). In the case of the ALPIDE chip, different read-out schemes are followed. In its default mode of operation a global strobe signal is used to capture the output of the comparator front end into a local memory. The effective integration time is about  $4\ \mu\text{s}$  and is given by the shaping time of the front end.

### 2.3 General requirements

The physics objectives and the design goals outlined in Chap. 1 have led to the following requirements for the Pixel Chip:

- **Silicon thickness:** To minimise its contribution to the overall material budget of the ITS, it is desirable to make the chip as thin as possible. The minimal thickness is determined by the epitaxial layer height (nominal value is  $18\ \mu\text{m}$ ) plus the height of the CMOS stack (around  $10\ \mu\text{m}$ ). The fabrication of such a chip is done by thinning a standard-height wafer from the back. To remain within a safety margin, a thickness of  $50\ \mu\text{m}$  is required.
- **Intrinsic spatial resolution:** The performance of the ITS upgrade and in particular its capability to separate secondary vertices of heavy flavour decays is determined by the impact parameter resolution. This is a convolution of the primary vertex resolution and the track pointing resolution and it is mainly determined by the performance of the Inner Barrel. An intrinsic spatial resolution of  $5\ \mu\text{m}$  ( $10\ \mu\text{m}$ ) for the Inner (Outer) Barrel is required.
- **Chip dimensions:** The TowerJazz  $0.18\ \mu\text{m}$  CMOS technology allows for a maximum chip length of  $30\ \text{mm}$  in  $z$ -direction. A longer sensor would require the use

of stitching technologies. The limitation of the chip width to 15 mm was motivated by geometrical considerations. For such width the deviation of the distance of each pixel from the nominal radius of each layer, the number of azimuthal segments and the deviation from an azimuthally vertical incidence angle are kept reasonably small. A chip size of 15 mm  $\times$  30 mm has consequently been chosen as baseline chip dimension.

For the Outer Layers it might turn out beneficial to have a differently sized chip. In particular, a rotated chip with a length of 30 mm in  $r\phi$  direction is an interesting option since it would reduce the needed overlap of the Outer Layers. This would, however, require the development of a modified chip for the Outer Layers with respect to the one adopted for the Inner Layers. This is not pursued by solutions presented below, but is kept as a future development option.

- **Maximum dead area:** To assure a hermetic detector configuration, overlaps of the chips are foreseen in  $r\phi$  to allow for placing digital circuitry at their boundaries. This leads to localised increases of the material budget and thus needs to be minimised. In  $z$  there is no such overlap foreseen and the dead area has a more stringent requirement. The performance simulations have been performed assuming a dead area of 2 mm in  $r\phi$ - and 25  $\mu$ m in  $z$ -direction.
- **Power density:** The maximum tolerable material budget puts severe limitations on the amount of material that can be used for power distribution and detector cooling. The power density on the sensor has thus to be brought to a minimum and should not exceed 300 mW cm<sup>-2</sup> for the Inner Layers and 100 mW cm<sup>-2</sup> for the Outer Layers, in order to be compatible with the material budget requirement of 0.3 %  $X_0$  and 0.8 %  $X_0$ , respectively.
- **Integration time<sup>1</sup>:** In order to cope with interaction rates of up to 50 kHz for Pb–Pb and up to 400 kHz for pp collisions, the maximum acceptable sensor integration time is about 30  $\mu$ s in order to limit pile-up effects and a consequent loss of tracking efficiency (see Chap. 7).
- **Dead time at 50 kHz interaction rate:** A dead time of 10 % at 50 kHz Pb–Pb interaction rate can be tolerated. On-chip memories and bandwidths must be dimensioned such that they can cope with the expected occupancy level.
- **Detection efficiency and fake hit rate:** A detection efficiency of at least 99 % and a fake hit rate of not more than 10<sup>-5</sup> per pixel and event are necessary to achieve the required track reconstruction performance.
- **Radiation hardness:** In order to ensure full functionality, especially for the ITS Inner Layers, the pixel detectors will have to be tolerant against the radiation levels expected for the innermost Layer (radius of 22 mm) of 700 krad of Total Ionising Dose (TID) and a fluence of 10<sup>13</sup> 1 MeV n<sub>eq</sub>/cm<sup>2</sup> of Non-Ionising Energy Loss (NIEL), including a safety factor of ten for a collected data set corresponding to 10 nb<sup>-1</sup> Pb–Pb and 6 pb<sup>-1</sup> pp, and 50 nb<sup>-1</sup> p–Pb collisions.

The main requirements are summarised in Tab. 2.1. The implementation of a MAPS detector matching these requirements greatly benefits from development efforts carried out for the STAR HFT detector, as explained in the next section.

<sup>1</sup>The architecture dependent read-out time will be discussed in the sections describing the ALICE developments.



**Table 2.1:** Pixel detector general requirements.

Parameter	Inner Barrel	Outer Barrel
Max. silicon thickness		50 $\mu\text{m}$
Intrinsic spatial resolution	5 $\mu\text{m}$	10 $\mu\text{m}$
Chip size	15 mm $\times$ 30 mm ( $r\phi \times z$ )	
Max. dead area on chip	2 mm ( $r\phi$ ), 25 $\mu\text{m}$ ( $z$ )	
Max. power density	300 mW/cm <sup>2</sup>	100 mW/cm <sup>2</sup>
Max. integration time		30 $\mu\text{s}$
Max. dead time	10 % at 50 kHz Pb–Pb	
Min. detection efficiency		99 %
Max. fake hit rate		10 <sup>−5</sup>
TID radiation hardness <sup>a</sup>	700 krad	10 krad
NIEL radiation hardness <sup>a</sup>	10 <sup>13</sup> 1 MeV n <sub>eq</sub> /cm <sup>2</sup>	3 $\times$ 10 <sup>10</sup> 1 MeV n <sub>eq</sub> /cm <sup>2</sup>

<sup>a</sup> This includes a safety factor of ten.

## 2.4 STAR pixel detector

The STAR Heavy Flavor Tracker (HFT) is conceived with a similar purpose as the upgraded ITS in ALICE, to construct a state-of-the-art silicon micro vertex detector, capable of displaced vertex identification in heavy-ion collisions below 50  $\mu\text{m}$ , opening the way to precision charm and beauty physics. The STAR HFT is the first vertex detector based on MAPS. The first three sectors were installed in May 2013 in the STAR experiment at RHIC and tested in an engineering run with proton and light ion beams, while the full pixel detector will be commissioned in early 2014.

The two innermost layers form the PXL detector [8] and consist of high resolution MAPS, the ULTIMATE (MIMOSA-28) sensors [9] developed at IPHC CNRS. The ULTIMATE sensor is manufactured in the AMS 0.35  $\mu\text{m}$  OPTO process, consisting of 928 rows and 960 columns (active area of 3.8 cm<sup>2</sup>, integration time 190  $\mu\text{s}$ ) with binary output and integrated zero suppression logic. The pixels have a 15  $\mu\text{m}$  thick epitaxial layer with a resistivity of above 400  $\Omega\text{ cm}$  and a pixel pitch of 20.7  $\mu\text{m}$ . The ULTIMATE architecture is based on a column-parallel (rolling-shutter) read-out with amplification and correlated double sampling (CDS) inside each pixel [10]. Each column is terminated by a high precision discriminator and read out in a rolling-shutter mode with 200 ns per row [11], yielding a power dissipation of about 150 mW cm<sup>−2</sup>. The discriminator outputs are processed by an integrated zero suppression logic and the results are stored in two memories, allowing a continuous read-out and 320 Mbit s<sup>−1</sup> data throughput capability. The ULTIMATE sensor can cope with a hit rate density of about 10<sup>6</sup> cm<sup>−2</sup> s<sup>−1</sup>.

While the ULTIMATE sensor characteristics are not orders of magnitude far from the ALICE requirements, further developments are needed to meet the ALICE requirements in terms of read-out time.

## 2.5 ALICE developments

The wide spectrum of possible implementations offered by the TowerJazz technology is being explored by four different design streams. The main operational features of these designs are summarised and contrasted in Tab. 2.2 and a description of the main design features of the four circuits is given below.

**Table 2.2:** Chip design options.

Architecture (discriminator, read-out)	Pitch ( $r\phi \times z$ ) ( $\mu\text{m}^2$ )	Integration time ( $\mu\text{s}$ )	Power consumption ( $\text{mW cm}^{-2}$ )
MISTRAL (end-of-column, rolling-shutter)	$22 \times 33.3$	30	200
ASTRAL (in-pixel, rolling-shutter)	$24 \times 31$ $36 \times 31$	20	85 60
CHERWELL (in-strixel <sup>a</sup> , rolling-shutter)	$20 \times 20$	30	90
ALPIDE (in-pixel, in-matrix sparsification)	$28 \times 28$	4	< 50

<sup>a</sup> A strixel is a 128-pixel column over which the electronics are distributed.

### 2.5.1 MISTRAL

MIMOSA sensors have been developed at IPHC since the late nineties and within a partnership with Irfu (Saclay) since the early 2000. MISTRAL will be built on the experience of the ULTIMATE (MIMOSA-28) chip [9, 10], designed for and operated in the STAR-PXL detector, with improved hit rate capability, pixel dimension and integrated circuitry.

The design is based on a column parallel (rolling-shutter) read-out with amplification and correlated double sampling (CDS) inside each pixel, where a prototype in-pixel circuit is shown in Fig. 2.5a. A single MISTRAL chip has a surface  $1.5 \text{ cm} \times 3.0 \text{ cm}$  containing 375 rows and 1300 columns. The sensor is built from three independent Full Scale Building Blocks (FSBB) as shown in Fig. 2.5c. The target pixel size is about  $22 \mu\text{m} \times 33.3 \mu\text{m}$ , providing a single point resolution of about  $5 \mu\text{m}$ . These values result from the necessary balance between the required spatial resolution, which favours small pixels, and read-out speed, which tends to minimise the number of rows. Moreover, the columns need to be wide enough to allow implementing two discriminators at each column end, a configuration imposed by the simultaneous read-out of two rows.

MISTRAL will be equipped with column level discriminators allowing simultaneous two-row read-out in rolling-shutter mode to achieve the full matrix read-out in about  $30 \mu\text{s}$ . This architecture is intrinsically nearly dead time free, since all the pixels remain sensitive during the readout period (also referred to as the integration time) and all the hits are registered. In case the integration time is larger than the mean time between collisions, event pile-up can occur. The rolling-shutter architecture leads to low power consumption, since only two rows are read out and powered at a time. The power consumption of the MISTRAL architecture is expected to be about  $200 \text{ mW cm}^{-2}$ . The first prototypes built in the TowerJazz technology were MIMOSA-32 and MIMOSA-32ter, fabricated and tested in 2012; their characterisation is presented in the ITS CDR [12].

The discriminator outputs will be processed through an integrated zero suppression logic: SUZE-02, that will provide the downstream part of both MISTRAL and ASTRAL. The data is stored in a memory of four SRAM blocks ( $32 \times 512$  bits), capable of holding about 600 clusters per frame on average and allowing either continuous or triggered read-out. The data is serialised onto a high speed serial link, with a maximum SUZE-02 output rate of  $640 \text{ Mbit s}^{-1}$ .

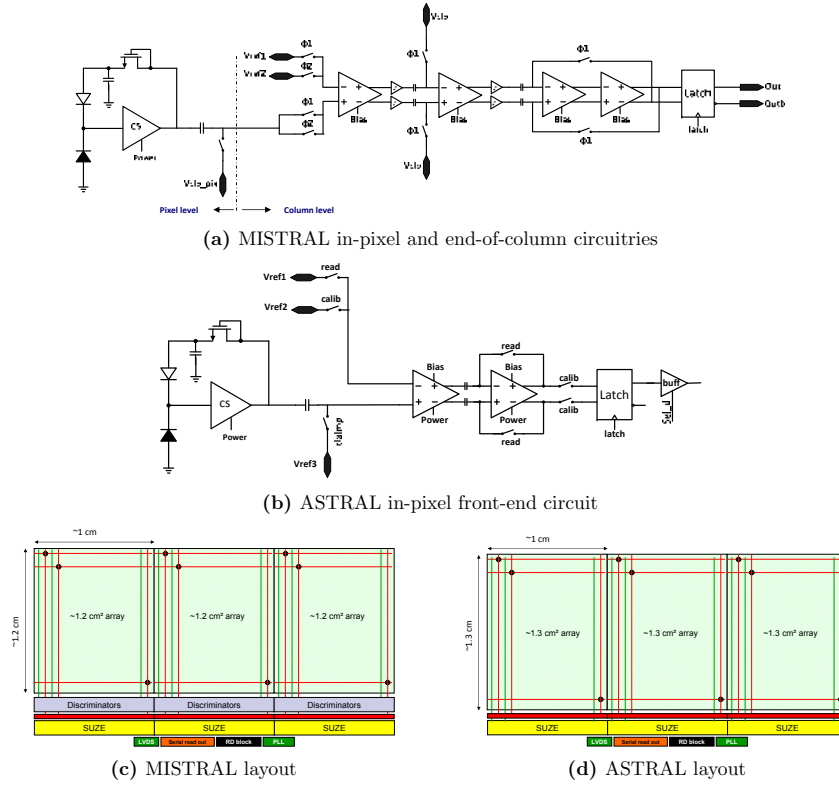


**Figure 2.5:** Schematic circuit and layout diagrams of MISTRAL and ASTRAL architectures.

### 2.5.2 ASTRAL

The second chip under development at IPHC, called ASTRAL (AROM sensor for the inner tracker of ALICE) is an alternative design to the MISTRAL development, based on a concept intrinsically faster and less power consuming. The ASTRAL design is derived from the ULTIMATE architecture as well, complemented with accelerated read-out based on the AROM (accelerated read-out MIMOSA) concept: exploiting the advantage of the TowerJazz technology, signal discrimination is embedded in each pixel, as shown in Fig. 2.5b. As a consequence, the analogue signals driving over centimetre long traces are replaced by digital signals.

This architecture has at least three advantages. The first one is a doubling of the pixel read-out frequency. The second is the power consumption reduction, the static current consumption per pixel being reduced from  $120 \mu\text{A}$  to  $15 \mu\text{A}$ . The third is a shrinking of the peripheral circuitry dimensions; i.e. the surface reserved for column-level discriminators in former sensors is removed, as shown in Fig. 2.5d.

Two variants of the sensor are considered, one (ASTRAL-IN) optimised for the Inner Layers which privileges spatial resolution and one (ASTRAL-OUT) best suited to the Outer Layers, where the relaxed requirement on the spatial resolution is used to further

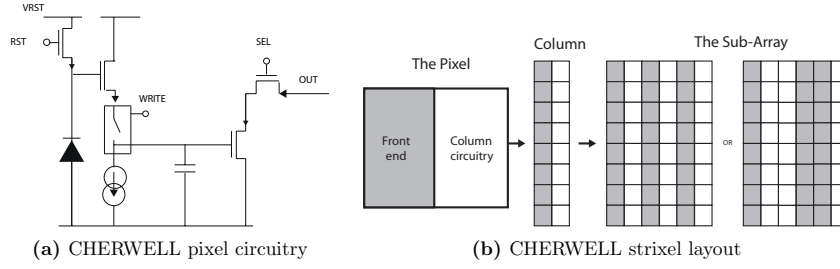


**Figure 2.6:** Layout of the pixel circuitry and strixel architecture for CHERWELL.

suppress power consumption.

The design of ASTRAL-IN is based on  $24\text{ }\mu\text{m} \times 31\text{ }\mu\text{m}$  pixels providing a single point resolution of about  $5\text{ }\mu\text{m}$  and composing a sensitive area of 1248 columns and 416 rows. The expected frame read-out time is approximately  $20\text{ }\mu\text{s}$  (assuming simultaneous double-row read-out) with a power density of  $85\text{ mW cm}^{-2}$ . A still lower power density of  $60\text{ mW cm}^{-2}$  is obtained with ASTRAL-OUT by enlarging the pixels to  $36\text{ }\mu\text{m} \times 31\text{ }\mu\text{m}$ , which reduces the number of columns to 832 and the number of sparse data scan units (SUZE) from three to two. The expected single point resolution amounts to  $7\text{ }\mu\text{m}$ .

At present, the two variants of ASTRAL act as baselines, MISTRAL being used as a back-up because of its more conservative design and more extensive validation of its components (see Sec. 2.6.2).

### 2.5.3 CHERWELL

The CHERWELL series of sensors has been designed by the STFC-RAL group in the UK. This group has pioneered over many years the design of CMOS sensors using the  $0.18\text{ }\mu\text{m}$  process provided by TowerJazz. The CHERWELL architecture is based on the novel concept of strixels, explained in more detail below.

The reverse-biased n-well to p-epitaxial layer diode acts as a charge collection node. The diode sensor can be reset to a defined voltage VRST through an NMOS transistor which is turned on/off by the RST input signal. After the integration time, the collected charge on the diode sensor is stored on the NMOS storage capacitor ( $100\text{ fF}$ ) through an NMOS source follower. The charge is transferred only when the switch WRITE is enabled. The accumulated voltage on the storage capacitor node is further buffered by a PMOS source follower when the row select switch SEL is enabled. When SEL is enabled, the voltage signal on the storage capacitor is transferred to a column memory capacitor ( $100\text{ fF}$ ) for further processing. This pixel architecture achieves low noise while operating at very low power. The pixel (front end) circuit diagram is shown in Fig. 2.6. It allows correlated double sampling (CDS) to achieve low noise operation.

The chip works in rolling-shutter operation and in order to achieve the desired frame rate, pixels are grouped into so-called strixels. This architecture allows reduction of the dead area at the periphery by incorporating the amplifiers, comparators and memories within the matrix. Unrelated n-wells, due to PMOS transistors used in the processing electronics, are shielded from the collecting diode by use of deep p-well, another concept that was first tested and proven in silicon by the STFC RAL group. The number of pixels per strixel as well as the exact geometry, i.e. vertical and horizontal pitch, can be tailored to the required specifications. We have designed a series of test structures in the CHERWELL architecture (CHERWELL-1, CHERWELL-2, etc.). Tests on the

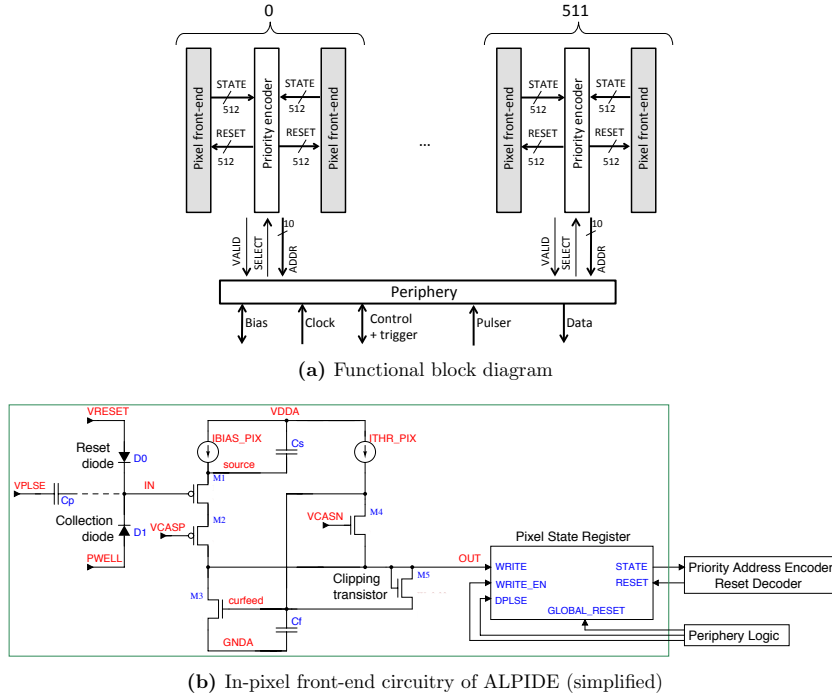


**Figure 2.7:** Building blocks of the ALPIDE chip.

CHERWELL-1 test structure are described in Sec. 2.6.3.

Within a strixel, the pixels are read in rolling-shutter mode and the pseudo-differential signal is compared against a defined threshold to identify the particle hits. The addresses of hit pixels are latched and stored in SRAMs within the strixel itself. In the current designs, only two memories per strixel are used. These memories can be used to store hits or to act as a buffer for reading the hits, so the trade-off can be made between power and occupancy. The strixel also includes a 6-bit DAC to trim the comparator threshold. The SRAMs are read through low-power, high-speed sense amplifiers.

As an example, in the new CHERWELL-2 test structure currently being prepared for testing, 128 pixels of dimensions  $20\ \mu\text{m} \times 20\ \mu\text{m}$  are put together in a strixel and there are 128 strixels placed next to each other to make a  $128 \times 128$  pixel array. The array has two different types of n-well to p-epitaxial layer diodes. Two variants of the diode have been used, one of them using a polysilicon ring to gate the diode to achieve higher radiation resistance at the expenses of extra capacitance.

#### 2.5.4 ALPIDE

ALPIDE (ALICE Pixel Detector) is the Pixel Chip developed by a collaboration formed by CCNU (Wuhan, China), CERN, INFN (Italy), and Yonsei (South Korea). It contains a novel low-power in-pixel discriminator circuit that drives an in-matrix asynchronous address encoder circuit, read out by an end-of-column lossless data compression and de-randomising circuit. The digitisation of the signal within the pixel eliminates the need for

an analogue column driver, reduces the power consumption significantly and allows for fast read-out. A functional diagram of the circuit is shown in Fig. 2.7a and the different elements are described in the subsequent paragraphs.

#### **In-pixel discriminator and digital memory**

The in-pixel discrimination circuit is depicted schematically in Fig. 2.7b. It is based on a current comparator circuit that works with a bias current of only 20 nA. To minimise its power consumption, the comparator has a slow response with a settling time of about 4  $\mu$ s. The logical and of the output of the comparator and an external WRITE\_EN is connected to a digital storage element on which the hit information is saved until read-out takes place. The circuit is meant to be operated in triggered mode: only upon arrival of a trigger signal, WRITE\_EN will be asserted for about 100 ns and the output of the front-end is latched. This minimises the time the circuit output is integrated and hence significantly reduces the number of spurious hits generated by electronics noise or beam background.

#### **In-column address encoder**

Within each double column, the addresses of the hit pixels are encoded using an asynchronous priority encoder network. It is organised as a tree to decrease the capacitive load of the lines, hence minimising the power consumption and at the same time optimising the speed. At its output the encoder generates a signal (VALID), which is asserted as long as there is a pixel that was hit but has not yet been read out, and an address bus (ADDR) which carries the address of the next valid pixel. When the end-of-column circuit has read the address of the hit pixel with the highest priority, it asserts a signal (SELECT) to the encoder that propagates back to reset the storage element inside the pixel that has just been read out. This scheme is extremely time efficient since it only reads out the pixels that are hit. The typical read-out time (time to transfer the information from the storage elements inside the pixels of the entire matrix to the memory at the periphery of the chip) for a central Pb–Pb collision is of the order of 100 ns. Moreover, it always preserves the full hit information; no information is lost even for the most unlikely event topologies.

#### **End-of-column read-out circuit**

The addresses and valid signals of the encoder are fed into a circuit that assembles and compresses the data, utilising the fact that addresses are likely to be consecutive. The latter is due to the fact that a particle typically creates hits in clusters of two to four adjacent pixels. After this compression, the data of all columns is multiplexed into a common multi-event memory (with a capacity to store four events), which serves as a de-randomising circuit. While data comes in bursts with high peak values obeying the (nearly) Poissonian statistics of the event/trigger process, its output can be read with constant, average bandwidth without introducing dead time.

## **2.6 Prototype circuits and experimental results**

Within the R&D phase, the different design teams have been submitting a number of circuits prototyping various building blocks of the final architectures (overview in Tab. 2.3). In the remainder of this section, results from the corresponding characterisation campaigns are reported.

**Table 2.3:** Prototype circuits.

Architecture	Prototype	Addressed design feature
MISTRAL	MIMOSA-32, MIMOSA-32ter	First 0.18 $\mu\text{m}$ design, in-pixel circuitry optimisation, improved radiation hardness
	MIMOSA-34	Sensing node design optimisation as a function of pixel dimensions and epitaxial layer characteristics
	MIMOSA-32N	Mitigation of RTS noise
	MIMOSA-32FEE	Combined sensing node and in-pixel circuitry optimisation, including RTS noise mitigation
	MIMOSA-22THRa	Overall pixel array read-out validation and optimisation based on single-row read-out (STAR-PXL chip architecture)
	MIMOSA-22THRb	Pixel array read-out validation with double-row read-out based on two discriminators ending each column
ASTRAL	AROM-0	Validation of in-pixel discrimination
MISTRAL ASTRAL	SUZE-02	Validation of zero-suppression and data sparsification
CHERWELL	CHERWELL-1	Strixel geometry demonstrator
	CHERWELL-2	Draft ALICE front end and in-strixel logic
ALPIDE	Explorer-0, Explorer-1	Pixel geometry optimisation, back-bias
	pALPIDE	In-pixel front end characterisation, feasibility of digital pixel read-out

### 2.6.1 Common characteristics and methods

The goal of the laboratory tests is to characterise and calibrate the pixel sensors. A standard method is to exploit the 5.9 keV X-rays of a  $^{55}\text{Fe}$  source. The impinging X-rays, in the majority of cases, deposit charge among several pixels (depending on the layout of the sensing diodes), forming a cluster. The seed pixel (the one with the highest signal within a cluster) collects typically 40 % to 50 % of the cluster charge. If an X-ray photon converts in the vicinity of the sensing diode, full charge collection occurs in the seed pixel, yielding about 1640  $e$ .

The spectrum of the collected cluster charges exhibits several peaks, as shown e.g. in Fig. 2.8 and in Fig. 2.15. The peak at the highest value (calibration peak) in the charge spectrum of the single pixel clusters corresponds to the full charge collection and gives an absolute charge calibration. To characterise the charge collection performance of the pixels, the seed Charge Collection Efficiency (seed CCE) or the cluster Charge Collection Efficiency (cluster CCE) can be used. The seed CCE is the ratio of the charge collected in the seed pixel over the total charge, while the cluster CCE is the ratio of the charge collected in a  $5 \times 5$ -pixel array over the total charge. It should be noted that the size of  $5 \times 5$  pixels for the latter is chosen such that it is large enough to easily accommodate a full cluster. The total charge is in both cases determined from the calibration peak.

Depending on the read-out architecture, the noise performance is assessed via a threshold scan or an analysis of the analogue output values in pedestal runs. This holds for both the random, or temporal, noise (TN) and the fixed pattern noise (FPN). In particular, the latter can also be identified from the fake hit rate in test beam and source measurements.

## 2.6.2 MIMOSA

### MIMOSA-34 and MIMOSA-22THRa(b) laboratory tests

Laboratory tests performed with various sensor prototypes addressing the different components of the charge sensing, signal processing and read-out chain of MISTRAL and ASTRAL are summarised hereafter. Each component was studied independently of the other ones. The studies cover the optimisation of the pixel sensing node and in-pixel circuitry, as well as the validation of the MISTRAL pixel-array read-out and of the in-pixel signal discrimination specific to ASTRAL.

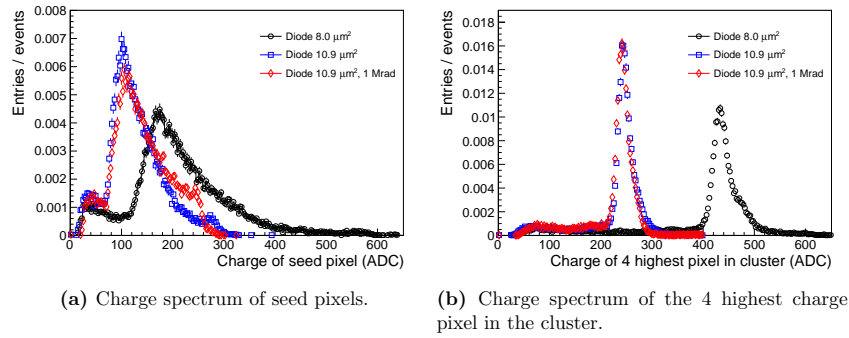


**Figure 2.8:** Charge collection properties of  $22\,\mu\text{m} \times 33\,\mu\text{m}$  pixels equipped with  $8\,\mu\text{m}^2$  and  $10.9\,\mu\text{m}^2$  sensing diodes. In the latter case, the measured charge distribution is shown before and after an exposure to 1 Mrad X-Rays.

The charge collection properties and noise performance of a variety of pixels were first investigated with pixels featuring no in-pixel pre-amplification and CDS circuitry (e.g. MIMOSA-34). The pixel dimensions range from  $22\,\mu\text{m} \times 27\,\mu\text{m}$  to  $33\,\mu\text{m} \times 66\,\mu\text{m}$ . Their (octagonal) sensing diodes have cross sections ranging from  $2\,\mu\text{m}^2$  to  $15\,\mu\text{m}^2$ , the value by default being  $10.9\,\mu\text{m}^2$ . The choice of small diodes was motivated by their reduced capacitive noise and by the in-pixel amplification gain enhancement they entail. In order to mitigate the potential decrease of the charge collection efficiency consecutive to the diode size reduction, a  $10.9\,\mu\text{m}^2$  or  $15\,\mu\text{m}^2$  large footprint, free of p- and n-wells, was implemented on top of the diode.

The influence of the epitaxial layer properties on the pixel performances was studied with three different epitaxial layers differing by their thickness (18, 20 and  $30\,\mu\text{m}$ ) and their resistivity (1, 6, and  $1\,\text{k}\Omega\text{cm}$ , respectively). They are labelled as HR-18, HR-20 and HR-30 hereafter.

Figure 2.8 shows distributions of the charge collected with two different  $22\,\mu\text{m} \times 33\,\mu\text{m}$  pixels illuminated with an  $^{55}\text{Fe}$  source. One pixel features a  $10.9\,\mu\text{m}^2$  large sensing diode while it is only  $8\,\mu\text{m}^2$  large in the other pixel. The gain enhancement originated by the  $8\,\mu\text{m}^2$  diode is clearly visible in the charge collection performance, confirming the advantage of the sensing concept based on a small diode underneath a larger footprint. Figure 2.8b shows the charge collected by the set of four pixels in a cluster collecting the



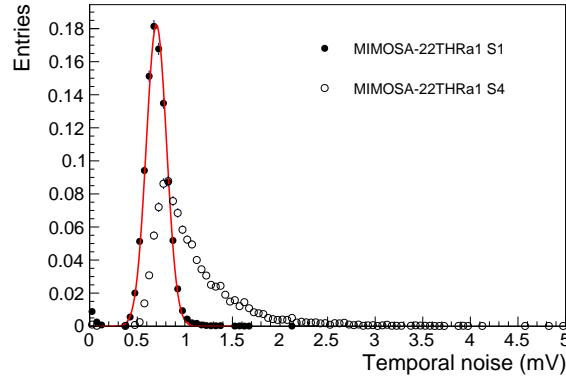


**Figure 2.9:** Temporal noise extracted from a threshold scan of the MIMOSA-22THRa1 discriminator outputs (HR-18). The TN distribution is displayed for pixels reproducing the circuitry known to be affected by RTS noise (pixel matrix S4) and for pixels incorporating a preamplifier input transistor with twice wider and longer gate (pixel matrix S1).

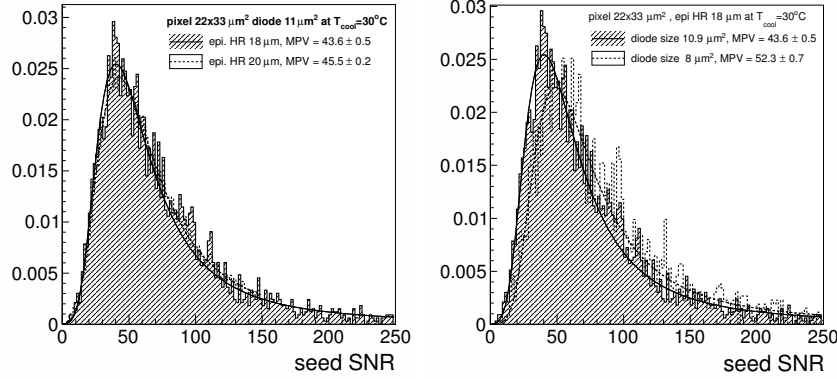
largest charges. One observes that the charge is nearly equal to that of the calibration peak, indicating that the cluster charge is almost fully contained in four pixels. The irradiation related results are discussed in Sec. 2.7.4.

The temporal noise (TN) of the different pixels was measured at a temperature of 30 °C. It was found to vary linearly with the diode cross section from about  $8 e$  ENC for  $2 \mu\text{m}^2$  diodes to about  $17 e$  ENC for  $10.9 \mu\text{m}^2$  ones, independently of the epitaxial layer characteristics. It was shown that large (e.g.  $22 \mu\text{m} \times 66 \mu\text{m}$ ) pixels featuring a sensing node composed of two interconnected small diodes for the sake of charge collection, exhibit a TN value similar to the one of the default,  $10.9 \mu\text{m}^2$  large, diode in smaller pixels (see example of Tab. 2.4).

The charge collection efficiency (CCE) of the different pixels was also investigated in particular for the  $22 \mu\text{m} \times 33 \mu\text{m}$  and  $33 \mu\text{m} \times 33 \mu\text{m}$  pixels, representative of the MISTRAL and ASTRAL-IN pixels, and of the ASTRAL-OUT pixel, respectively. The seed CCE was observed to be in the 40 % to 50 % range (depending on the sensing node details) for the MISTRAL/ASTRAL-IN pixel and a few percent less for the ASTRAL-OUT pixel. Several different larger pixel designs were also shown to exhibit satisfactory charge collection performances (see Fig. 2.12a). This observation offers attractive power-saving perspectives, reflecting the reduced sensing node density associated to large pixels, an

**Table 2.4:** Temporal noise measurements of MIMOSA-34 featuring one pixel type with  $22 \mu\text{m} \times 33 \mu\text{m}$  pitch,  $10.9 \mu\text{m}^2$  footprint and  $10.9 \mu\text{m}^2$  diode cross section and one with  $22 \mu\text{m} \times 66 \mu\text{m}$  pitch,  $15 \mu\text{m}^2$  footprint and two interconnected  $5 \mu\text{m}^2$  diodes. Measurements were performed at 30 °C and for three different starting materials.

Pixel pitch ( $\mu\text{m}^2$ )	Temporal noise ( $e$ )		
	HR-18	HR-20	HR-30
$22 \times 33$	15.4	14.3	15.5
$22 \times 66$	16.9	15.7	16.2



(a) Comparison of the HR-18 and HR-20 epitaxial layers featuring  $22\,\mu\text{m} \times 33\,\mu\text{m}$  pixels with  $10.9\,\mu\text{m}^2$  diode. (b) Comparison of  $8\,\mu\text{m}^2$  and  $10.9\,\mu\text{m}^2$  diode pixels for the HR-18 epitaxial layer.

**Figure 2.10:** Signal-to-noise ratio (SNR) of seed pixel measured in test beam for different MIMOSA-34 pixels.

approach becoming relevant whenever the demanded single point resolution is not particularly constraining.

The noise distribution of the pixels mentioned above still exhibits a significant contribution from RTS noise. Former studies exposed in the ITS CDR [12] have shown that this component generates an unacceptable fake hit rate. Its mitigation was addressed with pixels incorporating pre-amplification and CDS circuitry organised in columns read out in parallel, each ended with a high resolution, offset compensated discriminator (MIMOSA-22THR chips). The mitigation strategy consisted in extending the dimensions of the input transistor of the in-pixel amplifier.

Threshold scans of the discriminator outputs were performed in order to derive the pixel TN and the Fixed Pattern Noise (FPN), which is dominated by residual discriminator offset dispersions. Figure 2.9 compares the TN distribution observed with pixels reproducing the original preamplifier circuitry (composing the pixel matrix called S4), known to be subject to RTS noise, to the one obtained with a twice longer and larger gate of the preamplifier input transistor (composing the pixel matrix called S1). While the former distribution exhibits a clear tail due to RTS noise, the second one is free of it as a consequence of the enlarged pre-amplifier input transistor gate. The mitigation of this potential source of high fake hit rate is thus established.

The validation of the double-row read-out in rolling-shutter mode was achieved in two steps, each based on a dedicated chip. The first step consisted in reproducing the single-row read-out concept used for the STAR-PXL. It was realised with the MIMOSA-22THRa prototype, made of 128, 1 cm long, parallel columns composed of 320 pixels and ended with discriminators. The second step was achieved with a prototype (MIMOSA-22THRb) addressing the simultaneous read-out of two rows. It features 56 columns, each made of 64 pixels and ended with the same discriminators as in MIMOSA-22THRa. Both sensors feature eight columns with analogue outputs allowing characterisation of the pixels independently from the discriminators.

A threshold scan of the discriminator outputs was performed with both chips at the nominal clock frequency of 100 MHz. The TN and FPN were derived in order to estimate

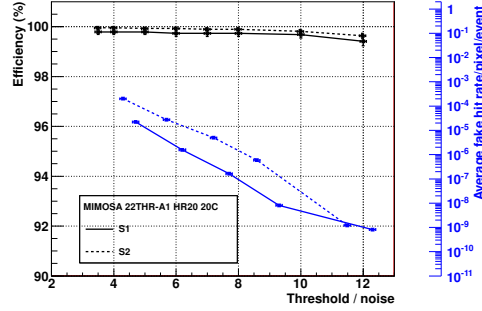


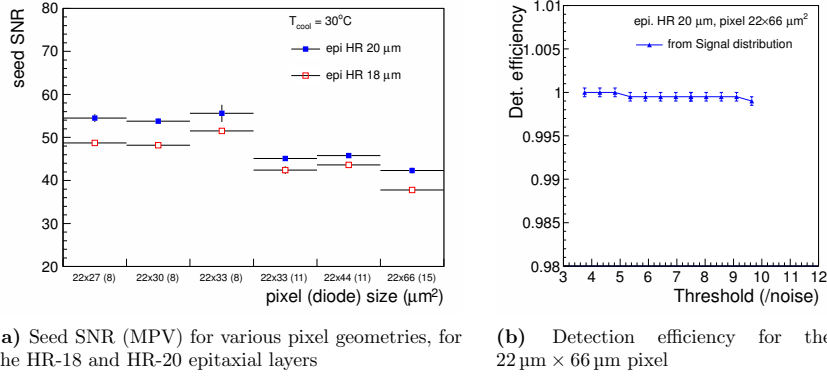
**Figure 2.11:** MIMOSA-22THRa1 performance of  $22\mu\text{m} \times 33\mu\text{m}$  pixels composing sub-matrix S1 and S2.

the impact of residual discriminator threshold dispersions and potential couplings between the analog and digital in-pixel micro-circuits introduced by the double-row read-out. The total noise observed amounts to  $19e$  ENC for the single-row read-out and  $20$  to  $23e$  ENC in case of a double-row read-out. These results validate the double-row read-out architecture and indicate a small noise increase due to the double-row read-out, which is expected to be suppressed by further optimisation of the in-pixel circuitry.

The upstream part of the MISTRAL architecture as well as most of the ASTRAL read-out can therefore be considered as validated. The specific aspect of the latter, i.e. the in-pixel signal discrimination, was investigated with essentially three different alternative micro-circuit designs implemented in sub-arrays composing the prototype AROM-0. The design differences focus on the amplification, clamping and discrimination functionalities complementing the pre-amplification and clamping circuits common with the MISTRAL pixel. The TN and FPN distributions were extracted from threshold scans of the chips. The observed noise indicates that the pixel TN matches the noise performance of the end-of-column discriminator structure of MIMOSA-22THR ( $\leq 1\text{ mV}$ ). On the other hand, the in-pixel discriminator TN and FPN are about twice higher ( $\approx 1.0\text{ mV}$  and  $\leq 0.5\text{ mV}$ ) than in MIMOSA-22THR ( $\ll 1.0\text{ mV}$  and  $\leq 0.2\text{ mV}$ ). The overall noise comes therefore out to be at least 50 % larger than in case of end-of-column discriminators. Its mitigation is expected to result from the next generation of chips (AROM-1) foreseen to be fabricated and tested by Q1 of 2014.

The validation of the downstream component of the read-out chain, common to MISTRAL and ASTRAL, was addressed in the SUZE-02 chip. The prototype includes the zero-suppression circuitry corresponding to 64 columns of the pixel array. The full signal sparsification sequence was tested at nominal frequency, using various types of patterns repeatedly processed up to 10 000 times. No signal processing error was observed.

In summary, the adequacy of all main components of the MISTRAL architecture has been verified and solutions have been found to mitigate the RTS noise at an acceptable level. Most of these results are also valid for ASTRAL. Moreover, two alternatives of the in-pixel discrimination circuitry needed for ASTRAL provide performances confirming the adequacy of the circuit concepts. Their noise level still needs to be suppressed by at least 30 %, a goal which seems within reach with the solutions implemented in the next generation of sensors (AROM-1) expected to be fully tested by Q1 of 2014.



(a) Seed SNR (MPV) for various pixel geometries, for the HR-18 and HR-20 epitaxial layers (b) Detection efficiency for the  $22\mu\text{m} \times 66\mu\text{m}$  pixel

Figure 2.12: MIMOSA-34 results.

### Summary of the MIMOSA test beam measurements

The detection performances of the upstream part of the MISTRAL architecture were further assessed with a  $4.4\text{ GeV}/c$  electron beam at DESY in August 2013. The study focussed on the sensitive area, composed of  $22\mu\text{m} \times 33\mu\text{m}$  pixels, connected to the end-of-column discriminators. It also addressed the performances of larger pixels, which become relevant in case of relaxed single point resolution requirements. The measurements concentrated on the signal charge collection, the hit cluster properties, the seed SNR, the detection efficiency and the spatial resolution. Several results of the study apply also to the ASTRAL detection performances.

The study was performed in two steps. First, the charge sensing properties were estimated for various pixel geometries, based on the MIMOSA-34 sensor and therefore not influenced by the signal processing circuitry. The latter, including in-pixel signal processing and end-of-column discriminators, was investigated in a second step with the MIMOSA-22THR sensor, concentrating on  $22\mu\text{m} \times 33\mu\text{m}$  pixels. The single point resolution measurements were achieved with  $50\mu\text{m}$  thin sensors and a selected sub-sample of beam electron tracks undergoing moderate multiple scattering in the components of the beam test set-up (beam telescope and sensor under test).

The seed SNR of the  $22\mu\text{m} \times 33\mu\text{m}$  MIMOSA-34 pixels featuring the  $10.9\mu\text{m}^2$  default sensing diode was observed to exhibit a most probable value (MPV) of about 44, with a small difference between the two epitaxial layers considered here (HR-18 and HR-20) favouring the HR-20 epitaxial layer, as shown in Fig. 2.10a. On the other hand, the MPV was observed to increase by 20 % when reducing the sensing diode cross section from its default value to  $8\mu\text{m}^2$  (see Fig. 2.10b).

The expected digital performance of the MIMOSA-34 sensor was emulated offline using the sensor analogue raw data. An emulated binary encoding of the charge collected by  $22\mu\text{m} \times 33\mu\text{m}$  pixels featuring the default sensing diode resulted in a single point resolution of  $(4.7 \pm 0.3)\mu\text{m}$ , thus complying with the Inner Layer specifications. This result is corroborated by the binary single point resolution observed with  $20\mu\text{m} \times 40\mu\text{m}$  pixels (MIMOSA-32) exposed in 2012 to a  $100\text{ GeV}/c$  hadron beam at the CERN-SPS, which amounted to  $(5.4 \pm 2.0)\mu\text{m}$  using the same offline charge encoding procedure [13].

Next, the detection performances of the full upstream part of the MISTRAL architecture was investigated with the MIMOSA-22THRa sensor to validate the read-out scheme at the nominal clock frequency of 100 MHz. The seed SNR distributions measured on the

narrow band of 8 columns delivering analogue outputs feature a MPV of 34 and 32 for the HR-20 and HR-18 epitaxial layers, respectively. These values agree with former data obtained in 2012 with the MIMOSA-32ter sensor at the CERN-SPS [12].

The detection efficiency was evaluated as a function of the discriminator thresholds. Particular attention was devoted to the two sub-arrays composed of pixels corrected for RTS noise (called S1 and S2). The detection efficiency was observed to exceed 99.5 % for threshold values of up to ten times the average noise, the fake hit rate being about  $10^{-5}$  only. This result confirms the RTS noise mitigation. Measurements performed with the S1 and S2 sub-arrays are shown in Fig. 2.11 for the HR20 epitaxial layer, the fake rate being extracted from large statistics laboratory measurements.

The relaxed constraint on the Outer Layers' spatial resolution may be used to squeeze the sensor power density well below  $100 \text{ mW/cm}^2$ , while keeping the same integration time as for the Inner Layers. The detection performances of  $22 \mu\text{m} \times 44 \mu\text{m}$  and  $22 \mu\text{m} \times 66 \mu\text{m}$  pixels were evaluated in this perspective. Figure 2.12 displays results obtained on beam at  $30^\circ\text{C}$  with  $22 \mu\text{m}$  wide and up to  $66 \mu\text{m}$  long pixels for HR-18 and HR-20 epitaxial layers. Various pixel sensing diode cross sections are considered, ranging up to  $15 \mu\text{m}^2$ . Figure 2.12a shows the MPV of the seed SNR distribution from small to large pixels, also indicating the sensing diode surface. Figure 2.12b displays the detection efficiency of the largest pixel as a function of the threshold over noise cut. The measured seed SNR MPV is quite large for all pixel configurations, and the high detection efficiency observed with the  $22 \mu\text{m} \times 44 \mu\text{m}$  and  $22 \mu\text{m} \times 66 \mu\text{m}$  pixels validates the approach followed to reduce the power density in the Outer Layers (see Tab. 2.2). The binary charge encoding was simulated on the data collected and resulted in a single point resolution around  $7 \mu\text{m}$  in both directions. The results support the pixel dimensions envisaged for ASTRAL-OUT ( $36 \mu\text{m} \times 31 \mu\text{m}$ ) and thus the associated low power density ( $60 \text{ mW/cm}^2$ ) predicted for its design.

In summary, the beam tests performed in 2013 confirm that the CMOS process investigated is well suited to the key features of the ASTRAL and MISTRAL architectures. The main charge sensing and signal processing elements of both architectures are shown to offer satisfactory performances, a result which validates both approaches followed.

The different elements of the chain addressed through the 2012 and 2013 prototyping need now to be combined in a single sensor unit (FSBB) featuring the final sensitive area, which will encompass the full signal collection and processing chain, incorporating various design improvements. Simultaneously, the optimisation of the in-pixel circuitry still needs dedicated prototyping, in particular as far as the ASTRAL in-pixel discrimination is concerned. Improvements are also expected in the design of the sensing node, which may be different for ASTRAL-IN and ASTRAL-OUT, accounting for the radiation tolerance required. Finally, the choice of the most appropriate epitaxial layer, which seems presently to be the HR-20 epitaxy, still needs further studies.

### 2.6.3 CHERWELL-1

CHERWELL-1 is a 4T Monolithic Active Pixel Sensor (MAPS) device designed at Rutherford Appleton Laboratory (RAL). The Cherwell sensor is a further development of two previous circuits, FORTIS and TPAC [14]. TPAC was designed for digital calorimetry in the context of the R&D for the ILC project. FORTIS was designed for use in tracking and vertexing, and as a test for the TowerJazz process with a deep p-well implant with no circuits inside. The CHERWELL-1 sensor includes many improvements based on the experience made with the two previous circuits and includes active circuitry within the pixel area shielded with the deep p-well. CHERWELL-1 uses 4T pixels, which allow low noise, in-pixel correlated double sampling and a high conversion gain. It has a  $12 \mu\text{m}$

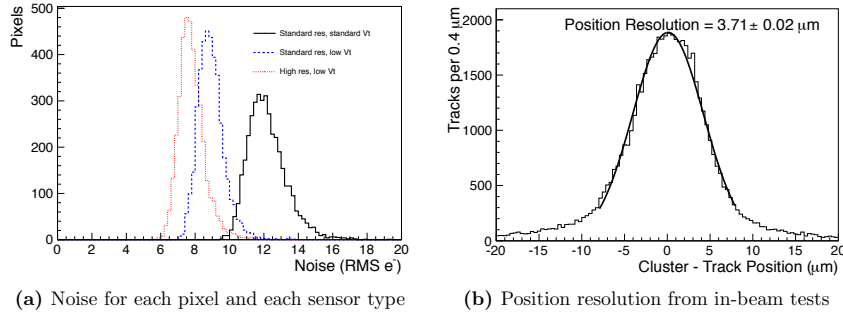


**Figure 2.13:** CHERWELL-1 characterisation results.

epitaxial layer. Different versions have been fabricated using standard and high resistivity substrates. The main innovation of CHERWELL-1 is that it incorporates the strixel array architecture. The strixel array allows for the addition of read-out circuits embedded in the space between the pixel diodes. This eliminates the end-of-column electronics and increases the active area of the chip.

#### Photon Transfer Curve scans

The basic characteristics of an imaging sensor can be obtained by taking images for different intensities of light and calculating the variance and mean for each intensity point. This forms the Photon Transfer Curve (PTC) from which the gain, noise and full well capacity can be measured. A PTC scan was performed in a light tight box where the sensor was illuminated with a uniform distribution of UV light from LEDs. The intensity of the light was increased until the pixels were saturated. At each intensity 200 events were recorded and a mean signal value was calculated. The noise was taken to be the RMS of the signal values. The signal was plotted against the square of the noise to produce the PTC. A PTC was recorded for all the reference and strixel pixels in the sensor. From these plots values of the gain and noise have been found for each pixel. Figure 2.13a shows the noise for each sensor type: (i) standard resistivity, standard  $V_t$ , (ii) standard resistivity, low  $V_t$ , (iii) high resistivity, low  $V_t$ .

The noise was observed to be uniform across the sensor. The width and mean of the noise decreases for the higher resistivity epitaxial layer and low  $V_t$  implant, as expected. The mean value of the noise is  $8e$  to  $12e$  RMS. The gain of each pixel is also uniform across the sensor with a mean value of  $0.17$  ADC counts per electron. The full well capacity of the sensor is taken as the maximum signal point of the PTC scan. The linear full well capacity is  $11\,500e$  and the maximum full well capacity is  $14\,700e$ . These values are consistent for all pixels.

#### Test beam

Measurements of the CHERWELL-1 sensors have been made using the  $120\text{ GeV}/c$  pion test beam at the CERN SPS in November 2012. The aims of the test beam were to understand the resolution, charge sharing and efficiency of CHERWELL-1. A stack of six CHERWELL-1 sensors was placed on the T4 beamline at H6 in front of the EUDET telescope. Scintillators at either end of the stack allowed a triple-coincidence trigger to be constructed. The stack consisted of two standard wafers with the low noise  $V_t$  implant for the source drain, two standard wafers with the standard noise  $V_t$  implant for the source

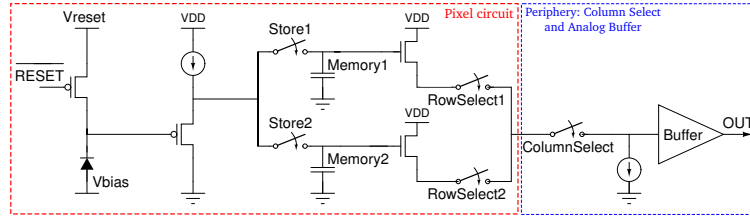


**Figure 2.14:** Explorer front-end circuitry (simplified).

drain and two high resistivity wafers with the low noise  $V_t$  implant for the source drain. Particles can be seen traversing the entire stack and are thus being used for alignment. From the clustering analysis, detection efficiencies have been extracted and are 99.73 % for the standard resistivity, standard  $V_t$ , 99.77 % for the standard resistivity, low  $V_t$  and 99.89 % for the high resistivity, low  $V_t$ . The position resolution can be seen from Fig. 2.13b and is of order  $3\text{ }\mu\text{m}$  to  $4\text{ }\mu\text{m}$ .

#### 2.6.4 Explorer-0, Explorer-1

The goal of the Explorer prototypes is to optimise the charge collection and diode layout as well as to study the effect of back-biasing the substrate and the susceptibility to radiation damage. A distinctive feature is the possibility to apply back bias to the substrate, which is effectively increasing the reverse bias on the collection diode, and which in turn leads to an increase of signal due to a reduction of input capacitance as well as a reduction of cluster size due to an increased depletion zone.

The chip is segmented in nine different electrode geometries, which exist in two pitches ( $20\text{ }\mu\text{m} \times 20\text{ }\mu\text{m}$  and  $30\text{ }\mu\text{m} \times 30\text{ }\mu\text{m}$ ) each. A first version of the chip, Explorer-0, was submitted in July 2012. In April 2013, 16 further variants, Explorer-1, were submitted to further study the observed trends. The Explorer-1 chips were fabricated on seven different substrates with different resistivities and epitaxial layer heights.

To allow for flexibility in the characterisation of the pixel sensing diode, the circuit in Fig. 2.14 was devised. Each pixel contains two independent analogue memory cells, which store the voltage level at the output of the sensing diode. At the periphery, a sequencing circuit is used to read out the memories of all pixels in a serial fashion. The pixel circuit operates from the functional point of view as follows. The voltage signal at the output of the sensing diode is first set to a nominal value by turning on (resetting) the PMOS transistor, which is connected to a well-defined voltage level. Immediately after the reset operation, the signal at the output of the sensing diode is stored in the first memory cell. After some time (integration time), the signal at the output of the sensing diode is stored in the second memory cell. The two voltage levels stored in the analogue memory cells are read out sequentially and shipped off-chip where digitisation and CDS calculation take place. It should be noted that this circuit configuration allows control of the integration time, which can be set to any desirable value, independently with respect to the read-out time. This mode of operation is for characterisation purposes only and not meant to be used for the final sensor. The Explorer-1 employs the same circuit but has a different routing and input transistor geometry to lower the front-end input capacitance from  $3.6\text{ fF}$  to  $1.4\text{ fF}$ , which allows for a better measurement of very low detector capacitances.

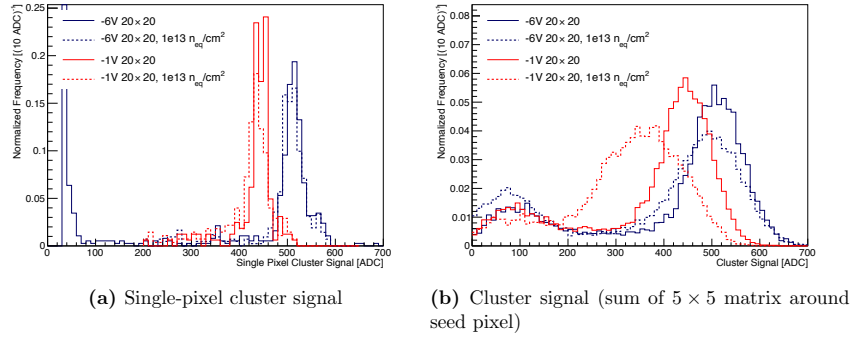


**Figure 2.15:** Comparison of  $^{55}\text{Fe}$  signals for an Explorer-0 pixel with a  $7.6\ \mu\text{m}^2$  octagonal n-well electrode and a  $1.04\ \mu\text{m}$  spacing between the n-well and the surrounding  $\text{p}^+$ -ring. The spectra are measured at back bias voltages of  $-1\ \text{V}$  and  $-6\ \text{V}$  as well as before and after irradiation with  $10^{13}\ 1\ \text{MeV}\ n_{\text{eq}}/\text{cm}^2$  neutrons.

### Laboratory measurements

The sensor was characterised using X-rays from an  $^{55}\text{Fe}$  source to determine its charge collection efficiency. Examples of the signal of single-pixel clusters and of arbitrarily shaped clusters (defined as the sum of a  $5 \times 5$  matrix around the seed) are shown in Fig. 2.15.

The noise figure of the Explorer-0 has been studied in the laboratory. It has found to be Gaussian for more than 99.9% of the pixels before irradiation and still more than 99% after irradiation with  $10^{13}\ 1\ \text{MeV}\ n_{\text{eq}}/\text{cm}^2$ . The remaining pixels show jumps of the baseline that appear with a period of several seconds. For Explorer-1, the situation worsens: RTS noise appears as a new noise source, significantly affecting a few percent of the pixels. This effect, very similar to what has been observed with the MIMOSA-32, can most likely be attributed to the decreased input transistor size.

It should, however, be noted that the Explorer front-end is not representative for the final chip. Apart from a different input transistor geometry, the ALPIDE mode of operation is not sensitive to a (quasi-)static shift of baseline, but only to shifts that occur within the integration time of the amplifier (some  $4\ \mu\text{s}$ ).

### Test beam measurements

To study the detection efficiency, the responses of the Explorer chips to electrons were measured using a  $4\ \text{GeV}/c$  to  $6\ \text{GeV}/c$  electron beam at DESY. Looking at the pixel with highest signal within a cluster (seed pixel), a Landau-like distribution is observed (Fig. 2.16a). After discriminating the signal, the detection inefficiency is given by the integral of this distribution below the threshold. By lowering the threshold, however, statistical base line fluctuations are also detected: fake hits. In order to distinguish fake hits from track-induced hits, detection planes were arranged around the device under test in a telescope and particle tracking was performed. The inefficiency is defined as the number of tracks found by the external planes that do not have a corresponding hit in the device under test. The result is plotted in Fig. 2.16b. The fake hit rate is computed from independent noise measurements.

Due to the high RTS noise in Explorer-1, 1% of the pixels with the highest noise were excluded from both efficiency and fake hit rate estimation. The still very high



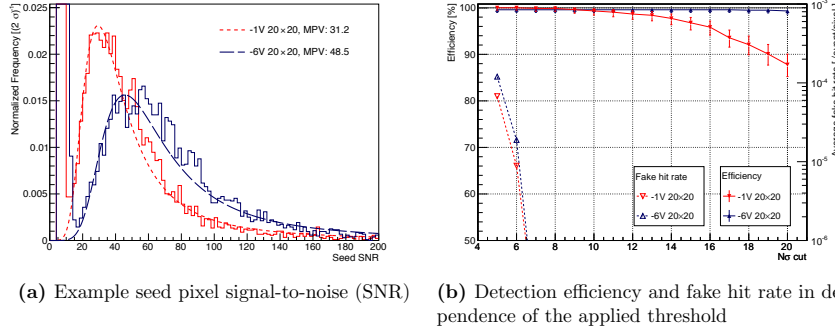


**Figure 2.16:** Explorer-1 response to 4 GeV/c electrons for a pixel with  $7.6 \mu\text{m}^2$  octagonal n-well electrode and a  $2.1 \mu\text{m}$  spacing between the n-well and the surrounding  $p^+$ -ring.

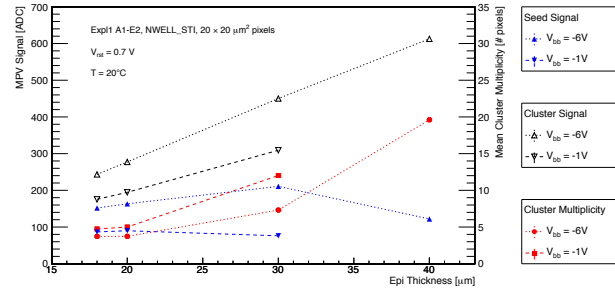


**Figure 2.17:** Comparison of different epitaxial layer thicknesses at a  $3.2 \text{ GeV}/c$  positron beam for Explorer-1.

detection efficiency is due to the fact that clusters extend over a few pixels and can still be detected if a single pixel is masked. Fig. 2.16b also shows the positive effect of the back bias, which not only yields slightly higher values at small cuts, but also a larger margin to apply a more comfortable threshold.

Four different starting materials (HR-18, HR-20, HR-30, HR-40B, see Tab. 3.1) were compared at another test beam at DESY with  $3.2 \text{ GeV}/c$  positrons. The summary is shown in Fig. 2.17 for the  $20 \mu\text{m} \times 20 \mu\text{m}$  pixels, while results from  $30 \mu\text{m} \times 30 \mu\text{m}$  look similar. The expected linear increase of the generated charge with the epitaxial layer's thickness is observed and, in addition, it can be seen that the cluster size increases. These two effects have a competing influence on the amount of charge that is collected in the seed pixel. Depending on the back-bias voltage, the optimum value in terms of seed signal is attained at different epitaxial layer thicknesses. While the optimum at a back-bias voltage of  $-6 \text{ V}$  is at  $30 \mu\text{m}$ , it is at  $20 \mu\text{m}$  for  $-1 \text{ V}$ . Due its possible significant improvement of SNR, the HR-30 material is further investigated and a test beam with an irradiated sample is planned for December 2013.

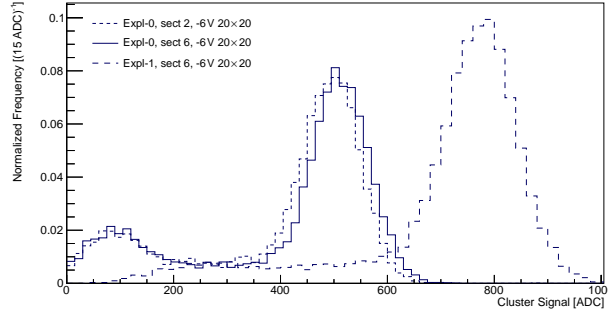


**Figure 2.18:** Comparison of  $^{55}\text{Fe}$  cluster signal for Explorer-0 sector 2 ( $7.6\ \mu\text{m}^2$  diode, no spacing) and sector 6 ( $7.6\ \mu\text{m}^2$  diode,  $1.04\ \mu\text{m}$  spacing) as well as for Explorer-1 sector 6 ( $7.6\ \mu\text{m}^2$  diode,  $2.1\ \mu\text{m}$  spacing). The analogue output signal is increased by 60 % by optimising the diode shape and circuit input capacitance.

### Comparison and conclusion

A summary of extracted parameters for the different diode geometries is given in App. A. By the comparison of the different anode types, the following trends can be observed:

- Most diode geometries provide the required charge collection efficiency.
- Larger spacing between the diode n-well and the surrounding deep p-well yields a better signal-over-noise ratio.
- Larger back bias yields a better signal-over-noise ratio.
- The Explorer-1 circuits show a 60 % better signal-over-noise ratio with respect to Explorer-0, if one masks the few percent of pixels with significant RTS noise contribution (Fig. 2.18).
- Only at larger back-bias voltages one may benefit largely from the increased charge created in a thicker epitaxial layer. Then, however, the increase in SNR can be substantial.

These observations can qualitatively be described by looking at the depletion volume, which is larger when increasing the reverse voltage of the collection diode (back bias) and when increasing the space towards the surrounding p-well. This argument is steering the optimisation of the layout of the ALPIDE and pALPIDE pixel geometries.

### 2.6.5 pALPIDE

pALPIDE, the first small-scale prototype matrix of ALPIDE, was designed to address the feasibility of both the analog front-end and the priority encoding scheme. It contains a 64-column, 512-row matrix with the ALPIDE front-end in  $22\ \mu\text{m} \times 22\ \mu\text{m}$  pixels and it is read out by a global priority encoder circuit. The priority encoder is organised column wise: an identical 512-bit encoder is placed within each column and at the periphery the global priority is formed based on the output of the column priorities. The circuit has been submitted together with Explorer-1 in March 2013, first test have been carried out, and their results are shown below.

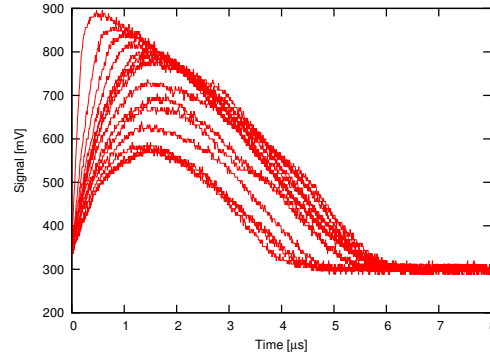
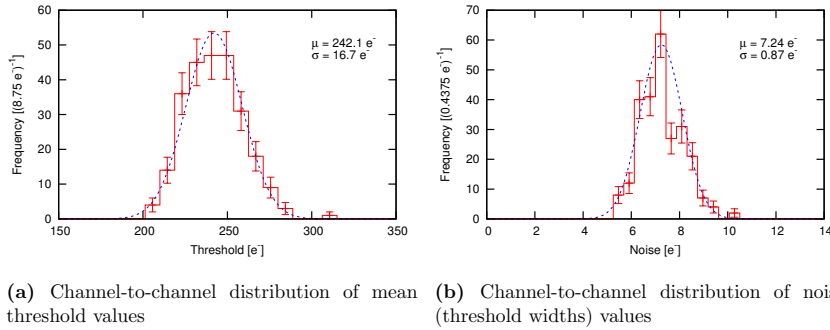


**Figure 2.19:** 20 pALPIDE in-pixel front-end responses (OUT in Fig. 2.7b) of a single pixel to  $^{55}\text{Fe}$  signals. A 500 mV trigger threshold was applied, but no selection on the position of the pixel within a cluster is performed.



(a) Channel-to-channel distribution of mean threshold values (b) Channel-to-channel distribution of noise (threshold widths) values

**Figure 2.20:** Parameters obtained from pALPIDE s-curve measurements at a back-bias of  $-2\text{ V}$  using an electrical pulsing of 256 pixels. 1 mV corresponds to  $0.88 \pm 0.08$  electrons. Threshold and noise values correspond to mean and standard deviations, respectively, as obtained from individual fits of the CDF of a normal distribution to the measured s-curves.

The analogue output (OUT in Fig. 2.7b) of the in-pixel discriminator front-end is available for a few pixels as a direct output and waveforms of  $^{55}\text{Fe}$  signals were recorded (Fig. 2.19). The FWHM of the majority of signals is seen to be  $3.5\text{ }\mu\text{s}$ . The existence of waveforms that are significantly lower than the majority can be explained by the (unknown) position of a pixel within a cluster; if the pixel happens to be at the periphery of a cluster its signal can be close to threshold.

To address the spatial uniformity as well as the noise of the response of the analogue front-end, a threshold, s-curve, scan was performed. 256 pixels have the possibility to pulse the front-end via  $0.14\text{ fF}$  pulsing capacitors that are connected to an input pin. An external voltage pulse is used to inject charge into the circuit and its amplitude is swept from  $0\text{ V}$  to  $1.8\text{ V}$ , corresponding to a charge of  $0\text{ e}$  to  $1575\text{ e}$ . Results (depicted in Fig. 2.20) show a good spatial uniformity with a variation of  $17\text{ e}$  as well as a low noise figure of  $7.2\text{ e}$ . The relatively high threshold of  $242\text{ e}$  depends on the threshold and bias currents ( $I_{th}$  and  $I_{bias}$ ) as well as the back-bias voltage,  $V_{bb}$ , and are shown for  $I_{th} = 0.5\text{ nA}$ ,  $I_{bias} = 20\text{ nA}$

(which are the nominal currents), and  $V_{bb} = -2\text{ V}$ .

The pALPIDE was characterised with 4 GeV/ $c$  to 6 GeV/ $c$  positrons at DESY in September 2013 using the EUDET telescope set-up. First results show a detection efficiency reaching 99.7% at  $V_{bb} = 0\text{ V}$ . Detailed studies on the spatial resolution as well as an irradiation campaign are currently ongoing.

## 2.7 Radiation hardness

### 2.7.1 Radiation effects

As described in more detail in Tab. 1.2 the radiation levels expected for the innermost Layer (radius of 22 mm) are about 700 krad (TID) and  $10^{13}$  1 MeV  $n_{\text{eq}}/\text{cm}^2$  (NIEL) including a safety factor of ten for a collected data set corresponding to 10 nb $^{-1}$  Pb–Pb, 50 pb $^{-1}$  p–Pb, and 6 pb $^{-1}$  pp collisions. To ensure full functionality within this radiation environment and to avoid a degradation of the detector performance, comprehensive radiation hardness studies are carried out throughout the prototyping process.

Ionising radiation essentially affects the surface oxide layers of sensors and electronics as well as the lateral isolation oxides of MOSFET transistors through radiation induced charge trapping and interface traps resulting in a change of threshold voltage and leakage current. NIEL generates bulk damage in the silicon lattice that in turn can degrade the sensor performance in terms of charge collection efficiency and signal-over-noise ratio. Furthermore, ionising radiation in digital structures can induce single event upset (SEU), a change of state caused by ions or electromagnetic radiation striking a sensitive node in a micro-electronic device. It can also cause single event latchup (SEL), a type of short circuit that triggers parasitic structures which can disrupt proper functioning of the element, or possibly can even lead to its destruction.

To simulate the impact of the expected radiation level on the ALICE ITS, systematic irradiation tests using X-rays, protons and neutrons are carried out throughout the R&D phase on various sensor, analogue and digital test structures.

### 2.7.2 Test set-ups and test structures

To assess the radiation hardness of the ITS prototypes, three types of structures are currently under investigation:

- Basic structures (diodes and transistors): three test structures were designed and implemented in TowerJazz technology in order to study basic operational parameters such as threshold voltage, transconductance, and dark current as a function of radiation type and dose as well as of the layout. RAL has provided a set of basic analogue structures to study TID effects on threshold voltage shift, transconductance and leakage current. The structures were manufactured with epitaxial thicknesses of 5.5  $\mu\text{m}$ , 12  $\mu\text{m}$  and 18  $\mu\text{m}$  with or without a deep p-well. Each structure consists of six high voltage (3.3 V) and six low voltage (1.8 V) NMOS and PMOS transistors. CERN has designed CMOS test structures (TID.TJ180) to study TID effects on threshold voltage and leakage current. They consist of single low voltage (1.8 V, 3 nm oxide thickness) and high voltage (3.3 V, 7 nm oxide thickness) NMOS and PMOS transistors of different lengths and widths. Some of these transistors have in addition a deep p-well layer underneath.
- Digital structures: a test chip for dedicated SEU tests (SEU.TJ180) has been designed and implemented at CERN and CCNU. It consists of single and dual port RAM structures and shift registers to measure the SEU cross sections of the digital registers and memories.

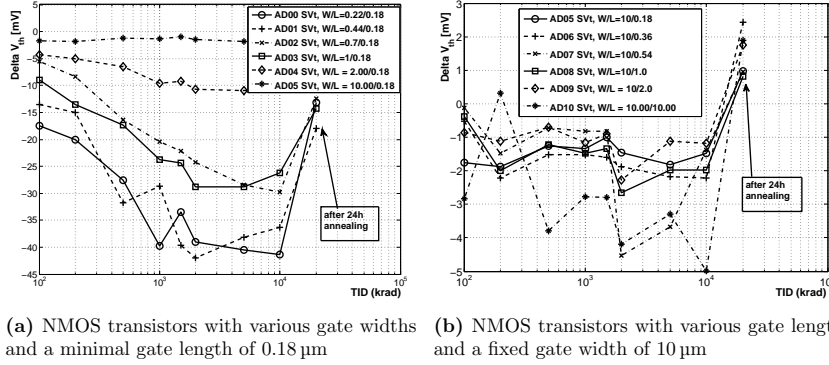


**Figure 2.21:** Threshold shift as a function of TID.

- Full sensor structures: the MIMOSA (Sec. 2.6.2) and Explorer (Sec. 2.6.4) prototype structures were characterised before and after irradiation.

### 2.7.3 Single device test

TID measurements were carried out on the TID-TJ180 structures using a 10 keV X-ray machine at CERN, which provided a fully automatised set-up to measure currents and/or voltages (typically  $I_d$  as a function of  $V_{gs}$  and  $V_{ds}$ ) using a semiconductor analyser that is connected to the pads of the test structure. The test structures are kept under worst bias conditions and irradiation was carried out up to 10 Mrad with a rate of 25 krad per minute. Figure 2.21 shows the threshold voltage shift as a function of the irradiation dose for low voltage NMOS transistors of different gate widths and a minimal gate length of 0.18  $\mu\text{m}$ . The most affected structure is the minimum size NMOS transistor (mask channel width  $W = 0.22 \mu\text{m}$ ) with a threshold shift of about 40 mV between 1 Mrad to 10 Mrad. NMOS transistors with a gate width of more than 1  $\mu\text{m}$  only show a marginal threshold shift of about 10 mV.

An even smaller sensitivity has been observed for NMOS transistor structures with a larger width of 10  $\mu\text{m}$  and various gate lengths as shown in Fig. 2.21. The observed threshold shift of less than 5 mV is very low and remains within the fluctuations of the measurement set-up. Both figures also confirm that in general the threshold shift decreases significantly with increasing transistor dimensions.

### 2.7.4 Tests of prototype structures

To test bulk effects generated by NIEL, MIMOSA and Explorer sensor prototype structures have been irradiated with a fluence of  $10^{13}$  1 MeV  $n_{eq}/\text{cm}^2$  and  $3 \times 10^{13}$  1 MeV  $n_{eq}/\text{cm}^2$  using neutrons from the FRM II reactor near Munich and the TRIGA MarkII Reactor at JSI in Ljubljana, respectively, before being bonded on hybrid carriers. Some MIMOSA-32 prototype structures (both n-irradiated and non n-irradiated) were, in addition, irradiated with TID up to 3 Mrad under worst bias conditions to study the impact of combined TID and NIEL. Both irradiated MIMOSA-32 and Explorer-0 prototype structures have been tested in laboratory set-ups using  $^{55}\text{Fe}$  sources and in test beams at CERN and DESY using pions and electrons to study the degradation of the sensor performance in terms of charge collection efficiency and SNR. The results are summarised in the following:

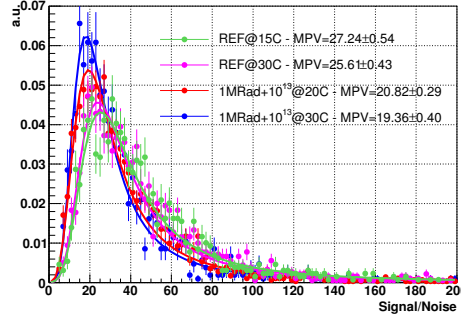


**Figure 2.22:** SNR of seed pixel measured with MIMOSA-32ter at the CERN-SPS, at two operating temperatures, before and after irradiation with the combined load of 1 Mrad and  $10^{13}$  1 MeV  $n_{eq}/cm^2$ .

- **Laboratory measurements:** Noise, charge collection efficiency and cluster size have been characterised by measuring the response of various MIMOSA and Explorer sensor prototype structures to 5.9 keV X-rays from a  $^{55}\text{Fe}$  source before and after TID and NIEL irradiation. An example of the detector response of MIMOSA-34 structures before and after irradiation with 1 Mrad is shown in Fig. 2.8 while results of MIMOSA-32 structures up to 3 Mrad irradiation can be found in [13]. The results show only a marginal degradation of the sensor response after TID irradiation. One can thus assume that the charge collection characteristics of the ITS innermost Layers will not degrade for the expected radiation load of 700 krad.

The effect of NIEL is shown for Explorer-0 in Fig. 2.15 before and after irradiation with  $10^{13}$  1 MeV  $n_{eq}/cm^2$  neutrons. The  $^{55}\text{Fe}$  peak position remains stable at a level of a few percent after irradiation. An increase of noise of 5 % to 15 % after irradiation with  $10^{13}$  1 MeV  $n_{eq}/cm^2$  neutrons has been observed for various pixel sizes and shapes operated at  $-1$  V and  $-6$  V, respectively. The charge collection efficiency drops by about 10 % at  $-1$  V regardless of pixel size and shape, whereas it remains almost unchanged for  $-6$  V. Due to the decrease in the SNR the cluster multiplicity decreases by about 10 % to 30 % for all structures.

- **Test beam measurements:** In order to study the full detection performance of the prototype structures (irradiated and non-irradiated MIMOSA-32ter/-34/-22THR and Explorer-0) before and after irradiation, test beam measurements were carried out at the CERN-SPS using negative pions of about 80 GeV/c to 120 GeV/c (MIMOSA-32ter prototypes) and at DESY using 4 GeV/c to 6 GeV/c electrons.

Seed pixel signal over noise before and after combined irradiation with 1 Mrad and  $10^{13}$  1 MeV  $n_{eq}/cm^2$  for a MIMOSA-32ter structure (Fig. 2.22) indicates a decrease of SNR from about 25 down to about 20 can mainly be attributed to the increase of noise after irradiation. These values are still affected by RTS noise and are therefore expected to improve after the ongoing design optimisation.

A similar behaviour has been observed for the Explorer-0 test structure. Appendix A summarises seed SNR and noise distributions measured with electrons before and after irradiation with  $10^{13}$  1 MeV  $n_{eq}/cm^2$  neutrons. In most of the cases, the seed SNR decreases by about 20 %, whereas the noise increases by about 5 % to 15 %.

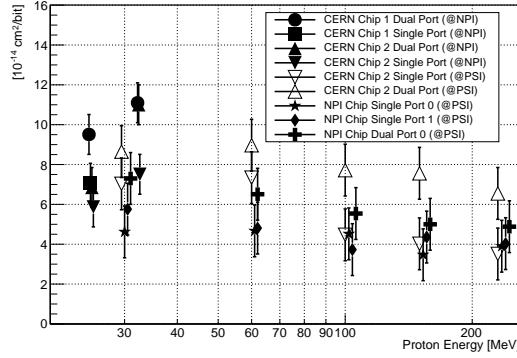


**Figure 2.23:** SEU cross sections as a function of proton beam energy measured for two SEU ASICs in single and dual port mode. For better readability, the values have been slightly separated horizontally.

### 2.7.5 Single event effects

SEU effects have been studied using the SEU\_TJ180 test structures read out by two different test systems, provided by CERN and NPI<sup>2</sup>, respectively. SEU cross section measurements were carried out using the proton beam from the NPI cyclotron in Rez near Prague and at PSI<sup>3</sup>. The SEU\_TJ180 structures were exposed to protons of 32.2 MeV and 24.8 MeV (NPI) and 29.5 MeV, 60 MeV, 100 MeV, 150 MeV and 230 MeV (PSI) at proton fluxes between  $1.1 \times 10^7 \text{ cm}^{-2} \text{ s}^{-1}$  and  $1.1 \times 10^8 \text{ cm}^{-2} \text{ s}^{-1}$ . All SEU tests were carried out in static mode, i.e. the memory was programmed with a fixed pattern prior to the irradiation cycle and bit flips were monitored as a function of the proton fluence. The results of the SEU cross section measurements are shown in Fig. 2.23.

Given a typical memory depth of  $N = 2 \text{ Mbit}$  and a throughput of  $\mu = 300 \text{ Mbit s}^{-1}$  as well as a total hit density of  $\rho = 1.6 \times 10^6 \text{ cm}^{-2} \text{ s}^{-1}$  and a SEU cross section of  $\sigma = 10^{-13} \text{ cm}^2 \text{ bit}^{-1}$ , one gets a mean error probability per bit,  $\lambda$ , of:

$$\lambda = N/\mu \cdot \rho \cdot \sigma \approx 10^{-9} \text{ bit}^{-1} . \quad (2.1)$$

This is the worst case scenario of a central chip and still low enough that the induced data corruption can be tolerated. Though much less likely (typically only a few hundred bits are concerned) but still more relevant is the aspect of SEUs in the configuration or the control logic within the chips. In contrast to errors in the data stream, any error in the configuration logic is persistent until the configuration is updated. Even worse, SEUs in the control logic of the chip can lead to electrical errors on the bus and even physical damage. Special means will therefore be taken to protect those parts of the chip by a redundant, radiation-hardened design.

Radiation hardness tests with regard to SEL require a dedicated test set-up and will be carried out in the near future for various test structures.

<sup>2</sup>Nuclear Physics Institute, Prague

<sup>3</sup>Paul Scherrer Institute

## 2.8 Summary and plans

Within the R&D phase, the TowerJazz technology has successfully been qualified as appropriate for the ALICE ITS pixel sensor. The different design streams have accomplished key achievements towards the development of large scale prototypes. In particular, radiation tolerance and particle detection efficiencies meeting the requirements have been achieved. Now, focus lies on the characterisation of bigger chips, including full-size building blocks of the final chips. After, a decision for the option to be adopted will be taken and forces will be joined to implement the final chip, characterise it and give the green light for mass production.





### 3 Pixel Chip mass production, testing and quality assurance

The full production of the monolithic silicon Pixel Chips for the upgrade of the ALICE ITS will require the processing of a large number of wafers. The wafers will be post-processed, thinned and diced to obtain individual Pixel Chips. Each chip will be tested and inspected prior to the assembly into larger modules. This chapter outlines the individual steps starting from the quality assurance of the starting wafers up to obtaining fully tested chips, ready for assembly. In Sec. 3.1 the different options for starting wafers and the materials used for the first engineering run are presented. This is followed by an outline on the quality assurance procedure proposed for the starting wafers. Section 3.2 presents the results from thinning and dicing tests. Section 3.3 outlines the different tests to be carried out on individual chips in order to qualify them for assembly. Finally, in Sec. 3.4 the post-processing for achieving solderable pads is presented.

#### 3.1 Wafers for CMOS production

The thickness and quality of the epitaxial layer of monolithic silicon pixel detectors play a crucial role for the overall performance of the detector. While in earlier monolithic pixel detectors relatively low resistivity and thinner epitaxial layers were used, TowerJazz offers the possibility of processing wafers with epitaxial layer resistivities of  $1\text{ k}\Omega\text{ cm}$  and thicknesses of up to  $18\text{ }\mu\text{m}$ . The higher resistivity allows partial depletion of the epitaxial layer and an increase in the fraction of charge collected by drift, as described in Chap. 2. In addition, the signal generated by a traversing charged particle scales with the thickness of the layer. TowerJazz offers wafers with epitaxial layer thicknesses ranging from about  $5\text{ }\mu\text{m}$  up to  $18\text{ }\mu\text{m}$  (where the latter corresponds to a signal charge of approximately 1100 electrons for minimum ionizing particles), but also has accepted processing wafers with different characteristics (see Tab. 3.1). The increase in thickness, and thus higher number of charges generated, is expected to improve the signal-to-noise ratio. Prototype chips have been produced on wafers with different epitaxial layer thicknesses for experimental verification of this effect (see Sec. 3.1.1).

The epitaxial silicon layer is grown on a single crystal substrate wafer by chemical vapour deposition (CVD) [15]. The purpose of growing an epitaxial layer on a silicon substrate is primarily to achieve a layer of a different, usually lighter concentration of dopants. In the present case the substrate resistivity is in the order of a few  $10\text{ m}\Omega\text{ cm}$  compared to the epitaxial layer resistivity which is in the order of  $1\text{ k}\Omega\text{ cm}$ . Epitaxial layers also contain less impurities, such as carbon and oxygen, and less grown-in defects, as observed in Czochralski-grown (CZ) wafers.

The substrate on which the epitaxial layer is deposited acts as a mechanical support and also as a potential barrier to reflect charges back into the epitaxial volume. The concentration of dopants in the two regions differs by several orders of magnitude, thus causing different levels of contraction of the silicon lattice, induced by the dopants. The epitaxial layer growth is accompanied by two different stresses (tensile and compressed) on the substrate and epitaxial side. The stress misfit increases as the epitaxial layer gets thicker and can cause misfit dislocations at the epitaxial-substrate interface [15]. For the

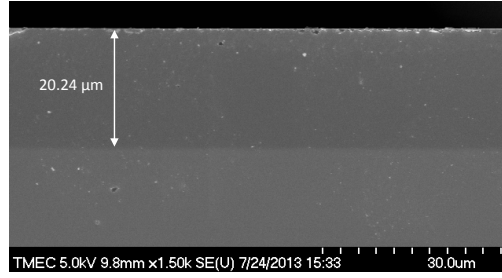


**Figure 3.1:** SEM image of the cross section of an unprocessed epitaxial wafer. The nominal epitaxial layer thickness is 20  $\mu\text{m}$ . The difference between the epitaxial layer and the substrate is visible as a difference in colour. The measured thickness is in good agreement with the expected one.

ALICE ITS, wafers with epitaxial layer thicknesses of up to 40  $\mu\text{m}$  have been successfully produced and processed in an engineering run in 2013. No indication of misfit dislocations was observed on these wafers.

Figure 3.1 shows a scanning electron microscope (SEM) image of a cross section of a blank epitaxial wafer from a custom production for the ALICE ITS. The difference between the epitaxial layer and the substrate in the SEM image is visible as a change in colour. The nominal thickness of the epitaxial layer on this wafer is 20  $\mu\text{m}$ , which is in good agreement with the 20.24  $\mu\text{m}$  measured. This wafer is part of a special production of epitaxial wafers with higher thickness, which is described in Sec. 3.1.1.

Monolithic silicon pixel detectors, as developed for the ALICE ITS, require wafers with a relatively thick epitaxial layer, with high-resistivity and a good interface quality to the substrate to generate sufficiently large signals. The following Sec. 3.1.1 describes the different types of epitaxial wafers used for the first engineering run in 2013.

Full-thickness high-resistivity wafers can also be used as starting material for producing monolithic silicon pixel detectors. High-resistivity CZ wafers have been introduced in CMOS processing for other applications, such as high radio frequency transceivers, and first prototype pixel matrices were already produced on this material [16]. However, this development is still in a very early phase and epitaxial wafers have been adopted as the baseline starting material for the ALICE ITS upgrade.

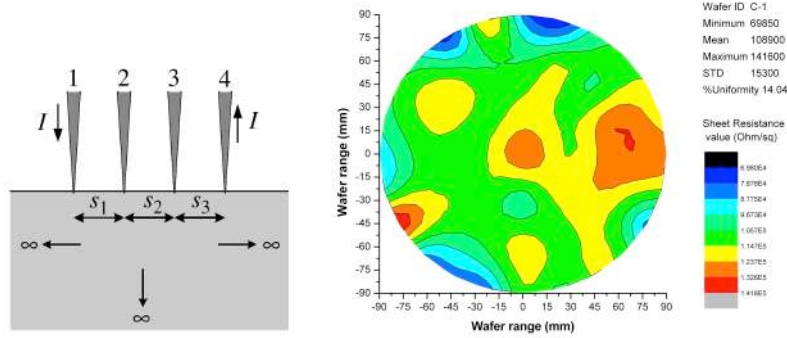
### 3.1.1 Different wafer starting material during the R&D phase

For the engineering run submitted in March 2013, a set of different wafers, with epitaxial layer and full-thickness CZ wafers, have been procured. The list of the different starting wafers is shown in Tab. 3.1. The epitaxial layer thicknesses range from 12  $\mu\text{m}$  up to 40  $\mu\text{m}$ . The wafers of type 1 are standard wafers used by TowerJazz and have been included in the run as monitoring wafers for the CMOS process.

As described in Chap. 2, each reticle on the wafer contains a set of prototype chips exploring different design options. The prototype chips from this run are presently under test and results exploring the different architectures and designs are reported in Chap. 2. First test results on Explorer-1 chips from type 2 (18  $\mu\text{m}$  epitaxial layer), type 3 (30  $\mu\text{m}$  epitaxial layer), type 5 (20  $\mu\text{m}$  epitaxial layer) and type 6 (40  $\mu\text{m}$  epitaxial layer) wafers indicate a cluster signal increase compatible with the increase in thickness of the epitaxial layer (see Fig. 2.17 and App. A). Further measurements on prototype chips from different starting wafers are presently being carried out including measurements on irradiated chips.

**Table 3.1:** Wafers used for the engineering run March 2013.

Type	Number of wafers	Epitaxial Thickness ( $\mu\text{m}$ )	Resistivity ( $\text{k}\Omega\text{ cm}$ )
1 (LR-12)	3	$12.0 \pm 0.5$	0.03
2 (HR-18)	4	$18.0 \pm 1.5$	$>1$
3 (HR-30)	3	$30.0 \pm 0.3$	$\approx 1$
4 (HR-40A)	3	$40.0 \pm 0.6$	$\approx 1$
5 (HR-20)	6	$20.0 \pm 1.9$	6.2
6 (HR-40B)	3	$40.0 \pm 1.9$	7.5
7 (CZ)	3	CZ	$>0.7$

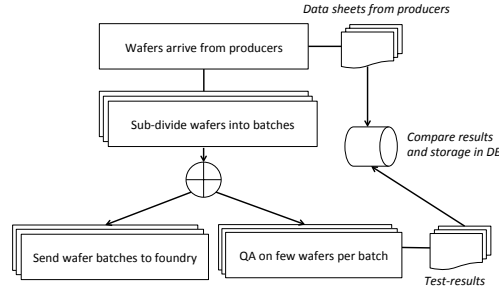


**Figure 3.2:** Example of a schematic arrangement for the four point probe measurement [17] (left). In case of epitaxial silicon wafers, the current path via the substrate has to be taken into consideration [15]. Resistivity map of one epitaxial wafer measured at TMEC with a RS30 KLA-Tencor four point probe system (right). Note that the resistivity values are indicated as  $\Omega/\text{sq}$ .

### 3.1.2 Quality assurance tests of wafer starting material

The wafer manufacturers provide information on epitaxial layer thickness and resistivity values derived from SRP (Spreading Resistance Profiling) measurements. For this purpose, a blank wafer is ground at an angle and the resistivity profile is measured at different depths. This measurement is destructive to the wafer and is carried out on a sample basis. The surface resistivity can be measured in a number of points across the wafer, using, for example, a four point probe measurement system. The quality assurance for the wafer procurement for the production will include the monitoring of the epitaxial layer resistivity and thickness on a sample basis as one of the key parameters for the performance of the final chips. The tests and procedures are presently being developed to put them in place well in advance of the start of production.

First surface resistivity ( $R_s$ ) measurements have been carried out on blank wafers (one wafer of type 5, one wafer of type 6) of the engineering run of March 2013 at the collaborating institute TMEC, Thailand. Figure 3.2 shows the schematic arrangement of a four point probe measurement on the left hand side. Prior to the measurement, the wafer was dipped in a 1% HydroFluoric bath to remove the native oxide layer on the surface. The resistivity was measured on 49 points across the surface, corresponding to the 49 reticles of the processed CMOS wafer. The  $R_s$  values measured on the wafer of type 6 are shown on the right hand side in Fig. 3.2. The corresponding average resistivity value measured is

**Figure 3.3:** Flow chart of the wafers qualification tests.**Table 3.2:** Dimensional requirements for the Pixel Chips.

	Target value	Variation
Thickness	50 $\mu\text{m}$	$\pm 5 \mu\text{m}$
Width	15 mm	$\pm 30 \mu\text{m}$
Length	30 mm	$\pm 30 \mu\text{m}$

7.9 k $\Omega$  cm with a standard deviation of 1.1 k $\Omega$  cm. The average value agrees within errors with the epitaxial layer resistivity value provided by the supplier, which was measured on a different wafer of the same batch (7.5 k $\Omega$  cm). The map also shows that for most of the surface area, the resistivity stays within about 30 % around the nominal value, while a stronger difference between the centre value and the values measured at the wafer rim are observed.

The monitoring of the wafer quality throughout the production will be part of the quality assurance procedure. The suppliers will provide information on the wafers, such as resistivity and thickness of the epitaxial layer. Monitoring the main wafer parameters is foreseen on a sub-set of every batch produced. The flow chart of the different operations to be performed to qualify the wafers is shown in Fig. 3.3.

### 3.2 Thinning and dicing

Starting from a standard thickness of 725  $\mu\text{m}$ , 8-inch wafers are routinely thinned in multi project wafer (MPW) runs to about 400  $\mu\text{m}$ . However, the target thickness for the ALICE ITS upgrade is significantly lower than that, aiming to achieve a thickness of 50  $\mu\text{m}$ . The STAR PXL detector is already using monolithic silicon pixel chips of 50  $\mu\text{m}$  thickness [6]. This corresponds to 0.054 % of radiation length.

Table 3.2 summarises the dimensional requirements for the Pixel Chips.

In case of an epitaxial layer thickness of 40  $\mu\text{m}$ , the total thickness has to be increased to about 70  $\mu\text{m}$ . For thinner epitaxial layers, the target thickness is 50  $\mu\text{m}$ .

In the module arrangement, individual chips will be placed with a nominal gap of 100  $\mu\text{m}$  next to each other. Therefore the edge quality and the dimensional precision of the chips has to be compatible with this requirement. A visual inspection of each chip, as described in Sec. 3.3.1, will ensure that only chips which meet these requirements will be mounted.

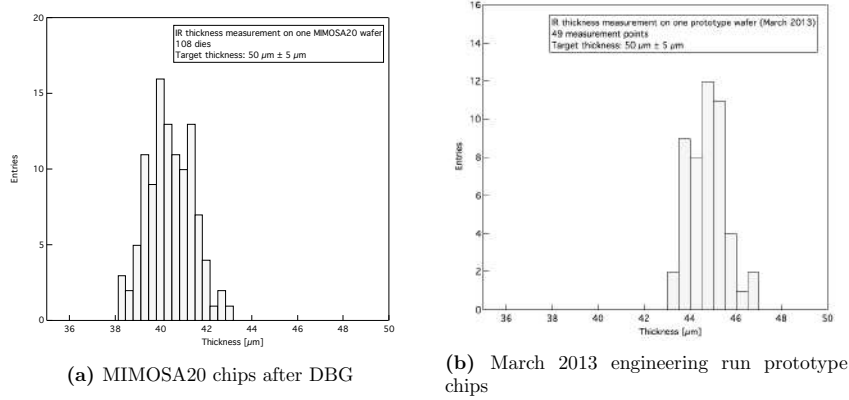


**Figure 3.4:** Interferometric thickness measurements of 50  $\mu\text{m}$  thick chips, not including the CMOS metal layers ( $\approx 10 \mu\text{m}$ ).

### 3.2.1 Thinning tests carried out in the R&D phase

Thinning and dicing has been carried out on blank wafers and fully processed wafers throughout 2012/13 to optimise a thinning process based on the Dice Before Grind (DBG) approach. The wafers are predicted to about 80  $\mu\text{m}$  depth and then back-grinded to 50  $\mu\text{m}$  which leads to the separation of the chips on the wafer. Table 3.3 summarises the results of the DBG on 30 wafers. The yield is defined as no visible damage to the chip, as no electrical tests could be carried out on chips from these wafers. In the future, electrical test results will be included when thinning fully processed CMOS wafers.

Measurements of the chip thickness are carried out immediately after grinding using an infrared interferometer. The results of these measurements on one wafer are reported in Fig. 3.4a. The interferometric measurement does not take into account the CMOS metal layer stack but only the silicon thickness. Thus about 10  $\mu\text{m}$  have to be added to the measured thickness value. The measured values are in good agreement with the target thickness of 50  $\mu\text{m}$  and are well within the limits of  $\pm 5 \mu\text{m}$ . Interferometric thickness control on a subset of chips has been included as part of the quality assurance on all wafers thinned in 2013.

The precision of the chip size is of crucial importance for the module construction where several chips will be aligned in a row, aiming to minimise the gap between chips to keep the insensitive region as small as possible. For standard diamond blade dicing, the dimensional

**Table 3.3:** List of wafers thinned and diced in 2012.

Type	Number	Chip size ( $\text{mm}^2$ )	Usage	Good (%)
blank	13	various	mech. and assembly tests	N/A
blank	5	$15 \times 30$	mech. and assembly tests	96
with Al pattern	5	$15 \times 30$	interconnection tests	89
with Ni/Au pattern	5	$15 \times 30$	interconnection tests	77
MIMOSA20	2	$10 \times 20$	CMOS wafers	100
Total	30			91

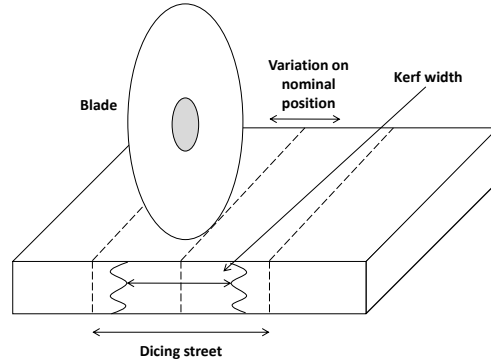


**Figure 3.5:** Simple scheme of the diamond blade dicing setup.

precision of the diced chips is determined by the choice of dicing blade, specifically the kerf width of the blade and the precision with which the blade can be placed on a dicing street of a given width. Figure 3.5 shows a schematic view of the dicing blade and the parameters which add to the uncertainty of the chip size during diamond blade dicing. The dicing blade used for the dicing of the first dummy and prototype wafers was not yet adjusted to reach the target precision. The total variation in geometrical dimensions is not  $60\text{ }\mu\text{m}$ , but approximately  $80\text{ }\mu\text{m}$ . Further tests and optimisation will be carried out to achieve the target values.

An alternative technique to separate the chips on the wafer is laser dicing. Different laser dicing techniques are presently available in industry. The laser cuts along the scribe line and the separation of the chips is usually carried out by tape expansion. First tests were done on blank wafers using laser dicing systems at different suppliers. Laser dicing can also be used to pre-dice the chips before back-grinding the wafers to  $50\text{ }\mu\text{m}$  thickness. Tests are presently underway to combine laser pre-dicing and back-grinding using blank wafers. The edge quality and the precision of the laser cut will be assessed on the first chips from these wafers, which are expected for spring 2014.

Three wafers from the engineering run have been thinned to  $450\text{ }\mu\text{m}$  and diced in order to provide first samples for characterization tests. Three wafers have been successfully thinned to  $50\text{ }\mu\text{m}$  and  $70\text{ }\mu\text{m}$  (in case of an epitaxial layer thickness of  $40\text{ }\mu\text{m}$ ). Presently, further wafers from the run are being thinned to  $50\text{ }\mu\text{m}$  and diced.

The results from the interferometric thickness measurement of  $50\text{ }\mu\text{m}$  thick chips are shown in Fig. 3.4b. The average thickness on 49 points measured across the full wafer is  $44.6\text{ }\mu\text{m}$ , with a maximum variation of  $3\text{ }\mu\text{m}$ .

### 3.3 Single chip test

Prior to mounting on the module, each chip will be tested according to a defined test-procedure. The results of each test will be recorded and stored in a commonly accessible database. The chips will be classified according to the test results and only good chips which are fully functional and meet the geometrical requirements will be used for module mounting. A detailed scheme for the classification of the chips will be defined once full size prototype chips are available and a sufficient number of chips have been tested to produce a large enough statistical sample.



**Figure 3.6:** Image of the visual inspection of a chip corner. The camera scans the edge of the chip. The position of the camera is indicated by the square with the target cross visible on the top right. The image has been taken just before the machine reaches the broken corner, thus no error is yet indicated.

Every tested chip has to be traceable, either electrically or via a visual mark, throughout the different testing and assembly steps. Several techniques are under consideration, but no final choice for the chip identification has yet been taken. First tests using laser marking have been carried out on dummy chips. Alternative options are currently under study.

The single chip tests will include a visual inspection, an electrical test and a test with radioactive source or laser for full verification of the functionality.

- The **visual inspection and metrological measurements** will ensure that no physical damage has occurred and that the contact pads are fully intact to ensure a good quality connection to the Flexible Printed Circuit (FPC). A metrological measurement will ensure that the chips geometrical dimensions are within the acceptable tolerances.
- The **electrical and functional tests** will address the full electrical functionality of the chip and validate the signal generation in the epitaxial layer.

The exact yield factors for each of the processing steps (production, dicing, thinning, etc.) prior to the single chip tests are not yet known. However, experience from other experiments (e.g. STAR) showed that a yield factor of about 50 % for thin chips of 50  $\mu\text{m}$  can be expected. Thus the total amount of chips to test for the ALICE ITS will be in the order of 50 000.

In order to efficiently test this large number of chips, the visual tests as well as the functional tests will be carried out using automated systems. It is planned to first carry out visual tests to select only those chips for the functional tests that comply with the dimensional requirements and show no damage. Chips which do not pass the visual test are discarded from the test flow, which will add to the reduction of testing time.

### 3.3.1 Visual and metrological inspection

The automated visual and metrological inspection of the chips will allow the detection of different anomalies such as dimensional errors (e.g. chip size, pad size and location), physical damage (e.g. cracks, missing parts, scratches) and surface damage (e.g. scratches, debris, pollution) and to classify the chips accordingly.



A feasibility study for visual and metrological inspection has been carried out together with a supplier of visual inspection systems, using an existing system at the company site (VEA, Italy). The dummy chips used for the study are similar in size and connection pads as assumed for a final chip ( $15\text{ mm} \times 30\text{ mm}$ , connection pads of  $400\text{ }\mu\text{m}$  diameter). Figure 3.6 shows an example of the visual inspection of a chip with a broken corner. The inspection system scans the edge of the chip and will indicate an error once it reaches the broken edge. The proposed machine can automatically handle each chip, picking it up from the tray and placing it under a camera for optical inspection. The camera is equipped with a pattern recognition software able to satisfy the test requirements in terms of resolution. The expected resolution is of the order of microns, depending on the speed of the measurement.

The time required for the visual and metrological inspections has to be kept as short as possible. A preliminary time estimate for the procedure including the handling is 40 s per chip. This includes picking up the chip from the tray and placing it underneath the inspection system, carrying out the measurements and again picking up the chip with a robotic arm and placing it back into the carrier tray.

### 3.3.2 Electrical and functional test

A first list of tests containing the main steps that should be included in the test sequence is shown in the following. The final list of tests can only be defined when the full size prototype chips are available.

- basic electrical test (smoke-test), power supply and current values;
- test of I/O connection (e.g. reading/writing configuration);
- noise run to identify noisy pixels in the matrix;
- test of the digital part of the chip (e.g. using a test pulse pattern);
- sensor response using either light or a radioactive source.

The tests will be automated and limited to the minimum required to identify faulty chips. Furthermore, carrying out the tests in different test centers in parallel will allow further reduction of the overall testing time and avoids that failure of a test system creates a bottleneck in the overall detector construction phase.

Two different techniques are presently under study to provide the electrical connection to the chip pads during mass testing:

- contact by using a probe card;
- contact by using a bed of needles probe.

In case of contacting the pads with a bed of needles probe, the fixture will host a defined number of chips. The test of the chips will be executed sequentially. By providing several fixtures that can be pre-mounted, the handling time will be further reduced. Direct test point inspection and test control can be performed using an integrated camera. Presently, a set of tests is being carried out using dummy chips with pad contacts to study how to control the contact. A test fixture is being designed for a bed of needles contact of these dummy chips and first test results are expected early 2014. In parallel tests are carried out together with a commercial probecard manufacturer developing a first prototype for a test station.

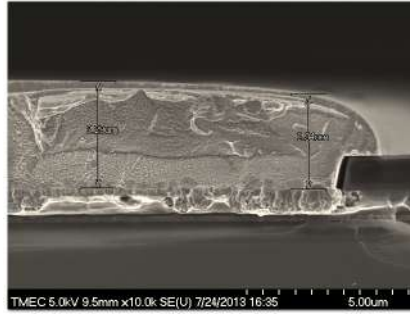


**Figure 3.7:** SEM image of a pad cross-section on a dummy chip wafer. The Ni-layer deposited is in the order of about  $3\text{ }\mu\text{m}$  thickness covered by a thin layer of Au. The Ni-layer has been deposited on the Al-pad by electroless Ni-deposition.

### 3.4 Wafer post-processing

The CMOS processing will provide aluminium metal pads on the chip for electrical connections. In case of using laser soldering to connect the chip pads with the FPC, it will be necessary to post-process the wafers to have solder-wettable metal pads. This will include the deposition of a Ni/Au layer on the Aluminium pad after finishing the CMOS processing.

First tests have been carried out by producing dummy chips with Al/Ni/Au pads. An example of a SEM cross-section view of an Al/Ni/Au pad on a dummy chip wafer is shown in Fig. 3.7.

In order to avoid additional losses in the post-processing of the wafers, it is envisaged to carry out this step immediately after CMOS processing and before thinning and dicing.



## 4 Detector Staves

The design of the new ITS is conceived as a two-barrel structure: the Inner Barrel (IB), formed by Layers 0 to 2, and the Outer Barrel (OB), formed by Layers 3 to 6. An overview of the new ITS layout is given in Chap. 1 and summarised in Tab. 1.1. The three Layers of the IB are also referred to as the Inner Layers, with Layers 3 and 4 as Middle Layers and Layers 5 and 6 as Outer Layers.

In the azimuthal direction, each Layer is segmented in elements called Staves. The Stave, which extends over the whole length of the respective Layer, is the basic building block of the detector. The Stave contains all structural and functional components, thus making it the smallest operable part of the detector. The three Inner Layers are built with identical Staves, while the Staves of the OB Layers have a different layout due to their longer length. The Staves of the Middle and Outer Layers have the same layout although those of the latter are almost twice the length of the Middle Layers ones.

This chapter is dedicated to the description of the Staves and their construction process. The design and layout of the Staves for the Inner and the Outer Barrel are described in Sec. 4.1. The developments and the technical choices of the Stave components (except the Pixel Chip, which is discussed in detail in Chap. 2) as well as their characterisation are illustrated in Sec. 4.2 and 4.3. The techniques that are being evaluated to interconnect the Pixel Chips, namely laser soldering and Single point Tape Automated Bonding (SpTAB), are discussed in Sec. 4.4. The assembly procedures and the prototyping of the Staves are described in Sec. 4.5. The ongoing R&D activities on some alternative options for the Stave implementation are reported in App. B.

### 4.1 Stave design

The conceptual design of both IB and OB Staves is based on the following elements:

- **Space Frame:** a carbon fibre support structure providing the mechanical support and the necessary stiffness;
- **Cold Plate:** a sheet of high-thermal conductivity carbon fibre with embedded polyimide cooling pipes, which is either integrated within the Space Frame (for the IB Staves) or attached to the Space Frame (for the OB Staves), as described in Sec. 4.2; the Cold Plate is in thermal contact with the Pixel Chips or with the Module carbon plate to remove the generated heat.
- **Hybrid Integrated Circuit (HIC):** an assembly of a polyimide Flexible Printed Circuit (FPC) on which a number of Pixel Chips, namely 9 and 14 for the IB and OB Staves respectively, and some passive components, are bonded;
- **Module:** the HIC glued to a Module carbon plate, which provides the necessary stiffness for the handling and possible replacement of a single Module in case of malfunctions, as described in Sec. 4.5.2.
- **Half-Stave:** the OB Staves are further segmented in azimuth in two halves, called Half-Staves. Each Half-Stave, extending over the full length of the Stave, consists

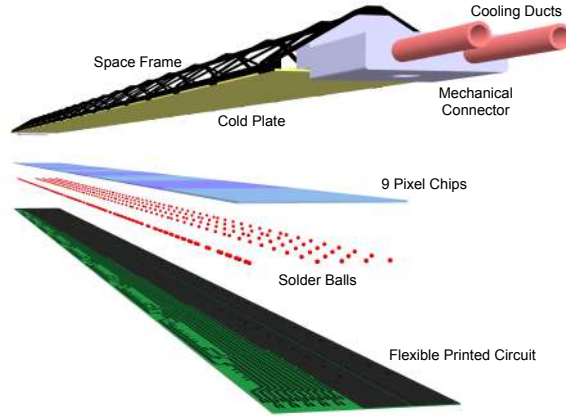


**Figure 4.1:** Schematic view of the Inner Barrel Stave.

of a Cold Plate on which a number of Modules are glued, namely four and seven for Middle Layers and Outer Layers, respectively.

The design of the Staves takes into account the specifications of the new ITS. The low material budget combined with very good rigidity and stability of a relatively large structure imposes severe constraints in terms of design and technical solutions that can be implemented. The requirements of the new ITS, which have been taken into account in the design of the Staves of the Inner and Outer Barrels, have been illustrated in Chap. 1.

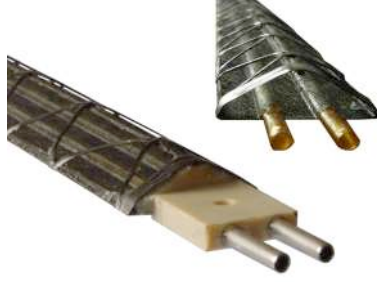
#### 4.1.1 Inner Barrel Stave

Each IB Stave will be instrumented with one HIC, which consists of nine Pixel Chips in a row connected to the FPC, hence covering a total active area of  $15\text{ mm} \times 270.8\text{ mm}$  (Tab. 1.1) including the  $100\text{ }\mu\text{m}$  gap between adjacent chips along  $z$ . The interconnection between Pixel Chips and FPC is achieved via laser soldering, described in Sec. 4.4. The HIC is glued to the Cold Plate with the Pixel Chips facing it in order to maximise the cooling efficiency. Figure 4.1 shows a schematic layout of the IB Stave. An extension of the FPC, not shown in Fig. 4.1, connects the Stave to a patch panel that is served by the electrical services entering the detector from one side only. A mechanical connector at each end of the Stave allows the fixation and alignment of the Stave itself on the end-wheels, as described in Chap. 5. The inlet and outlet of the closed-loop cooling circuitry are located at the same end of the Stave because also the cooling is served only from the same side as all other services.

The prototyping of the IB Stave is well advanced. Figure 4.2 shows the detail of the end-Stave with and without the mechanics connector and the cooling ducts.

#### Material budget

The design of the Stave accounts for the tight requirement on the material budget, which is limited to  $0.3\% X_0$ . Table. 4.1 reports the estimated contributions of the IB Stave to the material budget.

**Figure 4.2:** Prototypes of the Inner Barrel Stave.**Table 4.1:** Estimated contributions of the Inner Layer Stave to the material budget.

Stave element	Component	Material	Thickness ( $\mu\text{m}$ )	$X_0$ (cm)	$X_0$ (%)
<b>HIC</b>	FPC Metal layers	Aluminium	50	8.896	0.056
	FPC Insulating layers	Polyimide	100	28.41	0.035
	Pixel Chip	Silicon	50	9.369	0.053
<b>Cold Plate</b>		Carbon fleece	40	106.80	0.004
		Carbon paper	30	26.56	0.011
	Cooling tube wall	Polyimide	25	28.41	0.003
	Cooling fluid	Water		35.76	0.032
	Carbon plate	Carbon fibre	70	26.08	0.027
	Glue	Eccobond 45	100	44.37	0.023
<b>Space Frame</b>		Carbon rowing			0.018
<b>Total</b>					<b>0.262</b>

A detailed study of the material distribution across the Stave has been performed after the optimisation of each component. In Fig. 4.3 the azimuthal distribution of the Layer 0 material traversed by the particles at  $\eta = 0$  is shown. Neighbouring Staves are partially superimposed to ensure the detector hermeticity. The highest peaks correspond to the overlap of the reinforced structures along the edges of the Space Frame to guarantee the required stiffness and the narrow spikes to the reinforcement implemented in the upper vertex. The peaks around 0.5%  $X_0$  are due to the polyimide cooling pipes embedded in the Cold Plate, which have an inner diameter of 1.024 mm and a wall thickness of 25  $\mu\text{m}$ , assuming they are fully filled with water. The average value of 0.282%  $X_0$  fulfils the specifications, which are of extreme importance for the achievable impact parameter resolution.

#### 4.1.2 Outer Barrel Stave

The Staves of the Middle and Outer Layers are identical, except that the Outer Layer Stave is nearly twice as long. The basic concept of the OB Staves is very similar to the IB ones. However, the Staves of the OB are split azimuthally in two Half-Staves, each longitudinally further segmented in four or seven Modules for the Middle and Outer Layers, respectively, as depicted in Fig. 4.4. The design of the Space Frame of the OB Staves is derived from the ladder frame of the outer layers of the current ITS [3]. It supports two Cold Plates,

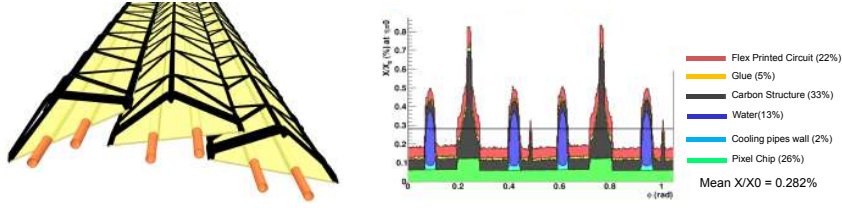


**Figure 4.3:** A detail of the Stave overlaps of the Inner Layers (left) and the corresponding material budget distribution (right). The highest peaks correspond to the overlap of the reinforced structures at the edges of the Space Frame, while the narrow spikes to the reinforcement at the upper vertex. The peaks around  $0.5\% X_0$  are due to the polyimide cooling pipes fully filled of water.

with the respective integrated cooling pipes, each carrying four or seven Modules. From here forward, all references will be made to the Stave layout of the Outer Layer, which are more challenging from the system and assembly point of view, unless otherwise specified. The layout and components of the OB Stave are highlighted in Fig. 4.4. The Cold Plates are connected to the Space Frame by U-shaped connectors. In order to achieve a nearly full coverage, the two Cold Plates of a Stave overlap in the  $r\phi$  direction, as shown by the Stave cross section in Fig. 4.4. The details of the support structure and the cooling system are described in Sec. 4.2.

The HIC of the OB Staves consists of an array of two rows of seven chips each, connected to a common FPC that is approximately 3 cm wide and 21 cm long. The HIC is glued to a 120  $\mu\text{m}$  thick carbon plate to ensure the required stiffness and to ease the handling during the assembly and testing phases. The assembly of the HIC with the carbon plate is called a Module. The FPC distributes the clock and configuration signals, as well as the data read-out and power connections to all Pixel Chip in a Module. The expected maximum data throughput for the OB Staves, illustrated in Chap. 6, allows the development of a serial read-out scheme of an entire chip row, which extends over the full length of the Stave. The read-out concept is described in more detail in Sec. 4.3 and in Chap. 6. Taking into account the estimated power density of  $100 \text{ mW cm}^{-2}$ , summing up analogue and digital power contributions, an additional bus to distribute the power is needed to fulfil the maximum acceptable voltage drop over the whole length of the Half-Stave. This bus, named Power Bus (PB), extends over all FPCs of the Half-Stave, providing analogue and digital power as well as ground connections. The baseline powering scheme is based on a conservative parallel connection: all chips in a Module are directly connected to the analogue and digital power planes of the FPC, which are in turn fed by the PB serving the Half-Stave.

Several components of the OB Staves have been prototyped; Fig. 4.5 shows a full size prototype of the Space Frame for the Outer Layers. The production process and characterisation tests are described in the following Sec. 4.2. It has been demonstrated that this design provides the required stiffness and thermal properties. The design and the ongoing development of the FPC and of the PB are described in Sec. 4.3.

### Material budget

Table. 4.2 reports the estimated contributions of the OB Stave to the material budget. It is worth underlining that the thickness of the aluminium power planes applies to the Outer Layers Stave and it could be less for the Middle Layers according to the smaller number

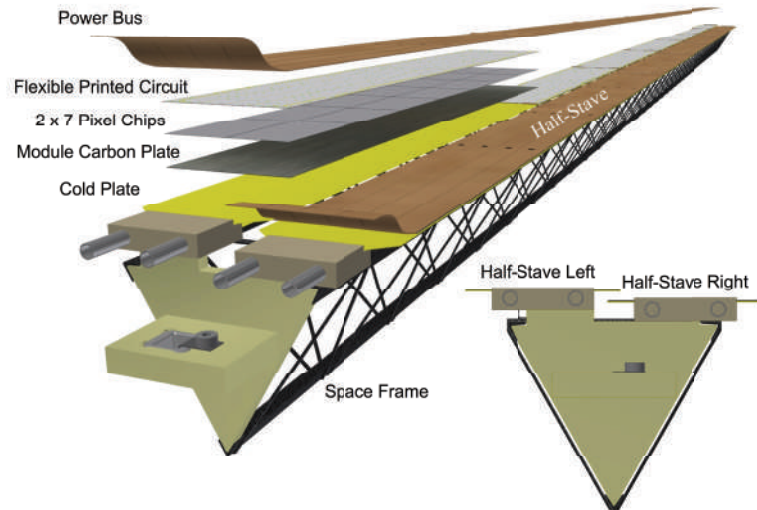


**Figure 4.4:** Schematic exploded view and cross section of the OB Stave.

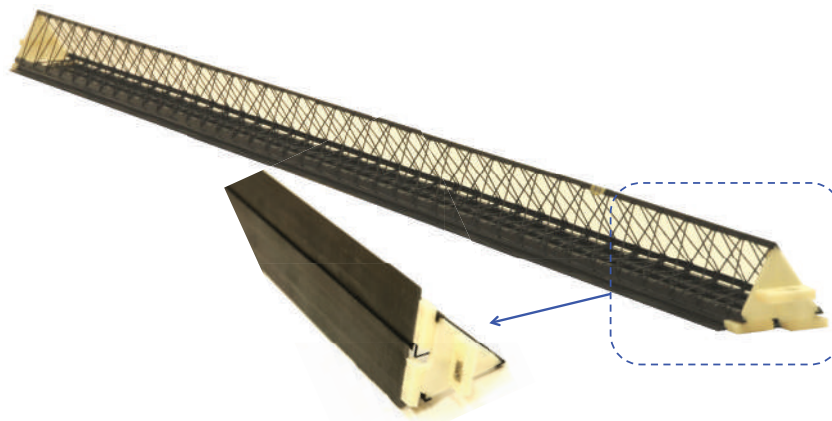


**Figure 4.5:** A prototype of the OB Stave Space Frame with Cold Plates.



**Table 4.2:** Estimated contributions of the Outer Layer Stave to the material budget.

Stave element	Component	Material	Thickness ( $\mu\text{m}$ )	$X_0$ (cm)	$X_0$ (%)
<b>Module</b>	FPC Metal layers	Aluminium	50	8.896	0.056
	FPC Insulating layers	Polyimide	100	28.41	0.035
	Module plate	Carbon fibre	120	26.08	0.046
	Pixel Chip	Silicon	50	9.369	0.053
	Glue	Eccobond 45	100	44.37	0.023
<b>Power Bus</b>	Metal layers	Aluminium	200	8.896	0.225
	Insulating layers	Polyimide	200	28.41	0.070
	Glue	Eccobond 45	100	44.37	0.023
<b>Cold Plate</b>		Carbon fleece	40	106.80	0.004
		Carbon paper	30	26.56	0.011
	Cooling tube wall	Polyimide	64	28.41	0.013
	Cooling fluid	Water		35.76	0.105
	Carbon plate	Carbon fibre	120	26.08	0.046
	Glue	Eccobond 45	100	44.37	0.023
<b>Space Frame</b>		Carbon rowing			0.080
<b>Total</b>					<b>0.813</b>

of Pixel Chips. The estimated overall material budget is within reach of the required 0.8 %  $X_0$ .

The detailed description of the azimuthal distribution of the material across the Outer Layer Stave is shown in Fig. 4.6. Similarly to the IB, neighbouring Half-Staves are partially superimposed to ensure the detector hermeticity, thus giving rise to the peaks around 1.25 %  $X_0$ . The highest peaks are due to the polyimide cooling pipes embedded in the Cold Plate, assuming they are fully filled with water.

## 4.2 Mechanical support structure and cooling

This section presents the studies carried out to identify and characterise materials, processes and technologies suitable for the construction of the mechanics and cooling of the Staves.

The Stave mechanical support must fulfil stringent requirements in terms of minimum mass and highest stiffness. Its design is inherently linked to the layout of the cooling system that will be adopted to remove the heat dissipated by the silicon sensors since the cooling system is integrated in the mechanical structure.

The layout of the Stave mechanics and cooling consists of a Space Frame and one or two Cold Plates. The Cold Plate is made of a high thermal conductive carbon fibre laminate, with embedded cooling pipes, on top of which the silicon chips are glued. The heat is conducted into the cooling pipes by the carbon fibre structure and is removed by the coolant flowing in the pipes. For mechanical stability the Cold Plate is stiffened by the Space Frame, a light filament wound carbon structure with a triangular cross section. The concept of a Cold Plate and a Space Frame applies to both the IB and OB Staves but the specific implementation of each Layer is tailored according to the different geometrical and thermal constraints. A mechanical connector at each of the two ends of a Stave provides the precise positioning of the Stave in the Layer configuration.

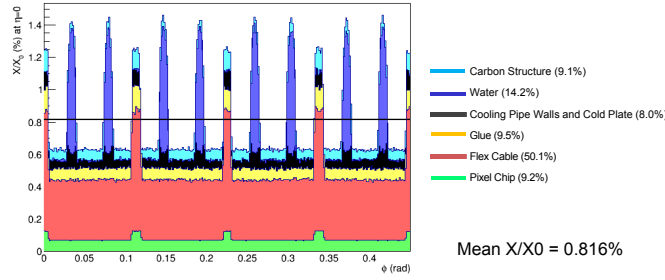


**Figure 4.6:** The azimuthal distribution of the Outer Layer Stave material traversed by the particles at  $\eta = 0$ . The highest peaks correspond to the polyimide cooling pipes embedded in the Cold Plate fully filled of water and the others to the Half-Stave overlaps to ensure the detector hermiticity.

#### 4.2.1 Materials and production processes

The obvious choice for material with high specific stiffness and high thermal conductivity with a long radiation length is Carbon Fibre Reinforced Plastics (CFRP).

For the Space Frame, the specific stiffness and the low  $Z$  are the parameters driving the design. Therefore, the choice is oriented to the use of high modulus carbon fibre with a Young's modulus larger than 300 GPa. For the Cold Plate, the carbon fibre has to comply with the tight requirements in terms of heat removal capacity; this leads to the use of high thermal conductivity carbon fibres,  $k$  larger than  $600 \text{ W mK}^{-1}$ .

The resin system for the CFRP considered for the ITS is mainly cyanate ester resin, RS-3 [18] or EX-1515 [19], which is preferable to epoxy resin for its low humidity absorption and better dimensional stability in time.

The choice of the material for the cooling pipes embedded in the structure is driven by the requirement of low material budget and high thermal conductivity. A suitable compromise among these requirements is the use of a plastic tube with a thin wall. Polyimide ( $X_0 \approx 28 \text{ cm}$ ) small diameter pipes with 1.024 mm (2.67 mm) inner diameter and 25  $\mu\text{m}$  (64  $\mu\text{m}$ ) thin walls are currently considered for the IB (OB) Staves. The pipes are always embedded in the carbon structure and never directly exposed. In this way their intrinsic fragility and tendency to pinch and buckle under localised load does not affect their use. Polyimide shows high radiation hardness up to at least  $10^7 \text{ Gy}$  [20]. The behaviour of the pipes under pressure loads was tested and polyimide erosion due to coolant flow in radiation environment is under study.

The Space Frame and the Cold Plate structures are manufactured using two standard processes for composite material production: “manual lay-up” and “filament winding”. Several tests have been performed to optimise the lay-up sequence for the Cold Plate and the winding angle for the rowing in the Space Frame.

After the lay-up or winding processes, the CFRP structure undergoes a curing process, obtained by a heating cycle, needed for the resin polymerisation, along with a pressure load which provides the force needed to squeeze the excess of resin. Gluing of different mechanical parts after curing has been minimised by assembling the CFRP structure before polymerisation. This results in a better control of the amount of glue used and in a minimisation of the material budget.

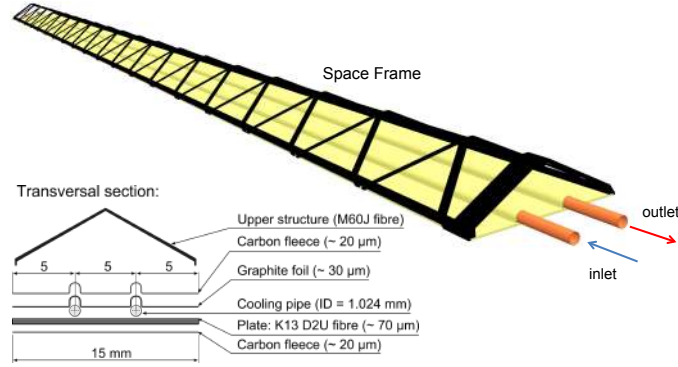


**Figure 4.7:** Schematic layout of the mechanical and cooling structure of the IB Stave.

### Inner Barrel Stave

For the IB Stave, the Cold Plate and the Space Frame are conceived as a single integrated light-structure as shown in Fig. 4.7.

The layout of the Cold Plate provides a thermal bridge between the two polyimide cooling tubes (1.024 mm inner diameter, 25  $\mu\text{m}$  wall thickness) by means of an unidirectional ply of high thermal conductivity carbon fibre (K13D2U, 70  $\mu\text{m}$  thick) oriented in the direction normal to the axis of the tubes. The tubes are glued on top of the carbon ply and the thermal contact is enhanced by a thermal graphite foil (30  $\mu\text{m}$  thick) [21] that is layered on top of the tubes and glued to the K13D2U [22] lamina. For structural reasons an additional thin ply of carbon fleece (20  $\mu\text{m}$  thick) is added on the top and bottom sides of the Cold Plate. Since the cooling manifolds are only at one side, the refrigerant inlet and outlet are provided by a connector at one end of the Stave while at the opposite end the two polyimide tubes are joined by a U-bent connector. These two connectors also provide the fixation at the two extremities of the Stave in the Layer.

A filament wound top cover, the Space Frame, stiffens the Cold Plate. It is obtained by winding a carbon rowing, M60J 3K (588 GPa) [23], at an angle of 45° with respect to the Stave axis. The winding angle and the number of helices have been optimised to achieve the best compromise between material budget and stiffness.

### Outer Barrel Stave

As for the IB, the cooling for the OB Staves is provided by a high thermal conductive Cold Plate with embedded pipes. However, due to the length of the OB Stave, up to 1.5 m, an independent support structure with a large inertial section is used to hold two Half-Staves in position, each one equipped with a Cold Plate. The mechanical and cooling structure of the OB Stave is shown in Fig. 4.8.

The Cold Plate is approximately 30 mm wide and is based on the same carbon-ply layout as for the IB Stave. Two pipes with an inner diameter of 2.67 mm and a wall thickness of 64  $\mu\text{m}$  have been used. The two pipes are interconnected at one end of the Cold Plate providing a loop, whose inlet and outlet are on the same side and correspond to the distribution manifolds.

The Space Frame design is adopted from the present ALICE ITS and is based on a light truss carbon structure. Structural analysis and tests finalised to the new geometries and

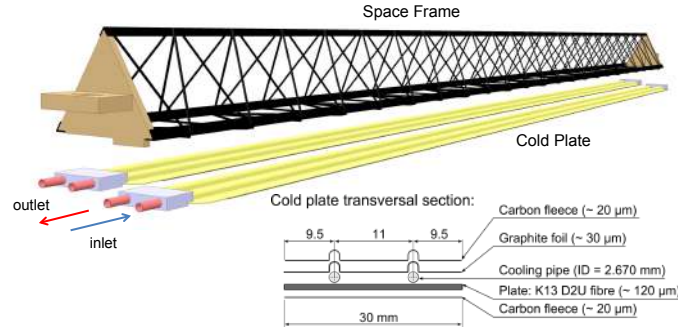


**Figure 4.8:** Schematic layout of the mechanical and cooling structure of the OB Stave.

requirements have led to an equilateral section of the frame with a 42 mm wide side, that provides almost the same rigidity for all the possible Stave positions.

The materials used in the prototype production are high modulus carbon fibre M55j-6k (540 GPa) [24], with K13C2U (900 GPa) [25] as a stiffer alternative. At both ends of the Space Frame, two mechanical connectors ensure the accurate positioning of the Stave within the Layer. The mechanical connectors are designed to permit mounting and dismantling of the Stave with high accuracy.

#### 4.2.2 Thermal characterisation

Thermal tests were conducted on several prototypes with the aim of optimising and characterising the Stave cooling design. Both water in leakless mode (absolute pressure at the Stave < 1 bar) and two-phase  $C_4F_{10}$  refrigerant [26] were used as coolants. The power dissipated by the Pixel Chips was simulated by means of a polyimide heater glued to the prototype Cold Plate, covering the same surface as the Pixel Chips. The heat load is transferred through the carbon fibre towards the embedded pipes and is finally removed by the coolant. Several temperature sensors were placed above the Stave heater, while an infrared (IR) camera mapped the heater temperature allowing the location of heat spots. Pressure and temperature of the refrigerant were recorded during the tests at the Stave inlet and outlet.

The following requirements have been considered for the thermal characterisation tests of both IB and OB Staves:

- the Stave operative temperature shall not exceed  $30^\circ\text{C}$ , based on the requirements of the chip, while the temperature uniformity along the Stave shall be kept within  $5^\circ\text{C}$ ;
- the power dissipated by the Pixel Chips shall not exceed  $300\text{ mW cm}^{-2}$  for the IB and  $100\text{ mW cm}^{-2}$  for the OB.

#### Inner Barrel Stave

Test results are reported for a chip power dissipation value of  $300\text{ mW cm}^{-2}$  as well as  $150\text{ mW cm}^{-2}$  and  $500\text{ mW cm}^{-2}$  as lower and upper limits, respectively.

A small portion of the applied power is exchanged directly with the environment by convective and radiative heat transfer. This heat load has been estimated by means of

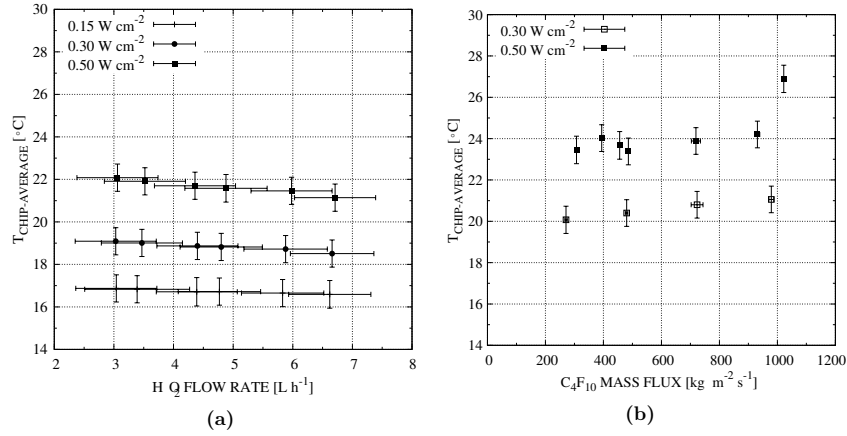


**Figure 4.9:** Test results: Inner Barrel Stave chips average temperature at different power densities; (a) water single-phase cooling, (b)  $C_4F_{10}$  evaporative cooling. The average temperature of the refrigerants is  $15^{\circ}C$ .

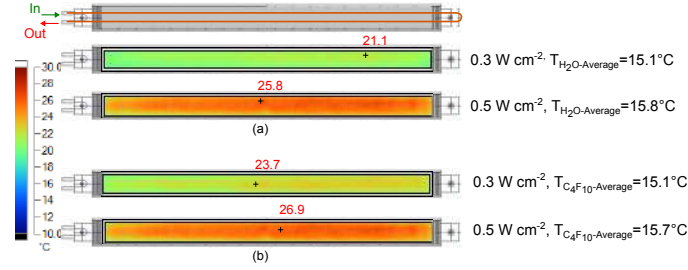


**Figure 4.10:** Thermographic images showing the chips temperature map at  $0.3$  and  $0.5 W cm^{-2}$  power densities for the Inner Barrel Stave prototype: a) water,  $31 h^{-1}$ ; b)  $C_4F_{10}$ ,  $480 kg m^{-2} s^{-1}$ .

experimental tests to be below 12% of the total applied power when the ambient temperature is approximately  $10^{\circ}C$  below the Stave temperature. This case would correspond to a Stave temperature of  $30^{\circ}C$  and an ambient temperature of  $20^{\circ}C$ .

The test results summarised in Fig. 4.9 show the average heater temperatures for different mass flow rates, at the power densities of  $150 mW cm^{-2}$ ,  $300 mW cm^{-2}$  and  $500 mW cm^{-2}$ . Tests were done keeping an average refrigerant temperature of approximately  $15^{\circ}C$ .

The thermographic pictures in Fig. 4.10 display the chip temperature map for the studied cases. The prototype shows a good temperature uniformity, with variations below  $5^{\circ}C$ . Also, the maximum heater temperature measured does not exceed in any case  $30^{\circ}C$ .

The results displayed in Figs. 4.9 and 4.10 show that there are no significant differences in terms of cooling performance when cooling with water or with evaporative  $C_4F_{10}$  at similar temperatures. Likewise, different mass flow rates have little impact on the thermal performance. This means that the conductive thermal resistance across the Stave

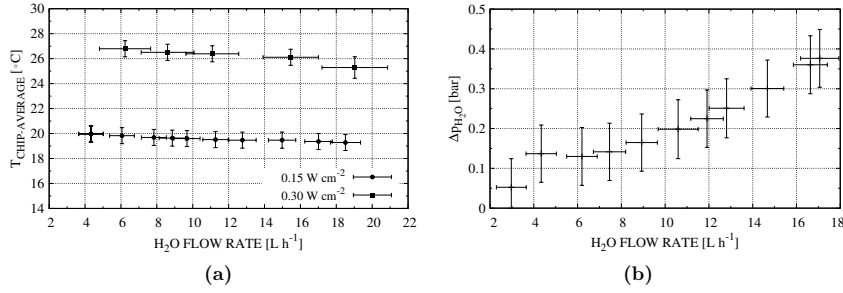


**Figure 4.11:** Test results: a) Chips average temperature for the Outer Barrel Stave at different power densities for different water flow rates at an average temperature of 15  $^{\circ}C$ , b) water pressure drop for the Outer Barrel Cold Plate, 2-pipe 2.67 mm inner diameter, 1475 mm long.

dominates over the convective thermal resistance between tube wall and fluid.

The choice of the refrigerant is then driven by the material budget requirements and by considerations on the cooling system and plant. For a given tube, a two-phase flow will display significantly lower average fluid density as a result of the large vapor fractions within the flow and subsequently result in a lower material budget than water. However, using water as a coolant already fulfils the material budget requirements, with a value lower than 0.3 %  $X_0$  for the fully assembled Stave; see Sec. 4.1.1. This drives the choice of the refrigerant towards considerations on system simplicity, reliability and easy integration with the Outer Barrel Staves, suggesting the use of water as the baseline of the current cooling design.

#### Outer Barrel Stave

Results for 150 and 300  $mW cm^{-2}$  power densities are reported for the baseline Stave cooling layout described in Sec. 4.2.1 and consisting of two pipes of 2.67 mm inner diameter each. Key results of the study are the cooling performance and the pressure drop along the Stave, since a leakless water cooling circuit will be used.

The average temperature of the chips of the OB Stave prototype, for a range of water flow rates and for the two aforementioned power densities, is shown in Fig. 4.11a. The chips can be cooled to average temperatures below 30  $^{\circ}C$  with water flow rates as low as 6  $l h^{-1}$ , the water average temperature in all the studied cases being 15  $^{\circ}C$ . Infrared camera verified that on the whole surface of the heaters there is no hot spot exceeding 30  $^{\circ}C$ .

Due to the large longitudinal dimensions of the OB Staves, it is critical to keep the pressure drop at minimum values, at least when cooling with water in leakless configuration. A full-size prototype of the Cold Plate with two pipes with 2.67 mm inner diameter, and consistent with the dimensions of a Stave of Layers 5 and 6 (i.e. 1475 mm long) was produced and hydraulically tested with water in single phase with the aim of providing insight on the Stave pressure drop.

The plot in Fig. 4.11b shows the recorded pressure drop during the experimental hydraulic tests over the full-length prototype described above. In order to be able to use a water leakless mode cooling system, it is recommended to choose a water flow rate such that the pressure drop across the full length does not exceed 0.3 bar. For this requirement to be fulfilled and according to the results reported in Fig. 4.11b, the Stave should

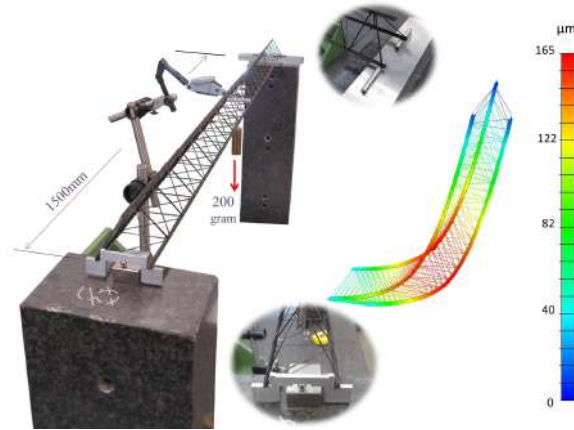


**Figure 4.12:** The stiffness of the Space Frame has been predicted by finite element analysis and validated by load test. The bending tests have been performed with the Space Frame simply supported at the two extremities and a concentrated mass in the centre.

be cooled with a water flow rate below  $12\text{ l h}^{-1}$ , which in view of Fig. 4.11a provides an adequate and reliable cooling performance for the nominal power density.

### 4.2.3 Structural characterisation

#### Stiffness test

The structural characterisation consisted of finite element simulations and load test validation. The two key structural parameters that define the achievable accuracy and stability in the position of the chips are the Stave sagging under its own weight and the first natural frequency of the Stave. The sag provides the information on the deviation of the chips final position respect to the nominal one while the first natural frequency indicates the frequency at which an external impulse can induce resonance phenomena in the structure resulting in oscillations of the chip positions. The sag and the natural frequency for a given Stave mass depend on the Stave stiffness that is provided by the Space Frame. As a conservative assumption, in both analysis and tests the contribution of the FPC to the overall stiffness has been neglected.

The Space Frame stiffness is the sum of three contributions: the elastic module of the material used, the shape rigidity defined by the inertia of the section of the Space Frame and finally the boundary conditions, i.e. the rigidity of the connection of the extremities of the Stave to the end-wheels.

Detailed finite element models of the IB/OB Space Frames have been developed and tuned on the basis of the test results. In the IB, the analysis has been used to drive the optimisation of the extremely light design required by the challenging target for the material budget. In the OB, the model has supported the selection of the composite material lay-up and carbon fibre type that provide maximum stiffness and stability to the 1.5 m long Space Frame. The carbon fibre with the larger Young's modulus, K13C2U, is preferred to the M55J fibre used in the present ITS (see Sec. 4.2.1). The use of such fibres requires additional tests to optimise the production process due to the fragility of

the fibres associated with the larger filament diameter (10  $\mu\text{m}$  for K13C2U with respect to 5  $\mu\text{m}$  for M55j).

A three-point bending test was performed to characterise the IB/OB structures. Tests were carried out by applying a lumped mass to the centre of the Space Frame, simply supported (free rotations) at the two extremities. From the test results, the Stave behaviour under working conditions, i.e. distributed mass and fixed extremities, has been extrapolated. The recorded sag has been used also to predict the first natural frequency of the structure.

For the IB Space Frame, under the assumption of a distributed mass of 0.002 kg, corresponding to the HIC weight, and of Stave with clamped extremities (all translations and rotations blocked), a maximum sag between 4  $\mu\text{m}$  and 9  $\mu\text{m}$  and a first natural frequency above 100 Hz have been predicted.

For the 1.5 m long OB Space Frame, a sag between 40  $\mu\text{m}$  and 110  $\mu\text{m}$ , depending on the stiffness of the connection at the extremities, and a first natural frequency above 50 Hz, have been derived from the test, see Fig. 4.12. This prediction is based on a 0.2 kg mass distributed uniformly along the Stave length and with the two Space Frame extremities fixed to the end-wheels with a spring connection, as described in Sec. 5.2. This connection will achieve a constraint between a “simply supported model” (free rotations) and a “clamped fixation model” (all translations and rotations blocked). A detailed test plan and the optimisation of this connection are under development.

### Pressure test

Even if the cooling system design is based on a leakless under-pressure concept in case of water as coolant, or a low over-pressure in case of  $\text{C}_4\text{F}_{10}$ , the polyimide pipes were tested at a pressure up to 10 bar. Tests were performed both on the naked pipes and on pipes embedded in the carbon plate, as for the Cold Plate design of the new ITS. While in the former case the pipe burst pressure was the objective of the test, in the latter case the aim was to verify that no de-lamination occurs at the interface between the pipes and the carbon structure. For this second set of tests, the samples were produced with pipes squeezed in the carbon plate in order to apply more severe conditions and to simulate any possible faulty workmanship introduced during the production.

Tests were performed up to 10 bar without observing any damage or de-lamination in the test samples based on the optimised final design. This test campaign has permitted not only the verification of the integrity of the polyimide pipes under severe pressure conditions but also to tune some of the production parameters, like resin viscosity and curing cycle, that affect the correct embedding of the pipes inside the carbon plate.

### Erosion test

A long term test with continuous water flow in several pipe samples is running to evaluate erosion effects on the polyimide tube walls. Five samples of 300 mm long pipes with 1.024 mm inner diameter and 25  $\mu\text{m}$  wall thickness and subjected to the same thermal cycle that they will undergo during the Cold Plate curing process have been connected to a derivation of the present installed tracker cooling plant located in the ALICE cavern. The advantage of this test setup is in the use of de-mineralised water circulating in an active detector and then exposed to real working conditions like system contamination and radiation environment.

A measurement of the surface roughness, a Scanning Electron Microscope (SEM) analysis and a weight measurement were carried out on the tube samples before starting the water erosion test. The measurements were repeated on the samples at long time intervals



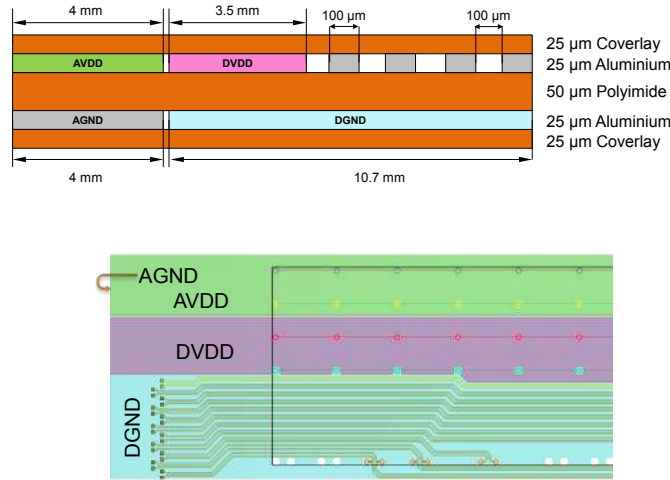


**Figure 4.13:** Schematic view of the stack-up (top) and layout (bottom) of the FPC for the IB Stave.

and compared to the previous ones in order to evaluate if any change in weight or surface roughness had occurred.

No erosion effect has been observed after more than six months. The test will continue until the installation of the new ITS.

The combined effects of direct radiation and radiolysis of de-mineralised water on the polyimide pipes is also under study. Even if radiation has shown to have limited effects on polyimide (see Sec. 4.2.1), plastic degradation can be influenced by radiolysis products of water [27]. The effects of radiolysis of water are known to be controllable by the use of ion-exchangers and recombiners and in ALICE they will be limited by the low radiation dose.

### 4.3 Flex Printed Circuit

#### 4.3.1 Inner Barrel

The layout of the FPC of the IB Module is shown in Fig. 4.13. The nine Pixel Chips in a Module are read out in parallel: each chip sends its data stream to the end of Stave by a dedicated differential pair. Two additional differential pairs distribute the clock and configuration signals to the nine chips.

In order to minimise the mechanical stress on the 50 µm-thin chips, polyimide PI2611 having a Coefficient of Thermal Expansion (CTE) of 5 ppm/K is considered as a possible option in alternative to standard material (having CTE of 21 ppm/K). For comparison the CTEs of Si and C are 3 ppm/K and 1.18 ppm/K, respectively. Dedicated thermal stress tests will be performed when first Stave prototypes will be available.

The choice of the material to be used for the metal layers of the FPC is dictated by the need to minimise the material budget, thus Al has been preferred to the standard Cu (the respective radiation lengths being 8.9 cm and 1.44 cm). Along the same line, the total thickness of the polyimide layer has been reduced to 100 µm and the hole diameter has been fixed at 200 µm to reduce the needed volume of SnAg for the soldering and the

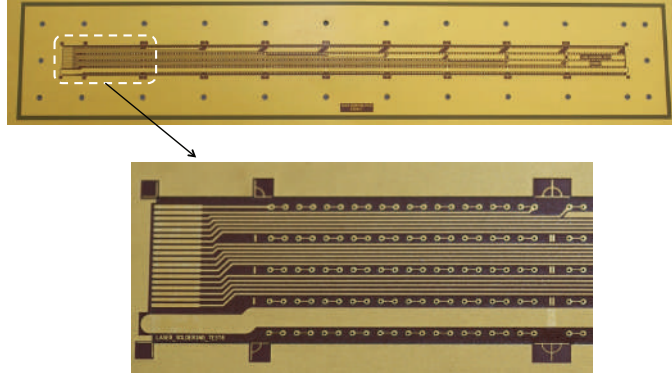


**Figure 4.14:** Cu prototype of the FPC for the IB Stave (top) and a close up view of the end-of-Stave section (bottom).

thermal stress to melt a larger amount of material, as explained in the following Section. For practical reasons the metal ring surrounding the FPC holes has a width of  $150\mu\text{m}$ , resulting from a compromise between a reasonable minimum pitch of  $600\mu\text{m}$  between holes and the needed pad diameter to compensate the tolerance in hole drilling during the various phases of the production.

The thickness of each Al layer is  $25\mu\text{m}$ , a value which is mainly dictated by the need of minimising the voltage drop along the power supply lines and ensuring a differential impedance of  $100\Omega$  in the signal lines.

The baseline procedure for the FPC production consists in Al sputtering under vacuum over both faces of a polyimide foil with drilled holes. Then I/O and power supply lines are engraved either by chemical etching or by laser etching and, finally, a coverlay is glued on both faces by lamination and vias are then opened.

The FPC is initially produced with an external frame of suitable width (few cm) to allow proper handling and flattening during the various assembly phases, from the chips soldering up to the gluing onto the carbon fibre support structures. Finally the excess polyimide is cut away by precision laser cutting. Figure 4.14 shows the FPC prototype with copper conductive layers.

#### 4.3.2 Outer Barrel

The FPC of the OB Module interconnects 14 Pixel Chips arranged in two rows: each row of seven chips is treated as an independent array in terms of power distribution and is driven by a master chip located at the end for the bi-directional data exchange. All master chips on one Half-Stave long row, i.e. four or seven depending on the Layer, receive the clock and configuration signals from the end of the Stave on a common differential pair and, after regeneration inside the chips themselves, distribute them to the remaining six chips in a Module row. The seven chips of a Module row are connected in daisy-chain mode, which refers to the respective master chip. The master chips send data on two independent differential pairs to the first chip of the adjacent Module and to the first chip of the following Module, thus allowing to skip a Module in case of failure. The serialised data of a Half-Stave-long row are transmitted to a readout link located at the end of Stave by the outermost master chip; each Half-Stave is served by two readout links. The proposed scheme, which provides a reasonable level of redundancy against single chip

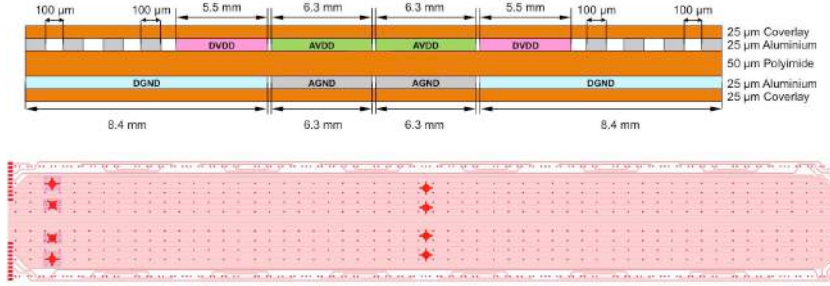


**Figure 4.15:** Schematic view of the cross-section (top) and layout (bottom) of the FPC for the OB Stave. The soldering pads for the connection between adjacent FPCs are visible at the two edges of the layout, the larger rounded pads allow the connections of the PB to the power and ground planes. A differential pair line for data readout that allows to by-pass a Module is also visible at each side edge of the layout.

failures or of an entire Module, has been implemented in the FPC layout shown in Fig. 4.15 that is currently being produced in a Cu version prototype.

Taking into account the estimated power consumption, the voltage drop along a row of seven chips is dealt with by the power planes of the FPC; however, the length of the OB Half-Staves requires the use of an additional Power Bus (PB) to limit the overall voltage drop to 100 mV, with respect to the nominal value of 1.8 V, which can guarantee the full functionality of the Pixel Chip.

The PB is a multilayer Al-polyimide bus, which brings analogue and digital power to all FPCs of a Half-Stave. The PB runs over the FPCs and is connected to them by tin soldering achieved by through vias to access the various layers. The overall thickness of the aluminium layers of the PB is 200 µm for the outermost Layers (see Tab. 4.2), while it could be thinner for the Middle Layers due to the smaller number of chips. The technical options to produce such a long flat cable are being developed, the main technical challenge being the proper metallisation of the through vias surface to fit the soldering. Two stack-up options are under evaluation: four layers of 50 µm Al and two layers of 100 µm Al.

#### 4.4 Pixel Chip to FPC connection

The Pixel Chips will be connected to the FPC for power supply and I/O connections. In present silicon pixel detectors, these connections are located on one or more edges of the silicon die and the connection to FPCs or standard printed circuit boards is carried out via ultrasonic wire bonding.

For the upgrade of the ALICE ITS a dedicated study was started to find a new connection scheme for monolithic silicon pixel detectors. The main requirements are:

- Compact Module layout, with a minimum of dead area in the chip periphery.
- High quality, low inductance electrical connection.
- Improved power connection scheme over the full chip surface.
- Highly robust and mechanically stable connection technique.

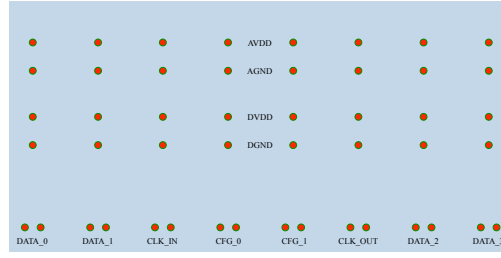


**Figure 4.16:** Sketch of principle of the connection pads array over the Pixel Chip top surface.

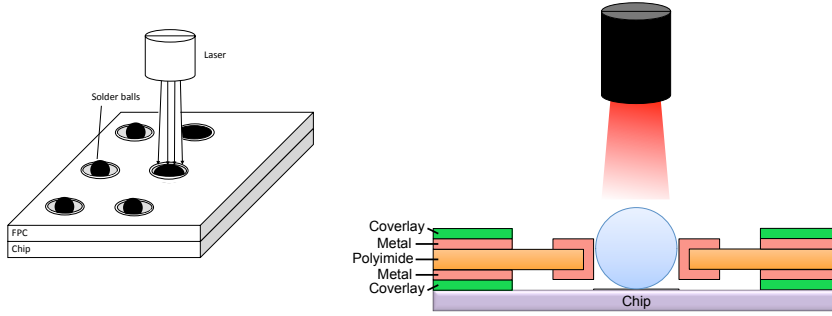


**Figure 4.17:** Schematic view of laser soldering.

The two main techniques that are being pursued and evaluated for the connection between the FPC and the Pixel Chips, namely the laser soldering and the SpTAB bonding, are described in the following.

All connection pads on the chip are located on the top surface: power supply connections are distributed over the full chip surface while I/O connections are concentrated along one edge of the chip, as schematically sketched in Fig. 4.16. The connection pads are made of aluminium pads of 400  $\mu\text{m}$  diameter, coated with a Ni/Au layer for proper wetting of SnAg balls in case of laser soldering. Dummy Pixel Chip prototypes, in particular of the Explorer-1 chip, with power connection pads distributed over the surface have already been produced and are being used to study the different techniques for Pixel Chip to FPC interconnection. They will allow validation of the power connection scheme via pads distributed over the chip surface and will permit investigation of any impact this might have on the chip performance, e.g. on the noise behaviour.

#### 4.4.1 Laser soldering

Laser soldering is an industrial application and can be used to connect the chip pad with the corresponding metal coated hole in the FPC, using a solder ball which is melted locally by a laser beam, as schematically shown in Fig. 4.17. This avoids thermal stress on the full Module structures as the heat is only generated in the small local area of the size of the connection pad.

First tests on polyimide substrate prototypes were carried out: 100 contacts were man-



**Figure 4.18:** A detail of the prototype sample for laser soldering test: three solder balls of  $250\text{ }\mu\text{m}$  diameter placed on top of the chip and FPC prior to laser soldering are visible

ufactured on a polyimide chip of  $15\text{ mm} \times 30\text{ mm}$  which could be connected to a polyimide cable. The contacts on both parts were arranged in a daisy chain, so that a simple electrical test could verify if all solder points had been connected. The test has been extensively repeated connecting a silicon dummy chip with an identical connection pattern to the FPC prototype. The chips used for these tests had previously been thinned to  $50\text{ }\mu\text{m}$ . Figure 4.18 shows three solder balls of  $250\text{ }\mu\text{m}$  diameter placed on top of the chip and FPC prior to laser soldering.

The optimization study presently carried out aims to establish a procedure that ensures a high precision positioning of the chip and a good flatness of the Module structure after soldering, as well as high quality and reliable electrical connections.

One of the key features of the presently used laser soldering system is the accurate control of the process temperature via a pyrometer read-out at  $10\text{ kHz}$  connected to the laser powering system. The laser spot size can be optimised for any solder ball diameter (down to  $100\text{ }\mu\text{m}$ ) and the region to be heated can be precisely limited within the hole edges ( $\approx 400\text{ }\mu\text{m}$  for a  $200\text{ }\mu\text{m}$  hole). As a result, thermal stresses are minimised and chips and FPC integrity are ensured.

Laser soldering requires high accuracy in the alignment of the components and the tooling necessary to place the solder micro-balls. In addition, there are constraints for chip positioning, as an overall accuracy of  $100\text{ }\mu\text{m}$  or better is aimed at. Various mechanical supports have been designed and manufactured in order to achieve the required precision; they will be described in Sec. 4.5 dedicated to the assembly procedure.

Several single-chip FPCs have been soldered to  $50\text{ }\mu\text{m}$ -thick dummy chips in order to optimise the temperature profile of the soldering process. The samples have been inspected using a microscope and have undergone a metallurgical inspection.

Figure 4.19 shows on the left hand side a top view picture of a melted ball after soldering and on the right hand side the metallurgical cross section analysis of a soldered connection after embedding the Module in resin, cutting and polishing. The good wetting of the solder on the chip pad and on the FPC is clearly visible.

Further tests to optimise the temperature profile and to study the repeatability will be carried out. It is planned to thermally cycle several soldered samples to verify the long-term stability of the connections.

#### 4.4.2 SpTAB interconnection

An alternative technique under consideration for the connection between the FPC and the Pixel Chips is the Single point Tape Automated Bonding (SpTAB) technique, which exploits an aluminium ribbon leads ultrasonic assembly process. This technique (developed by Ukrainian team in Kharkov and Kiev) has been successfully used for Silicon Strip and Silicon Drift Detectors in the present ITS.

Several different material combinations will be investigated according to the impedance

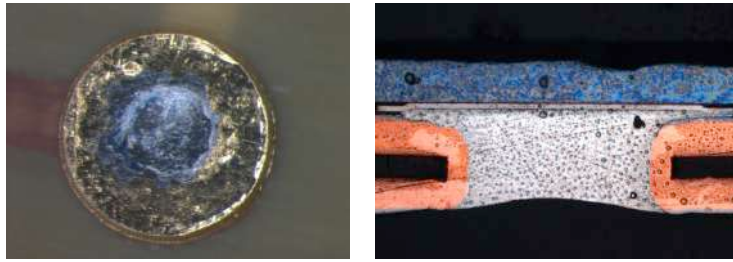


**Figure 4.19:** Pictures of solder contacts of test samples using 50  $\mu\text{m}$  thick chips and single chip FPCs, top view on the left and cross section view on the right. The cross section view demonstrates the good wetting of the contact surfaces.

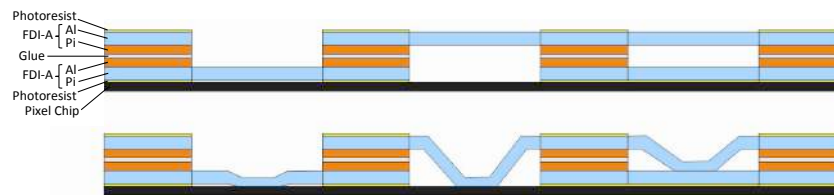


**Figure 4.20:** Possible combination of used materials for multilayer FPC and bottom layer to chip (left area), top layer to chip (middle area) and interlayer (right area) before (top) and after bonding (bottom) connections.

requirements for the FPC layout. One possible combination of materials for a multilayer FPC, consisting of two FDI-A (a flexible layer laminated together with a photo-resist cover layer) is schematically shown in Fig. 4.20, which also depicts several possible cases of ribbon leads bonding.

The main advantages of this technique are the following:

- Connection of aluminium leads of FPC to aluminium contact pads of Pixel Chips that ensure highly robust and mechanically stable connection;
- Absence of heavy metals (Au, Sn) necessary for laser soldering, whose deposition requires a costly wafer processing after the CMOS manufacturing;
- Potential possibility to use this technique for connection of the PB and FPC for Middle and Outer Layers via special interconnection elements;
- For main assembly processes (bonding and encapsulating) high-precision and high-throughput automated equipment can be used.

## 4.5 Assembly procedures

In this Section, the assembly procedures that are being developed for IB and OB Staves are illustrated. The main requirements are a reliable high quality technique to connect the Pixel Chips to the FPC and a geometrical placement accuracy of the individual chip in the horizontal plane of the order of 100  $\mu\text{m}$  or better. The interconnect technique assumed in



**Figure 4.21:** Prototype vacuum tables to hold (A) chips and (B) FPC.

the following is laser soldering. Two approaches are being considered for the HIC assembly of both IB and OB Staves. The first one assumes that the micrometric alignment of the HIC components is performed by technicians operating a coordinate measuring machine, equipped with custom developed tools and jigs for the handling of the components. The second option is a fully automated positioning system, which is being investigated in collaboration with an external company specialised in the field of artificial vision and automated systems.

#### 4.5.1 Inner Barrel Stave

Specific jigs have been developed for the assembly of the HIC of the IB Stave:

- A vacuum table A, with  $x, y, z$  micrometric adjustment, holding the chips (see Fig. 4.21).
- A vacuum table B holding the flex, having a suitable slot to insert the table A and overlap the flex onto the chips (see Fig. 4.21).
- A solder ball pick-up tool consisting of a stainless steel box closed by a peek foil with 100  $\mu\text{m}$  holes array matching the flex holes layout. It is a vacuum jig that allows to pick-up the solder balls from a reservoir and to place them in the dedicated positions on the pre-aligned chip and FPC. The jig is the size of one chip and is connected to either a small vacuum pump to pick up and hold the solder balls or to a compressed air system, with adjustment of pressure and blow duration, to release them.
- A soldering grid consisting of a macor plate, 1 mm thick, with an array of conical holes (0.4 mm at the bottom and 1 mm on top) matching the flex holes layout. Such a grid has a double function: pressing the flex against the chip to avoid any gap, which might degrade the soldering quality, and guiding the solder balls into the FPC holes when released from the ball pick-up tool.

The first step of the IB Stave construction is the assembly of the HIC, which foresees the following operations:

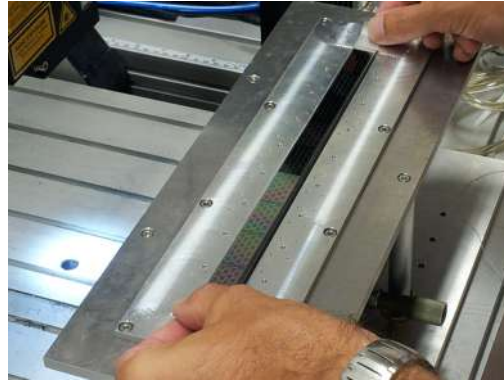


**Figure 4.22:** Placement of nine chips on the vacuum table A.

1. Nine chips are placed above the vacuum table A and precisely aligned with respect to each other (see Fig. 4.22).
2. The FPC is placed above the vacuum table B and held in a position defined by reference pinholes.
3. The FPC is aligned with respect to the underlying array of chips by matching the holes with the connection pads on the chips surface (see Fig. 4.23).
4. The soldering grid, aiming to gently press the FPC against the chip, is placed above the stack-up and aligned with respect to the holes in the FPC.
5. The loaded solder ball pick-up tool is aligned above the stack-up corresponding to the first chip, brought very close to the soldering grid and then the solder balls are released.
6. The laser soldering of each connection is performed in sequence.
7. The last four steps are repeated to connect all remaining chips and complete the HIC.

Once fully assembled, the HIC is tested, the chip positions are surveyed and finally the HIC is glued on the Cold Plate. The full Stave undergoes a final validation before the integration in Layers.

#### 4.5.2 Outer Barrel Stave

The assembly procedure of the HIC of the OB is very similar to that one of the IB. In this case, 14 Pixel Chips are precisely aligned in two parallel rows of seven chips, each using a suitable jig that holds them in place by vacuum suction, shown in Fig. 4.24. The chips are connected to the FPC one by one following the same steps as illustrated above for the IB Module. The HIC undergoes a qualification test before it is glued to the Module carbon plate on the chip side to form the Module. The Module is tested again to select those to be attached to the Cold Plates for the construction of the Half-Staves. The main purpose of the Module carbon plate is to provide an interface between the Module and the Cold Plate that would allow an easier detachment of malfunctioning Modules for their



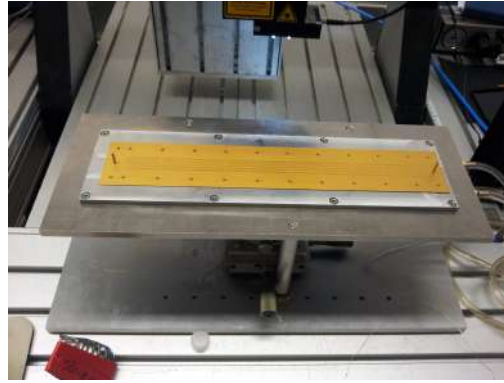


**Figure 4.23:** Placement of FPC on top of a row of nine chips.

replacement. If it turns out that for other reasons the reworking is not feasible, the Module carbon plate could be eliminated thus simplifying the assembly procedure. Moreover, the overall material budget would benefit from the suppression of the Module carbon plate. The HIC assembly could be further simplified by a  $90^\circ$  rotation of the Pixel Chips with respect to the layout assumed so far, which however would imply a slightly modified Pixel Chip compared with the one for the IB Stave. In this configuration, the Module of the OB Stave would consist of a single row of 14 chips, separated by a gap of  $100\ \mu\text{m}$  in the  $z$ -direction. The rotation of  $90^\circ$  could also be a valuable option to reduce the extension of the overlap regions between adjacent Half-Staves.

The two Half-Staves of a Stave will be assembled and qualified separately, and then mounted in sequence on the Space Frame. They are connected to the Space Frame by means of the U-shaped support, starting with the one closer to the Space Frame itself (see Fig. 4.4) in order to ease the dealing of the azimuthal overlap and avoid mechanical interference during their positioning. Each Half-Stave contains four or seven Modules, depending on the Layer, which have to be aligned and glued on the Cold Plate. The thermal contact between the Module carbon plate and the Cold Plate must ensure an efficient removal of the overall power dissipated by the electronics in the Module.

The baseline procedure for the Half-Stave build-up assumes that all Modules of a Half-Stave are first aligned on a dedicated jig with the Module carbon plate face up and then the Cold Plate is approached from the top for gluing. Figure 4.25 shows an artistic view of the main jig being developed for the Half-Stave assembly. The jig embeds the reference system at the two edges, which is based on ruby spheres placed above the plane of the connectors at the ends of the Stave. All elements of the assembly tooling, as for instance the Module support base and the rails for the alignment, are built and mounted referring to this reference system. The same reference system is used to align and position every element of the Half-Stave and afterwards of the Stave. This jig will be fixed on the marble plane of a coordinate measuring machine. The steps of the assembly sequence of a Half-Stave can be summarised as follows:

- The first Module of a Half-Stave, held by a vacuum based pick-up tool equipped with micrometric stages, is aligned with respect to the reference system and placed on the support base, where it is kept in place by vacuum suction;
- All four or seven Modules of a Half-Stave are aligned and placed one after the other

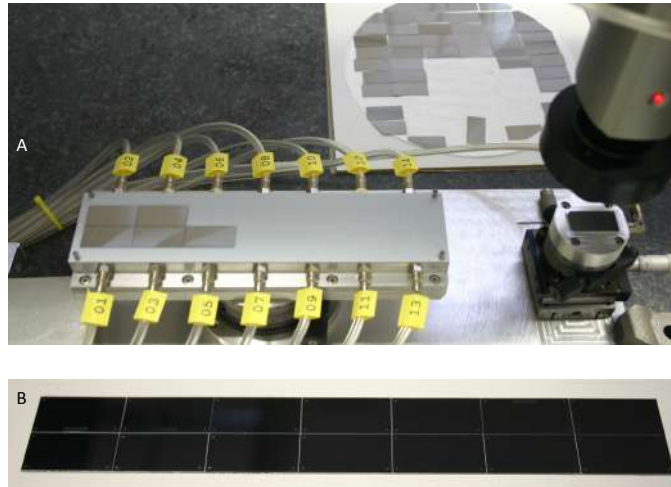


**Figure 4.24:** Development of the assembly procedure for the OB Module: A) the 14 chips are aligned one after the other in two rows of 7 chips each on a vacuum jig, before they are connected to the FPC and then glued to the Module Carbon Plate; B) first assemblies of dummy Module prototypes.

on the support base;

- The Cold Plate, sputtered with glue and thermal grease to ensure the thermal contact with the Module carbon plate, is placed on the array of aligned Modules;
- The Cold Plate is gradually loaded over the whole length to avoid stressing the structure and achieve a proper wetting of the surfaces;
- Once the glue is fully cured, the Half-Stave can be flipped upside-down in order to have access to the FPCs and interconnect control signals and read-out lines between adjacent FPCs;
- Finally, the PB is placed on top of the FPCs and connected to them.

The connection of the PB to the FPCs can be established either through dedicated vias manufactured in the PB or by shaping the FPC with wing extensions that can be then folded over the PB for soldering, which is a more conservative option that has been adopted for the construction of the current ITS. The integrity of the Half-Staves will be verified before they are attached to the Space Frame in order to discard those which are defective and eventually rework them.

An alternative option for the Half-Stave build-up foresees the alignment and gluing of all Modules in sequence on the Cold Plate, which is supported face up by an appropriate jig. Once all Modules are glued on the Cold Plate, the interconnection between neighbouring FPCs can be established and following the PB can be stretched over all FPCs and soldered to them. This option would have the advantage that the FPC-to-FPC and PB-to-FPC connections could be performed without a prior flipping of the Half-Stave. On the other hand, it is more time consuming because once a Module is placed on the Cold Plate, a curing of the glue is required before the next Module can be mounted.

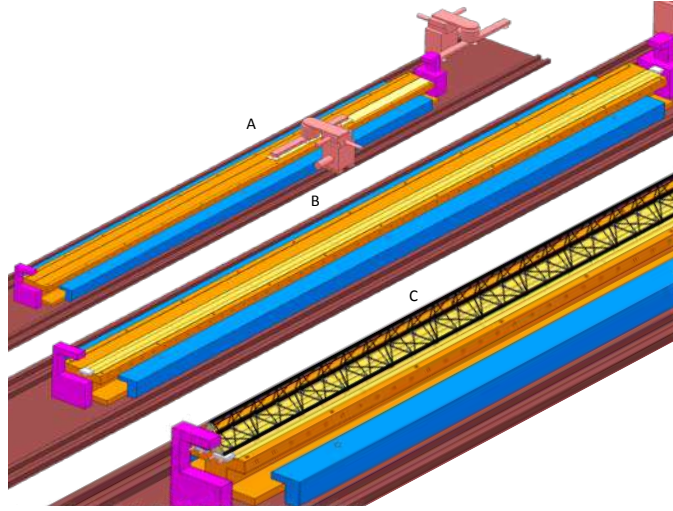


**Figure 4.25:** A sketch of the jig and the assembly procedure being developed for the construction of the OB Staves: A) the Modules are aligned one after the other on the support base with the Module face up; B) the Cold Plate is glued on the Module carbon plates; C) the Space Frame is attached to the two Half-Staves once they are fully assembled and qualified.

The Stave assembly procedure, consisting in mounting two Half-Staves on the Space Frame, will rely on the same reference system as used for the Half-Stave assembly, which matches a similar system implemented on the end-wheels (see Chap. 5) for the Layer integration. This approach, which was adopted for the construction of the current ITS, ensures the precise positioning in space of the Staves and was proven to fulfil the requirements in terms of space accuracy reliability. Moreover, it allows a precise re-positioning in space of an individual Stave that needs to be replaced[3].

As for the Module assembly, the Half-Stave and the Stave assemblies are performed by means of a coordinate measuring machine equipped with custom developed tools and jigs. The use of a coordinate measuring machine allows the survey of the position of each element, down to the single Pixel Chip. Reference markers will be implemented on each component such that their position with respect to the reference system can be mapped, with a precision of the order of  $5\text{ }\mu\text{m}$  to  $10\text{ }\mu\text{m}$ .

#### 4.5.3 Stave test and characterisation

During the whole assembly procedure, a detailed test protocol will be set in place to verify the electrical functionality and the mechanical integrity of each individual detector element before it is handed over to the following step. A thorough test is mandatory because even if the layout of the new ITS is conceived to give an easy access for the replacement of a failing Stave, this remains a risky and time consuming operation, in particular for the OB Layers, which should be avoided.

The electrical tests of the HIC and of the Module will follow a similar, though more light-weight, procedure as the single chip tests. In addition to the electrical and functional tests which ensure that the chips are operating correctly and are well connected to the

FPC, a visual and metrological inspection will be carried out. The visual inspection ensures that no mechanical damage has been inflicted during the assembly. The metrology measurement will verify that the geometrical dimensions and the flatness of the HIC and of the Module are in agreement with the requirements for mounting on the Space Frame. The Module of the OB Staves will be assembled in several production sites and shipped to a few facilities equipped for the assembly of the Staves, where a further reception test is foreseen to cross-check against possible damage during transport and handling.

Once a HIC or a Module has been successfully tested, it will undergo a burn-in test which will ensure the stable operation over a sufficiently long time. The burn-in test will be carried out in parallel on several HICs and Modules for a period of several hours, operating them at nominal voltages and settings while monitoring basic parameters such as currents and temperatures. For this purpose a test-bench will be developed, which will allow to power and operate up to ten HICs or Modules in parallel. Once the burn-in test has been completed, they will undergo a final visual inspection before being mounted on the Space Frames. The same test procedure will be applied to the fully equipped Staves, which will be connected to a cooling plant for a complete qualification, before the integration in Layers and then in Barrels, which will take place in the dedicated laboratory under construction at CERN.



## 5 Global support structure, services and integration

A description of the mechanics and the services for the ITS detector is provided in this chapter, together with an overview of the ITS installation and removal sequence. The mechanical structure that supports the Staves in layers and in barrels is illustrated in Sec. 5.2, while Sec. 5.3 describes the cooling system and the cable routing to the Staves through the service barrels. Section 5.4 is devoted to the description of the layout, installation, and bake-out of the beam pipe, which dictate the boundary conditions between ITS and LHC. The new ITS installation and removal scheme, based on the requirement of rapid accessibility, as well as the mechanics associated to it, is outlined in Sec. 5.5. Finally, the strategy to survey and align the detector elements at different assembly and installation steps is presented in Sec. 5.6.

### 5.1 General requirements

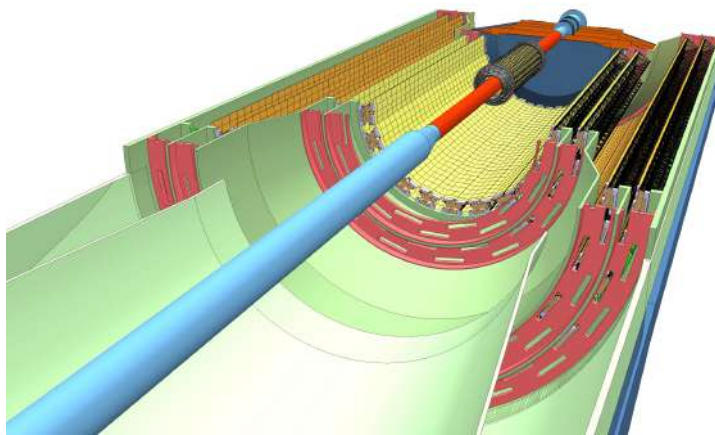


**Figure 5.1:** ITS overall mechanical layout.

The layout of the new ITS mechanical structure (Fig. 5.1) has been developed to fulfil the following design criteria:

- minimise material in the sensitive region;
- ensure high accuracy in the relative position of the detector sensors;
- provide an accurate position of the detector with respect to the TPC and the beam pipe;

- locate the first detector layer at a minimum distance to the beam pipe wall;
- ensure structure thermo-mechanical stability in time;
- facilitate accessibility for maintenance and inspection;
- facilitate assembly and disassembly of the detector layers and Staves.

In addition, the new ITS has to fulfil the requirements set by the integration of the new Muon Forward Tracker (MFT) [5] and a new set of detectors that will be part of the Fast Interaction Trigger system (FIT) [28]. The integration of these additional detectors and their services is taken into account in the design of the ITS detector and services support and in the installation sequence. The integration and installation sequence of the ITS and the MFT detectors are discussed in Sec. 5.5.2.

The main mechanical support structures of the ITS have the shape of barrels (Fig. 5.2) that extend over the whole length of the TPC. Two barrels, the Inner Barrel (IB) and the Outer Barrel (OB), hold in position, respectively, the three Inner Layers and the four Outer Layers of the ITS. Furthermore, each barrel is divided into two halves, top and bottom, which are mounted separately around the beam pipe.

Each barrel is composed of a detector section and a service section. The Staves are housed in the detector barrel and are connected via electrical signal connections (e-links) and power cables to patch panels. The patch panels are located immediately outside of the TPC, and are accessible from the ALICE miniframe. The service barrel integrates the cable trays that support the e-links and power cables through their routes from the detector Staves to the patch panels. Pipes that connect the ITS on-detector cooling system to the cooling plant in the cavern are also routed through the service barrels.

## 5.2 Detector support structure

The main structural components of the detector barrels are the end-wheels and the Cylindrical and Conical Structural Shells (CCSS).

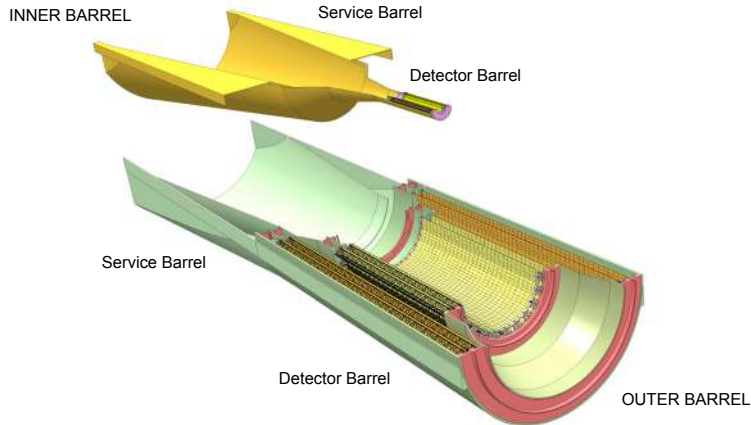
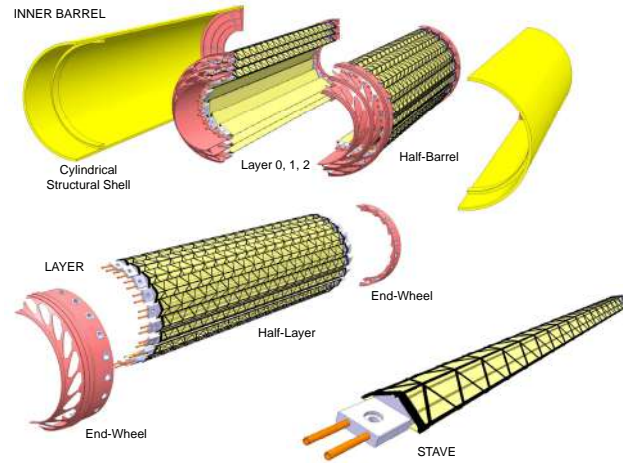


**Figure 5.2:** ITS Barrels: The Inner Barrel (IB) and Outer Barrel (OB) are divided into two halves. Each half-barrel is composed of a detector section and a services section.



(a) ITS Inner Barrel design.



(b) ITS Inner Barrel prototype.

**Figure 5.3:** Inner Barrel.



The end-wheels, which are light composite end-rings, ensure the precise positioning of the Staves in a layer. They provide the reference plane for the fixation of the two extremities of each Stave.

In the IB, Staves are positioned on the reference plane by two connectors that engage a locating pin fixed in the end-wheels at both ends. The Stave position is then frozen by a bolt that passes through the end-wheels and is screwed inside the connectors (Fig. 5.4a).

In the OB, the position of the Staves in the reference plane is given by a ruby sphere, screwed in the reference plane and matching an insert in the mechanical connectors at both extremities (Fig. 5.4b). At one end of the Stave, the insert is V-shaped, while at the other end it is square-shaped. Springs push the ruby spheres against the vertex of the V-insert and against the flat wall of the square insert. The V-shape locks two degrees of freedom of the Stave in the reference plane, while the square shape locks the remaining degree of freedom, allowing at the same time for free thermoelastic deformations. This system ensures accurate positioning, within 10  $\mu\text{m}$ , during the assembly and provides the possibility to dismount and reposition the Stave with the same accuracy in case of maintenance. Finally, the Staves are clamped by means of two springs pressing the end-connectors against the planes of the end-wheels. The end-wheels on the A-side also provide the feed-through for the services, see Sec. 5.3.

The different layers are connected together to form the barrel, see Fig. 5.3a for the Inner Barrel and Fig. 5.5a for the Outer Barrel. An outer Cylindrical Structural Shell (CYSS) connects the opposite end-wheels of the barrel and avoids that external loads are transferred directly to the Staves.

In order to minimise the material budget in the detection area, the following design choices have been adopted:

- The IB is conceived as a cantilever structure supported at one end outside the OB acceptance (Fig. 5.2);
- The OB has no intermediate mechanical structures amongst the four detection layers (Fig. 5.5a).

The OB is designed to allow each half to be opened in two concentric parts, constituted by the sub-assembly of layers 3–4 and layers 5–6. This modularity permits the independent assembly of the Middle Layers (3–4) and Outer Layers (5–6) and their connection at the end of the integration phase.

The connection of the two sets of layers is obtained by two Conical Structural Shells (COSS) located at the extremities of the detection area (Fig. 5.5a). CYSS and COSS are light sandwich structures made of two skins of carbon fibre spaced by an Airex core ( $X_0 = 1380\text{ cm}$ ) [29].

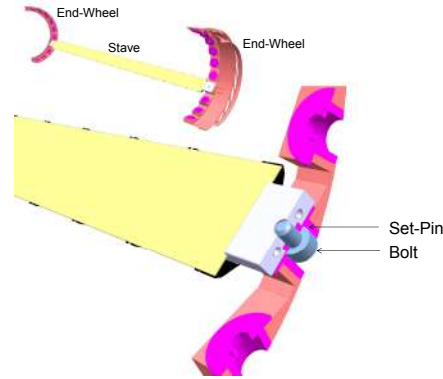
Full scale prototypes have been developed for the IB (Fig. 5.3b) and OB Staves (Fig. 5.5b) to verify the production process and the assembly procedure.

## 5.3 Services

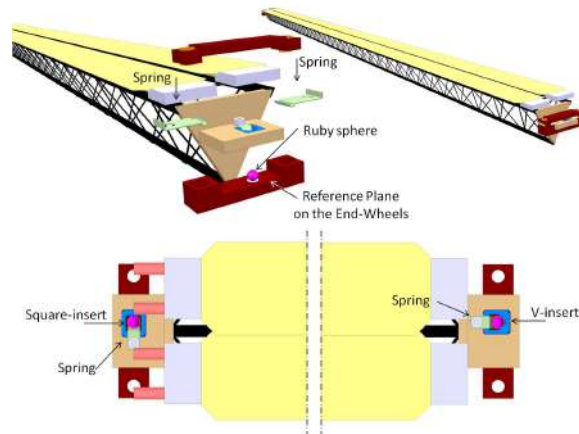
### 5.3.1 Cooling

The Pixel Chips are expected to generate a maximum specific heat of  $300\text{ mW cm}^{-2}$  for the IB and  $100\text{ mW cm}^{-2}$  for the OB. An additional heat load, about 30% of the chip load, coming from the power regulators should be considered for each Stave. The total power dissipated for the whole new ITS detector is about 15 kW.

The cooling system has to remove this heat from the detector barrels. The design of the cooling system is driven by several requirements related to the material budget, long-term



(a) ITS Inner Barrel Stave positioning. The Stave is fixed on the end-wheels at the two extremities by a precise locating pin and a bolt.

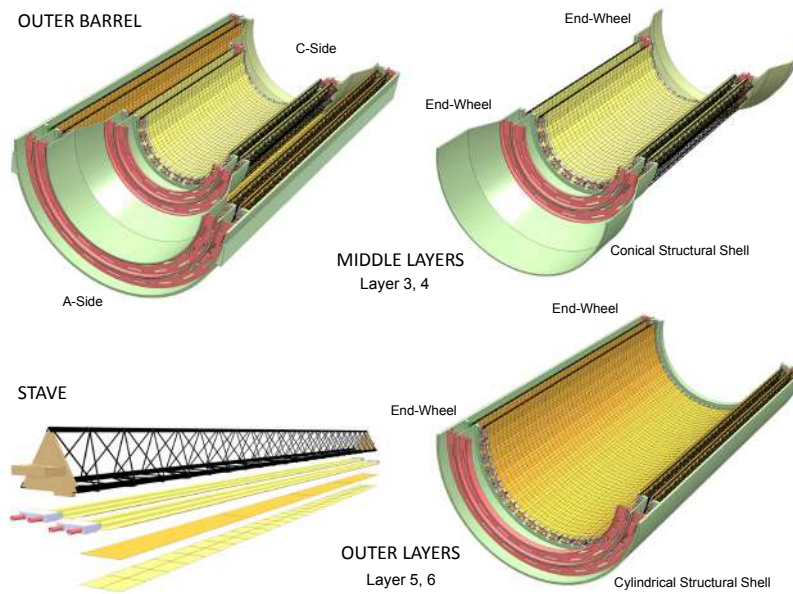


(b) ITS Outer Barrel Stave positioning. The Stave is fixed on the end-wheels by a precise locating system based on ruby spheres.

**Figure 5.4:** Stave fixation concept.

stability, erosion resistance, chemical compatibility, minimal temperature gradients and cooling duct temperature above the dew point. The detector will be operated around room temperature. Each Stave will have a cooling duct embedded in a carbon structure which will remove the dissipated heat by a leakless (below atmospheric pressure) de-mineralized water flow. Alternative coolants such as  $C_4F_{10}$  are being considered for the Inner Layers.

Unavoidably, some fraction of the power will propagate in the barrel volume by convection. An external thermal shield, integrated in the cage (see Sec. 5.5.3) where the detector is housed, will ensure that no heat is irradiated towards the TPC. A moderate



(a) ITS Outer Barrel design.



(b) ITS outer Stave prototype.

**Figure 5.5:** Outer Barrel.

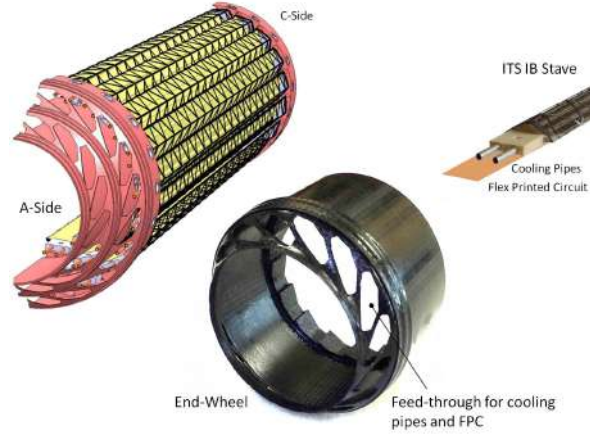


**Figure 5.6:** Inner Barrel (IB) feed-through for service connections on the A-side.

flow of dry air through the detector volume will remove the residual power and control the humidity level. The presence of the front absorber will make it necessary to guide the air-flow into the space between the absorber and the TPC, which will limit the flow-rate and subsequently the amount of heat that can be removed.

The dry air-flow will remove small temperature gradients and will help to protect against dust and to control the humidity. In fact, air moisture content has an impact on the silicon detectors and on the composite mechanical stability.

A central cooling unit, connected to the CERN water system, will be located close to the ALICE solenoid magnet. Inner, Middle and Outer Layers will have a dedicated circulation system connected to the central unit, allowing an individual temperature regulation. In order to avoid condensation, the fluid temperature at the inlet of the detector should be above the dew point temperature in the cavern. Each circuit will be equipped with flow control and monitoring devices, as well as temperature sensors. The control system operates the flow regulation valves of each circuit to stabilize the temperature as required. Interlocks will automatically turn off the power supplies (HV and LV) in case of cooling system failure. A dedicated control system will guarantee the correct flow and pressure drops required in the different barrel regions.

### 5.3.2 Cabling

Data, clock and slow control signals, together with power, from and to the Pixel Chips of a Stave, are provided through the FPC. The FPC design minimises the material in the sensitive volume and is customised for the Inner and Middle-Outer Layers based on the different requirements (see Chap. 6).

The FPC extends outside the sensitive volume, on the detector A-side, where a connection to commercial high speed cables is made. The cables run for about 4 m from the Staves through the service barrels and out on the TPC service support wheel before they reach a patch panel accessible from the miniframe. Standard connectors can be used at the patch panel, while custom made connectors or direct soldering are being considered for the connection at the Stave extremity where there is only limited space available. In particular, for the Inner Layers the FPC and its connection to the cable has to cope with

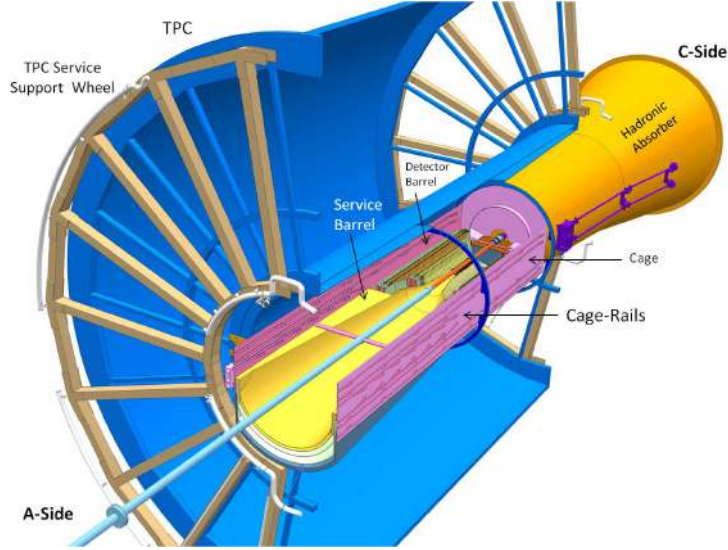


**Figure 5.7:** ITS installed inside the TPC bore.

the limitation imposed by the feed-through on the end-wheels, where the space has to be shared with the pipes that provide the refrigerant to the on-detector cooling system (Fig. 5.6).

The large number of cables for the whole ITS, coming out from the A-side, will be arranged into groups distributed into several sectors of the service barrels, using the complete circumference, in order to avoid local material concentrations. A compromise must be found between the electrical requirements and the mechanical stiffness of the cables for safe handling and smooth assembly.

For access reasons, all cables run on the A-side. Should the routing of some services to the C-side be necessary, for example the cables that distribute the low-voltage power to the detector Outer Layers, they will be implemented so as to be remotely connected and disconnected. Similar connectors are already used for the distribution of the high-voltage power inside the current ALICE TPC. These connectors consist of a crown of flexible contacts providing the electrical connection to the detector power rod. A similar system could be adopted for the ITS.

### 5.3.3 Service support structure

The closest point of access to the TPC bore is at one side of the Experiment (A-side) at about  $z = -3$  m. Therefore, the services attached to the detector barrel and extending out to  $z = -3$  m must be inserted or retracted together with the detectors.

All services, including cooling pipes, power, and signal cables, will be integrated into the service barrel, that is an extension of the detector barrel. Power cables will be grouped with the cooling tubes in the service barrel in order to remove the heat they generate.

The services layout will follow the detector modularity. The services will be grouped per detector half-barrel and routed from the detector to a patch panel located in an accessible area outside the TPC on the TPC service support wheels (Fig. 5.7). Inside the TPC, the

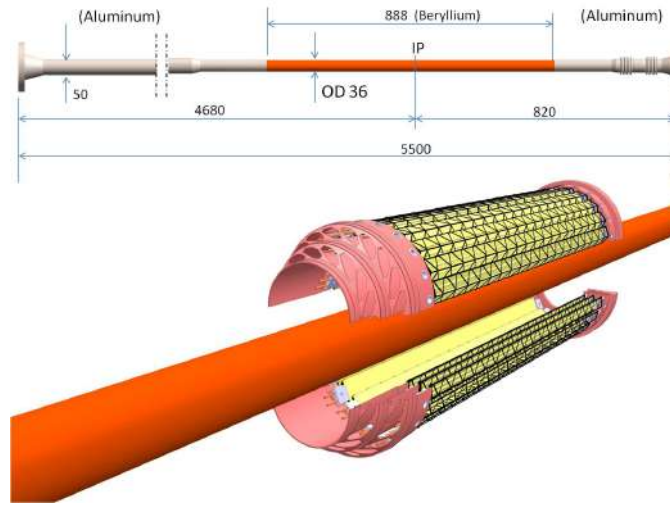


**Figure 5.8:** New layout of the beam pipe central section (dimensions in mm).

service barrels will form a half-cone, jutting from the ITS to the TPC service support wheel. The service barrel copies the shape of the TPC cone in order to distribute the services outside the acceptance of the forward detectors.

The assembly composed of half detector barrel and half service barrel is inserted or extracted from the TPC bore by means of two sets of lateral rollers fixed on the barrels and sliding on their corresponding rails provided by the cage.

The service barrel itself is a light composite structure that has to provide both structural stiffness and dimensional stability, to guarantee a precise installation of the ITS inside the TPC.

## 5.4 Beam pipe

The beam vacuum pipe represents the main interface between the experiment and the LHC machine. It must therefore fulfil a dual set of requirements.

The ALICE experimental requirements include maximum transparency to particles, limited beam-gas background, and conformity with the environmental and installation constraints. The accelerator requirements include safe operation of the machine, adequate beam aperture, and severe vacuum conditions compatible with ultimate LHC performance. The ALICE beam pipes extend over 19 m on either side of the interaction point and consist of three sections: RB24-section, central section, RB26-section. The present central section of the beam pipe is 4.8 m long with about 4 m in beryllium inside the TPC [30]. One side is limited by the hadronic absorber, which penetrates inside the TPC, and on the opposite side by a large vacuum valve. The connection to the contiguous beam pipe sections is made via bellows to avoid induced displacements. With respect to the beam pipe currently installed in ALICE, the central section of the new beam pipe will have a total length of 5.5 m (Fig. 5.8). This implies relocating the vacuum valve 1.5 m away from the TPC. This modification of the central section of the beam pipe is necessary to allow the positioning of the new ITS around the beam pipe before it is moved inside the TPC.

The RB26-section consists of three chambers of conical stainless steel tubes, which are up to 450 mm in diameter. The RB24-section uses standard LHC machine components and consists of copper tubes. The layout of the beam pipe central section affects the ITS performance and integration. The most critical parameters (radius, wall thickness, material, sag and bake-out procedure) are discussed below.

#### 5.4.1 Beam pipe radius and wall thickness

Current studies indicate that it should be possible to reduce the inner radius of the beam pipe central section from the present value of 29 mm to 17.2 mm. Estimates for the linear sum of fabrication tolerance, survey precision and alignment uncertainties amount to 5.1 mm, resulting in a minimum clearance of 12.1 mm radius with respect to the nominal beamline. The LHC aperture is quoted in terms of the so-called  $n_1$  parameter [31], which is a function of this mechanical clearance as well as the position along the beam line due to the varying beta function. The 12.1 mm clearance corresponds to an aperture of  $n_1 = 13.9$  at the ALICE interaction point for nominal injection optics. Beyond a distance of 2 m from the interaction point, the minimal aperture requirement of  $n_1 > 10$  is violated and a larger beam pipe radius is foreseen. Therefore, in the current layout, we assume a cylindrical beam pipe with larger diameter beyond a distance of 1 m from the interaction point. The wall thickness of the central Beryllium beam pipe section, 888 mm long, is assumed to be 0.8 mm. Using a smaller value of 0.5 mm is challenging due to possible issues with gas tightness and mechanical stability. The wall thickness and material for the beam pipe section beyond 1 m from the interaction point will be decided by background simulations and practical considerations. A conservative number of 19.0 mm for the beam pipe inner radius is assumed until further studies confirm the feasibility of the 17.2 mm radius (see Fig. 5.8).

#### 5.4.2 Beam pipe supports

A study has been carried out in order to evaluate the minimum number of supports necessary to contain the sag, which has to be sufficiently small to allow the installation of the new ITS at 2 mm radial distance from the beam pipe wall. These studies show a large deflection if the beam pipe is supported only at the two extremities and suggests the use of an additional intermediate support. However, this support complicates the installation procedure. Since the ITS is inserted from one side, it has to pass through the intermediate support to reach its final position. The maximum sag in the middle of an unsupported length of 5.0 m (corresponding to an overall length of 5.5 m) is 4.64 mm for a beam pipe with the layout proposed in Fig. 5.8. The addition of an intermediate support reduces the sag to 0.214 mm see Fig. 5.9. The beam pipe sag reduces its aperture and, therefore, containing the sag permits the reduction of its inner diameter. Moreover, a stiffer layout provides higher natural vibration frequencies, which is also an important requirement in order to avoid structural resonances. Resonance phenomena may occur when an impulse frequency approaches the natural vibration of the beam pipe and oscillations with large amplitude may be induced, leading to fatigue and premature failure. Potential sources of impulses are mechanical vacuum pumps connected to the chambers.

The main failure mode for the beampipes has been shown to be elastic instability, leading to local collapse (buckling). The beam pipe thin wall thickness exposes the structure to possible buckling under an external pressure of 1 bar. Additional compressive forces may arise from the chamber geometry and reaction forces of bellows. A safety factor of four is applied to the buckling pressure to allow for uncertainties in supports. Analysis for the central section beam pipe shows a buckling pressure larger than 6 bar, i.e. a safety factor of six, well within the requirement. However, particular attention should be paid

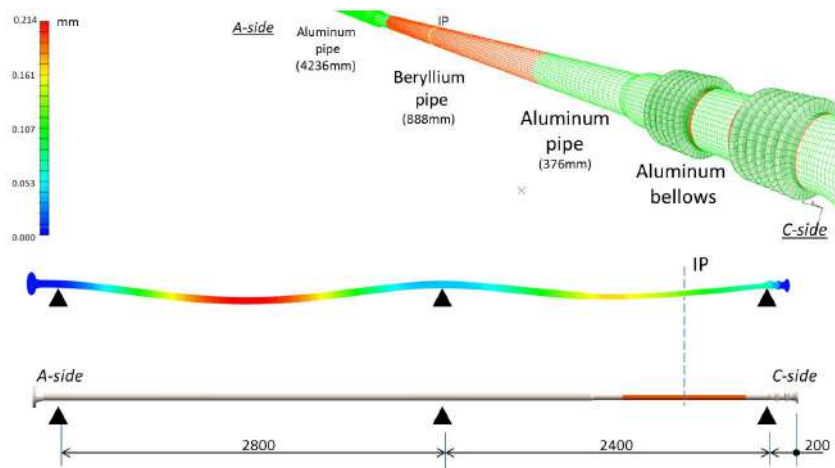


**Figure 5.9:** Beam pipe Finite Element Analysis used to predict sag, natural frequencies and buckling: max displacement 0.214 mm

during its handling and installation. The installation of the beam pipe inside the TPC and its connection to the LHC ring is a delicate procedure that is closely coupled to the ITS installation (see Sec. 5.5).

#### 5.4.3 Beam pipe bake-out

The beam pipe chamber is an ultra-high vacuum (UHV) system, which is pumped by a combination of lumped sputter-ion and distributed Non-Evaporable Getter (NEG) pumps. The NEG system consists of a thin sputtered coating along the whole internal surface of the vacuum chambers. After activation by heating under vacuum to above 200 °C, the NEG film gives a high distributed pumping speed for most gases. Gases not pumped by the NEG system are removed by sputter-ion pumps.

All vacuum chamber sections are permanently equipped with bake-out heaters for periodic re-activation of the NEG coating, with the exception of the beam pipe central section, where a removable oven will be used.

In the unlikely case that a bake-out of the beam pipe is required when the detector is installed, the ITS detector barrels need to be extracted, and the removable oven inserted inside the TPC. For this insertion, the oven will use the same rail system used for the installation of the half-barrels.

### 5.5 Installation and removal

The new ITS installation scheme is driven by the requirement of rapid access to the ITS barrels during the yearly LHC winter shutdown lasting 3-4 months. This requirement excludes the possibility of displacing or dismounting the surrounding detectors.

Any intervention that requires direct access to the current ITS implies approximately seven months from initiation of the procedure to restoration of the ALICE nominal configuration. The services of the current ITS are connected on both sides of the TPC. On the side of the hadronic absorber (C-side) the services are not accessible without moving the



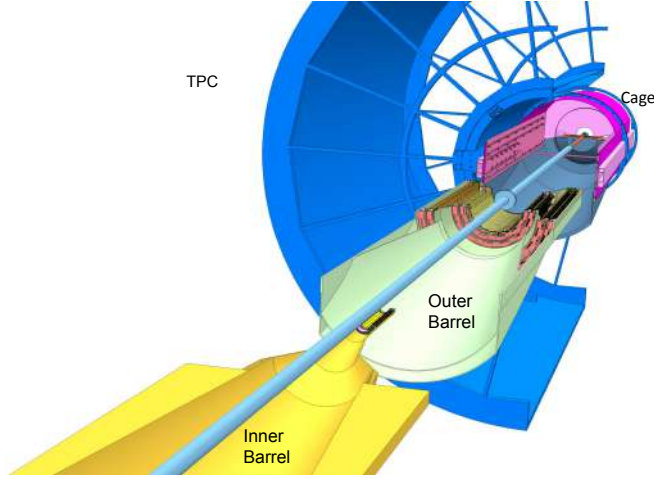


**Figure 5.10:** ITS IB and OB installation scheme: the insertion and extraction of the ITS is done per half-barrel. To extract the ITS outer half-barrels, it is necessary to first remove the inner half-barrels. Temporary rails (not shown) outside the TPC are used as extensions of the cage rails for the insertion-extraction of the half-barrels.

TPC by about 4 m along the beam axis, in the direction opposite to the hadronic absorber (i.e. towards the A-side), to the so-called “parking position”. Moving the TPC to the parking position and back in place is a complex and lengthy operation, which requires about seven months [32]. The requirement of fast accessibility to the new ITS therefore implies a new detector layout, with the services connected only on the A-side, as well as a new installation concept.

### 5.5.1 Sequence

The proposed installation scheme foresees a translation of the ITS by approximately 3 m along the beam pipe for accessibility. This translation is needed to move the ITS out of the inner bore of the TPC, which is the operational position of the ITS. Hence, it is envisaged to insert the ITS detector together with all its services along the  $z$ -axis, with the beam pipe installed and baked prior to the detector installation (Fig. 5.10). From the parking position, where it is mounted around the beam pipe outside the TPC, the ITS will be translated over a distance of about 3 m to reach its final position, with the innermost layers at 2 mm radial distance from the outer wall of the beryllium beam pipe. During the translation, the detector progressively approaches the final radial distance, in order to account for the different diameters of the central section of the beam pipe, and to pass the beam pipe supports. The ITS barrels are therefore composed of two halves, separated along the plane defined by the LHC ring. The two halves slide separately on the rails, forming a hermetic structure when they reach the final position.

The rails are designed to keep the axis of the barrels parallel to the beam axis at all times. This avoids interferences during the installation. In the last few centimeters of translation along the  $z$ -axis, the half-barrel approaches the beam pipe with a radial movement to reach the final position (Fig. 5.11). The accurate positioning of the half-barrels in  $z$  is

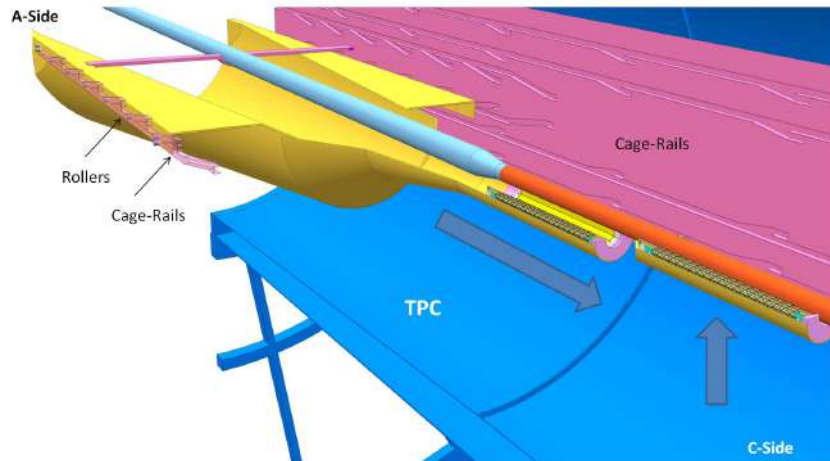


**Figure 5.11:** ITS half Inner Barrel installation: the half-barrel utilises rollers fixed at the side of the service barrel to slide along a rail system supported by the cage. In the last part of the translation the half-barrel approaches the beam pipe with a radial movement to reach the final position.

provided by precise mechanical stops located at the end of the translation route.

The rail system is fixed to a common carbon structure, the detector cage, which is in turn attached to the TPC inner bore, where it is permanently installed. The cage also provides the support and positioning of the beam pipe and of the Muon Forward Tracker. The relative precision in the positioning of the detector barrels and the beam pipe is provided by the manufacturing accuracy of the cage and by its stiffness under full load. The relative position of the cage, i.e. of the detectors and beam pipe, with respect to the beam axis can be tuned by means of remotely adjustable feet at the cage. This feature provides the possibility to center the new ITS and the beam pipe with respect to the beam during the installation and at any time during the operation, if required. The cage and its installation procedure are described in Sec. 5.5.3.

### 5.5.2 Muon Forward Tracker installation

The Muon Forward Tracker (MFT), which consists of six detection disks equipped with CMOS pixel sensors, is located in the free space between the ITS and the hadronic absorber. The MFT and the ITS share several design elements: the CMOS pixel technology, the detector layout and supports, and the installation and removal concept.

In the MFT, the CMOS pixels are assembled on flexible printed circuits, in a linear arrangement, to form ladders. The ladders are then installed on half-disk and six half-disks are assembled into a half-cone support structure (Fig. 5.12). The half-cone is fixed at the end of the MFT service half-barrel that, as for the ITS, provides the way out for the services to the A-side. The services consist in the electrical power cables for the sensors and the front-end electronics, the optical fibres for the slow control and data transfer, and finally the cooling lines.

The MFT service barrel is located between the ITS and the TPC detectors, therefore the amount of services and their distribution have been optimised in order to reduce the

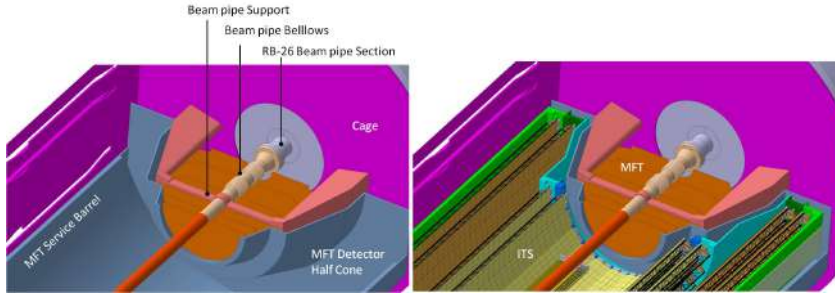


**Figure 5.12:** The MFT detection half-disks are assembled inside the detector half-cone that is fixed at the extremity of the service barrel. The MFT boundaries are defined by the ITS and the beam pipe hardware.

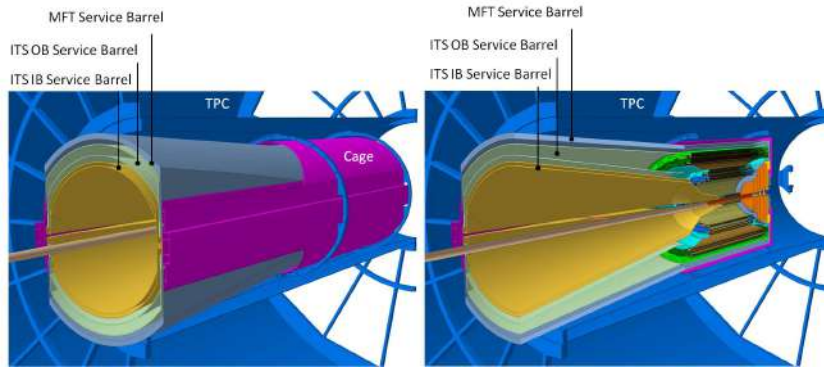


**Figure 5.13:** The ITS and MFT detector and service barrels are housed inside the TPC bore. The MFT service barrel is in between the ITS and the TPC.

material thickness in the central rapidity region (Fig. 5.13).

The MFT barrel needs to be in place before the ITS can be installed, and its removal implies the removal of the ITS barrels.

The insertion and extraction of the MFT inside the cage, housed in the TPC bore, is based on the same concept adopted for the ITS. The extraction from the A-side permits the removal and the maintenance of the detector during an LHC winter shutdown. As for the ITS, the MFT half-barrels will be inserted separately and will be positioned by means of rollers sliding on the guides which are part of the cage. The MFT half-barrel, during the translation, clears the beam pipe and its supports and moves to the minimum radial distance from the beam pipe when the operational position is reached.

The position of the MFT detection disks along the beam line is constrained by the complex layout of the beam pipe central section at the C-side. In this area two bellows are foreseen to absorb both the thermoelastic expansion of the beam pipe central section, during the bake-out, and the displacement of the connected RB26-section, occurring when the ALICE solenoid magnet is switched on. A bracket fixed to the cage provides a support

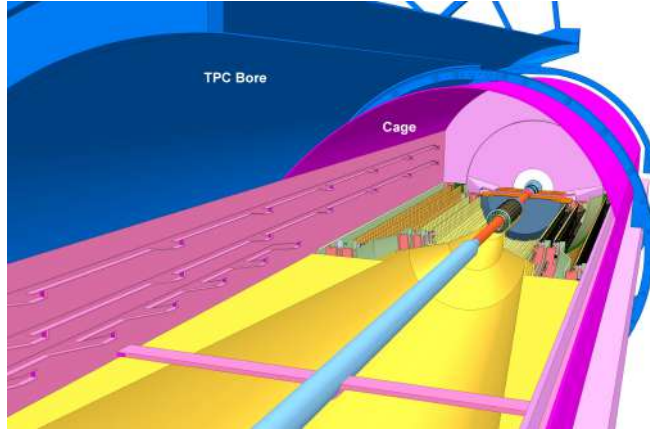


**Figure 5.14:** Detector cage housing the ITS and MFT detector barrels and supporting the beam pipe central section.

to the beam pipe just before the bellows.

### 5.5.3 Detector cage

The cage is the mechanical structure which holds the detectors during its insertion and removal, and in the operational position. The detector cage is a stiff cylindrical shell based on a light composite sandwich, which is fixed inside the TPC bore and provides a common support for the ITS and MFT barrels and the beam pipe (Fig. 5.14).

The cage incorporates two of the three supports of the beam pipe central section, one at the C-side and one in the middle, while the third support (A-side) is outside of the TPC on a bracket directly fixed to it (Fig. 5.15). The beam pipe central section is temporarily installed inside the cage before the insertion into the TPC, on a stand outside the ALICE solenoid magnet called the DELPHI frame. The cage is then slid inside the ALICE space frame by means of temporary rails connecting the DELPHI frame to the TPC. The connection between the central section of the beam pipe in the cage and the RB26-section at the hadronic absorber side is made with the TPC in parking position (displaced by  $-4$  m in the  $z$ -direction). This provides access for the connection and verification of the beam pipe mating flanges. After the connection is made, the TPC is moved to the nominal position, and the third support of the beam pipe (the one in front of the TPC) is added. The cage load is transferred to the TPC and the temporary rails are removed.

The miniframe, a large frame on the A-side that carries the services of the central detectors, is installed and the services connected. The RB24-section of the beam pipe, which is on the miniframe, is then connected to the central section. The beam pipe is aligned and the bake-out procedure is carried out (Fig. 5.15). At this point, the detector barrels can be installed. The installation sequence foresees the insertion of the MFT barrel followed by the ITS outer barrel and the ITS inner barrel.

The cage sits on brackets fixed at the two stiff rings of the TPC cylindrical bore, in the middle horizontal plane. An additional support point is provided on the external ring of the TPC conical bore on A-side. At the interface with the TPC, the cage provides a levelling system that allows for a fine-tuning of its position with respect to the beam.

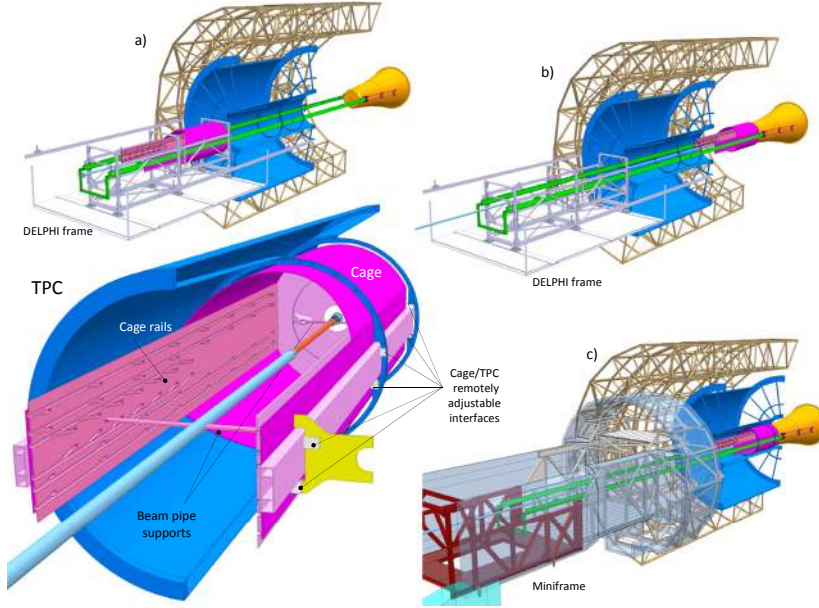


**Figure 5.15:** Cage installation: (a) The beam pipe is installed in the cage outside the TPC on the DELPHI frame; (b) the cage is slid inside the TPC, while in parking position, and the beam pipe is connected on the C-side to the RB26-section; (c) the TPC is moved into the interaction point position and the external beam pipe support is added; the DELPHI frame is removed and the miniframe is put back; the beam pipe is connected on the A-side to the RB24-section and the bake-out takes place.

The system, based on remotely controlled movable mechanical parts, can be used at the different stages of the beam pipe and detectors alignment.

At its interior, the cage provides the precise guiding rails needed for the insertion of the detector-service half-barrels. One set of rails for each half-barrel is used at the vertical side wall of the cage. The rails are in CFRP, directly realised in the composite sandwich structure that constitutes the cage side wall. During insertion, the half-barrels move on wheels guided by the rails. The rail design is such to keep the barrel at a safe distance from the beam pipe and its support. The clearance reaches the design value only a few centimetres before the final position.

The cage will remain permanently inside the TPC after its installation. While removal of the cage is in principle possible, it would imply the opening of the beam pipe vacuum (i.e. moving the TPC).

## 5.6 Survey and mechanical alignment

The survey and alignment requirements for the ITS detector elements can be separated into two different categories.

First, the different ITS elements must be placed at the nominal position within a specified tolerance, typically of the order of few tenths of millimetres, to permit adequate

positioning of sensors in terms of overlapping and to preserve proper clearance for smooth installation and maintenance.

Second, the position of the silicon sensors and their stability in time during operation have to be known with a tight accuracy, of the order of few microns for the IB and few tens of microns for the OB.

Although the mechanical structure of the ITS is designed to provide precision and stability with the required level of accuracy, several factors influence the uncertainty of the position of the detectors:

- the manufacturing accuracy of all components;
- the tolerance after assembly of the components in the barrel;
- the deformation of the components under load;
- the global positioning uncertainties related to the installation procedure;
- possible vibrations of the mechanical support structure;
- thermal expansion of the components;
- other long-term effects such as the settling of different parts of the ITS structure and surrounding ALICE interfaces.

The required precision of the final position of the ITS detectors can only be ensured if the position of the components relative to each other is measured during each step of the assembly process.

Each Pixel Chip in the Stave will have reference marks on the visible side of the sensor which are very accurately related to the pixel array. By using a 3-dimensional Control Measuring Machine (CMM), equipped with an optical probe, these marks will allow the determination of the relative positions of the Pixel Chips within a Stave. Their positions will be known with respect to external reference markers on the FPC and on the Stave.

The next step will be the precise measurement of the position of the Staves on the end-wheels to form a half-layer. The Stave's relative position will be measured and referred to reference points on the end-wheels. Depending on accessibility, all reference markers on the Stave, both on the FPC and on the Pixel Chips, will be used.

At this level, non-contact optical measurement of the pixel sensor positions will be related to contact measurement of targets on the end-wheels. Targets for contact measurement will be housed in metrology holes provided in the end-wheel structures.

After the layers are assembled in a half-barrel, they will be related to each other and to common reference targets on the detector barrels, which will be visible to an external survey system.

Following insertion of the half-barrels, their position will be surveyed by a tracking system, through line of sight along the beam pipe from the A-side. By using targets on the end-wheels and on the barrels, the ITS local coordinate system will be related to the ALICE global system, i.e. to the beam axis.

As the quite small angle of view of the inserted ITS from A-side degrades the quality of a photogrammetric measurement, a laser tracking system is preferred.

The precision of the measured position of the detectors in the global ALICE coordinate system is determined by the accumulation of the measurement errors in each of the steps described above. To ensure that the detector position does not change in time, active monitoring of some elements of the ITS will be required during its operation. The construction of the ITS and its location within ALICE limits the choice of the monitoring techniques that can be used. On the C-side, where access is prevented by the hadronic

absorber, a fixed measuring device will provide the measurement of the position of the targets on the detectors barrels. The relative position of the ITS and the TPC will be monitored by an optical system.

These metrology and survey data serve as starting points for the final alignment, based on the reconstruction of tracks. The continuous tracking of the barrel position can be used to crosscheck the possible relative displacement of sensors made evident by the tracks reconstruction, caused by displacement or deformation due to external factors e.g. vibration, thermoelastic movement and settling of different parts. The alignment process must therefore be repeated periodically.

## 6 Read-out electronics

This chapter deals with the specification of the I/O stages embedded into the Pixel Chips, the definition of a communication channel(s) and protocol to transfer the data off-detector and the coordination of all electronic signals travelling inside the ITS up to the patch panels in the Miniframe. In the Miniframe a read-out unit (RU) interfaces the ITS on-detector electronics with the Data Acquisition (DAQ), Trigger, and Detector Control (DCS) systems. The definition and preliminary design of the ITS powering scheme and components is also sketched in this chapter.

### 6.1 General layout

As described in Chap. 1, the ITS active surface is arranged in seven cylindrical Layers positioned at different radii from the beam axis, with the Layers getting longer at outer radii to keep the angular coverage constant with respect to the interaction point. Physics simulations provide an estimation of the number of hits (passing tracks) each Layer will record for each interaction. In addition to the hits induced by crossing particles, electronic noise will contribute and may become dominant in the Outer Layers where the track density is relatively low. Table 6.1 summarises the hit and data rates expected for the different Layers. A single 30 mm × 15 mm Pixel Chip will be used to instrument the whole sensitive surface of the tracker (about 10.7 m<sup>2</sup>).

Sensors will be arranged in Staves to form the Layers. Inner Layers (Layers 0 to 3) will share the same Stave design, each Stave holding nine sensors in line for a width of about 15 mm and a total length of about 270 mm. Middle Layers (Layers 3 and 4) and Outer Layers (Layers 5 and 6) Staves have a different design, and will carry sensors grouped in Modules, each Module being composed of two parallel lines of seven sensors each. Modules will be further assembled in Half-Staves, each composed of four Modules in a row in the Middle Layers, and of seven Modules in a row in the Outer Layers. Middle Layers Half-Staves are 843 mm long, while Outer Layers Half-Staves are 1475 mm long, as detailed in Tab. 6.1. Each Stave/Module has a custom-made Flexible Printed Circuit (FPC) which connects the sensors to the outside world. The FPC is custom-made in order to minimise the material budget in the sensitive volume. Once outside the sensitive volume, using commercial high-speed cables to reach the patch panels (some 4 m to 5 m away) is the favoured solution. A schematic representation for a single Stave/Half-Stave is sketched in Fig. 6.1. Two Half-Staves are mechanically supported by the same Space Frame (see Chap. 4), forming what is called a complete Stave.

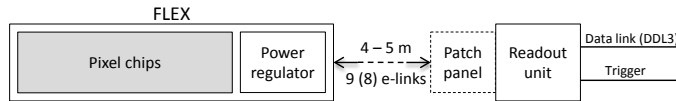


**Figure 6.1:** Schematic representation of the read-out path. The number of e-links per Stave is nine for Inner Layers and eight for Middle and Outer Layers.

While at the patch panel end the cables will use standard connectors, at the Staves end



**Table 6.1:** ITS geometrical parameters, sensors count and maximum hit density ( $|\eta| = 0$ ) for a minimum-bias Pb–Pb event. The hit density figure is derived considering Pb–Pb collisions at 100 kHz rate and accounts for both primary and secondary hadronic interaction, QED background assuming an integration time of 30  $\mu$ s and a detector noise of  $10^{-5}$  fake hits/pixel.

Layer	Length (mm)	Radius (mm)	(Half-)Staves <sup>a</sup> (#)	Chips (#)	Hit density (cm <sup>-2</sup> )
0	271	23	12	108	18.6
1	271	31	16	144	12.2
2	271	39	20	180	9.1
3	843	194	44	2464	2.8
4	843	247	56	3136	2.7
5	1475	353	80	7840	2.6
6	1475	405	92	9016	2.6

<sup>a</sup> Staves for Inner Layers (0–2), Half-Staves for Middle and Outer Layers (3–6)

it is still under investigation which solution actually offers the most effective connection. Direct soldering yields better impedance matching, but the use of commercial or custom-made connectors would simplify both assembly and handling. Whichever the final solution, the extremely lightweight structure of the Staves supporting the bus makes it unlikely to have direct soldering or, even worse, a connector placed in the terminal part of the FPC. A flexible extension of the FPC, reaching a firmer holder out of the sensitive volume, is foreseen.

## 6.2 Pixel Chip read-out architectures

The first stage of the detector read-out system is the circuit that gathers the data registered at pixel level into event buffers, and is integrated in the Pixel Chip periphery. The read-out architecture has to cope with different detector operating conditions, which are determined by the collision system (Pb–Pb or pp) and the event rate, which in turn define the average hit density per event on each Layer. Such operating conditions, including a safety factor of two, can be summarised in two classes:

1. Pb–Pb collisions at rates up to 100 kHz and “high” hit density.
2. pp collisions at rates up to 400 kHz and “low” hit density.

For both collisions type it should be possible to operate the detector in continuous or triggered mode. In triggered mode, the level zero (L0) trigger will have a latency of about  $\tau_{L0} \approx 1.2 \mu$ s. The two architectures currently under consideration will be briefly discussed below.

### 6.2.1 ALPIDE architecture

The ALPIDE architecture implements a pixel-level sparsified read-out. In such an architecture, each pixel cell contains a comparator followed by one (or more) latch. Each time a pixel has an analogue signal greater than the comparator threshold, it sets the latch to 1. Asynchronously, every pixel set to one is read out according to its priority in the chain, the pixel priority being determined by their position within the chip. The pixels of two

adjacent columns are connected to the same priority encoder. All double columns are read out in parallel. The time it takes to read one single pixel is about 25 ns. The analogue part of the pixel, the front-end circuit, has a shaping time that makes it integrating over a time of 4  $\mu$ s.

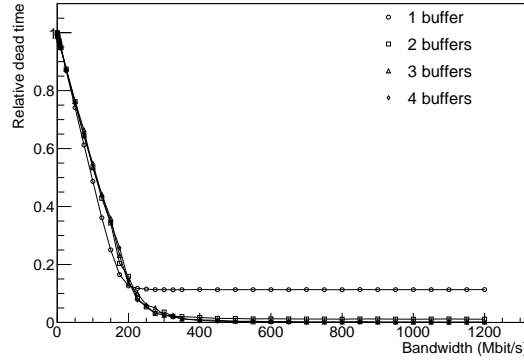


**Figure 6.2:** Relative dead-time for different output bandwidths and the number of front-end latches.

At the column end the triggered pixel's addresses are stored in a regional buffer. Simulated minimum-bias Pb–Pb events were used with a model of the priority encoder architecture to estimate the optimal buffer and region (adjacent columns) size. The data throughput resulting at the buffer output (which effectively smooths the data rate) sets the bandwidth requirement for the data link. For a region consisting of 32 columns (20 800 pixels), a 256-word deep memory proved to be sufficient for storing four consecutive minimum-bias Pb–Pb events. Using that configuration, simulations showed that a link with a bandwidth of 1 Gbit s<sup>-1</sup> does not limit the read-out speed of the full Pixel Chip with a safety factor greater than two. It has hence established that 1 Gbit s<sup>-1</sup> is the link bandwidth design goal. Figure 6.2 presents the simulated dead-time of the complete chain (analogue shaping, priority encoder read-out, regional buffer, read-out) when running at 100 kHz. Upon trigger, assuming a latency of 1.2  $\mu$ s), the pixel signals are stored in a latch after a time of 600 ns, which allows matching the peaking time of the front-end. If there is only a single latch present in the pixel, this delay introduces a small constant dead-time after each accepted trigger. Additional dead-time comes from the matrix read-out process. Both of those effects can be reduced by embedding additional latches in the pixel cell. With two front-end buffers, the relative dead-time is significantly reduced and is eliminated by introducing the third one. Figure 6.3 presents the probability of event pile-up.

### 6.2.2 Rolling-shutter architecture

In the rolling-shutter architecture, each pixel is read out one after the other independently of their content, and the sparsification happens later in the periphery. Immediately after reading the current value and resetting a pixel, the pixel is left integrating the incoming signals until the read-out of all the others pixels finishes and the process restarts. The time the process takes is roughly equal to the integration time of a single pixel. Assuming zero suppression is achieved by checking the analogue value of every read pixel and recording

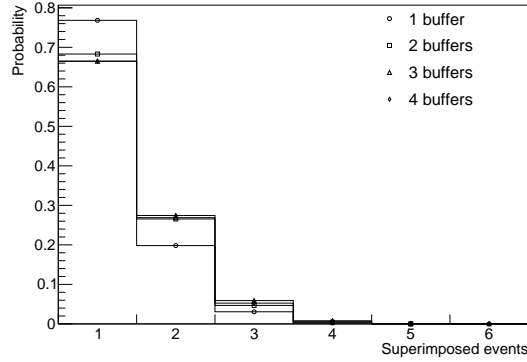


**Figure 6.3:** Probability of recording different numbers of events on a single strobe for an output link of 1 Gbit/s and four values of front-end latches.

only those pixels over a given threshold (Fig. 6.4), the continuous and triggered mode could be easily achieved by enabling the recording of values only when a trigger happens. In case of multiple triggers, the recording window stays open until no more trigger occur (Fig. 6.5).

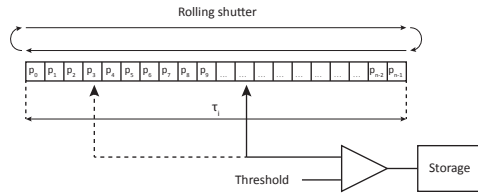


**Figure 6.4:** Rolling-shutter zero suppression mechanism.

The rolling-shutter architecture has no way to distinguish between different events recorded in the same time window, hence in case of ambiguity, clusters must be assigned to the correct event using tracking information outside the sensor.

### 6.2.3 Data transmission

The expected data rates of the different parts of the ITS do not depend on the specific pixel read-out architecture, as long as it reduces the data to the relevant pixels, as both proposed options do. Table 6.2 reports the data rate expected for various parts of the ITS. Therefore, as far as it concerns the data read-out, there will be no practical difference between the Inner Layers and the Middle and Outer Layers Pixel Chips. Every Pixel Chip will embed a High Speed Output (HSO) driver capable of driving a differential line at high speed. A slow control receiver/transmitter will make it possible to dynamically configure the chip, while a dedicated block will manage the incoming reference clock. What changes from the Inner to the Middle and Outer Layer is the Pixel Chip connection topology. While in the Inner Layers each Pixel Chip is directly connected to the read-out unit via a single link,

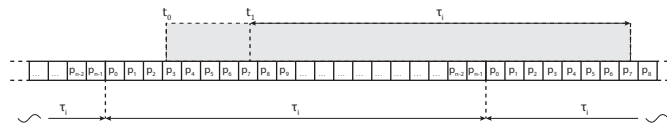


**Figure 6.5:** Read-out trigger gating for the rolling-shutter architecture. The recording window stays open for a read-out cycle, guaranteeing each data due to the triggered event is recorded. In case of multiple consecutive triggers, the recording windows remains open until no more triggers arrive.

in the Middle and Outer Layers the Pixel Chips are grouped in Modules to optimise the link capacity (see Sec. 6.3.2). The implementation of one (or more) data input block(s) will make grouping possible by daisy-chaining multiple Pixel Chips.

## High Speed Output

The high speed output block (HSO) will drive data from the sensor periphery to the patch panel. As the foreseen arrangement includes no active component between the sensor and the first patch panel, the HSO driver needs the strength to drive the entire communication line, which is 5 m long in the worst case. Layer 0 sets the maximum requirement in term of single sensor occupancy, hence defining the requirements for the HSO. The architectural simulations discussed in Sec. 6.2.1 set the design goal data rate for the HSO block to  $1 \text{ Gbit s}^{-1}$ . To successfully transmit data at  $1 \text{ Gbit s}^{-1}$  over a length up to 5 m, de/pre-emphasis on chip is almost mandatory. Preliminary studies detailed in Sec. 6.4 and literature from companies operating in the network business actually show how pre/de-emphasis on chip output and Constant Time Linear Equalisation (CTLE) on the receiver could both ensure the necessary transmission performance.

A preliminary version of the HSO layout has been designed and simulated and a first prototype is currently under test. To comply with the ITS goal of low material budget, a great effort has been made to minimise the power consumption of this part. Simulations show how power consumption ranges between 20 mW and 30 mW (serialiser + driver) according to the level of pre/de-emphasis, which will be possible to select remotely via the slow control. These figures translate in an added power dissipation of about  $5 \text{ mW cm}^{-2}$  to  $8 \text{ mW cm}^{-2}$  to that of the pixel matrix itself.

The HSO will run at 0.5 GHz in double data rate driving a transmission line made by a differential pair (generically called e-link). The link is current-driven, with the receiver at the patch panel sensing the voltage swing over a shunt resistor. To maximise bandwidth, an encoded clock protocol will be adopted. The widespread commercial standard 64b/66b encoding offers a low overhead of 3.12% and the opportunity to use standard IP cores both in the transmitter (Pixel Chip) and the receiver (patch panel unit). In the 64b/66b protocol, data is split in 66-bit packets, where 64 bit carry the actual data and two bits of opposite value are prepended. The latter assure transition of the data line and enable clock recovery.

## Flexible Data Routing

A Flexible Data Routing (FDR) implementation is mandatory in order to have the same chip for both the Inner (single) and Middle/Outer (grouped) Layers. Figure 6.6 gives a glimpse of such flexible data routing implementation. Data coming from the sensor pixel matrix and data from the external input ports (used to directly connect other chips or

bypass lines) are actually handled the very same way by a fast multiplexer, which then outputs the data in a FIFO fashion mode, masking their origin to the driver stage. The multiplexer can be programmed to watch for an arbitrary combination of data inputs. Data are then read out from the multiplexer by the HSO driver, whose speed and power consumption can be programmed as well depending, for example, on the position of the Pixel Chip in the daisy chain.

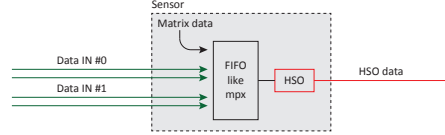


**Figure 6.6:** Functional diagram of a possible FDR implementation.

### Clock and slow control

Slow control and chip-to-chip communication need a much slower data rate than the high-speed output. The master clock runs at 40 MHz and is connected to the chips via a multi-drop line. The same happens for the slow control, which runs with the same frequency. Considering the slow speed of such signals, standard I/O IP blocks optimised for low power consumption will be embedded into the sensors to perform slow I/O operations.

### 6.3 Staves layout

The organisation of the data path in a Stave/Half-Stave and the way to transmit data from the Staves to the patch panel depends on the data rate generated by each single sensor, and the way the sensors are physically arranged. Such organisation of the Pixel Chips will also drive the requirements for the Flexible Printed Circuit (FPC) which will actually connect the chips. Table 6.2 summarises the data rate for various system elements for each Layer at  $z = 0$ , where the rate is maximal. The quoted numbers are calculated for minimum-bias Pb–Pb events at 100 kHz bunch crossing rate and using an integration time of 30  $\mu$ s (33 kHz frame read-out). Apart the contribution from primary and secondary particle tracks, they account also for both the QED electron background and fake hits due to electronic noise.

Table 6.2 shows that in Layers 0 to 2, each chip has its own link, therefore making all the Inner Layers Staves identical. This scenario implies every chip is driving its own link, further enhancing the reliability of the system in case of a chip failure. The link capacity has been specified to be 1 Gbit s<sup>-1</sup> as detailed in Sec. 6.2.3, hence the bandwidth margin is close to a factor four for the worst case central chip in Layer 0. To standardise the system and streamline the construction phase, it has been decided to adopt the very same link technology across the seven Layers of the ITS: sensors in the Middle and Outer Layer will be in turn daisy-chained to match the link performance at best. The minimal number of links needed to read out each ITS Layer is therefore defined by the data load of each Layer (Tab. 6.1) and the speed of the link. Practical considerations related to the physical connections between links and Staves/Modules, design standardisation and assembly simplicity will again set the actual links count larger than the theoretical one for both the Middle and the Outer Layers.

**Table 6.2:** ITS data throughput computed for various system levels. Pixel pitch, which is relevant for the electronic noise amount, has been assumed for worst case equal to  $20\ \mu\text{m}$  for all Layers (an option is to use larger pixels for the Middle and Outer Layers). Electronic noise (fake pixels), in particular, linearly scales with the pixel area, hence larger pixels would result in reduced noise-due data throughput for the Middle and Outer Layers.

Layer	Chip (Mbit s <sup>-1</sup> )	Module (Mbit s <sup>-1</sup> )	(Half-)Stave <sup>a</sup> (Gbit s <sup>-1</sup> )	Layer (Gbit s <sup>-1</sup> )	E-links (#)	DDLs (#)
0	284	—	2.5	29.4	108	12
1	174	—	1.53	24.5	144	16
2	121	—	1.06	21.3	180	20
3	14	196	0.76	36.5	96	22
4	12	168	0.65	39.0	120	28
5	11	144	0.98	82.3	168	40
6	10	139	0.95	91.2	192	46

<sup>a</sup> Staves for Inner Layers (0–2), Half-Staves for Middle and Outer Layers (3–6)

### 6.3.1 Inner Layers

With every sensor driving its own link, the FPC must provide at least eleven links (nine high-speed data links, one slow control, one clock) and dedicated supply planes, as illustrated in Fig. 6.7. In such a scenario, the cable connected to the FPC should contain a minimum of eleven differential pairs, realising a one-to-one Stave/cable mating through all Inner Layers.

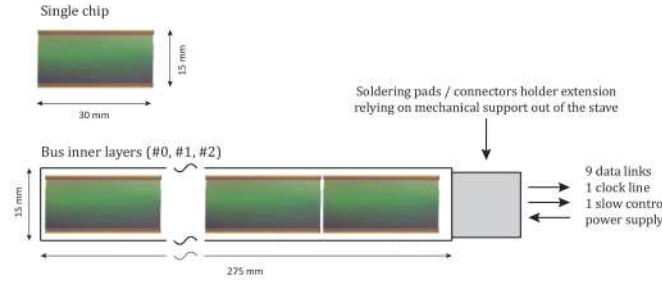


**Figure 6.7:** Connections for an Inner Layer Stave.

The FPC will hence contain at least eleven data differential pairs plus the power supply planes, all implemented in a double-side printed circuit board 15 mm wide and about 32 cm long. One possible option for the realisation of the data and power connection for the Inner Layer is sketched in Fig. 6.8, where the FPC is shown housing both the data and power lines. As the data lines are far more critical than the power lines in terms of medium discontinuity, the idea is to stop the power lines at the Stave end, while the data lines continue through the feed-through.

A soldered flexible strip will connect the power line to the side of the Stave flange, while the data lines should be stretched apart inside the FPC itself just after the feed-through, providing a larger available surface for connection (via soldering or custom-made connector) with the long cables. Such a solution will ensure better data integrity for the

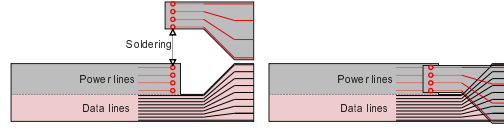


**Figure 6.8:** Power and data lines on the Inner Layers bus.

high-speed transmission as well as wider tracks for the power lines.

Producing such a shaped FPC has been investigated and proven possible, and detailed mechanical design is already ongoing. One possible FPC implementation currently being considered is illustrated in Fig. 6.9.

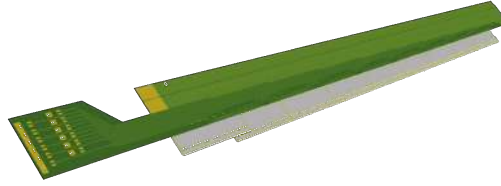


**Figure 6.9:** Layout of the Flexible Printed Circuit for the Inner Layer Staves.

### 6.3.2 Middle and Outer Layers

As detailed in Chap. 4 the Pixel Chips are grouped in Modules in the Middle and Outer Layers. A single Module will host 14 Pixel Chips, arranged in two lines of seven chips each, as seen in Fig. 6.10a. Middle Layer Half-Staves contain four Modules each, while the Outer Layer Half-Staves will contain seven Modules each. To minimise the line density into the bus, each Module is foreseen feeding data to the neighbouring one in a daisy-chain fashion, the latest one connecting to the patch panel by one (or more, as spare) physical links. Each Module hosts two master Pixel Chips managing the Module-to-Module communication, one per row. The other Pixel Chips in the Module send their data to the masters in daisy-chain fashion as well. The read-out network interconnecting the Pixel Chips to the master inside the Module is sketched in Fig. 6.11. The Pixel Chips will be physically identical: the master-slave I/O blocks is activated and set up by slow control programming. Such an arrangement would impose no tighter constraints on the bus technology than what is necessary for the Inner Layers, as the line density, even assuming the case of two physical links per Half-Stave to increase redundancy, would be lower than that of the inner Staves. The actual link bandwidth requirement, discussed in detail in Sec. 6.2.3, is far below that of the Inner Layer.

To maximise single chip fault tolerance, the possibility of changing the function of master in a Module during operations by slow control is foreseen; this case is discussed in detail in Sec. 6.2.3. The Module/Half-Stave abstract layout is sketched in Figs. 6.10a and 6.10b for the Middle and Outer Layers, respectively.

### 6.3.3 Modules interconnection topology

As illustrated in Sec. 6.3.2, the lower data rate in the Middle and Outer Layers makes it conceivable to share data links among sensors, therefore prompting the grouping of Pixel Chips in Modules. The modular approach provides great design, production and

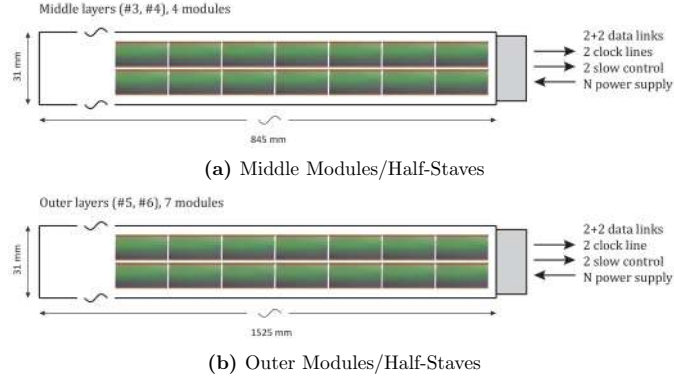


**Figure 6.10:** Conceptual sketch of the Middle (a) and Outer Modules/Half-Staves (b). The “2 + 2” for the data lines means one active plus one spare data line for each chip row in the Module.

mounting simplification. To effectively share the bandwidth guaranteed by a single link (up to  $1 \text{ Gbit s}^{-1}$ ), chips inside a Module must be able to deliver their data to neighbouring chips until they reach a chip connected to the high speed link, the so-called master chip. Every chip is physically identical to each other, but only those having their HSO block connected to the high speed links act as masters. The chips not connected to any physical link will move their data to the neighbouring chip in a daisy-chain fashion always using their HSO block, but programmed for a different speed depending on the data load to save power. The short distance of the communication lines between chips (order of cm) makes a much weaker driving of the line possible.

Table 6.2 shows that the maximum data load for a Module is less than  $250 \text{ Mbit s}^{-1}$ , hence a single master chip per Module would suffice. Considering that the numbers of Tab. 6.2 are derived for the occupancy corresponding to chips positioned at  $z = 0$ , and are therefore representing an upper limit that will never be reached by an entire Module/Stave, the daisy chain can actually be extended to the full Half-Stave, each chip delivering its data to the next one even across the Modules. In such a configuration, the two rows of chips in each Module would be completely autonomous from another, each one being part of one of the two daisy chains running along the full Half-Stave. Figure 6.11 sketches this solution.

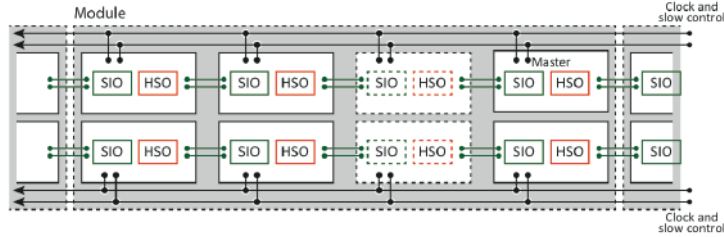


**Figure 6.11:** Half-Stave double daisy-chain data transmission topology.

In this arrangement, every Half-Stave hosts two independent daisy chains, each one



connected to a physical link. Table 6.2 shows that two links of  $1 \text{ Gbit s}^{-1}$  each can accommodate the data of the busiest Half-Stave, which is in total less than  $1 \text{ Gbit s}^{-1}$ . It has to be stressed that the figures in the table have been derived for a central chip with a  $20 \mu\text{m}$  pixel pitch, which is the worst case assumption.

To ensure redundancy in case of single chip failure, a full row of seven chips can be bypassed by a completely passive line embedded into the Module FPC. Each chip at the end side of the Module (right-hand side of Fig. 6.11) would therefore drive two lines in parallel: an extremely short one toward the input of the leftmost chip of the next Module, and a longer one running in parallel to the seven chips of the Module. The leftmost chip of each Module would therefore have two identical data inputs: one fed by the previous Module rightmost chip; the other connected to the bypass line, to be enabled in case of problems in the preceding Module (chip failure or contact problems).

## 6.4 Data transmission lines

In the Inner Layers, the Pixel Chip high-speed differential output signals will run along the Stave inside the Flex Printed Circuit (see Sec. 6.3.1), which acts as a bus. At the end of the Staves, the bus connects to longer cables with no active components in between (see Sec. 6.3). Proper impedance matching between the FPC and the cable is critical for minimising insertion losses, ensuring data integrity at high transmission speeds. In the Middle and Outer Layers, instead, the lower rate allows daisy-chaining of the signal from chip to chip and from Module to Module, therefore simplifying the Module's connections and FPC design, a critical aspect considering that the Outer Layer runs for 1.5 m. Considering the whole ITS, moving the data from the end of the Staves to the patch panel involves using many hundreds of links in the current design (Tab. 6.2). The mechanical characteristics of the cables, together with the electrical ones, will therefore play a major role in determining which particular solution to be adopted.

### 6.4.1 Long cables

The performance of the long cables running from the ITS to the Common Read-out Unit (CRU) is critical. A convenient compromise between electrical characteristics and mechanical constraints (space requirement, rigidity, environmental compliance) must be found. The sheer number of cables also calls for an economically viable solution. After investigating various off-the-shelf products, a good candidate cable was found with the Samtec AWG30 Twinax "Firefly" ( $100 \Omega$  nominal impedance) cable assembly. The cable is by default soldered to a small PCB which serves as connector (Fig. 6.12). The manufacturer ensured it can both provide bare cables (without PCB) or ones directly soldered to the bus/FPC.

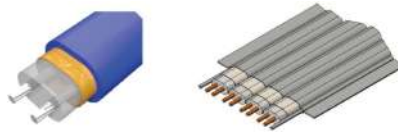


**Figure 6.12:** Samtec Twinax cables pair (left) and laminated assembly (right).

The cables have been characterised for both differential insertion loss and return loss (S-parameters) up to 4 GHz. Figure 6.13 shows the S-parameters for insertion and return losses, each for the setup only as well as for the setup together with the 4 m long cable. The results match the vendor specifications perfectly. The test fixture and cable assembly

differential S-parameters measurements, other than providing a cross-check of the vendor specifications, provided the necessary information to perform data rate measurement by disentangling the cable from the test fixture contributions.

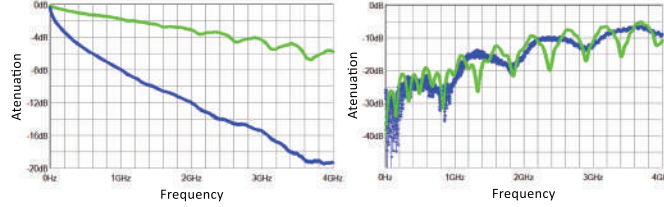


**Figure 6.13:** 4 m Samtec Twinax insertion loss (left) and return loss (right). The green line represents the contribution of the measurement system reference (which was characterised on purpose); the blue line the cable plus the test system.

Figure 6.14 shows eye-diagram measurements for a test setup using 4 m Samtec Twinax cable at a transmission speed of  $1 \text{ Gbit s}^{-1}$ . The first measurement has been done simulating a standard receiver and transmitter, with no active signal conditioning. The second measurement uses the very same transmitter, but a receiver applying a Constant Time Linear Equalisation (CTLE) of 2 dB. The last graph in Fig. 6.14 shows the measurement results in the case the transmitter applies a 2 dB pre-emphasis on the signal. The very promising results obtained by applying CTLE in the receiver and the increasing availability of COTS ICs embedding such capability, led to considering the possibility of moving the signal conditioning from the Pixel Chip to the receiver, further reducing the power dissipation of the sensors.

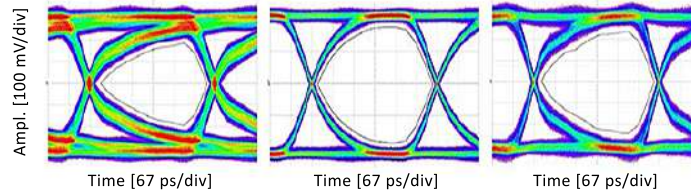


**Figure 6.14:** Eye diagrams of 4 m long Samtec AWG30 Twinax at  $1 \text{ Gbit s}^{-1}$  for a better than  $10^{-12}$  BER. At left the eye diagram for “passive” transmitter and receiver, in the centre with the receiver applying an equalisation of 2 dB and on the right with the transmitter applying a 2 dB pre-emphasis.

## 6.5 Power distribution and regulation

The very tight requirements on material budget imply that the optimum balance between power cables gauge and power dissipation has to be found in order to minimise the cooling system load while maintaining the cables’ routability through the services paths. To address the issue, the starting step is to consider the power consumption of the Pixel Chip. As discussed in Chap. 2, depending on the Pixel Chip design that will be adopted the power density will vary up to a maximum of about  $100 \text{ mW cm}^{-2}$ .

**Table 6.3:** 4 m long Samtec Twinax cable eye diagram characteristics ( $10^{-12}$  BER) for various signal conditioning and different transmission speeds.

	1 Gbit s <sup>-1</sup>			2.5 Gbit s <sup>-1</sup>		
	direct	2 dB CTLE <sup>a</sup>	2 dB PE <sup>b</sup>	direct	4 dB CTLE <sup>a</sup>	3 dB PE <sup>b</sup>
Height (mV)	320	350	438	160	260	285
Width (ps)	851	918	901	254	308	295
Tot. jitter (ps)	121	68	80	150	86	107
Rnd. jitter (ps)	4.2	3.4	4.5	3.9	3.4	3.5
Det. jitter (ps)	62	20	17	9.6	38	58

<sup>a</sup> Constant Time Linear Equalisation<sup>b</sup> pre-emphasis

### 6.5.1 DC-DC conversion

The electrical power and current to be distributed to the ITS detector are very large. Under the assumption of a Pixel Chip with a power density of  $100 \text{ mW cm}^{-2}$  the total power per Layer goes from about 48 W for the Inner Layers to about 1100 W, for the Middle Layers and about 4000 W for the Outer Layers. In order to reduce the mass of the cables that transport the supply currents from the power supplies to the detector, the baseline solution is to use the CERN custom-made DC-DC converter [33]. These thin and small (PCB of  $28.5 \text{ mm} \times 13.5 \text{ mm}$ ) converters, which will be placed at the entrance of each Stave, convert the supply voltages from 12 V down to 1.8 V with 70 % efficiency. The EMI characteristic have not been tested, and will require careful evaluation due to the short distance between the regulators and the first sensors on the Staves. The CERN DC-DC converter has been specifically designed to withstand radiation levels and magnetic fields far exceeding those expected for the ALICE ITS.

## 7 Detector performance

In this chapter we describe the performance of the upgraded ITS, the simulations carried out for the investigation of this performance, and the main algorithms of the corresponding reconstruction software. Section 7.1 gives an overview of the experimental conditions that have been assumed in the simulations. In Secs. 7.2 and 7.3 we discuss the detector requirements and specifications, respectively. Section 7.4 is devoted to the description of the simulation tools and models. The reconstruction algorithms are outlined in Sec. 7.5, whereas the performance of these algorithms is presented in Sec. 7.6. As explained in Chap. 1, the new ITS will not include Particle-Identification (PID) capabilities because this would lead to a marginal physics performance improvement as compared to the PID done with the TPC and TOF detectors (see Chap. 8 for a detailed discussion). Nevertheless, for completeness, Sec. 7.7 presents the studies that have been carried out on the potential PID performance that could be achieved with the new ITS by including the measurement of the charge signal amplitude. Finally, Sec. 7.8 presents the performance of a few alternative detector configurations.

### 7.1 Experimental conditions

- **Beam pipe:** The present beam pipe is 4.82 m long with a central part made of a straight beryllium tube of length 3.95 m, wall thickness 0.8 mm and outer radius 29.8 mm [34]. For the ALICE upgrade, the baseline scenario includes the installation of a new beam pipe with a wall thickness of 0.8 mm and an outer radius of 19.8 mm. See Sec. 5.4 for a detailed discussion.
- **Particle load:** The charged particle density in central Pb–Pb collisions at the top LHC energy determines the maximum density of particles in the different detector layers and consequently the occupancy per layer and in the individual channels. A relevant contribution to the hit density in a given layer comes from secondary particles, which are mostly produced in the interaction of other particles with the material of the beam pipe and of the Inner Layers.

By extrapolating the measured charged particle density in central Pb–Pb collisions at  $\sqrt{s_{NN}} = 2.76$  TeV using the  $s_{NN}^{0.15}$  scaling [35], one obtains  $dN_{ch}/d\eta \simeq 1970$  for central Pb–Pb collisions at  $\sqrt{s_{NN}} = 5.5$  TeV. Based on a Monte Carlo simulation for central Pb–Pb collisions, which uses the HIJING generator [36] tuned to such a charged particle multiplicity, the hit density of both primary and secondary charged particles has been estimated.

An additional contribution to the overall particle load comes from the electromagnetic interactions of the colliding ions, among which the dominant process in terms of cross section is the  $e^+e^-$  pair production (QED electrons) [37, 38]. The cross section of single pair production (about 220 kb) is about 98 % of the total cross section. The flux of these electrons through the detectors which are close to the beam pipe can be rather high [39]. The flux of QED electrons was estimated by means of a Monte Carlo generator [40] implemented in the ALICE software framework [41].

Table 1.2 summarises the expected maximum hit densities for primaries, secondaries and QED electrons. The latter contribution depends linearly on the detector integ-

ration time. The values reported in the table refer to the radial position of the layers of the new detector.

- **Detector acceptance:** This study focuses on the central rapidity region and therefore the detector has been assumed to have a barrel geometry. The ITS acceptance has been determined based on its matching with the current external barrel detectors, as discussed in Sec. 7.3.

## 7.2 Requirements

In order to achieve the physics goals that are discussed in [4] and further in the next chapter, it has been demonstrated in the ITS upgrade Conceptual Design Report (CDR) [12] that the upgraded ITS detector should:

- allow improvement of the resolution of the track impact parameter by a factor of three or better (at  $p_T = 1 \text{ GeV}/c$ ) with respect to the present ITS;
- have stand-alone tracking capability with a momentum resolution of a few percent up to  $20 \text{ GeV}/c$ , and coverage in transverse momentum as complete as possible, in particular down to very low momenta;
- have read-out rate capabilities to exploit the expected Pb–Pb interaction rate of up to  $50 \text{ kHz}$ .

## 7.3 Detector specifications

- **Acceptance:** The ITS acceptance has been determined based on its matching with the other external barrel detectors. The acceptance of the TPC, for tracks traversing its full radial extension, corresponds to  $|\eta| < 0.92$ . The TRD and TOF have the same acceptance as the TPC, while the EMCAL acceptance is smaller. The TPC can also efficiently reconstruct tracks traversing half of the TPC radial extension. In this case, the acceptance of the TPC extends to  $|\eta| < 1.22$ . So far, we have considered the acceptance for tracks emitted from the nominal interaction point. However, in the Pb–Pb interactions at  $\sqrt{s_{NN}} = 5.5 \text{ TeV}$ , the luminous region would spread around the nominal interaction point with a longitudinal Gaussian distribution with  $\sigma_z^{\text{lumi}} = 5.61 \text{ cm}$  [42]. The requirement of accepting all tracks within a given  $\eta$  range from this luminous region determines the longitudinal length of each ITS layer. In particular, we have assumed a longitudinal extension such that the new ITS would accept tracks with  $|\eta| < 1.22$  coming from the 90% most luminous region ( $|z_{vtx}| < 1.39\sigma_z^{\text{lumi}}$ ).
- **Radial positions of layers:** A high stand-alone tracking efficiency allows the reconstruction of low- $p_T$  particles that cannot be reconstructed by the TPC. This is particularly important for certain analyses as, for example, the low-mass di-electrons and the mesons  $D^{*+}$  and  $D_s^+$ . In addition, the stand-alone ITS tracking will reconstruct the high- $p_T$  tracks that cross the TPC in the dead area between sectors, or close to it, where the TPC tracking performance degrades. More in general, a high ITS stand-alone tracking efficiency provides more robustness to the global tracking for the reconstruction of events with high pileup in the TPC and large distortions of its electric field. As an example, the calibration and correction of the electric field distortions will be done by associating the TPC clusters to the tracks reconstructed in the ITS and extrapolated into the TPC volume. Finally, the availability of an ITS

track reconstruction, which is independent of other detectors and efficient in a large momentum range, allows the evaluation of the overall ALICE tracking efficiency, as well as other systematic effects in the reconstruction, in a data-driven way.

The performance of two ITS layouts, optimized respectively for ITS stand-alone tracking and the ITS-TPC combined tracking, have been compared using a Fast Estimation Tool (see Sec. 7.4). This tool does not account for the energy loss in the material and, therefore, overestimates the absolute TPC tracking efficiency, especially at low- $p_T$ . This study shows (see Fig. 7.1) that the two configurations have very similar performance. At low- $p_T$ , the layout optimized for combined ITS+TPC tracking, shows a slightly higher ITS+TPC matching efficiency and a slightly lower ITS stand-alone tracking efficiency. However, we expect that the layout optimized for ITS stand-alone tracking would yield a better absolute efficiency at low- $p_T$ , once the degradation of the TPC tracking due to the energy loss is taken into account. It should be noted that, as better detailed below, the two layouts differ only for the position of the middle layers. The optimal position of these layers depends also on the material thickness of the ITS outer layers. Therefore, the optimal position of the middle layers can be determined only once the material budget of the outer layers is well defined. The final optimisation will be done by performing a comparative study based on a detailed Monte Carlo simulation.

Based on the considerations discussed above, the optimisation of the radial positions of the layers was performed to achieve the following objectives:

- good tracking efficiency and  $p_T$  resolution for both tracking modes: ITS stand-alone and combined ITS+TPC;
- good pointing precision for track extrapolation towards the vertex;
- provide some redundancy against failures of detector modules.

In order to minimise the cluster-to-track association ambiguities, it is important to have the track extrapolation errors as small as possible at each layer. The optimisation procedure was performed minimising the cluster-to-track association ambiguities in the vicinity of the Kalman-smoothed estimate of the seed position. The latter is provided by two Kalman filters propagating in opposite directions (inward and outward). Since the extrapolation precision depends on the extrapolation distance and on the error of the track curvature, the detector is organised such to form groups of at least three consecutive layers, the minimum needed to define the curvature, with relatively small radial distance. The main difference between the layout optimised for ITS stand-alone tracking and the one optimised for combined ITS+TPC tracking is that, for the latter one, the track curvature is already defined by the TPC. Therefore, for the layout optimized for ITS+TPC combined tracking, the requirement of three consecutive outer layers with small radial distance is not relevant.

The pointing resolution is mainly determined by the two innermost measurements of the track position, with obvious advantage of having the first measurement as close as possible to the beam line. In order to guarantee that the pointing resolution of a track does not strongly deteriorate if one of the points close to the primary vertex is not attached to it, the first three layers (Inner Barrel) should have a radial distance, from each other, as small as possible. Such a layout appears to be quite optimal for both ITS stand-alone and ITS+TPC combined tracking modes. In order to maximise the  $p_T$  resolution, the distance between the innermost and outermost layers should be as large as possible. Moreover, also the matching with the TPC tracks profits from a small extrapolation distance between the TPC inner wall and the ITS outermost layer. Therefore, the two outer layers were positioned at the largest

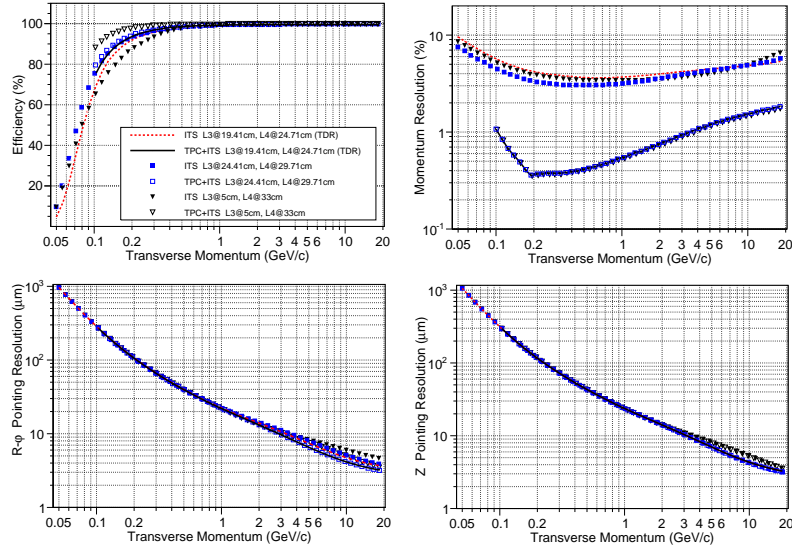


**Figure 7.1:** Performance of the ITS stand-alone and TPC+ITS combined reconstruction for different radial positions of the ITS layers.

possible radii that comply with the available space and integration constraints. Since the track curvature in the ITS+TPC combined tracking is already constrained in the inward propagation, it is advantageous to place an extra layer(s) as close as possible to the inner barrel, as a bridge between the high-occupancy region close to the primary vertex and the outer layers. The calculations done using the Fast Estimation Tool confirm that an extra layer at a radial distance of 5 cm from the beam line, would slightly improve the matching efficiency at low- $p_T$  (see Fig. 7.1, “L3@5 cm, L4@33 cm” setup). In these calculations, another layer was positioned at a radius of 33 cm in order to add redundancy to the measurements in the outer region, although its contribution to the overall reconstruction efficiency is negligible. The  $p_T$  resolution obtained with the TPC–ITS tracking mode is almost insensitive to the position of the intermediate layers. The ITS stand-alone tracking requires a good curvature estimate at large radii. This requires shifting the middle layers close to the outer layers (see Fig. 7.1, “L3@24.41 cm, L4@29.71 cm” setup).

- **Material budget:** Based on the most recent developments in pixel detector technologies, a substantial reduction of the material budget can be achieved by reducing the thickness of the silicon pixel sensors and the material budget of the services (mechanical support, power distribution, cooling system, read-out system). In the simulations described in Sec. 7.4, an effective material budget of 0.3% and 0.8% of the radiation length was assumed for the three Inner and the four Outer Layers respectively.
- **Detector segmentation:** The segmentation of the detector determines the intrinsic spatial resolution of the reconstructed track points. A small segmentation is also important to keep the occupancy at a low value. An excellent resolution of the first layer is fundamental for the resolution of the impact parameter at high

particle momenta where the effect of the multiple scattering becomes negligible. For the Outer Layers, a good resolution is also important to improve the momentum resolution and the tracking efficiency in the ITS stand-alone mode.

Detailed Monte Carlo simulations (see Sec. 7.4.2) were based on a pixel size of  $20\ \mu\text{m} \times 20\ \mu\text{m}$ , leading to a spatial resolution of  $4\ \mu\text{m}$  in both  $r\varphi$  and  $z$  directions. The expected performance with the segmentation quoted in Chap. 2 (i.e. resolutions of  $5\ \mu\text{m}$ ,  $6\ \mu\text{m}$  and  $9\ \mu\text{m}$ ) is only slightly degraded, as discussed in Sec. 7.8.

- **Timing and read-out rate:** The interaction rates considered in this section are 200 kHz for pp and 50 kHz for Pb–Pb. These values may imply a significant pile-up rate in the detector, depending on the integration time, which has an impact on event reconstruction and analysis.

If the total occupancy from triggered and pile-up interactions significantly exceeds the occupancy of a central Pb–Pb collision, the reconstruction efficiency drops due to the ambiguity of the cluster to track association. With a 50 kHz interaction rate and  $20\ \mu\text{s}$  ( $30\ \mu\text{s}$ ) integration time window, on average about one (two) extra Pb–Pb collision will be read-out on top of the triggered event. In about 10 % of the triggers, five or more extra collisions will be piled up assuming an integration time window of  $30\ \mu\text{s}$ . To prevent significant losses of the reconstruction efficiency, especially at low  $p_T$ , the integration time in the highest occupancy layers should not exceed about  $45\ \mu\text{s}$ . A similar time resolution is desirable also for the Outer Layers in order to facilitate the cluster matching throughout the whole detector.

In pp collisions, where a large pile-up is expected, the issue is the correct assignment of each track to its own interaction vertex. For primary tracks, assuming the vertexing and tracking capabilities of the upgraded ITS, the pile-up vertices should be separated from the triggered one by at least 1 mm in order to correctly assign the tracks to the triggered vertex. For the heavy flavour decay tracks, about 1 mm isolation should be enough for the short lived  $\Lambda_c$ , while for the B-mesons an isolation up to about 1 cm may be required. For an interaction rate of 200 kHz, which is the nominal value assumed for the pp run, and a  $30\ \mu\text{s}$  integration time, about 7 % (40 %) of the triggered vertices will be separated by less than 1 mm (1 cm)<sup>1</sup>. The pile up ambiguities can be further reduced if at least one point for each track carries a precise time-stamp provided by other detectors (the TPC and/or TOF).

## 7.4 Simulation tools and models

### 7.4.1 Fast estimation tools

The tracking performance was initially studied using an analytical method, referred to as the “Fast Estimation Tool” (FET) which was further developed into a Fast Monte Carlo Tool (FMCT). The FET and the FMCT provide accurate determination of the tracking resolution (both for the spatial and the momentum components) as a function of the detector configuration and a good estimate of the tracking efficiency. They have been used to optimise the layout of the detector in terms of number of layers, their radial positions, material budget, and detector resolution as it was discussed in the CDR [12]. The results of the FET and FMCT have been confirmed (within about 5 % accuracy) by the study with a Monte Carlo (MC) based on transport code and a detailed description of the geometry, as discussed later.

<sup>1</sup>By imposing the 1 cm isolation cut, an overall gain of about a factor of 3.5 is obtained in terms of number of triggered events that can be analysed with respect to the case of one interaction per read-out cycle [12].



The FET is based on a code originally developed by the STAR Heavy Flavour Tracker (HFT) collaboration [6]. It allows a simplified description of the detector layout and adopts a tracking method as described in [43]. The original STAR HFT code was extended and adapted in various ways, e.g. to describe also the ITS upgrade stand-alone tracking capabilities. The tracking code itself was replaced with the Kalman filter technique [43, 44], which is implemented in the ALICE software framework [41]. A detailed description of the method and its extensions can be found in [45]. The intrinsic (or cluster) resolution of a layer and the traversed material, which both depend on the inclination angle of the charged particle with respect to the layer normal, are taken into account in the method by calculating the track-parameter covariance matrix elements at the various stages of the track reconstruction.

The evolution of FET method, called the Fast Monte Carlo Tool (FMCT), allows the estimation of the tracking performance from the reconstruction of a probing particle embedded in the background as expected from collisions. In contrast to the FET, the FMCT is able to disentangle the performance of a detector layout from the efficiency of specific track-finding algorithms. This is done by accounting for the competition between track candidates of different length and quality, and represents an approach much closer to that of the full MC-based simulation and reconstruction.

### 7.4.2 Detailed Monte Carlo simulations

#### Pixel response simulation input

Detailed Monte Carlo simulations, beyond the physics processes available in the GEANT transport code, require knowledge of the detector response. In our case, the simulation relies on the Pixel Chip response. While the currently pursued pixel design alternatives differ in the front-end circuit and read-out architecture (see Sec. 2.5), common characteristics can be extracted from test beam measurements as input for simulation studies:

- the average pixel noise distribution;
- the noisy pixel rate;
- and the charge spread function.

The average pixel noise distribution, representing the analogue noise charge in the pixels, can be described by a Gaussian or Landau distribution depending on the pixel chip design. The fake pixel rate describes the number of fake pixels fired, after the pixel charge digitisation. The charge spread function describes the fraction of the cluster charge measured in a given pixel of the cluster (at the diode position) at a given distance from the impinging track. Since the charge spread function can have a complex shape, instead of applying different fit functions for different pixel chip prototypes, the measured charge spread distribution was directly fed into the simulation as a map.

These three input elements were extracted from test beam data for several kinds of pixel designs, operating temperatures and irradiation levels. For the performance results presented in this chapter, we used square  $20\,\mu\text{m} \times 20\,\mu\text{m}$  pixels, corresponding to the MIMOSA-32Ter P26 prototype, non-irradiated and operated at  $30\,^{\circ}\text{C}$ .

#### Simulation parameters and algorithm

The full list of simulation parameters is presented in Tab. 7.1. The first step of the pixel response simulation starts with the generated list of GEANT3 [46] hits in the sensitive volume ( $18\,\mu\text{m}$  thick Si). To be accepted, the hits must fall within the read-out window either in a triggered read-out mode or in the rolling-shutter read-out mode. The current

**Table 7.1:** Pixel response parameters used for the detailed Monte Carlo simulations.

Simulation parameter name	Parameter value
Charge spread in row direction	2 pixels
Charge spread in column direction	2 pixels
Minimum number of charge injection steps	10
Global charge scale	1.037
Threshold over noise cut	5
Minimum number of electrons to add	1
Average pixel noise	17.53 electrons
Average pixel noise sigma	2.93 electrons

simulation is using rolling-shutter read-out (details can be found in Chap. 2), but the framework is capable of simulating the triggered data-taking mode as well.

To ensure proper response for inclined tracks, the charge deposition in the sensitive volume is divided into  $n$  charge injection points along the particle trajectory. The charge of the hit (in electrons) is calculated based on the conversion factor of 3.6 eV per electron-hole pair in Si from the hit energy deposit. Each charge injection point has a charge of  $Q_{hit}^{scaled}/n$ , where the  $Q_{hit}^{scaled}$  is the total charge generated by the hit multiplied by the *Global charge scale* factor to account for the difference between the pure GEANT3 response and the test beam measurement. The charge in a given injection step does not depend on the depth of the hit in the epitaxial layer. The number of charge injection points  $n$  is calculated on a hit-by-hit basis, depending on the pixel dimensions and the number of pixels traversed, to ensure that each pixel along the particle trajectory in the sensitive volume has at least one charge injection point. The automatic injection point number calculation is overwritten with the simulation parameter *Minimum number of charge injection steps* in case the calculated number of injection points is smaller than the *Minimum number of charge injection steps* input parameter.

The total charge of the given charge injection step  $Q_{hit}^{scaled}/n$  is distributed around the pixel in which the charge injection point is located, based on the charged spread function and the distance between the charge injection point and the pixel diode location. The simulation parameters *Charge spread in row direction* and *Charge spread in column direction* control the extent of the charge spread. Currently, both parameters are set to an optimal value of two pixels, allowing charge spread up to the second crown around the seed pixel, translating to a maximum distance of  $\pm 40 \mu\text{m}$ . Pixels with at least one electron are kept, controlled by the *Minimum number of electrons to add* input parameter, and added to the corresponding list. The procedure is repeated for all charge injection points. At the end of the procedure, each pixel contains a sum of charges generated by one or more charged particles.

In the second step of pixel response simulation, the noise component of the pixel charge is generated. The noise can come from constantly noisy pixels or random pixels. The list of constantly noisy pixels can be retrieved from the data base with the corresponding noise charge. The random pixel noise is calculated based on the average pixel noise input distribution given by the *Average pixel noise* and the *Average pixel noise sigma* input parameters. First, the probability is calculated to achieve a noise larger than digitisation threshold. The digitisation threshold ( $\sim 100$  electrons) is calculated as the product of the *Threshold over noise cut* input parameter and the *Average pixel noise*. In the second step-based on the calculated probability, the noise charge is calculated randomly above the digitisation threshold.

**Table 7.2:** *Global charge scale* factors tuned for MIMOSA-32Ter P26 pixels at 30 °C as implemented in the ALICE software framework. The medium load refers to irradiation level: 300 krad and  $3 \times 10^{12}$  1 MeV  $n_{eq}/cm^2$  while the heavy load refers to irradiation level: 1 Mrad and  $1 \times 10^{13}$  1 MeV  $n_{eq}/cm^2$ .

Pixel name, irradiation level, scale	Threshold over noise cut					
	5	6	7	8	9	10
P26 reference sensor, averaged scale	1.037	1.055	1.084	1.099	1.126	1.146
P26 reference sensor, cluster multiplicity scale	0.970	1.001	1.036	1.138	1.108	1.140
P26 reference sensor, cluster charge scale	1.019	1.110	1.132	1.059	1.144	1.151
P26 sensor, medium load, averaged scale	0.446	0.452	0.406	0.457	0.488	0.509
P26 sensor, medium load, cluster multiplicity scale	0.538	0.568	0.571	0.607	0.637	0.680
P26 sensor, medium load, cluster charge scale	0.355	0.336	0.241	0.307	0.340	0.139
P26 sensor, heavy load, averaged scale	0.407	0.418	0.411	0.406	0.356	0.479
P26 sensor, heavy load, cluster multiplicity scale	0.484	0.513	0.537	0.557	0.606	0.645
P26 sensor, heavy load, cluster charge scale	0.330	0.324	0.285	0.256	0.106	0.313

In the third and last step of the pixel response simulation, the charge contributions from charged particle(s) and noise are summed up for each pixel and compared to the digitisation threshold (unless the pixel is marked as a dead pixel in the database and removed from the list of active pixels). If the total pixel charge is above the digitisation threshold, a Digit is created for the given pixel. The list of Digits is then passed to the reconstruction for clusterisation.

### Results of the pixel response simulations

To achieve a similar setup as in the test beam measurement, we simulated a single negative pion per event with  $p = 120$  GeV/ $c$  at azimuthal angle  $\varphi = 90^\circ$  and at mid-rapidity  $\eta = 0$ . The magnetic field in these simulations was switched off.

To better describe the average cluster size and the average cluster charge obtained from test beam measurements, a tuning of the *Global charge scale* simulation parameter as a function of the *Threshold over noise cut* was performed. Other input parameters listed in Tab. 7.1 were kept fixed.

Table 7.2 shows the results of the simulation tuning for the MIMOSA-32Ter P26 pixel and the *Global charge scale* factors as a function of the *Threshold over noise cut* and the irradiation load. The scaling factors derived from the cluster multiplicity and cluster charge are close for reference sensors, but with increasing *Threshold over noise cut* and irradiation levels, the scale values depart from each other.

To compare simulated data and test beam measurements, we introduced the definition of a *discriminated cluster*. A discriminated test beam cluster consists of an ensemble of maximum 25 pixels (up to the second crown around the seed pixel), where each pixel is above the digitisation threshold (*Threshold over noise cut*  $\times$  *Average pixel noise*). A discriminated simulated cluster consists of an ensemble of clusters created by the injected particle or by the injected particle and one or more secondary particles, with the clusters formed through the standard clusterisation process of Digits (pixels above the digitisation threshold calculated in the third pixel simulation response step).

Compared with the real data, the simulated cluster multiplicity distribution is more peaked, underestimating the number of clusters with cluster multiplicity 1, and tending to overestimate the trend for larger cluster multiplicities. However, the simulation is able to reproduce the measured average cluster multiplicity. Further improvements in the

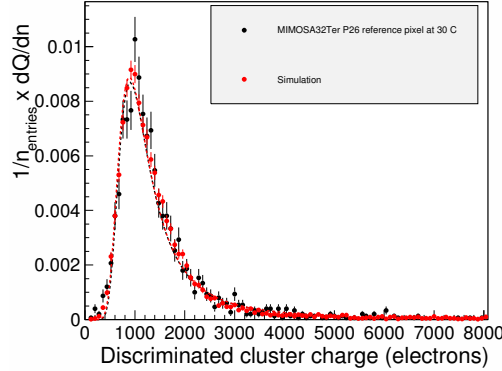


**Figure 7.2:** Comparison of cluster charge from tuned simulation and test beam measurement for MIMOSA-32Ter P26 reference pixel at 30 °C.

response simulation would require a detailed study of the charge spread function with high real data statistics.

The cluster charge distribution is already well reproduced by these simulations. Figure 7.2 shows the comparison of the tuned simulated and test beam data for MIMOSA-32Ter P26 reference pixel at 30 °C.

It should be noted that the current parametrisation and tuning are not appropriate for highly ionizing charged particles and charged particles at very low momentum.

## 7.5 Reconstruction tools

### 7.5.1 Cluster finding

This procedure groups adjacent fired pixels into a single cluster. The definition of “adjacent pixels” currently has two definitions of which either can be selected:

- only pixels with common sides are treated as belonging to the same cluster (default);
- clusters with pixels having either a common side or a corner are allowed.

For each cluster, space-point coordinates are then calculated and passed to the subsequent track-finding procedure. The cluster-finding is performed for each sensor independently from others and can, in principle, be executed in parallel.

The algorithm assumes that the information about the fired pixels is ordered in read-out cycle index, and in row and column numbers. This allows for performing the clusterisation without storing the full matrix of the whole sensor in memory, keeping instead only transient structures corresponding to the candidates for unfinished clusters. On arrival of new fired pixel data (row, column and read-out cycle indices) the algorithm checks if it matches to the “adjacent” definition for cluster candidates left unfinished from the processing of current and previous rows. If this turns out to be the case, the corresponding cluster candidate is updated with the new pixel information. Otherwise, the unfinished cluster is considered as a new cluster candidate.

Whenever a new row is detected (or when the data from the next sensor arrives), all cluster candidates that were not updated during the processing of the previous row (or if

the latter did not have any fired pixel) are converted to final clusters and stored. All the associated transient information is then cleared. The conversion to final cluster consists of calculating the centre of gravity of its constituent pixels, accounting for the possible shift of the collecting diode from the geometrical centre of the pixels.

The cluster coordinates are stored in the local frame of a sensor. This frame has its origin in the geometrical centre of a sensor, with the  $x$  and  $z$  axes going along the sensor sides in the direction of increasing row and column numbers, respectively. Using the transformation matrix associated with each sensor, these coordinates can be converted to the global ALICE frame or to the tracking frame of the sensor. The tracking frame is obtained from the global one by rotating around the  $z$  (beam axis) in such a way that the  $x$  axis becomes normal to the sensor plane.

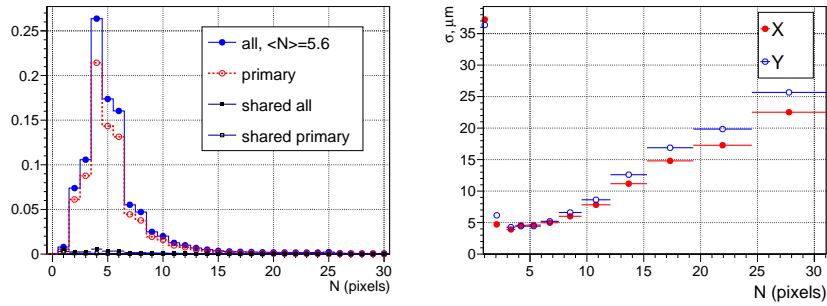


**Figure 7.3:** Cluster size distributions for all the charged particles and for primary charged particles (empty red circles). The term *shared* denotes hits that contribute to more than one cluster (left). Resolution on  $x$  (red full circles) and  $z$  (blue empty circles) directions as a function of the cluster size (right).

At the moment, no attempt is made to unfold the large clusters from overlapping hits of different particles, since the pixel occupancy for the innermost layer in Pb–Pb collision is expected to be less than one per mill, even taking into account the contribution of QED electrons. Figure 7.3 shows the frequency distribution of the cluster size and the space-point resolution for the sensors of the baseline scenario.

### 7.5.2 Track finding

Historically, ALICE performs two kinds of track-finding in the ITS. First, the tracks found in the TPC are used as seeds to find their prolongation in the ITS using a Kalman filter approach [43, 44]. Since the acceptance in the TPC drops sharply below  $p_T \approx 100$  MeV/ $c$ , this step is followed by the stand-alone ITS tracking. In this case, the ITS clusters not attached to TPC+ITS matched tracks are associated with tracks started from helical seeds constructed out of the primary vertex and two points taken from the two innermost pixel layers of the ITS.

When reconstructing pp collisions, the stand-alone ITS tracking can also be run over all the existing clusters, with the results used mostly for studies of systematic effects in the reconstruction.

It is not yet clear to which extent this approach can be used for data reconstruction in Run3, since the track reconstruction in the upgraded TPC is still in development. In any case, the stand-alone track finding in the ITS is necessary. As a good candidate for this stand-alone tracking, we are evaluating an approach based on the Cellular Automaton (see

below) fast track-finding algorithm which is already deployed in the High Level Trigger TPC reconstruction.

#### Track finding by prolongation from the TPC

A track seed is created for every track found in the TPC and is extrapolated to the Outer Layers of the ITS. Then, a few (currently two) iterations are performed, with the aim to find first the longest tracks traversing the full ITS, and then to reconstruct shorter ones originating from the decays in the detector. Each of these iterations uses only those TPC tracks that do not yet have any validated ITS prolongation. Only not previously attached clusters are associated with these tracks.

Each iteration consists of the following steps:

- A seed made out of a TPC track extrapolated to the ITS Outer Layer is considered as a root of a prolongation-hypothesis tree.
- All the clusters in the proximity of seed extrapolation points are subjected to a track-to-cluster  $\chi^2_{cl}$  cut, and those passing it are used for the Kalman filter update of a new branch in the hypothesis tree. The  $\chi^2_{cl}$  is used to increment the global  $\chi^2$  of the hypothesis.
- In order to account for possible detection inefficiencies, seeds without cluster attachments on layers can also be used for the creation of new hypothesis branches. The  $\chi^2$  of such branches is incremented by a layer-dependent penalty value, giving a preference to longer tracks.
- The created track-hypothesis branches are sorted in increasing order of the total  $\chi^2$ . Then, a predefined number (tuned using dedicated simulations) of best branches are in turn considered as seeds for track prolongations to the next layer.
- Once the innermost layer is reached, the hypotheses are subjected to backward Kalman filter, using for the clusters already attached to the branch being followed and propagating back to the original TPC track extrapolation at the outermost layer. A cut on the matching  $\chi^2$  between the TPC track parameters and those of the ITS stand-alone fit eliminates a large fraction of prolongations containing at least one ITS cluster not produced by the physical particle corresponding to the original TPC track (so called “fake” prolongations).
- For each TPC track, the prolongation hypotheses with best total  $\chi^2$  are considered as preliminary winners and the ITS clusters sharing among them are analysed. If the winner hypotheses of two TPC track prolongations share the same cluster, the one with the largest value of  $\chi^2/p_T$  is discarded and the next hypotheses for this track are declared to be winners. The procedure continues until no cluster sharing remains between the winner hypotheses. At this stage, all the winner hypotheses are validated and their clusters are flagged as “used”, to prevent their usage in following iterations.

In order to prevent extensive growth of the hypothesis tree and to save CPU time, the seeds that cannot fulfil specific iteration-dependent conditions are abandoned as soon as possible. Apart from the cuts on the total and track-to-cluster  $\chi^2$  values, these conditions include certain hit contribution patterns. In particular, the tracks sought in the first iteration must contain hits at least on five (out of seven) layers and have contributions from at least two of three Inner Layers, as well as at least one contribution from pairs of Middle and Outer Layers. The second iteration, intended to find tracks from strange

particle decays, considers only the external four layers, requiring each of them to contribute to the track.

### Stand-alone ITS track finding

The ITS stand-alone tracking aims to reconstruct tracks by using the information provided by the ITS only. Like in the case of the previously described combined TPC+ITS method, the final track parameters are estimated using the Kalman filter. However, the algorithm used for pattern recognition is different. The algorithm that is currently under study is based on a Cellular Automaton (CA) [47, 48]. This algorithm does not rely on any particular track model and can operate on highly optimised data structures. It can also be efficiently implemented for parallel computing architectures.

The CA method creates short track segments (tracklets) in neighbouring detector layers and then links them into tracks. First, the clusters (hits) in the detector are sorted according to their radial position, and the tracklets are generated in groups with the same outermost hit. Every hit has two pointers: to the first and the last tracklets of its group. Each tracklet has a counter that assigns its possible position on a track. Next, the tracklets are extrapolated by one layer in the direction of the primary vertex. At this step, a new portion of tracklets is generated, one or two layers closer to the interaction point. Using the already stored pointers, the algorithm finds neighbouring tracklets by selecting pairs of tracklets sharing a common hit. When a pair of neighbours is found, the counter of a current tracklet is incremented with respect to the neighbour with the largest counter. Once these steps are done for all layers, the algorithm builds track candidates out of the tracklets.

The track candidates are then sorted according to the number of assigned hits. A Kalman-filter track fitting starts from the candidates having the largest number of assigned hits. For every set of candidates with the same overall number of hits and a certain number of shared hits, only the candidate with the best  $\chi^2$  value is retained. The hits belonging to this candidate are then flagged as used. The program proceeds with the next track candidate, checks if the number of used hits is less than a certain number (depending on the track density), flags the assigned hits as used and stores or deletes this candidate, depending on whether the selection criteria are met or not. The whole procedure is repeated until the shortest track candidates become considered.

Optionally, in case of a significant detector sensor inefficiency, the program can merge short tracks with similar parameters (clones) into longer ones. There is also a possibility to reduce the number of reconstructed false tracks by applying additional quality cuts to the (mostly short) track candidates.

### 7.5.3 Vertex finding and track-to-vertex association

The reconstruction of the interaction vertex position is one of the key tasks that the ITS has to fulfil. This is currently done with the present ITS at three different levels with different purposes: at run time, the vertex position is reconstructed for a fraction of the collected events, without performing a full reconstruction, using only the information of the two innermost layers of the ITS. This first measurement, averaging over the collected events, is recorded on the offline conditions database and is used to monitor the luminous region during the data taking and, subsequently, as an optional constraint for the vertex position in the transverse plane. The same fast vertex reconstruction is carried out offline event-by-event to have a seed of the tracking procedure in the TPC. Finally, a precise vertex measurement, to be used for the data analysis, is obtained from the tracks reconstructed in the barrel.

This approach will be partly modified with the upgraded ITS, since, given the significant pile-up rate expected, it will be necessary to reconstruct the coordinates of all the interactions occurring in the same read-out window. For the fast reconstruction, an algorithm based on the information of the three innermost layers, instead of two, is being developed with the purpose of reducing the CPU time with respect to the present implementation. This approach is based on the local reconstruction of the three innermost layers: for each cluster of the first layer a matching cluster on the second layer is searched under the hypothesis of a high momentum particle, little affected by the magnetic field. The main matching criterion is the azimuthal angle of the two clusters. The tracklet selection is performed in a multi-step way with azimuthal cuts of increasing tightness. The availability of a third layer located at approximately 4 cm (see Tab. 1.1) from the beam axis allows for a tracklet validation in presence of the high combinatorial background expected in high rate Pb–Pb collisions. In the present ITS, a candidate vertex is accepted when at least three tracklets are associated to it and multiple interactions can be efficiently tagged, if they are spaced along the beam axis by more than 8 mm. Given that in the upgraded setup, the distance of the layers from the beam axis is lower and three points per tracklet are used instead of two, the present performance has to be regarded as a lower limit.

The vertex reconstruction with tracklets relies on a straight-line approximation for particle tracks. Since the tracks found in the procedure described in Sec. 7.5.2 are registered in the Event Summary Data (ESD) in the same format as for the current detector, the data analysed for the preparation of this document profits from the standard algorithm for the interaction vertexing finding. It is based on the iterative vertex finding and fitting [49] using Tukey bi-square weights for the outliers suppression.

A scaling factor applied to the uncertainties of tracks extrapolated to the nominal beam axis is gradually inflated until at least two tracks with non-zero Tukey weights are found to create an initial vertex guess (its exact position has little importance). A fit like that used in [50], but accounting for these weights, is performed, with the fitted vertex moving to its true position as the scaling factor decreases. Once the distance between successively fitted vertices is below a certain threshold, the iterations stop.

If at this stage the scaling factor is not decreased to a value close to 1 or the maximum number iterations is reached, the vertex candidate is abandoned, and the search is done with a different seeding position. Otherwise, a final fit with weighted tracks is done, the tracks with non-zero weights are removed from the pool, the vertex is validated, and a search for the next vertex is performed.

The expected vertex resolution for central Pb–Pb events is of the order of few  $\mu\text{m}$  in both transverse and longitudinal directions.

## 7.6 Track and vertex reconstruction performance

The assessment of the performance of the tracking and vertexing procedures was done by means of a Full Monte Carlo simulation, using the detector response described in Sec. 7.4.2. The detailed description of the Inner Barrel used for this simulation corresponded to the design discussed in Sec. 4.1.1. At the same time, since the exact design of the Outer Barrel was not yet completely defined at the moment the simulation started, these layers were coded in the Monte Carlo geometry as assembled out of simplified Staves made of silicon with an effective thickness of 0.8% of  $X_0$ , as estimated in Sec. 4.1.2.

Some properties have been evaluated with the Fast Estimation Tool and are shown here for comparison. The presented results have been obtained with a magnetic field of 0.5 T.

- **Primary vertex reconstruction:** The performance of the primary vertex reconstruction is shown in Fig. 7.4 with a full simulation of Pb–Pb collisions. The vertex



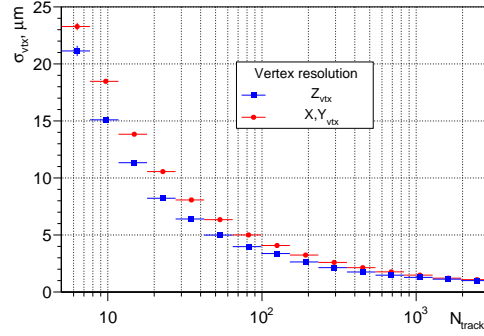


**Figure 7.4:** Resolution on the primary vertex reconstruction as a function of the number of tracks used to determine the primary collision coordinates.

determination is done with tracks reconstructed in the ALICE barrel as described in Sec. 7.5.3. The obtained precision of the position determination is, for low multiplicity Pb–Pb events, less than  $25\,\mu\text{m}$  and goes down to  $2\text{--}3\,\mu\text{m}$  at high multiplicity.

- **Tracking efficiency:** Figure 7.5 shows the track-matching efficiency between the TPC and ITS in the combined tracking mode, assuming the performance of the present TPC, and different levels of event pileup. A track was considered as matched if at least five (out of seven) clusters were correctly attached in the ITS, with at least two of these clusters being attached in the Inner Barrel. If at least one of the attached ITS clusters did not in fact belong to this track, such a track was considered as “fake”. Only well reconstructed (having less than 10 % of wrongly assigned clusters, and not going too close to the TPC sector boundaries) TPC tracks were selected for this analysis. Tuning of the tracking cuts was done to minimise the fake-track rate and to achieve a high efficiency for tracks with  $p_T < 5\,\text{GeV}/c$  (the bulk). The reason for the visible deterioration of the efficiency at  $p_T < 1\,\text{GeV}/c$  is the increasing probability to pick up a wrong cluster in the ITS.

The most impressive improvement in tracking efficiency compared to the current performance is expected for tracks with  $p_T < 0.5\,\text{GeV}/c$  and below, with the upgraded ITS run in the stand-alone mode, as was demonstrated with the fast simulation studies done in the ITS upgrade CDR [12], and also shown in Fig. 7.11 and 7.12. The exact amount of the gain in the tracking performance at very low  $p_T$  is to be evaluated by the detailed Monte Carlo simulation and full realistic reconstruction.

- **Impact-parameter resolution:** An important measure of the achieved tracking precision is the track impact-parameter resolution. It is the impact-parameter resolution that defines the capability of a vertex detector to separate secondary vertices of heavy-flavour decays from the main interaction vertex. This resolution is defined as the dispersion of the distribution of the Distance of Closest Approach (DCA) between reconstructed (primary) tracks and the main collision vertex.

A comparison of this resolution between the present and upgraded ITS is shown in Fig. 7.6. At  $p_T$  below  $1\,\text{GeV}/c$ , it is a factor of about three better than that for the present ITS. At higher momenta, the gain in resolution is even higher, reaching a factor of about five at  $p_T$  above  $10\,\text{GeV}/c$ . Since the impact-parameter resolution depends mainly on the radial position, thickness, and granularity of the innermost

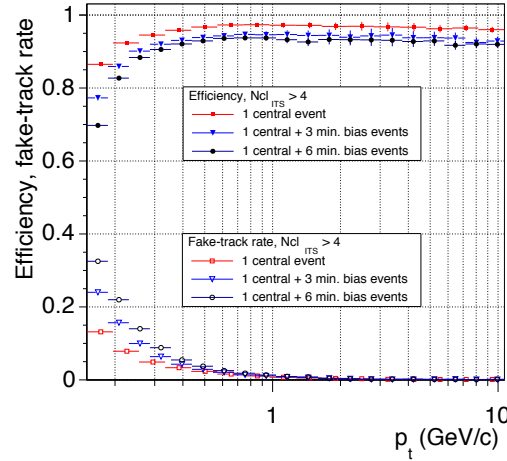


**Figure 7.5:** Track-matching efficiency between the TPC and upgraded ITS for different levels of event pileup.

layer(s), it is essentially identical for both combined TPC+ITS and ITS stand-alone tracking modes.

As can also be seen in Fig. 7.6, the results obtained with the Fast Monte Carlo Tool and with the detailed simulations agree quite well.

- **Momentum resolution:** Figure 7.7 shows the momentum resolution obtained in the combined TPC+ITS and ITS stand-alone tracking modes. For the stand-alone tracking mode, the upgraded ITS yields a dramatic improvement. The  $p_T$  resolution in the stand-alone mode benefits significantly from the intrinsic resolution of the Outer Layers and the overall low material budget of the upgraded ITS.

In the ITS+TPC combined tracking mode, at  $p_T$  below 0.5 GeV/c, both upgraded ITS configurations would improve the resolution with respect to the current performance due to the reduction of the material budget of the innermost layers.

We once again note that the predictions of the Fast Monte Carlo Tool are confirmed by the results of the detailed simulations presented here (see Fig. 7.7).

## 7.7 Particle identification

In this section, we present, for completeness, the studies that have been carried out on the potential PID performance that could be achieved with the new ITS by including the measurement of the specific energy loss ( $dE/dx$ ) of the charged particles in the Outer Barrel. With the adoption of a digital read-out, as in the present design, the ITS may still be used to tag heavily ionizing particles like light nuclei thanks to an analysis of the size of the clusters associated to these particles: the effectiveness of this approach will be also addressed in this section. The impact of the PID capabilities on the physics reach of the ITS will be discussed in Chap. 8.

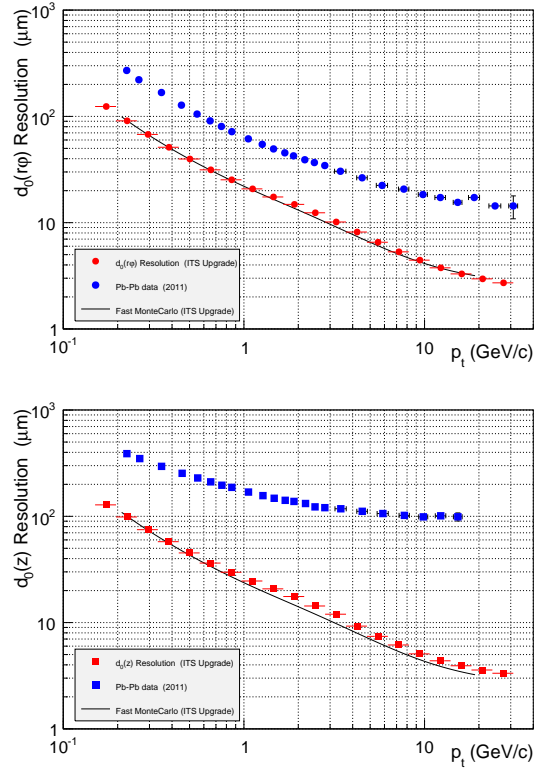


**Figure 7.6:** Impact-parameter resolution for primary charged pions as a function of the transverse momentum for the current ITS and the upgraded ITS in the transverse plane (upper panel) and in the longitudinal direction (lower panel).

### 7.7.1 Simulation tool and truncated mean method

The approach considered to study the PID capabilities of the upgraded ITS detector is the same used for the PID studies presented in the CDR [12]: the particle identification is based on a specific ionisation estimate done with a *Truncated-Mean* of the  $dE/dx$  measurements on the ITS layers. This method was developed for the current ITS detector [51] and has been adapted to the detector configuration under study in which a seven-layer layout has been assumed: each layer is equipped with monolithic pixels and an analogue read-out for the four Outer Layers has been considered.

To account for the thin detectors assumed for the upgrade scenario, a dedicated Monte Carlo simulation has been performed to study the energy deposition per unit length for  $20 \mu\text{m}$  and  $40 \mu\text{m}$  thick detectors. The diffusion, charge-collecting inefficiency, noise and digitisation of the detector response have been introduced in the simulation considering an 8-bit ADC in order to have a direct comparison of the result obtained for the CDR [12] with an ITS configuration with seven layers of  $15 \mu\text{m}$ .

This approach consists of computing a truncated mean of the charge values in the various

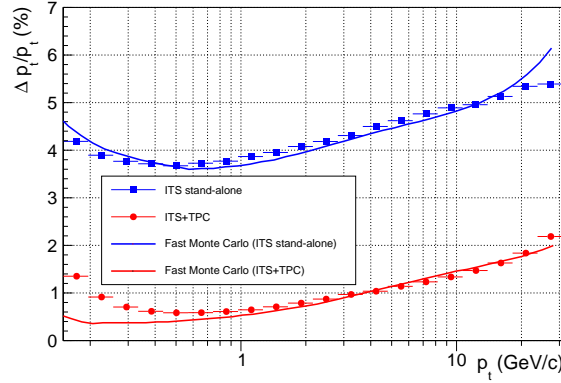


**Figure 7.7:** Transverse momentum resolution as a function of  $p_T$  for primary charged pions for the upgraded ITS. The results for the ITS stand-alone and ITS-TPC combined tracking mode are shown.

layers crossed by the track. A single value of the  $dE/dx$ , obtained after normalising to the length of the track segment in the silicon volume, is assigned to each track. The truncated mean algorithm used in this analysis consists of computing the arithmetic mean of the  $n$  lowest  $dE/dx$  values among the ones of the clusters attached to the track. The number  $n$  of used  $dE/dx$  values is set to a fixed fraction  $f$  of the total number of clusters attached to the track. By default, the value  $f = 1/2$  is used. The calibration of the PID algorithm is based on building the distribution of the  $dE/dx$  for tracks of each hadron species in a given momentum interval. These distributions are fitted with Gaussian functions. The distribution of the mean values of the Gaussian fits as a function of their momentum is then fitted to a parametrised formula (taken from the PHOBOS experiment [52]):

$$dE/dx = \frac{E_0}{\beta^2} (b + 2 \cdot \ln \gamma - \beta^2) \quad (7.1)$$

where  $E_0$  and  $b$  are the free parameters. The fitted function, for a given particle type  $i$ , will be indicated with  $M_G[i]$ . The sigma of the Gaussian fits  $\sigma_G[i]$ , corresponding to the resolution, is found to be independent of the track momentum. With this method, the particle identity of a reconstructed track is assigned to the species  $i$  for which the quantity  $|dE/dx - M_G[i]| / \sigma_G[i]$  is lowest.

### 7.7.2 PID efficiency and contamination

The results obtained for three detector configurations in terms of number and thickness of layers providing PID information will be shown. The first one, representing the current ITS configuration, was presented in the CDR [12]:

- **Four layers 300  $\mu\text{m}$  thick each:** The performance of the present ITS in pp collisions was used to extract the specific energy loss information. A noise of 700 electrons and a charge collection efficiency of 95% were assumed in the simulation, by means of the fast Monte Carlo tool, as well as an 11-bit ADC with a dynamic range of 20 in units of minimum ionisation.

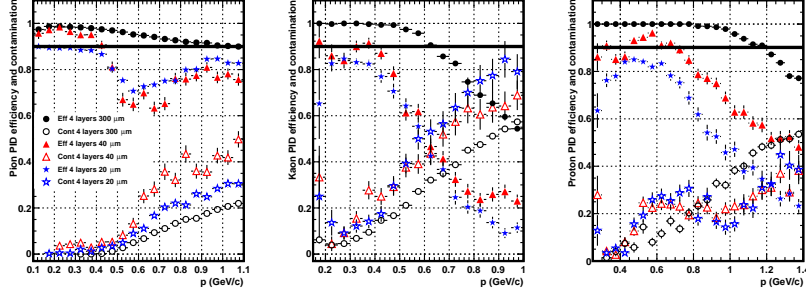


**Figure 7.8:** PID efficiency (closed symbols) and contamination (open symbols) as a function of the particle momentum assuming the relative abundances of  $\pi^+$ ,  $K^+$  and  $p$  as obtained from preliminary Pb–Pb data at  $\sqrt{s_{NN}} = 2.76$  GeV for different configurations: four layers 300  $\mu\text{m}$  thick (black circles), four Outer Layers 40  $\mu\text{m}$  thick of pixel detectors (red triangles) and four layers 20  $\mu\text{m}$  thick silicon detectors (blue stars). Pions, kaons, and protons are shown in the left, middle and right panels respectively. In all plots, a line corresponding to a PID efficiency of 90 % is drawn as a reference.

- **Four Outer Layers 20  $\mu\text{m}$  thick each:** The size of the pixel is assumed to be 20  $\mu\text{m} \times 20 \mu\text{m}$  and an analogue read-out has been considered using an 8-bit ADC.
- **Four Outer Layers 40  $\mu\text{m}$  thick each:** As for the 20  $\mu\text{m}$  case, the size of the pixel is assumed to be 20  $\mu\text{m} \times 20 \mu\text{m}$  and an analogue read-out has been considered using an 8-bit ADC

Events with pions, kaons and protons with a flat transverse momentum in the 0 GeV/ $c$  to 1.5 GeV/ $c$  range have been generated using the abundances extracted from the 2.76 TeV Pb–Pb data [53]. The efficiency  $\epsilon(i;p)$  and the contamination  $K(i;p)$  for the particle type  $i$  (pions, kaons and protons) in each momentum bin  $[p, p + \Delta p]$  are defined as follows:

$$\epsilon(i;p) = \frac{N_{\text{Good}}(i;p)}{N_{\text{True}}(i;p)} \quad (7.2)$$

$$K(i;p) = \frac{N_{\text{Fake}}(i;p)}{N_{\text{ID}}(i;p)} \quad , \quad (7.3)$$

where  $N_{\text{Good}}(i;p)$  is the number of particles of type  $i$  correctly tagged as  $i$ ,  $N_{\text{True}}(i;p)$  is the number of generated particles of type  $i$  in the momentum range  $[p, p + \Delta p]$ ,  $N_{\text{Fake}}(i;p)$  is the number of particles tagged as  $i$  without being of type  $i$  and

$$N_{\text{ID}}(i;p) = N_{\text{Good}}(i;p) + N_{\text{Fake}}(i;p) \quad (7.4)$$

is the total number of tracks identified as  $i$ .

The efficiency and the contamination in all detector configurations are shown in Fig. 7.8. The simulations lead to comparable results for the two configurations having four layers with detector thickness of 20  $\mu\text{m}$  and 40  $\mu\text{m}$  respectively. Furthermore, with both the configurations a good performance in terms of PID efficiency and contamination is still possible, although in a reduced momentum range with respect to that of the present ITS, which has four layers featuring analog read-out, each of them 300  $\mu\text{m}$  thick.

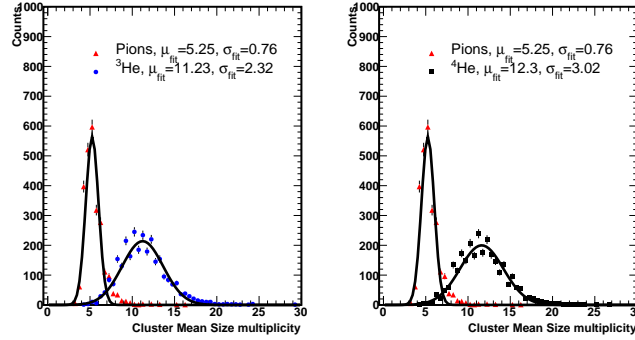


**Figure 7.9:** Multiplicity distribution of the mean value of the cluster size for pions (red triangles) and  $^3\text{He}$  (blue dots) in the 6.1 GeV/c to 6.2 GeV/c momentum range (left). Multiplicity distribution of the mean value of the cluster size for pions (red triangles) and  $^4\text{He}$  (black squares) in the 6.1 GeV/c to 6.2 GeV/c momentum range (right). In both figures, a Gaussian fit is superimposed to the distributions and the  $\mu$  and  $\sigma$  values of the fits are reported in the legend.

### 7.7.3 Heavily ionizing particles

In this section, the approach used to identify heavily ionizing particles like  $^3\text{He}$  and  $^4\text{He}$  will be described. This study was performed assuming that an analogue read-out will be not available for the upgraded ITS. In order to exploit the identification capabilities of the new ITS in such a case, an analysis of the size of clusters associated to tracks has been conducted, assuming an ITS configuration with seven layers of pixels with a pixel dimension of  $20\text{ }\mu\text{m} \times 20\text{ }\mu\text{m}$  and with an effective thickness of  $18\text{ }\mu\text{m}$ .

The data sample analysed consisted of 150 Monte Carlo events, each of them having an underlying event simulated with a parametrization of the HIJING [36] generator with a charged particle density  $dN/dy = 1000$ , together with extra 100 pions, 100 protons, 100 deuterons, 100  $^3\text{He}$  and 100  $^4\text{He}$ . These additional particles were generated with a flat transverse momentum in the 0 GeV/c to 10 GeV/c range and with  $|\eta| < 2.5$ . In the analysis, only tracks with seven points in the ITS were taken into account and only primary particles were selected.

In order to tag the tracks corresponding to heavily ionizing particles, the information on the cluster size of each layer was used and the following method was applied: the arithmetic mean of the seven cluster size values associated to the track was computed and the calibration of the PID algorithm was based on building, for each particle type, the distribution of the mean cluster size in different momentum intervals of 100 MeV/c width.

These distributions were then fitted with Gaussian functions and their mean values ( $\mu$ ) were finally fitted with second-degree polynomials as a function of the particle momentum. In the left panel of Fig. 7.9, the multiplicity distribution of the mean value of the cluster size for pions (red triangles) and  $^3\text{He}$  (blue dots) in the 6.1 GeV/c to 6.2 GeV/c momentum range are shown. In the right panel of Fig. 7.9, the multiplicity distribution of the mean value of the cluster size for pions (red triangles) and  $^4\text{He}$  (black squares) in the same momentum bin is shown. For  $^3\text{He}$  and  $^4\text{He}$  the distributions show very different values of  $\mu$  and  $\sigma$  with respect to the pions and this feature is the one that will be exploited for the heavily ionizing particles tagging. In particular, in Fig. 7.10 the distribution of the

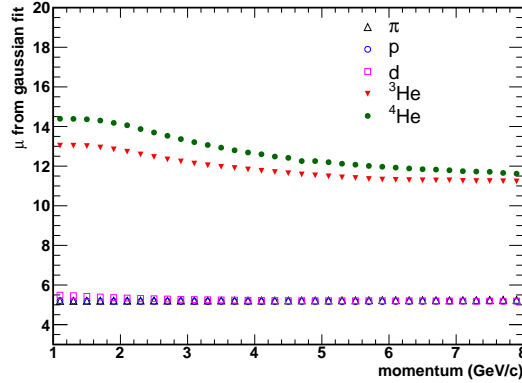


**Figure 7.10:** Mean values extracted from the Gaussian fit to the cluster size multiplicity distribution as a function of the momentum for the different simulated particle species (pions – black triangles, protons – blue circles, deuterons – magenta squares,  $^3\text{He}$  – red triangles, and  $^4\text{He}$  – green dots).

mean values extracted from the Gaussian fit to the cluster size multiplicity distribution as a function of the momentum for the different simulated particle species is reported. Looking to that trend, it is possible to draw the conclusion that pions, protons and deuterons are not distinguishable on the basis of the clusters associated to the track. On the other hand, a cut of  $2\sigma$  on the mean value of the cluster size is a very good tool to tag nuclei, for example for the detection of the weak decays of  $\Lambda$  hypernuclei in which a nucleus and a pion are emitted with a V0-like topology. In the selection of these kind of events, even under the assumption that an analogue read-out will be not present, the ITS will provide useful complementary PID information.

## 7.8 Performance for improved or degraded sensor parameters

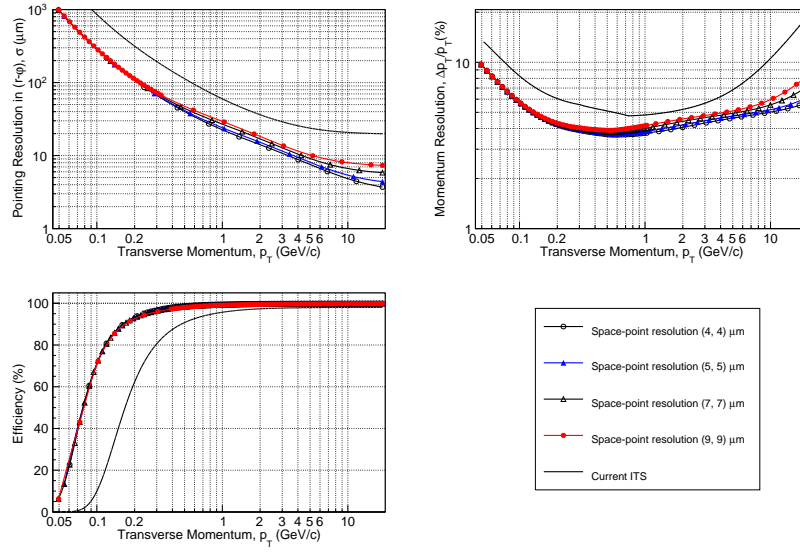
The design goal of the ITS upgrade is to have pixels with the same granularity for all layers corresponding to an intrinsic resolution of ( $5\text{ }\mu\text{m}$ ,  $5\text{ }\mu\text{m}$ ) in  $r-\phi$  and  $z$  respectively. In this section, we study the tracking performance of Pixel Chips with different intrinsic resolutions. In particular, we study the effects of increased pixel size in the Outer Barrel, which may be an option in order to decrease the power consumption and material budget.

Fig. 7.11 shows the ITS stand-alone tracking performance for some alternative configurations with different intrinsic resolution compared with the segmentation used in the detailed Monte Carlo studies, i.e. ( $4\text{ }\mu\text{m}$ ,  $4\text{ }\mu\text{m}$ ) in  $r-\phi$  and  $z$  respectively for all layers.

For all configurations, the total material budget per layer is assumed to be  $X/X_0 = 0.3\%$  and  $X/X_0 = 0.8\%$  for the Inner and Outer Barrel, respectively.

The variation of the intrinsic resolution hardly affects the tracking efficiency. The pointing resolution (in  $r-\phi$ ) is affected only by the variations of the innermost layers resolution. At  $p_T = 0.8\text{ GeV}/c$ , the pointing resolution for an intrinsic resolution of ( $9\text{ }\mu\text{m}$ ,  $9\text{ }\mu\text{m}$ ) is degraded by a factor of about 1.2 compared to an intrinsic resolution of ( $5\text{ }\mu\text{m}$ ,  $5\text{ }\mu\text{m}$ ).

The momentum resolution is unaffected by the variation of the intrinsic resolution at  $p_T < 0.3\text{ GeV}/c$ . The relative transverse momentum resolution is in the range 3.7% to 4.5% for  $0.3\text{ GeV}/c < p_T < 2\text{ GeV}/c$ . For  $p_T > 2\text{ GeV}/c$ , the  $p_T$  resolution for the



**Figure 7.11:** Pointing resolution, momentum resolution, and tracking efficiency obtained with the stand-alone upgraded ITS reconstruction assuming different space-point resolutions. For comparison, the performance of the current ITS is shown as well.

configurations with higher Outer Barrel intrinsic resolution starts to deteriorate.

The worsening of the performance of the upgraded detector for larger values of the material budget per layer was studied. The material budget of the Outer Barrel was increased with respect to the nominal value ( $X/X_0 = 0.8\%$ ) while keeping that of the Inner Barrel constant ( $X/X_0 = 0.3\%$  per layer). In particular, with reference to Fig. 7.12, the following configurations have been considered:

- blue lines: the baseline configuration,  $X/X_0 = 0.3\%$  per layer for the Inner Barrel and  $X/X_0 = 0.8\%$  per layer for the Outer Barrel;
- green lines:  $X/X_0 = 0.3\%$  per layer for the Inner Barrel and  $X/X_0 = 1.0\%$  per layer for the Outer Barrel;
- red lines:  $X/X_0 = 0.3\%$  per layer for the Inner Barrel and  $X/X_0 = 1.2\%$  per layer for the Outer Barrel.

In all cases, the detector resolution is kept equal to the one used for the detailed Monte Carlo studies ( $4\mu\text{m}, 4\mu\text{m}$ ). In Fig. 7.12, the performance of the current ITS has been also shown for comparison (black lines).

The pointing resolution is not affected by variations of the material budget in the range considered for these simulations. The stand-alone tracking efficiency and momentum resolution are slightly affected by the increase of the material budget of the Outer Barrel. At 200 MeV, the tracking efficiency is in the range 92% to 94%. The relative transverse momentum resolution is in the range 3.9% to 4.5% for  $200\text{ GeV}/c < p_T < 1\text{ GeV}/c$ . The momentum resolutions for the ITS-TPC combined tracking is slightly affected only at high  $p_T$ .



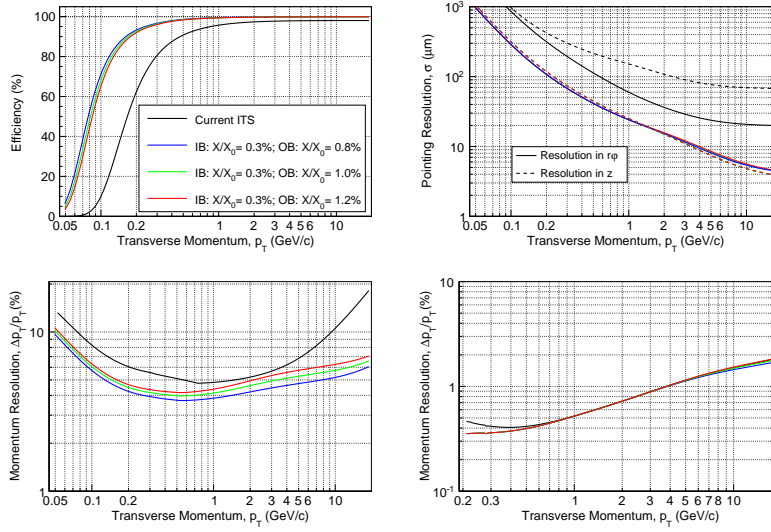


**Figure 7.12:** Top panels: Stand-alone tracking efficiency (left) and pointing resolution (right) for charged pions as a function of the transverse momentum for the current ITS and different material-budget options for the upgraded detector. Bottom panels: transverse momentum resolution for charged pions as a function of  $p_T$  for the current ITS and different material-budget options for the upgraded detector (the results for the ITS stand-alone and ITS+TPC combined tracking are shown on the left and on the right, respectively).

### 7.8.1 Tracking efficiency vs. layer detection efficiency and redundancy

In this section, we study the effect on the global tracking efficiency under the assumption of a reduced overall detection efficiency of the layers. The reduced detection efficiency might be due to either limited acceptance and dead areas, or intrinsic inefficiency of the detector. The case of having all the seven layers (at the same time) with an efficiency of 95 %, 85 %, 75 % and 65 % have been simulated. The tracking efficiency has been defined as the ratio of the number of reconstructed tracks with at least four correct clusters associated to the tracks and no wrongly associated cluster (from other particles) to the number of “trackable” tracks (i.e. tracks passing through at least four layers). The results are shown in Fig. 7.13. It is worth stressing that typical values of detection efficiency for non-dead zones of silicon detectors are close to 100 %.

The detector performance in the event of a dramatic reduction of the detector efficiency has also been studied. In particular, we consider the case of one of the layers being completely dead. Figures 7.14 and 7.15 show the performance for the worst cases with respect to the tracking efficiency and tracking resolution, respectively.

This study confirms that rapid accessibility to the detector is a key priority in the design of the upgraded ITS.

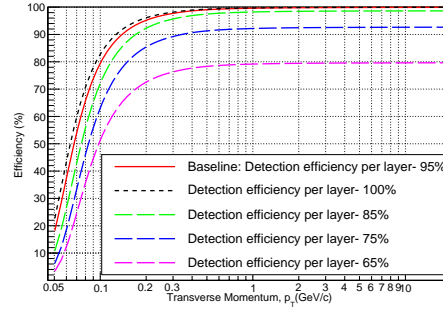


**Figure 7.13:** Tracking efficiency as a function of  $p_T$  for the upgraded ITS detector, assuming different reduced detection efficiency for all seven layers of the layout.

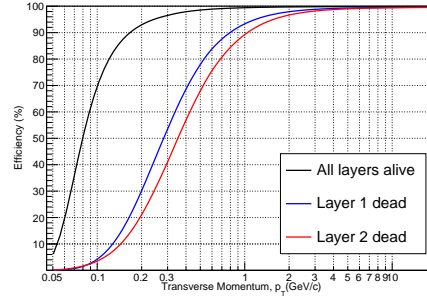


**Figure 7.14:** Tracking efficiency for the upgraded ITS. The two worst scenarios for the tracking efficiency where layer 3 (red) or layer 2 (blue) is dead is compared to the case of all layers working properly.

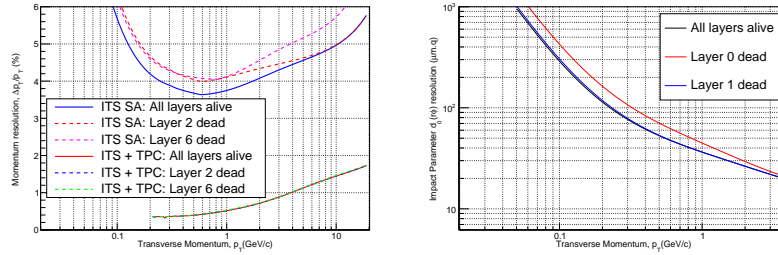


**Figure 7.15:** Momentum (left) and impact parameter (right) resolution for the upgraded ITS. The worst scenarios for the momentum (left) and impact parameter (right) resolution are compared to the case of all layers properly working. The momentum resolution for combined ITS and TPC tracking stays practically unchanged.



## 8 Physics performance

For the estimation of the physics performance, we consider as a baseline the running scenario that is presented in the ALICE Upgrade LOI [4].

The target integrated luminosity for the upgrade physics programme is  $10 \text{ nb}^{-1}$  in Pb–Pb collisions at design LHC energy  $\sqrt{s_{\text{NN}}} = 5.5 \text{ TeV}$ . This integrated luminosity represents an increase, with respect to the original programme of the experiment, of a factor of ten in statistics for the data sample collected with rare triggers and of a factor of 100 for the minimum-bias data sample. The latter is relevant for many measurements of the Upgrade physics programme, for instance low- $p_{\text{T}}$  heavy flavour and charmonium production and low-mass dilepton production.

Indeed, it was shown in the ITS Upgrade CDR [12] that, due to the very low signal-to-background ratio that is expected in the low- $p_{\text{T}}$  region for most of the relevant channels (e.g.  $D^0 \rightarrow K\pi$  and  $\Lambda_c \rightarrow pK\pi$ ), the rate of events of interest, containing a signal candidate will be of the same order as the interaction rate. Therefore, it was concluded that online event filtering is not an adequate strategy for these low- $p_{\text{T}}$  measurements. Rather, all interactions will be recorded on tape, as allowed by the High Level Trigger data compression [4].

The Pb–Pb programme for the ALICE Upgrade requires  $3^{1/2}$  months of operation to arrive at the  $10 \text{ nb}^{-1}$  of integrated luminosity. A one-month run at low field (0.2 T) in the solenoid magnet for the dielectron measurement is also needed.

In this chapter we present the physics performance estimated on the basis of simulations for Pb–Pb collisions, assuming that the pp reference measurements will have a statistical uncertainty much smaller than for the Pb–Pb measurements.

The chapter is organized as follows. The simulation methods and conditions are described in Sec. 8.1. The physics performance studies for heavy flavour, low-mass dielectrons and hypernuclei are presented in Secs. 8.2, 8.3 and 8.4, respectively. Finally, the physics reach is summarized in a table in Sec. 8.5.

### 8.1 Simulation methods and conditions

All studies presented in this chapter are based on detailed simulations of the ALICE apparatus. The geometry and parameters of the new ITS detector are those described in Tab. 1.1 (Chap. 1).

Some benchmark studies, namely  $D^0$ ,  $B^+$ ,  $\Lambda_c$ ,  $\Lambda_b$  and  ${}^3_{\Lambda}\text{H}$  reconstruction, use the full simulation of the geometry and response of the new ITS detector, as described in Chap. 7.

For the other studies, simulation samples with the current ITS detector were used and the improved tracking performance, in terms of position and momentum resolutions, was included with the *Hybrid method*, which was also used for the ITS Upgrade CDR [12].

#### 8.1.1 Hybrid simulation method

This method is based on existing Monte Carlo productions including the detailed geometry and response of the current ALICE detector setup. The impact of the new ITS is obtained by recomputing reconstructed track parameters according to the  $p_{\text{T}}$  and particle species dependent scaling laws, as obtained by the Fast Estimation Tool described in

Chap. 7. This is done by scaling the residuals of the impact parameters in  $r\varphi$  and  $z$ ,  $d_{0,r\varphi}$  and  $d_{0,z}$ , as well as of the transverse momentum  $p_T$ , with respect to their true values, known from the generated particle kinematics. The scaling factors are the ratios of the upgrade/current resolutions on these variables. This approach is called *Hybrid*, because it applies the detector performance of the upgraded ITS to full simulations of the current ITS. Comparisons of the *Hybrid* method and full simulation, which will be shown for some of the heavy-flavour studies, indicate the validity of the former for a conservative assessment of the physics performance.

### 8.1.2 Simulation conditions

For the performance studies, where not differently specified, the underlying Pb–Pb event was simulated using the HIJING 1.23 [36] generator. The centre-of-mass energy was set to  $\sqrt{s_{NN}} = 5.5$  TeV and the collision impact parameter was sampled in the range  $0 < b < 5$  fm (corresponding to the 0–10% centrality class), according to  $d\sigma/db \propto b$ . The average charged-particle pseudo-rapidity density is  $dN_{ch}/d\eta = 2000$ , which is a reasonable expectation for this energy (see for example an empirical extrapolation in [35]). Heavy-flavour and hyper-nuclei signals were added to the HIJING event using a cocktail of parametric generators and heavy-quark pairs generated with PYTHIA 6 [54]. Tracks originating from injected signals were not considered in the evaluation of the background level. The value of the magnetic field in the solenoid magnet was set to 0.5 T. For the low-mass dielectron study, a dedicated sample with a field of 0.2 T was utilised.

The sample with the full simulation of the new ITS consisted of  $10^6$  events. Various samples with the current ITS were analyzed with the *Hybrid* method.

## 8.2 Heavy flavour

### 8.2.1 Motivation

Heavy quarks play a special role in heavy-ion physics because they preserve their identity (mass, flavour, and colour charge) while interacting with the medium. Therefore, they constitute a tagged (identified) probe (from production to observation), which enables a unique access to their interactions in the QGP. This allows us to gain microscopic insights into the transport properties of the medium. Heavy-flavour particles may be thought of as “Brownian motion” markers, the kinematical distributions of which reflect their reinteraction history.

The two main open questions concerning heavy-flavour interactions with the QGP medium—and the corresponding experimental handles—are:

- Thermalisation and hadronization of heavy quarks in the medium, which can be studied by measuring the baryon/meson ratio for charm ( $\Lambda_c/D$ ) and for beauty ( $\Lambda_b/B$ ), the strange/non-strange ratio for charm ( $D_s/D$ ), the azimuthal anisotropy  $v_2$  for charm and beauty mesons<sup>1</sup>, and the possible in-medium thermal production of charm quarks.
- Heavy-quark in-medium energy loss and its mass dependence, which can be addressed by measuring the nuclear modification factors  $R_{AA}$  of the  $p_T$  distributions of D and B mesons separately in a wide momentum range<sup>2</sup>.

<sup>1</sup>  $v_2$  is the second order Fourier coefficient of the azimuthal distribution of particles with respect to the reaction plane.

<sup>2</sup>  $R_{AA}$  is the ratio of particle production in nucleus–nucleus collisions to particle production in proton–proton collisions scaled by the average number of nucleon–nucleon collisions:  $R_{AA} = (dN_{AA}/dp_T)/(\langle N_{coll} \rangle dN_{pp}/dp_T)$ .

These two topics are closely related. The high-momentum heavy quarks quenched by in-medium energy loss are shifted towards low momentum and may ultimately thermalise in the system, through QCD interaction mechanisms that are essentially the same as those responsible for the energy loss, and participate in the collective expansion dynamics. Therefore, the simultaneous experimental investigation and theoretical understanding of the thermalisation-related observables and of the energy-loss-related observables constitute a unique opportunity for the characterization of the QGP properties, in particular of the flavour-dependent transport coefficients. An in-depth discussion of these topics and of the most relevant measurements can be found in the ITS Upgrade CDR [12].

The following physics performance studies for heavy-flavour measurements are presented.

#### *Charm production via D meson decays*

- $D^0 \rightarrow K^- \pi^+$ ;
- $D^{*+} \rightarrow D^0 \pi^+$ ;
- $D_s^+ \rightarrow K^+ K^- \pi^+$ .

#### *Beauty production*

- $B^+ \rightarrow D^0 + X$ ;
- $B \rightarrow J/\psi (\rightarrow e^+ e^-) + X$ ;
- $B^+ \rightarrow \bar{D}^0 \pi^+$ .

#### *Heavy-flavour baryon production*

- $\Lambda_c^+ \rightarrow p K^- \pi^+$ ;
- $\Lambda_b \rightarrow \Lambda_c^+ \pi^-$ .

#### *Heavy-flavour and jets*

- $D^0$  fragmentation function in jets.

### 8.2.2 Expected yields

In Tab. 8.1 we summarise the expected production yields for  $c\bar{c}$  and  $b\bar{b}$  pairs in central (0–10 %) and minimum-bias (0–100 %) Pb–Pb collisions at  $\sqrt{s_{NN}} = 5.5$  TeV (and for other energies and systems for comparison). The numbers are obtained by applying binary  $N_{\text{coll}}$  scaling to next-to-leading order perturbative QCD (pQCD) predictions from the HVQMNR calculation [58]. The value of the charm and beauty quark masses and of the pQCD scales are set as:  $m_c = 1.2 \text{ GeV}/c^2$ ,  $m_b = 4.75 \text{ GeV}/c^2$ ,  $\mu_R = \mu_F = 2 m_c$  for charm and  $\mu_R = \mu_F = m_b$  for beauty production. CTEQ6M parton distribution functions are used with the EPS09NLO [59] correction for nuclear shadowing. These predictions are affected by a theoretical uncertainty of a factor of 2–3. For comparison, the charm and beauty production cross sections measured in pp collisions at  $\sqrt{s} = 7$  TeV are also reported [55, 56].

In Tab. 8.2 we report, for central Pb–Pb at 5.5 TeV, the corresponding yields for the production of heavy-flavour hadrons (+ their anti-particles), using the branching fractions for c and b quarks as given by the PYTHIA6 event generator [54]. The mean proper decay lengths ( $c\tau$ ), the relevant final states and their branching ratios are reported as

**Table 8.1:** Heavy quark production at the LHC, as expected from pQCD calculations at NLO with nuclear shadowing corrections. For comparison, the charm and beauty production cross sections measured in pp collisions at  $\sqrt{s} = 7$  TeV [55, 56] are also reported, in parentheses.

System	Pb–Pb	Pb–Pb	pp	pp
$\sqrt{s_{NN}}$	2.76 TeV	5.5 TeV	7 TeV (measured)	14 TeV
$\sigma_{NN}^{cc}$ [mb]	2.1	3.4	6.9 ( $8.5^{+5.1}_{-2.5}$ )	11.2
$N_{tot}^{cc}$ min.-bias, 0–10 % central	12, 50	19, 80	0.10	0.16
$\sigma_{NN}^{bb}$ [mb]	0.08	0.14	0.23 ( $0.28 \pm 0.06$ )	0.50
$N_{tot}^{bb}$ min.-bias, 0–10 % central	0.5, 1.9	0.8, 3.3	0.003	0.007

**Table 8.2:** Expected production yields (total and per unit of rapidity at mid-rapidity) for charm and beauty particles (+ anti-particles) in minimum-bias and 0–10 % central Pb–Pb collisions at 5.5 TeV, mean proper decay length, branching ratios to the relevant decay channels [57].

Part.	Yield	$dN/dy _{y=0}$	$c\tau$ ( $\mu\text{m}$ )	decay channel	B.R.
	m.b., 0–10 %	m.b., 0–10 %			
$D^0$	23, 110	2.3, 11	$\approx 120$	$K^-\pi^+$	3.8 %
$D^{*+}$	9, 44	0.9, 4.4	$\approx 0$	$D^0\pi^+$	67.7 %
$D_s^+$	4.3, 20	0.4, 2.0	$\approx 150$	$\phi(\rightarrow K^+K^-)\pi^+$	4.4 % ( $\times 49$ %)
$\Lambda_c^+$	2.9, 14	0.29, 1.4	$\approx 60$	$pK^-\pi^+$	5.0 %
				$p\bar{K}^0(K_S^0 \rightarrow \pi^+\pi^-)$	1.15 % ( $\times 69.2$ %)
				$\Lambda\pi^+(\rightarrow p\pi^-)$	1.1 % ( $\times 63.9$ %)
B	1.3, 6.2	0.2, 0.9	$\approx 500$	$J/\psi(\rightarrow e^+e^-) + X$	1.2 % ( $\times 6$ %)
				$D^0(\rightarrow K^-\pi^+) + X$	60 % ( $\times 3.8$ %)
				$e^+ + X$	10.9 %
$B^+$	0.6, 2.7	0.1, 0.4	$\approx 500$	$\bar{D}^0(\rightarrow K^+\pi^-\pi^+)\pi^+$	0.5 % ( $\times 3.8$ %)
$B^0$	0.6, 2.7	0.1, 0.4	$\approx 500$	$D^{*-}(\rightarrow K^+\pi^-\pi^-)\pi^+$	0.3 % ( $\times 2.6$ %)
$\Lambda_b^0$	0.1, 0.5	0.015, 0.07	$\approx 400$	$\Lambda_c^+(\rightarrow pK^-\pi^+) + e^- + X$	9.9 % ( $\times 5$ %)
				$\Lambda_c^+(\rightarrow pK^-\pi^+) + \pi^-$	0.6 % ( $\times 5$ %)

well. Where not differently specified, these total production yields are used as baseline for the simulation studies presented in this chapter. The  $p_T$  dependence of the yields is obtained from FONLL calculations [60] and it is directly included in the simulations using a parametric event generator.

### 8.2.3 D mesons

#### Reconstruction of $D^0$ mesons

The  $D^0 \rightarrow K^-\pi^+$  reconstruction with the upgraded ITS was studied with the *Hybrid* method in [12], for Pb–Pb collisions at  $\sqrt{s_{NN}} = 2.76$  TeV in the centrality class 0–20 %. Here, the results obtained with a new study based on the detailed simulation of the new detector are presented. Pb–Pb collisions at  $\sqrt{s_{NN}} = 5.5$  TeV in the centrality class 0–10 % are considered.

The resolutions on the reconstructed position of the  $D^0 \rightarrow K^-\pi^+$  decay vertex are shown in Fig. 8.1 for the current ITS, the upgraded ITS with full simulation of the new detector and with the *Hybrid* method. With the upgraded ITS, the resolution improves by a factor of about three for the  $x$  (and  $y$ ) coordinates and about six for  $z$ . The resolution obtained with the *Hybrid* method is worse than with the full simulation, by up to 50 % at

high momentum. This could be due to the fact that, in this method, the track covariance matrix is not modified to account for the better tracking precision. The comparison indicates that the performance estimated with the *Hybrid* method should be considered as a conservative projection, as will be shown for the  $\Lambda_c$  reconstruction in Sec. 8.2.5.

Two simulation samples were used, both with Pb-Pb events in the 0–10% centrality class at  $\sqrt{s_{NN}} = 5.5$  TeV generated with HIJING [36] and enriched with heavy flavour signals generated with PYTHIA 6 [54]. In one sample, the current ITS detector was simulated; in the other sample, the new ITS detector. The other ALICE detectors were included in both samples. The simulation study was performed using the same cut values for the two ITS configurations, in order to single out the effect of the improved tracking resolutions. The cuts were fixed to values close to those used for the 2010 Pb-Pb data analysis [61], as well as the particle identification selection, based on the TPC and TOF detectors. In particular, the kaon identification up to a momentum of about 2 GeV/c provides a reduction by a factor of about three of the combinatorial background at low  $D^0$   $p_T$ .

The selected signal (raw) yield was obtained by multiplying the corrected  $D^0$   $p_T$  spectrum  $dN/dp_T$  measured with data at 2.76 TeV by the ratio of the  $D^0$  cross section at 5.5 and at 2.76 TeV from the FONLL calculation [60] and by the efficiency obtained from the simulation for the current or upgraded ITS configuration. The background yield in the  $D^0$  mass region was scaled to account for the difference between the HIJING simulations and the data. To this purpose a third simulation sample was used, with HIJING events at 2.76 TeV and the same detector conditions as for the data collection. The background scaling factor was defined as the ratio of the background observed in data to the background from this sample.

The left-hand panel of Fig. 8.2 shows the significance normalized to the number of events for both the current and upgraded ITS. The right-hand panel shows the comparison for the signal-to-background ratio. The error bars indicate the statistical uncertainty of the estimate (determined by the size of the simulation samples), while the error box at  $0 < p_T < 1$  GeV/c reflects the assumed value of the  $D^0$  nuclear modification factor  $R_{AA} = 0.8^{+0.7}_{-0.4}$ . In general, the efficiency of the signal selection with the current and upgraded ITS is comparable. On the other hand, with the upgraded ITS the background rejection improves by a factor of 4–5 for  $p_T > 2$  GeV/c and by a factor almost 10 for  $p_T < 2$  GeV/c, so that a strong increase of the signal-to-background ratio is obtained. Considering an integrated luminosity of  $10 \text{ nb}^{-1}$ , the number of central events in the class 0–10% is  $8 \times 10^9$ . The resulting significance is obtained by multiplying the numbers in

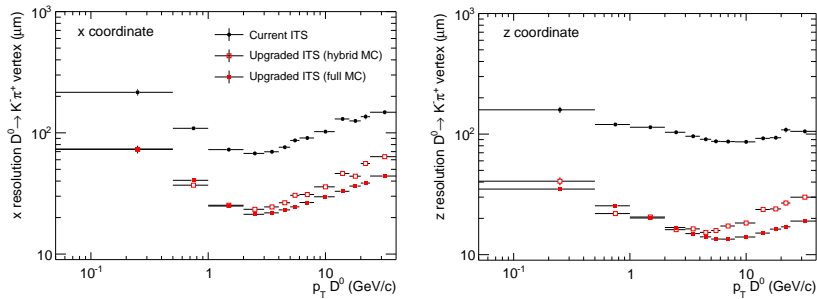


**Figure 8.1:**  $D^0 \rightarrow K^- \pi^+$  secondary vertex position resolutions for current and upgrade scenarios:  $x$  (left) and  $z$  (right) coordinates.



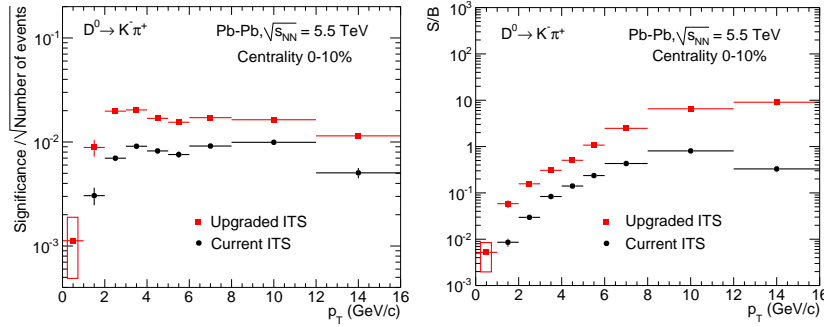


**Figure 8.2:**  $D^0 \rightarrow K^- \pi^+$ : comparison of the significance (left) and signal-to-background ratio (right) obtained for the current and upgraded ITS. The box indicates the systematic uncertainty of the estimate for the interval  $0 < p_T < 1 \text{ GeV}/c$ .

Fig. 8.2 (left) by about  $10^5$ , i.e. of the order of a thousand for  $p_T > 1 \text{ GeV}/c$  and larger than 50 in the interval  $0 \text{ GeV}/c$  to  $1 \text{ GeV}/c$ . A  $p_T$  binning finer than that considered in this study (e.g.  $0.25$  or  $0.5 \text{ GeV}/c$ ) will be possible.

The expected systematic uncertainties on the measurement of prompt  $D^0$  production were estimated on the basis of those evaluated for the first measurement in the centrality class  $0-20\%$  [61]. The following considerations were used to define the systematic uncertainties with the upgrade. A reduction of the systematic uncertainties will derive from: (a) improved spatial and momentum resolutions, which provide higher signal-to-background ratio; (b) higher statistics, which will allow for a precise estimation of systematic effects, unaffected by statistical fluctuations. A strong improvement in the accuracy of the measurement will come from the direct measurement of the fraction of prompt and secondary (from B decay) D mesons. As described in Sec. 8.2.4, the statistical and systematic uncertainties on the fraction of prompt  $D^0$  are expected to be  $< 1\%$  and  $< 5\%$ , respectively. In the published measurement [61] and in the ITS Upgrade CDR [12], the systematic uncertainties were given as a maximum confidence interval, corresponding to  $\pm 3\sigma$  in case of a Gaussian error distribution. Here, the systematic uncertainties are given as  $\pm 1\sigma$ , in order to have a more direct comparison of the relative importance of the statistical and systematic uncertainties. In addition, at variance with the approach followed in [61] and [12], some of the systematic uncertainties are here assumed to be partly correlated in the Pb-Pb and pp measurements and to cancel in the  $R_{AA}$  ratios. In particular, this is the case for all uncertainties related to the description of the detector response in the simulation (e.g. tracking and selection efficiency). For these contributions, the uncertainty on  $R_{AA}$  was defined as  $\approx 1/2$  of the uncertainty on the Pb-Pb measurement. Figure 8.3 shows the  $p_T$  dependence of the various contributions to the relative systematic uncertainty on  $R_{AA}$ .

The expected performance for the measurement of  $R_{AA}$  and  $v_2$  will be shown in Sec. 8.2.6.

### Reconstruction of $D^{*+}$ mesons

The  $D^{*+}$  reconstruction starts from the invariant mass analysis of the resolved secondary vertex of the  $D^0 \rightarrow K^- \pi^+$  decay. The  $D^0$  candidates are selected in a  $\pm 3\sigma$  interval around the  $D^0$  peak position. A third track is added to construct the  $D^{*+}$  meson candidates and the signal is extracted from a fit of the distribution of  $\Delta m = m(K\pi\pi) - m(K\pi)$  [61]. For

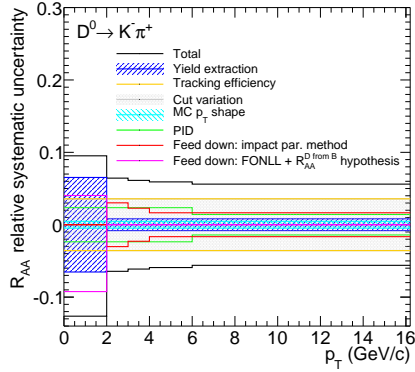


**Figure 8.3:** Relative systematic uncertainties on  $R_{AA}$  of prompt  $D^0$  mesons.

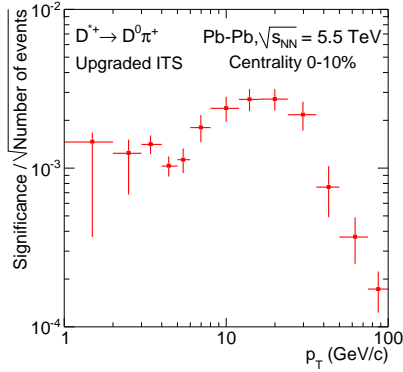


**Figure 8.4:**  $D^{*+}$  statistical significance, normalized to one event, for Pb-Pb collisions at  $\sqrt{s_{NN}} = 5.5$  TeV in the centrality class 0–10 %, with the upgraded ITS.

low  $p_T$   $D^{*+}$ , the decay pion has a very low momentum, down to a few tens of MeV/ $c$ , because of the small decay momentum ( $q = 39$  MeV). Therefore, the pion may not reach the TPC and it is often reconstructed as an ITS stand-alone track.

The simulation study for the  $D^{*+}$  measurement was carried out using the *Hybrid* method. The basic performance (signal selection efficiency and background rejection) was checked with the full simulation of the new ITS and found to be consistent with the *Hybrid* method. Like for the case of the  $D^0$  meson, the signal and background yields observed in data were used to normalize the corresponding yields in the simulation with the current ITS. In addition, the effect of the increase of the centre-of-mass energy from 2.76 to 5.5 TeV was accounted for using FONLL calculations [60] for the signal and HIJING simulations [36] at the two energies for the background. The same ingredients were also used to estimate the performance beyond the  $p_T$  interval (3–36 GeV/ $c$ ) covered by the current measurement [61]. The topological and PID selections used in this analysis are similar to those used for the  $D^0$  reconstruction.

The background reduction with the new ITS is found to be significantly smaller than for the  $D^0$ . This is due to the fact that the selection on the  $D^0$  decay topology is looser in the  $D^{*+}$  analysis, where the additional constraint on  $\Delta m$  can be used. On the other hand, the large increase of the ITS stand-alone tracking efficiency with the new ITS (see Chap. 7) will determine an increase of the  $D^{*+}$  signal in the low  $p_T$  range (below 3 GeV/ $c$ ). This effect is not included in the present study and it will be quantified in the detail using the full simulation of the new detector.

The significance, normalized to one event, for the centrality class 0–10 % is shown in Fig. 8.4. The significance for an integrated luminosity of  $10 \text{ nb}^{-1}$  is larger than one hundred up to 36 GeV/ $c$ , corresponding to a statistical uncertainty of less than 1 %. The  $D^{*+}$  meson has higher signal-to-background ratio at large  $p_T$  with respect to  $D^0$  and  $D^+$  already in the current analysis [61]. Therefore, it was used as a benchmark to estimate the high- $p_T$  reach for the charm measurements with  $10 \text{ nb}^{-1}$ . Using the FONLL cross section at 5.5 TeV multiplied by the number of binary collisions in central Pb-Pb, an assumed  $R_{AA} = 0.5$ , and constant acceptance and efficiency for  $p_T > 30$  GeV/ $c$ , a significance of 20–30 was estimated for  $75 < p_T < 100$  GeV/ $c$  in the 0–10 % centrality class, corresponding to a

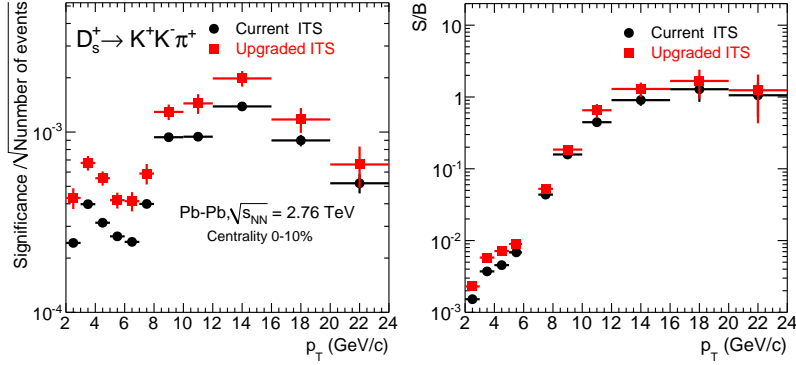


**Figure 8.5:** Significance (left) and signal-to-background ratio (right) for  $D_s^+$  reconstruction in central Pb–Pb collisions (0–10 %) at  $\sqrt{s_{NN}} = 2.76$  TeV.

statistical uncertainty below 5 %.

The systematic uncertainties for the  $D^{*+}$   $R_{AA}$  measurement were estimated using the same prescription as for the  $D^0$  meson. The expected performance for the measurement of  $R_{AA}$  up to  $p_T = 100$  GeV/c will be shown in Sec. 8.2.6.

### Reconstruction of $D_s^+$ mesons

$D_s^+$  mesons and their antiparticles ( $c\tau \approx 150 \mu\text{m}$ ) are reconstructed in the decay chain  $D_s^+ \rightarrow \phi\pi^+$  (and its charge conjugate) followed by  $\phi \rightarrow K^-K^+$ . In order to reduce the large combinatorial background,  $D_s^+$  candidates are selected using cuts on geometrical quantities (e.g. decay length, pointing of reconstructed momentum and flight line) and on the invariant mass of the reconstructed  $\phi$  meson. Since the final state contains two kaons, a large background rejection is also obtained using a particle identification selection, based on the TPC  $dE/dx$  and TOF time-of-flight. The PID selection provides a background rejection of a factor of 20–30 at low  $p_T$  (2 GeV/c to 3 GeV/c).

The simulation study was carried out using the *Hybrid* method. The background from the HIJING generator was scaled to match the background observed in data, in the same way as for the  $D^0$  study. The signal was normalized according to a binary scaling of the pQCD estimation of  $D_s^+$  production in pp collisions at 2.76 TeV and a model prediction for the  $D_s^+$   $R_{AA}$  [62].

In Fig. 8.5, the signal-to-background ratio and significance normalized to one event are presented for the current and the upgraded ITS, for Pb–Pb collisions in the 0–10 % centrality class. The improvement with the ITS upgrade is of a factor of about two for  $S/B$  at low  $p_T$ . The effect of the resolution is smaller than for  $D^0$  mesons, because the  $D_s^+$  selection strategy relies more on the PID than on the separation of the secondary vertex. The statistical significance for an integrated luminosity of  $10 \text{ nb}^{-1}$  is of the order of 50 at low  $p_T$ . The corresponding statistical uncertainties on the yield are of a few percent. The expected performance for the measurement of  $R_{AA}$  and  $v_2$  will be shown in Sec. 8.2.6.

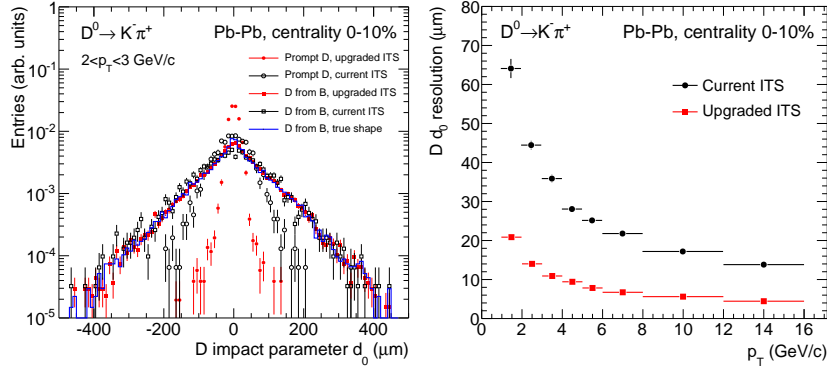


**Figure 8.6:** Impact parameter distributions for prompt and secondary (from B decays)  $D^0$  obtained with the current and upgraded ITS configurations in the interval  $2 < p_T < 3$  GeV/c (left). Impact parameter resolution as a function of  $p_T$  (right).

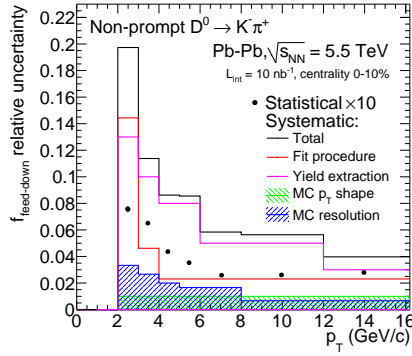


**Figure 8.7:** Relative statistical and systematic uncertainties on the fraction  $f_{\text{feed-down}}$  of  $D^0$  mesons from B decays, with the upgraded ITS in the centrality class 0-10% for  $L_{\text{int}} = 10 \text{ nb}^{-1}$ . The statistical uncertainty is multiplied by 10 for better visibility.

## 8.2.4 Beauty

### Beauty measurement via non-prompt $D^0$ mesons

Most of the B meson decay channels include a  $D^0$  ( $\bar{D}^0$ ) particle (the branching ratio  $B \rightarrow D^0 + X$  is about 60% [57]).

Since B mesons have a mean proper decay length  $c\tau \approx 460\text{--}490 \mu\text{m}$ , the fraction of prompt and secondary  $D^0$  mesons can be measured by exploiting the different shapes of their impact parameter distributions. This approach has been already used in pp collisions by the CDF Collaboration to measure the production of prompt D mesons at  $\sqrt{s} = 1.96 \text{ TeV}$  [63]. It has also been used by the LHCb Collaboration to measure the production of B mesons at  $\sqrt{s} = 7 \text{ TeV}$  at forward rapidity [64].

The left-hand panel of Fig. 8.6 shows the impact parameter distributions for prompt and secondary  $D^0$  in  $2 < p_T < 3 \text{ GeV}/c$  as obtained from the two simulation samples described in Sec. 8.2.3, with the current and upgraded ITS (in both cases with detailed simulation). The resolution on the  $D^0$  impact parameter, shown in the right-hand panel of the figure as a function of  $p_T$ , improves by a factor of about three with the upgraded ITS. This allows for a much better separation of the two components.

An estimation of the performance for the measurement of beauty production in central Pb–Pb collisions using the fraction of non-prompt  $D^0$  mesons was carried out, starting from the simulation results on the impact parameter resolution, the  $D^0$   $S/B$  ratio, and the expected  $D^0$  signal statistics. The relative statistical uncertainty on the fraction of  $D^0$  mesons from B decays is shown in Fig. 8.7. Since the statistical uncertainty on the measurement of the total  $D^0$  yields is expected to be of the order of 1 %, the values shown in the figure coincide in practice with the relative statistical uncertainty on the measurement of beauty production. The results are very promising, with a statistical uncertainty smaller than 1 % down to  $D^0$   $p_T$  of  $2 \text{ GeV}/c$ , for  $10 \text{ nb}^{-1}$ . Since the mass difference of B and D mesons is larger than  $3 \text{ GeV}/c^2$ , the decay of a B meson with transverse momentum below  $1 \text{ GeV}/c$  can yield a D meson with  $p_T > 2 \text{ GeV}/c$ . Therefore, the measurement will give access to B mesons with  $p_T$  down to almost 0.

The systematic uncertainties were studied by biasing the input parameters of the fit procedure in the simulation, and evaluated by comparing the mean and the spread of the residual distributions with and without a given bias. The  $p_T$  dependence of each contribution to the uncertainty is reported in Fig. 8.7. The expected performance for the measurement of  $R_{AA}$  and  $v_2$  of  $D^0$  mesons from B decay will be shown in Sec. 8.2.6.

#### Beauty measurement via non-prompt $J/\psi$ in the $e^+e^-$ decay channel

The measurement of the fraction  $f_B$  of the  $J/\psi$  yield coming from B meson decays relies on the discrimination of  $J/\psi$  mesons displaced from the interaction vertex. The signed projection of the  $J/\psi$  flight distance onto its transverse momentum vector,  $\vec{p}_T(J/\psi)$ , is defined as  $L_{xy} = \vec{L} \cdot \vec{p}_T(J/\psi)$  where  $\vec{L}$  is the vector from the primary vertex to the  $J/\psi$  decay vertex. The variable  $x$ , referred to as “pseudo-proper decay length” in the following, is introduced to separate prompt  $J/\psi$  from those produced by the decay of B mesons:  $x = c L_{xy} m_{J/\psi} / p_T(J/\psi)$ , where  $m_{J/\psi}$  is the  $J/\psi$  mass (world average [57]). In particular, a simultaneous fit of the pseudo-proper decay length and  $e^+e^-$  invariant mass distributions is carried out, in intervals of transverse momentum, using an unbinned log-likelihood fit procedure [65].

The simulation study to estimate the statistical precision of the measurement with the new ITS and an integrated luminosity of  $10 \text{ nb}^{-1}$  was carried out using the *Hybrid* approach. Electron identification is based on specific energy deposition  $dE/dx$  in the TPC. One of the main ingredients of the likelihood fit is the function used to describe the  $x$  distribution of prompt  $J/\psi$ , called “resolution function”. This function was extracted from the simulation. The left-hand panel of Fig. 8.8 shows the resolution function for the current and upgraded ITS for prompt  $J/\psi$  with  $p_T > 1.3 \text{ GeV}/c$ . The right-hand panel of Fig. 8.8 shows the  $p_T$  dependence of the RMS of the resolution function. The resolution improves by a factor of about three with the new ITS. The results obtained with the full simulation of the new ITS are shown as well: like for the case of the  $D^0$  secondary vertex resolution, they are consistent with *Hybrid* method at low  $p_T$  and better at high  $p_T$ . This validates the study with the *Hybrid* method as a conservative assessment of the physics performance.

The transverse momentum distribution for the signal was parametrized with a phenomenological function described in [66]. The background  $p_T$  shape was modelled on data

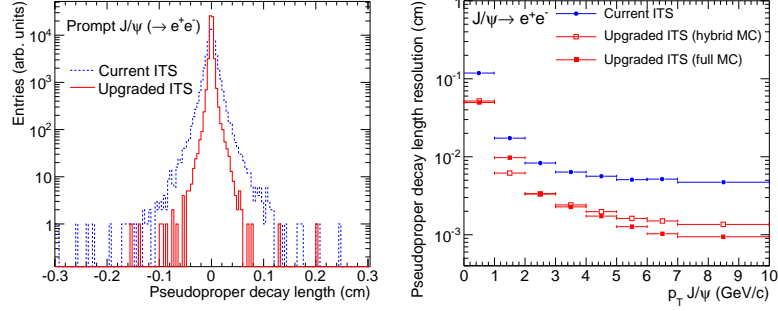


**Figure 8.8:** Left: Pseudo-proper decay length distribution for prompt  $J/\psi$  for the current and new ITS (*Hybrid* method). Right: Resolution as a function of  $p_T$  for the current and new ITS (*Hybrid* and full simulation).

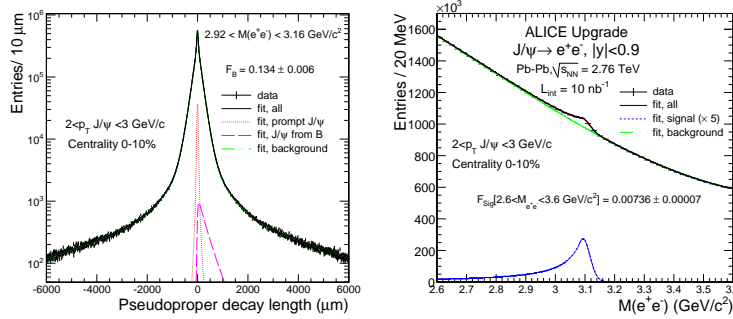


**Figure 8.9:** Pseudo-proper decay length (left) and invariant mass (right) distributions in the centrality class 0–10% and  $p_T$  interval 2–3 GeV/c with likelihood fit results superimposed.

(Pb–Pb collisions collected in 2011) considering the  $p_T$  distribution of candidates outside the signal region (i.e. in the “sidebands” of the invariant mass). The two distributions were rescaled according to the expected number of events for  $L_{int} = 10 \text{ nb}^{-1}$  and in order to match the signal-to-background ratio ( $S/B$ ) observed in Pb–Pb data. The non-prompt  $J/\psi$  fraction  $f_B$  was assumed to be the same as measured in pp collisions at  $\sqrt{s} = 7$  TeV.

The likelihood fit procedure was performed in transverse momentum bins in the range  $1 < p_T < 10 \text{ GeV}/c$  for central and semi-central collisions. A sample of dielectron candidates similar to that expected with  $10 \text{ nb}^{-1}$  was generated using a fast Monte Carlo method. For the invariant mass distribution, a Crystal Ball function was assumed for the signal and a third order polynomial function for the background, using the same shape as obtained from Pb–Pb data. The  $x$  and mass distributions were then fitted with the maximum likelihood technique. Figure 8.9 shows an example of fit in the centrality class 0–10% and in the transverse momentum interval 2–3 GeV/c.

The statistical uncertainty on the non-prompt  $J/\psi$  yield was obtained by combining the relative uncertainty on the inclusive  $J/\psi$  yield [4] with the one on the non-prompt  $J/\psi$  fraction. The statistical uncertainty of the measurement of the non-prompt  $J/\psi$  yield is

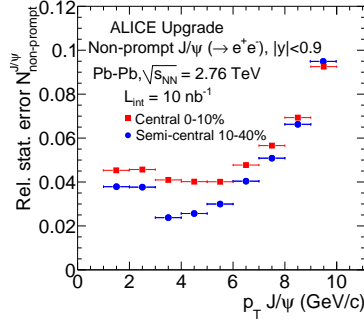


**Figure 8.10:** Statistical uncertainties on the non-prompt  $J/\psi$  yield as a function of transverse momentum for central and semi-central collisions.

shown in Fig. 8.10. Assuming that the statistical uncertainty of the pp reference will be smaller than that of yields in Pb–Pb, this figure corresponds to the expected precision of the non-prompt  $J/\psi$   $R_{AA}$  measurement. An illustration of the projected measurement of  $R_{AA}$  will be shown in Sec. 8.2.6, along with the  $v_2$  measurement.

The systematic uncertainty on the beauty fraction  $f_B$  was estimated with the same procedure used in the current data analysis: the combined fits were repeated varying by  $\pm 10\%$  the value of the resolution function shown in Fig. 8.8 (right). The resulting variation of  $f_B$  was found to be of about 8% at  $p_T = 1$  GeV/ $c$  and linearly decreasing for increasing  $p_T$ , down to 3% at 10 GeV/ $c$ .

#### Full reconstruction of $B^+ \rightarrow \bar{D}^0 \pi^+$ decays

With the ITS upgrade, full kinematic reconstruction of beauty hadrons will become accessible. A performance study was carried out for the decay  $B^+ \rightarrow \bar{D}^0 \pi^+$  (B.R.  $\approx 0.48\%$ ,  $c\tau \approx 492 \mu\text{m}$ ), with  $\bar{D}^0 \rightarrow K^+ \pi^-$  (B.R.  $\approx 3.88\%$ ,  $c\tau \approx 123 \mu\text{m}$ ) [57].

The signal as a function of transverse momentum in Pb–Pb collisions at  $\sqrt{s_{NN}} = 5.5$  TeV in the 0–10% centrality class was estimated by scaling the FONLL [60] cross section for B meson production in pp collisions by the nuclear overlap function  $T_{AA}$  and by a model prediction for the nuclear modification factor  $R_{AA}$  [67]. Integrating in  $p_T$ , about  $(9 \pm 3) \times 10^5$  B mesons are expected in the considered decay channel with all decay tracks within the acceptance of the central barrel in  $8 \times 10^9$  Pb–Pb events ( $L_{int} = 10 \text{ nb}^{-1}$ ).

The resolution on the  $B^+ \rightarrow \bar{D}^0 \pi^+$  decay vertex is shown in Fig. 8.11, as obtained using the current ITS, the upgraded ITS with full simulation, and with the *Hybrid* method. The resolution in  $x$  and  $y$  ( $z$ ) improves by a factor of about three (six) compared to the current ITS. As also observed for the  $D^0$  vertex (Sec. 8.2.3), the *Hybrid* method yields a constantly lower resolution of about 20–30%. The performance study described in the following was carried out using the full simulation of the upgraded detector. The simulation sample consisted of  $10^6$  central Pb–Pb collisions, produced with the HIJING event generator [36], with enhanced heavy-flavour signals from the PYTHIA 6 generator [54].

The moderate production yields and the small branching ratios require an efficient selection to enhance the signal-to-background ratio. A loose set of cuts is applied for the selection of  $D^0$  candidates, including particle identification information from TPC and TOF. As a consequence of the large mass of the B meson (5.28 GeV/ $c^2$ ), the transverse

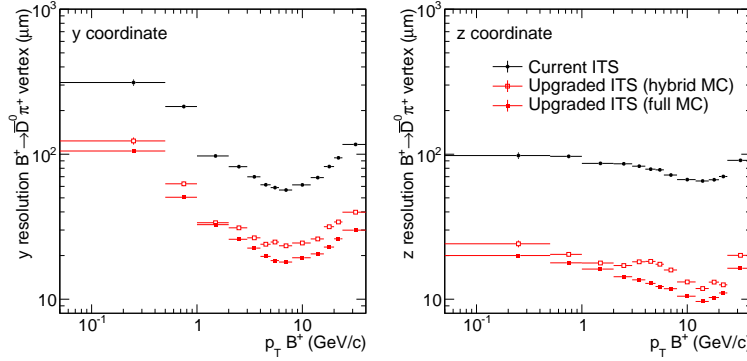


**Figure 8.11:**  $B^+ \rightarrow \bar{D}^0 \pi^+$  secondary vertex position resolution for current and upgraded ITS:  $y$  (left) and  $z$  (right) coordinates.

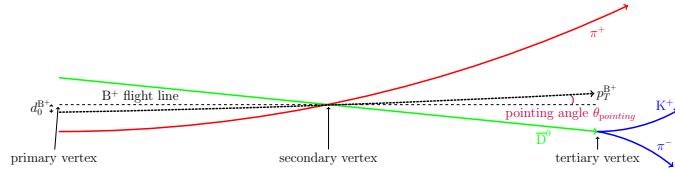


**Figure 8.12:** Topology of the decay  $B^+ \rightarrow \bar{D}^0 \pi^+$  and subsequent decay of  $\bar{D}^0 \rightarrow K^+ \pi^-$ . The reconstructed transverse momentum  $p_T^B$ , the impact parameter  $d_0^B$  and the pointing angle  $\theta_{\text{pointing}}$  are shown.

momentum of the decay tracks is typically larger than  $1 \text{ GeV}/c$ . Therefore, a large reduction of the combinatorial background is achieved by selecting pions with  $p_T > 1 \text{ GeV}/c$ . Further reduction of the background is obtained by reconstructing the secondary vertex of the  $B^+$  decay and the tertiary vertex of the  $D^0$  decay, which are separated from the primary vertex by several hundreds of  $\mu\text{m}$  (Fig. 8.12). Requirements of a large  $B$  decay length, small  $B$  impact parameter to the primary vertex and small pointing angle  $\theta_{\text{pointing}}$  are used for signal selection. These selection criteria were optimized to maximize the statistical significance as a function of  $p_T$ , using the signal and background from the simulation. The enhanced  $B^+$  signal was downscaled according to the expected production yield. Within the available simulation statistics of  $10^6$  central Pb–Pb events, the selection criteria rejected all background candidates with invariant mass in a  $\pm 3\sigma$  range around the  $B^+$  mass, while preserving a significant amount of signal. Thus, in order to increase the combinatorial background statistics, a *multiple rotations* method was applied. Each  $D^0$  candidate was combined with each pion candidate track thirteen times, rotating the track by  $180^\circ$  in azimuthal angle and then every time by  $5^\circ$ . It was verified that the rotated background reproduces the shape of the original background for the relevant selection variables. The rotational background after selections was divided by a factor of 13 to obtain an estimate of the background yield, which was then used to compute the signal-to-background ratio and the significance. In a conservative approach, a systematic uncertainty of 40 % on the background was introduced, to account for possible differences between the rotational and the original background. Figure 8.13 shows the significance (left) and the signal-to-background ratio (right) for  $8 \times 10^9$  central Pb–Pb collisions, cor-



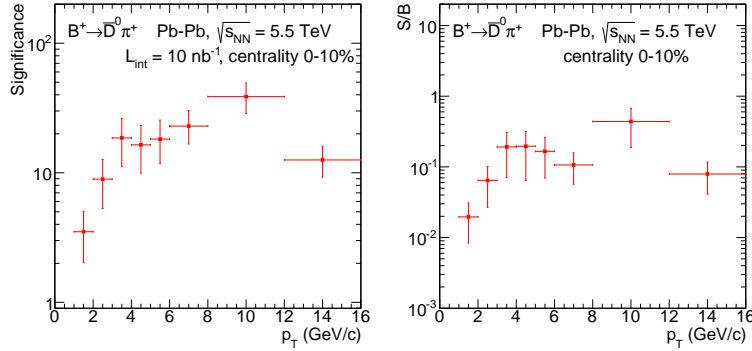


**Figure 8.13:**  $B^+ \rightarrow \bar{D}^0 \pi^+$  in Pb–Pb collisions at  $\sqrt{s_{NN}} = 5.5$  TeV: the significance (left) is scaled to  $8 \times 10^9$  events for 0–10% centrality, corresponding to  $L_{int} = 10 \text{ nb}^{-1}$ . The signal-to-background ratio is shown on the right.

responding to  $L_{int} = 10 \text{ nb}^{-1}$ . Uncertainties on the signal expectation, track rotation and statistics were taken into account and added in quadrature. Considering the uncertainties, it is expected that a significant measurement will be possible down to  $p_T$  of 2–3 GeV/c.

Further studies on more advanced selection criteria are ongoing, for example signal selection by comparison of the secondary and tertiary vertex position. However, for such an analysis, a much larger sample of simulated Pb–Pb events is needed. For this reason, a *fast-track-simulation* method, based on the parametrization of the detector performance, is currently being developed.

### 8.2.5 Heavy-flavour baryons

#### Reconstruction of $\Lambda_c^+ \rightarrow pK^-\pi^+$ decays

The most promising heavy-flavour baryon measurement is the decay of the  $\Lambda_c^+$  into three charged prongs (p,  $K^-$  and  $\pi^+$ ) with a B.R. of about 5.0% [57]. Because of the short mean proper decay length of the  $\Lambda_c$  ( $c\tau \approx 60 \mu\text{m}$  [57]), very high tracking precision is needed to separate the decay vertex from the primary vertex.

The simulation study to assess the performance with the upgraded ITS in central Pb–Pb collisions at  $\sqrt{s_{NN}} = 5.5$  TeV was carried out using the full detailed simulation and reconstruction of the new ITS. The results were compared with those obtained using a simulation of the current ITS and the *Hybrid* method with parametrized resolutions of the new detector. The HIJING event generator [36] was used to simulate Pb–Pb events in the 0–10% centrality class. The signal, added with a parametrized event generator, was scaled to the expected  $dN/dy = 1.4$  (see Tab. 8.2), with the FONLL  $p_T$  shape for  $D^{*+}$  mesons (which have a mass close to that of the  $\Lambda_c$ ). The following  $R_{AA}$  values were assumed and used to scale the signal yield: 1 for  $p_T < 4$  GeV/c, 0.7 for 4–5 GeV/c, 0.5 for 5–6 GeV/c and 0.3 for  $p_T > 6$  GeV/c. These values are consistent with the measured  $R_{AA}$  of  $\Lambda$  baryons [68].

The most effective cut variables for the reduction of the large three-prong combinatorial background are: the cosine of the pointing angle, with a typical selection  $\cos \theta_{pointing} > 0.98$ ; the decay length (distance between the primary and the secondary vertex), with a typical selection  $L > 120\text{--}180 \mu\text{m}$ , depending on  $p_T$ ; and the minimum  $p_T$  of the three decay tracks, with a typical selection  $p_T > 800 \text{ MeV/c}$ .

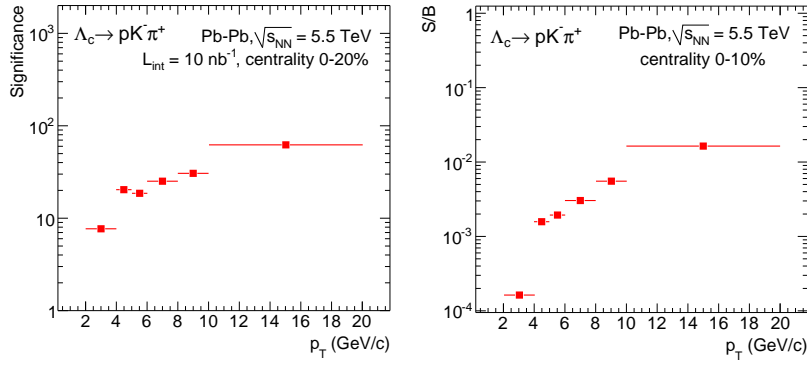


**Figure 8.14:**  $\Lambda_c \rightarrow pK\pi$  in Pb–Pb collisions at  $\sqrt{s_{\text{NN}}} = 5.5$  TeV: significance (left) and  $S/B$  ratio (right) as a function of  $p_T$ . The significance is scaled to  $1.6 \times 10^{10}$  events, which correspond to the statistics in the centrality class 0–20% for  $L_{\text{int}} = 10 \text{ nb}^{-1}$ .

The particle identification selection was implemented using cuts in units of the resolution ( $\pm 3\sigma$ ) on the measured relative to expected signals in the TPC and TOF detectors, for pions, kaons and protons.

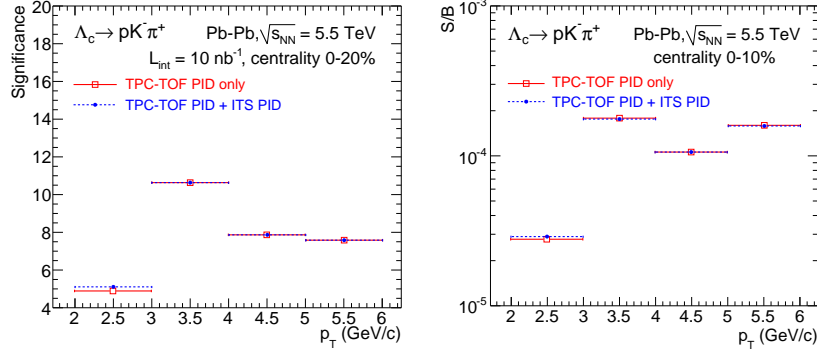
Figure 8.14 shows the significance (left) and signal-to-background ratio (right) for central Pb–Pb collisions. The significance is scaled to  $1.6 \times 10^{10}$  events, corresponding to the centrality class 0–20% for  $L_{\text{int}} = 10 \text{ nb}^{-1}$ , assuming that  $\text{significance}/\sqrt{N_{\text{events}}}$  is the same in 0–10% and in 0–20%. Using the class 0–20% (i.e. twice more events than in 0–10%), the measurement is expected to reach down to the 2–4 GeV/ $c$   $p_T$  interval, with a significance of about eight, corresponding to a statistical uncertainty of 12%.

Table 8.3 reports the comparison of the significance obtained with the full simulation of the new ITS and with the *Hybrid method*. The same event generators and selection cuts were used for the two cases. The significance values are larger for the full simulation. This is consistent with the observation of better secondary vertex resolution (see Fig. 8.1), which implies a more effective background rejection.

A dedicated study was carried out to assess the possible benefit of having particle identification (PID) capabilities in the new ITS. It has been shown [12] that instrumenting the four outermost layers with silicon strip detectors would provide PID capabilities via  $dE/dx$  with a performance, in terms for charged particle separation for  $e/\pi/K/p$ , similar to that of the current ITS. Among all heavy-flavour measurements, the  $\Lambda_c \rightarrow pK^-\pi^+$  reconstruction should be the most sensitive to low-momentum PID. The identification of the proton and kaon is important in the  $\Lambda_c$  analysis for the reduction of the very large combinatorial background. It is more crucial than for other heavy-flavour channels (e.g.  $D^0 \rightarrow K^-\pi^+$  or  $D_s^+ \rightarrow K^-K^+\pi^+$ ) because of the presence of the proton in the final state and, most importantly, because the separation of the secondary and primary vertex

**Table 8.3:** Comparison of  $\Lambda_c$  significance in  $1.6 \times 10^{10}$  central Pb–Pb collisions, as estimated with the full simulation of the new ITS or with the *Hybrid method*.

	$2 < p_T < 4 \text{ GeV}/c$	4–5	5–6	6–8	8–10	$> 10$
Full sim.	8	20	18	25	30	60
<i>Hybrid</i> sim.	8	13	11	12	12	50



**Figure 8.15:**  $\Lambda_c \rightarrow pK\pi^+$  significance (left) and  $S/B$  ratio (right), with ITS PID and without ITS PID. The same selection cuts are used in the two cases, with single track  $p_T^{\min} = 400 \text{ MeV}/c$ . The significance is scaled to  $1.6 \times 10^{10}$  events, which correspond to the statistics in the centrality class 0–20 % for  $L_{\text{int}} = 10 \text{ nb}^{-1}$ .

is much smaller ( $c\tau \approx 60 \mu\text{m}$  for  $\Lambda_c$ , with respect to  $123 \mu\text{m}$  for  $D^0$  and  $150 \mu\text{m}$  for  $D_s$ ), hence geometrical cuts are less effective.

For this study, the PID performance of the current ITS was assumed, with  $K/\pi$  ( $p/\pi$ ) separation for  $p < 0.6 \text{ GeV}/c$  ( $p < 1 \text{ GeV}/c$ ). Therefore, the cuts on the minimum  $p_T$  of single tracks were fixed to  $p_T > 0.4 \text{ GeV}/c$  (instead of  $0.8 \text{ GeV}/c$ ), in order to retain the candidates on which the ITS PID would be effective. The geometrical cuts were kept unchanged. The study used a simulation sample with the current ITS, so that the ITS PID could be enabled and disabled in the  $\Lambda_c$  selection. The tracking resolutions of the new ITS were included with the *Hybrid* method.

Figure 8.15 shows a comparison of the significance (left) and signal-to-background ratio (right) as obtained with and without ITS PID, for the same cut values and same TPC and TOF PID selection. The benefit of the ITS PID is marginal: at most 5–10 % improvement on the significance. In addition, the comparison with Fig. 8.14 shows clearly that the best results are obtained applying a larger single-track  $p_T$  threshold, which excludes the momentum region where the ITS can contribute to particle identification.

Figure 8.14 (right) shows that the signal-to-background ratio is expected to be very

**Table 8.4:** Expected systematic uncertainties for the various  $\Lambda_c$  measurements.

	Systematic uncertainty (%)					
	$N_{\Lambda_c}^{\text{Pb-Pb}}$	$N_{\Lambda_c}^{\text{pp}}$	$R_{\text{AA}}$	$(\Lambda_c/D^0)_{\text{Pb-Pb}}$	$(\Lambda_c/D^0)_{\text{pp}}$	$\frac{(\Lambda_c/D^0)_{\text{Pb-Pb}}}{(\Lambda_c/D^0)_{\text{pp}}}$
Tracking efficiency	7	7	5	2	2	2
PID	7	7	5	5	5	4
Yield extraction	5	5	7	5	5	7
MC correction	5	5	4	7	7	6
MC $p_t$ shape	3	3	5	3	3	5
Feed-down	20	10	17	20	10	17
B.R.	26	26	0	26	26	0
Total (excl. B.R.)	24	16	21	23	15	21
Total (incl. B.R.)	35	31	21	35	30	21

small:  $4 \times 10^{-4}$  in 2–3 GeV/ $c$  and  $10^{-3}$  in 3–4 GeV/ $c$ . Therefore, the signal yield extraction from the invariant mass distributions will require a dedicated strategy to minimize the systematic effects from background fluctuations and correlated backgrounds. Two main sources of background have been considered: the combinations of three uncorrelated tracks and the combinations of two or three tracks coming from a common particle decay (correlated background). The uncorrelated background accounts for a large fraction of the total background. This contribution can be estimated precisely using the event mixing technique, and subtracted from the invariant mass distribution prior to the fit that is used to extract the signal yield. The correlated background can feature structures in the invariant mass distribution that can affect the signal extraction, if they are comparable with the position and width of the  $\Lambda_c$  signal. The effect of the correlated background is discussed in detail in [12]. The conclusion of that study is that the correlated background sources are not expected to introduce a systematic bias for the  $\Lambda_c$  signal extraction.

Since  $\Lambda_c$  production was not measured in Pb–Pb so far, the estimation of the systematic uncertainty is made on the basis of the experience with D meson measurements and of the uncertainties expected for the  $D^0$  case. A summary of systematic uncertainties for the  $\Lambda_c$  yield, for the  $R_{AA}$  and the  $\Lambda_c/D^0$  ratio is given in Tab. 8.4. Some of the uncertainties cancel to some extent in the ratio observables.

The expected performance for the measurement of the  $\Lambda_c$   $R_{AA}$ , of the  $\Lambda_c/D^0$  double ratio in Pb–Pb relative to pp collisions and of the  $\Lambda_c$   $v_2$  will be presented in Sec. 8.2.6.

The possible advance of extending the  $\Lambda_c \rightarrow pK\pi$  reconstruction beyond the pseudorapidity acceptance of the TPC and TOF detectors ( $|\eta| < 0.9$ ), using ITS standalone tracks, was studied. The acceptance of the new ITS in the baseline scenario described in this document is  $|\eta| < 1.3$ . The case  $|\eta| < 1.5$  was considered for this study, in order to assess the benefit of a more extended coverage. In the region of  $|\eta|$  between 0.9 and 1.5, in addition to lacking particle identification information from TPC and TOF, the ITS standalone tracks would have a poorer momentum resolution, because of the shorter lever arm, and a poorer impact parameter resolution at low  $p_T$ , because of the larger multiple scattering for inclined tracks. These effects were neglected, assuming the same tracking precision as for tracks reconstructed in both the ITS and the TPC. The study was carried out starting from the simulation results in  $|\eta| < 0.9$  (described in this section) and using generator-level estimations of the signal and background to compute the contributions of the region up to  $|\eta| = 1.5$ . The signal is observed to increase by a factor of up to 3–4 at  $p_T \approx 2$  GeV/ $c$ , but the background increases by a larger factor, about 5, because of the lack of rejection by particle identification. The signal-to-background ratio decreases by about 30–40 %, while the statistical significance increases by 30–40 % at low  $p_T$  and 10 % at high  $p_T$ . Considering that the poorer tracking resolution was not accounted for, this represents an upper limit of the gain in significance. The conclusion is that, for the  $\Lambda_c$  measurement, there is no strong advantage in extending the acceptance of the ITS.

### Reconstruction of $\Lambda_b \rightarrow \Lambda_c^+ \pi^-$ decays

The  $\Lambda_b$  reconstruction was investigated considering its decay to  $\Lambda_b \rightarrow \Lambda_c^+ \pi^-$  (and charge conjugates), where the  $\Lambda_c^+$  further decays to a  $pK^-\pi^+$  final state. This decay has a combined branching ratio of approximately  $0.6\% \times 5\% = 3 \times 10^{-4}$  [57]. The mean proper decay lengths of the  $\Lambda_b$  and  $\Lambda_c$  are, respectively, 417  $\mu\text{m}$  and 59  $\mu\text{m}$  [57]. Therefore, the separation from the primary vertex is much larger for the  $\Lambda_b$  than for the  $\Lambda_c$ . Nevertheless, given the small production yields (see Tab. 8.2) and the large combinatorial background for a four-prong final state, a selection strategy with very tight topological cuts is required.

The study used a sample of about  $10^6$  central Pb–Pb events at  $\sqrt{s_{NN}} = 5.5$  TeV, generated with HIJING [36], including the full simulation and reconstruction of the new ITS.

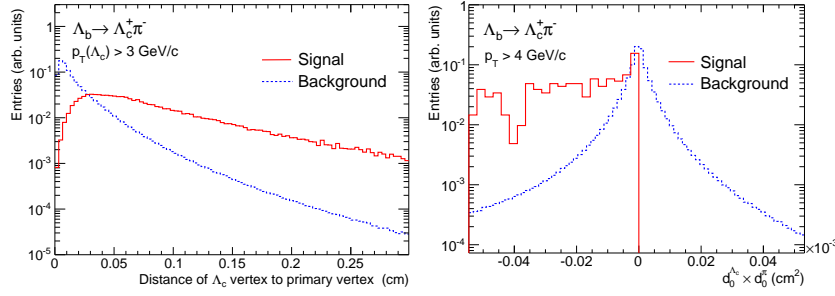


**Figure 8.16:** Distance of the  $\Lambda_c$  vertex from the primary vertex for  $\Lambda_c$  from  $\Lambda_b$  decay and for the background (left). Product of the  $\Lambda_c$  and pion impact parameters,  $d_0^{\Lambda_c} \times d_0^\pi$ , for  $\Lambda_b$  signal and for the background (right).

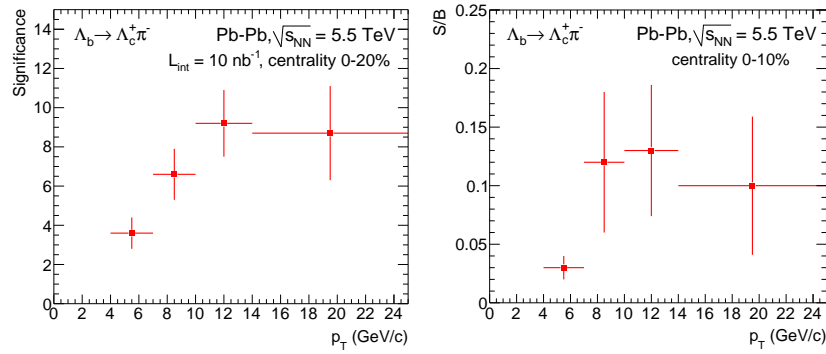


**Figure 8.17:**  $\Lambda_b \rightarrow \Lambda_c^+ \pi^-$  in Pb-Pb collisions at  $\sqrt{s_{NN}} = 5.5$  TeV: significance for  $L_{int} = 10$  nb<sup>-1</sup> (left) and  $S/B$  ratio (right) as a function of  $p_T$ .

Twenty  $\Lambda_b$  particles, with decays forced in the channels of interest, were added to each Pb-Pb event. The signal was then scaled using the  $p_T$  distribution of B mesons from the FONLL calculation [60], normalized to the expected yield, given in Tab. 8.2.

The  $\Lambda_b$  reconstruction starts from  $\Lambda_c \rightarrow pK\pi$  candidates, which are selected with similar particle identification and topological criteria as described in the previous section and required to have invariant mass within  $\pm 3\sigma$  of the  $\Lambda_c$  mass. These candidates are then combined with the opposite-sign tracks with  $p_T > 1-2$  GeV/c (depending on the  $\Lambda_b$   $p_T$ ) and a tertiary vertex is reconstructed. The  $\Lambda_b$  selection strategy is similar to that used for the  $B^+$  reconstruction. The selection of a large distance of the  $\Lambda_c$  vertex from the primary vertex is among the most effective cuts to reject the combinatorial background, because of the larger  $c\tau$  of the  $\Lambda_b$ . The distribution of this distance for signal and background is shown in the left-hand panel of Fig. 8.16. The product of the impact parameters of the  $\Lambda_c$  and of the pion (right-hand panel of Fig. 8.16) and the pointing angle of the  $\Lambda_b$  are exploited as well.

The limited simulation sample was not sufficient to optimize the selection cuts, because the number of background candidates were reduced to very small levels. In order to increase the background statistics, the *multiple rotations* method, also used for the  $B^+ \rightarrow$

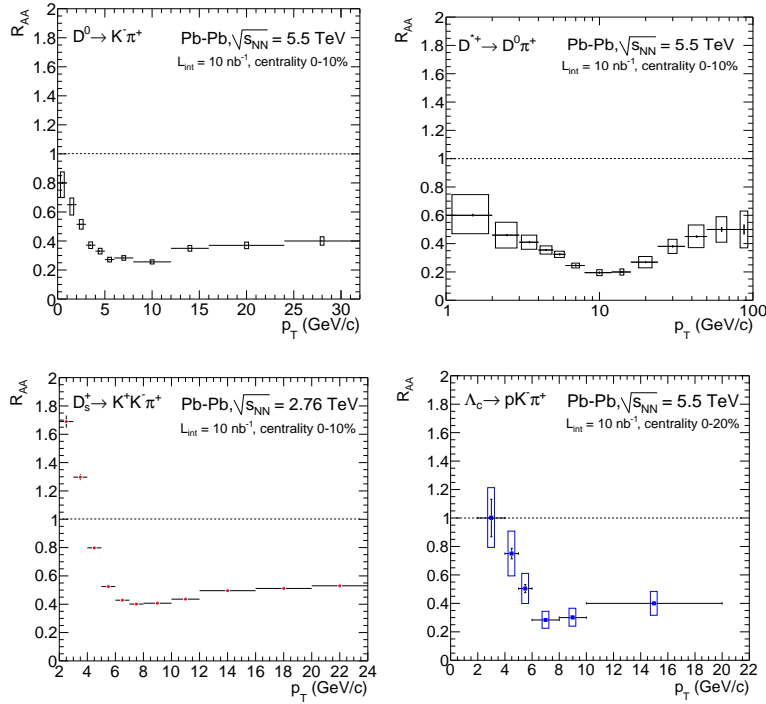
$\bar{D}^0 \pi^+$  study, was applied. The pion candidate tracks that are associated to the  $\Lambda_c$ 's were rotated multiple times in azimuthal angle in steps of  $5^\circ$ . For this study, 13 to 20 rotations were applied, depending on the  $p_T$  interval. As for the case of  $B^+$  reconstruction, a systematic uncertainty of 40 % was associated with the procedure, to account for a possible inaccuracy in the background description with the track rotation method.

Figure 8.17 shows the significance (left) and signal-to-background ratio (right) for central Pb–Pb collisions. The error bars include the statistical uncertainty from the simulation and the systematic uncertainty associated with the track rotation method. The significance is scaled to  $1.6 \times 10^{10}$  Pb–Pb events, as expected in the 0–20 % centrality class for an integrated luminosity of  $10 \text{ nb}^{-1}$ . The observation of the  $\Lambda_b$  signal could be possible down to  $p_t = 4 \text{ GeV}/c$ . From  $p_T > 7 \text{ GeV}/c$  the significance is larger than 5, corresponding to a statistical uncertainty on the yield smaller than 20 %.

### 8.2.6 Heavy flavour $R_{AA}$ and $v_2$

#### Charm and beauty nuclear modification factors

The expected performance on the nuclear modification factor of  $D^0$ ,  $D^{*+}$ ,  $D_s^+$  and  $\Lambda_c^+$  is shown in Fig. 8.18 for an integrated luminosity of  $10 \text{ nb}^{-1}$ . The expected performance on



**Figure 8.18:** Nuclear modification factor of  $D^0$  (top-left),  $D^{*+}$  (top-right),  $D_s^+$  (bottom-left, only statistical uncertainties) and  $\Lambda_c^+$  (bottom-right) for central Pb–Pb collisions ( $L_{\text{int}} = 10 \text{ nb}^{-1}$ ).

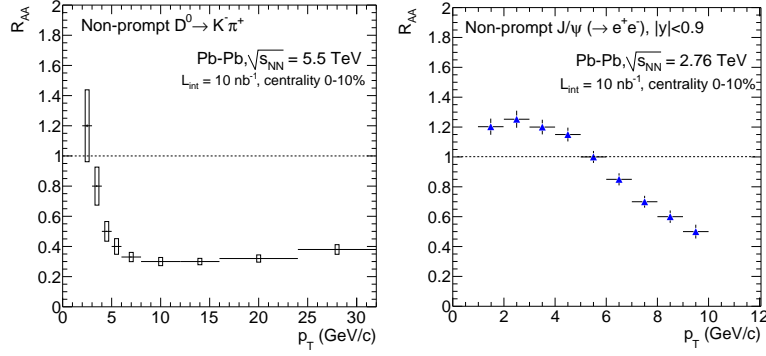


**Figure 8.19:** Nuclear modification factor of  $D^0$  from B decays (left) and  $J/\psi$  from B decays (right, only statistical uncertainties) for central Pb–Pb collisions ( $L_{int} = 10$  nb $^{-1}$ ).

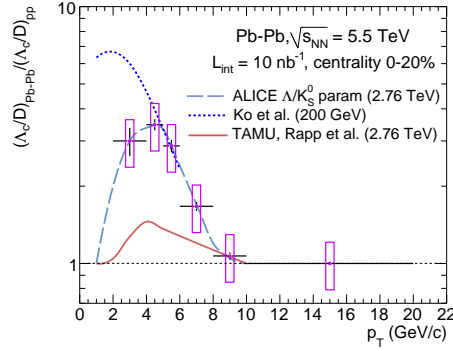


**Figure 8.20:** Enhancement of the  $\Lambda_c/D^0$  ratio in central Pb–Pb (0–20% for  $L_{int} = 10$  nb $^{-1}$ ) with respect to pp collisions. Two model calculations [62, 69] are also shown.

the nuclear modification factor of  $D^0$  and  $J/\psi$  from B decays is shown in Fig. 8.19. For prompt and non-prompt  $D^0$  mesons, the uncertainties for  $p_T > 16$  GeV/c were extrapolated from those estimated at low  $p_T$ . For all particles, it is assumed that the pp reference has negligible statistical uncertainties with respect to Pb–Pb. Some of the systematic uncertainties are partly cancelled in the ratio (tracking and cut selection efficiency).

Figure 8.20 shows the enhancement of the  $\Lambda_c/D^0$  ratio in central Pb–Pb (0–20% for  $L_{int} = 10$  nb $^{-1}$ ) with respect to pp collisions. It is assumed that the statistical uncertainties for the  $D^0$  measurements and for the  $\Lambda_c$  measurement in pp are negligible with respect to those for the  $\Lambda_c$  measurements in Pb–Pb. The points are drawn on a line that captures the trend and magnitude of the  $\Lambda/K_S^0$  double-ratio. Two model calculations [62, 69] are shown to illustrate the expected sensitivity of the measurement.

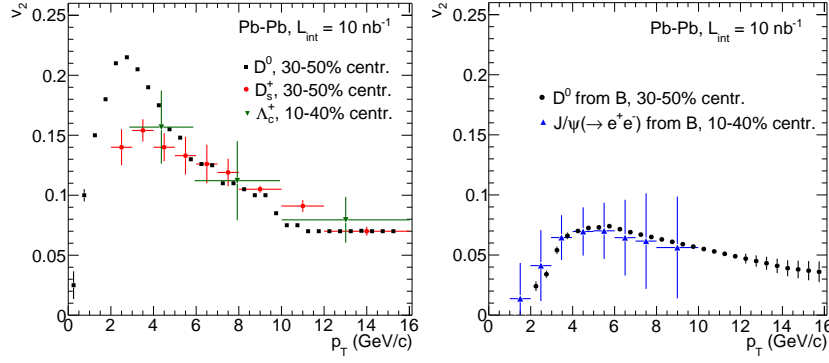


**Figure 8.21:**  $v_2$  of  $D^0$ ,  $D_s^+$  and  $\Lambda_c$  (left) and of  $D^0$  and  $J/\psi$  from B decays (right) with estimated statistical uncertainties for  $L_{\text{int}} = 10 \text{ nb}^{-1}$ .

### Charm and beauty $v_2$

The expected precision on the measurement of  $v_2$  was estimated for  $D^0$  and  $D_s^+$  mesons and for  $D^0$  from B decays and  $J/\psi$  from B decays, with the upgraded ITS and with an integrated luminosity of  $10 \text{ nb}^{-1}$ .

For  $D^0$ ,  $D_s^+$  and  $D^0$  from B decays, the statistical uncertainties obtained from the simulation studies were scaled, considering that the significance/event is the same for central and semi-central events (30–50 %). This feature is observed in the  $D^0$  [61] and  $D_s^+$  data analyses. For the  $\Lambda_c$ , the statistical uncertainties were scaled from central to semi-central events (10–40 %) using a scaling with  $\langle N_{\text{coll}} \rangle$  for the signal and a scaling factor obtained from the data for the background. For  $J/\psi$  from B decays, a dedicated study to assess the significance in the class 10–40 % was carried out. The centrality class 10–40 % was found to be optimal for the measurements with lower significance, because the signal yield and the expected number of events are larger than in 30–50 %.

The  $v_2$  measurement can be performed using the raw signal yields in two large intervals of azimuthal angle  $\varphi$  with respect to the Event Plane (EP) direction  $\Psi_{\text{EP}}$ , determined for each collision [70]:  $[-\pi/4 < \Delta\varphi < \pi/4] \cup [3\pi/4 < \Delta\varphi < 5\pi/4]$  (in-plane) and  $[\pi/4 < \Delta\varphi < 3\pi/4] \cup [5\pi/4 < \Delta\varphi < 7\pi/4]$  (out-of-plane). Given the in-plane and out-of-plane yields,  $N_{\text{in}}$  and  $N_{\text{out}}$ , one has  $v_2 = (\pi/4) \cdot (N_{\text{in}} - N_{\text{out}})/(N_{\text{in}} + N_{\text{out}})$ . In order to measure separately  $v_2$  for prompt (charm) and secondary (beauty) D and  $J/\psi$  mesons, the prompt fraction will be determined for the in-plane and out-of-plane signal using the impact parameter and pseudo-proper decay length fits described in the previous sections. The statistical uncertainties on  $v_2$  were estimated considering that the relative statistical uncertainties on  $N_{\text{in}}$  and  $N_{\text{out}}$  are  $\sqrt{2/(1 \pm v_2)}$  times larger, respectively, than those on the total raw yield  $N_{\text{tot}}$ . This results in the absolute statistical uncertainty  $\sigma_{v_2} \approx (\pi/4) \cdot (1 - (4v_2/\pi)^2)/\sqrt{1 - v_2^2} \cdot (\sigma_{N_{\text{tot}}}/N_{\text{tot}})$ . The actual numerical values of the uncertainties were calculated using  $v_2(p_T)$  for charm and beauty mesons, as in the predictions of the BAMPS model [71].

Figure 8.21 (right) shows the  $v_2$  for charm (left) and beauty (right) with the statistical uncertainties for  $L_{\text{int}} = 10 \text{ nb}^{-1}$ . The systematic uncertainties can be expected to be rather small, since most of them are common for the  $N_{\text{in}}$  and  $N_{\text{out}}$  raw yields and cancel in the  $v_2$  ratio.



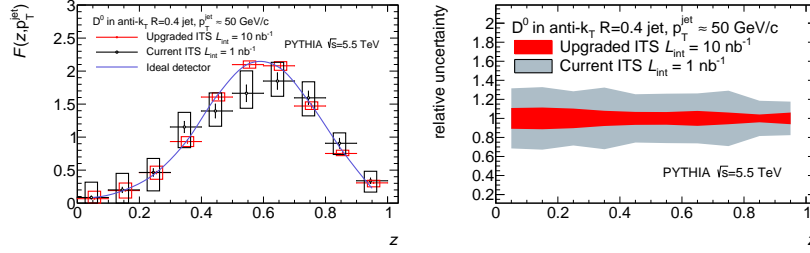


**Figure 8.22:** Projected D-jet fragmentation  $z$  distribution for 50 GeV/ $c$   $c$  quark jets in central (0–10 %) Pb–Pb collisions for the current detector for 1  $\text{nb}^{-1}$  and upgraded detector for 10  $\text{nb}^{-1}$  (left). Comparison of the total uncertainties (systematic and statistical added in quadrature) for the two cases (right).

### 8.2.7 D meson fragmentation function in jets

The upgraded detector and the large integrated luminosity will enable the study of charm production in jets in heavy-ion collisions, over a large range of the fragmentation momentum fraction  $z = p_T^D/p_T^{\text{jet}}$ . Such measurements may provide insight into the energy loss of high-momentum leading charm quarks, resulting in lower momentum (lower  $z$ ) open charm particles reconstructed in jets, as well as on the importance of gluon splitting in heavy-flavour production [72]. The improved reconstruction of the various heavy-flavour decay channels will largely enhance the performance for tagging jets that contain heavy flavour.

Simulation studies with the new ITS show a modest improvement in the jet reconstruction performance (with the anti- $k_T$  algorithm and a radius  $R = 0.4$ ): both the jet energy resolution and jet energy scale determination are expected to improve by about 5 % as compared to the current apparatus [73]. Concurrently, the large statistics recorded after LS2 will have a strong impact on the precision of the background characterization, resulting in improved systematic uncertainties on measurements in heavy-ion collisions. Moreover, the large signal-to-background ratio for D meson reconstruction with the new ITS will directly improve the capabilities for studying the details of  $c$ -quark jet fragmentation.

Figure 8.22 shows the projected performance for the measurement of the fragmentation function of  $D^0$  mesons within charm quark induced jets ( $45 < p_T < 55 \text{ GeV}/c$ ) in central Pb–Pb collisions (0–10 % centrality class). The fragmentation function shape was extracted from pp simulations with PYTHIA 8 [74]. The statistical and systematic uncertainties for the current setup for 1  $\text{nb}^{-1}$  and upgraded ITS with 10  $\text{nb}^{-1}$  are shown.

For the evaluation of the measurement precision, the following parameters were considered:

- Statistics of D meson within jets for 1 and 10  $\text{nb}^{-1}$  (including branching ratios of charm quark and  $D^0$  hadronic decays) within the 10 % most central Pb–Pb collisions and EMCAL acceptance estimated using FONLL predictions [60];
- Systematic uncertainties due to D meson reconstruction (discussed in Sec. 8.2.3);
- Systematic uncertainties due to corrections for the detector effects (jet energy scale and jet energy resolution) for fully reconstructed jets with the two (current and upgraded) ALICE setups.

The reported error bars include the uncertainties from the unfolding procedure (correction for detector effects) done via Singular Value Decomposition [75].

The existing measurements of inclusive jets suggest that the modifications of the fragmentation pattern is rather modest. Expecting a similar, subtle effect, for the D meson fragmentation, it is clear that a high precision over the complete  $z$  range is crucial. In this respect, the fragmentation pattern shown in the left panel of Fig. 8.22 is an illustration based on an assumed shape of the distribution. The right panel of Fig. 8.22 illustrates the relative total uncertainty on the measurement.

## 8.3 Low-mass dielectrons

### 8.3.1 Motivation

Electromagnetic radiation is produced at all stages of the collision, and since leptons couple only weakly to the surrounding medium, their spectrum retains information of the entire system evolution. The fundamental questions to be addressed by a comprehensive measurement of thermal dileptons in heavy-ion collisions at the LHC are the following (for a more detailed discussion see [4, 12]):

- The generation of hadron masses, which is driven by the spontaneous breaking of QCD chiral symmetry in the vacuum. Chiral restoration leads to substantial modifications of the vector and axial-vector spectral functions. Such modifications, in particular of the  $\rho$  meson, can be inferred from low-mass dilepton spectra.
- The temperature of the emitting medium. The invariant mass of thermal dileptons, in particular, is not subject to blue-shift in collectively expanding systems and therefore is most directly related to temperature. The study of low-mass dileptons allows also an estimate of real direct photon production.
- The space-time evolution of the system. The fireball lifetime can be extracted from low-mass dilepton measurements. The potential to disentangle early from late contributions gives access to the evolution of collectivity and, thus, to fundamental properties such as transport coefficients, viscosity, and the equation of state.

### 8.3.2 Experimental aspects and simulation inputs

The measurement of low-mass  $e^+e^-$  pairs in Pb–Pb collisions at LHC energies poses major experimental challenges, because it requires acceptance for dilepton pairs at invariant masses and transverse momenta as low as  $M_{ee} \approx p_{T,ee} \approx T \approx 150$  MeV. This implies electron detection down to  $p_T = 0.1\text{--}0.2$  GeV/ $c$ . Since the production rates of thermal dileptons are low (suppressed by  $\propto \alpha_{\text{e.m.}}^2$ ), a very good electron identification is mandatory for the suppression of combinatorial background from hadronic contamination. Moreover, electrons from  $\pi^0$  Dalitz decays and photon conversions (mainly from  $\pi^0 \rightarrow \gamma\gamma$ ) form a substantial combinatorial background. This demands a low material budget before the first active detector layer and offline strategies to detect  $e^+e^-$  pairs from photon conversions and Dalitz pairs for further rejection. The large combinatorial background prevents also a straightforward online trigger scheme. Therefore, the analysis will be carried out using minimum-bias samples.

The enhanced low- $p_T$  tracking capability of the upgraded ITS allows the track of electrons down to  $p_T \geq 0.05$  GeV/ $c$ , improving the reconstruction efficiency of photon conversions and Dalitz pairs for combinatorial background suppression. The better impact parameter resolution of the upgraded ITS also enables efficient tagging of electrons from semi-leptonic charm decays, which can be separated from prompt dileptons. In order to

optimize the low- $p_T$  acceptance for electron identification with the TPC and TOF detectors, the measurement will be carried out with a reduced value of 0.2 T for the magnetic field in the ALICE central barrel.

The study presented here is an update of the results included in the ITS Upgrade CDR [12] and in the ALICE Upgrade LOI [4] (see these documents for full details on the methodology and the signal and background inputs). In the present analysis, the possible benefit of separating electrons from charged hadrons at very low momentum using PID information from the ITS has also been investigated. Results are presented at the level of the final statistical and systematic uncertainties.

The physics performance is given for an integrated luminosity  $L_{\text{int}} \approx 3 \text{ nb}^{-1}$ , which can be collected in one month in a dedicated Pb–Pb run with the ALICE barrel field at 0.2 T. The corresponding number of events is  $2.5 \times 10^9$  in the centrality class 0–10 %, and  $5 \times 10^9$  in the class 40–60 %.

A realistic physics input into the simulation of the expected dilepton signal is mandatory in order to achieve a solid estimate of the physics performance. To this end, these dielectron contributions were considered (see [4] for the details):

- The hadronic cocktail, including contributions from the decays of light pseudoscalar and vector mesons.
- The contribution from correlated semi-leptonic charm decays.
- The calculation of thermal dilepton radiation from the hadronic phase and the QGP, based on a hadronic many-body approach [76] and on perturbative emission rates.
- Medium-modified spectral functions and a realistic space-time evolution [77].

The measured dilepton yield is dominated by  $e^+e^-$  combinatorial pairs, which arise from random combinations of tracks from uncorrelated decays, mainly  $\pi^0$ -Dalitz, and from conversions. In order to estimate the combinatorial background, a sample of simulated pp events with a realistic modelling of conversions via the GEANT3 transport code and a detailed description of the ALICE apparatus was utilised. In turn, to mimic the combinatorial background in Pb–Pb, a number of pp events were overlaid to match the corresponding  $\langle dN_{\text{ch}}/d\eta \rangle$  in semi-central or central Pb–Pb collisions.

### 8.3.3 Electron reconstruction and background rejection

Electron reconstruction is based on charged particle tracking in the ITS and the TPC. Particle identification is included from the TPC, where a  $\pm 3\sigma$  band of the  $dE/dx$  resolution around the nominal electron peak position is applied. It is furthermore assumed that the performance of the upgraded TPC in terms of tracking efficiency and  $dE/dx$  resolution is the same as for the current TPC. Additionally, a TOF signal within  $\pm 3\sigma$  of the TOF resolution around the nominal electron position is required to suppress hadrons at  $p < 3 \text{ GeV}/c$ . Operation at the nominal magnetic solenoid field of  $B = 0.5 \text{ T}$  implies that soft particles do not reach the TOF, leading to a drastic efficiency loss for  $p_T < 0.4 \text{ GeV}/c$ . Therefore, a dedicated running period with a reduced magnetic field of  $B = 0.2 \text{ T}$  is foreseen for the measurement of low-mass dileptons. This improves the acceptance for low- $p_T$  electrons in TOF down to  $p_T \sim 0.2 \text{ GeV}/c$ .

The combinatorial background contribution can be estimated by means of like-sign pair combinations or event-mixing techniques, and subtracted from the unlike-sign distribution. However, a small signal-to-background ratio limits the statistical significance of the signal and a systematic uncertainty can arise from the background subtraction method. To minimize the contribution of combinatorial pairs, leptons from conversions and Dalitz

decays must be identified and removed from the sample. To this end, one exploits the improved stand-alone tracking efficiency of the upgraded ITS. As discussed above, the tracks from the global tracking are limited to  $p_T > 0.2$  GeV/c. In the ITS stand-alone tracking, the tracks from the remaining ITS hits not used in the global tracking are reconstructed. These tracks are added to those from the global tracking extending the tracking down to  $p_T \sim 0.06$  GeV/c. In the dielectron pairs from a conversion or  $\pi^0$ -Dalitz decay, one partner has typically very low energy. Therefore, using also ITS stand-alone tracks, the probability of tagging the tracks from a conversion or Dalitz decay is maximized. Pairs are rejected if they form a “close pair” with small invariant mass ( $M_{ee} < 0.01$  GeV/c<sup>2</sup>) and small opening angle ( $\theta_{ee} < 0.05$ ).

The possible benefit of particle identification of the ITS stand-alone tracks was investigated. To this end, the particle identification capability of the current ITS was assumed. The usage of the ITS PID to identify soft electron partners from conversion allows one to have a smaller reduction of signal when applying the “close pair” rejection ( $\sim 40\%$  with PID versus  $\sim 60\%$  without PID). This is due to the fact that, with the PID, the rejection of pairs that are not from a conversion or a Dalitz decay is minimized. Also, the rejection of the combinatorial background is slightly less effective, but, overall, the signal-to-background ratio is larger if the ITS PID is used. The effect on the significance will be quantified in the following.

Another important feature of the upgraded ITS is the improved capability to separate prompt from displaced electrons. Prompt electrons originate from all thermal sources and decays of the mesons ( $\rho$ ,  $\omega$ ,  $\phi$ , and the Dalitz decays of  $\pi^0$ ,  $\eta$ ,  $\eta'$ ,  $\omega$ ). Displaced electrons include those from semi-leptonic decays of charmed hadrons and conversions in the detector material. The separation is based on the impact parameter ( $d_0$ ) to the primary vertex in the transverse plane, which can be measured with significantly improved resolution with the upgraded ITS. Figure 8.23 shows the efficiency of displaced electrons from conversions and charm decays for the current and the upgraded ITS, as a function of the prompt efficiency. While the separation of displaced electrons from charm is significantly improved with the upgraded ITS, there is only a small improvement for conversions. The reason is that the upgraded ITS requires also a new beam pipe with smaller radius, which is the main converter before the first detector layer. The smaller lever arm to the primary vertex compensates the improved intrinsic resolution of the upgraded ITS. On the other hand, a tight cut on the  $d_0$  reduces the ratio of electrons from charm over prompt electrons by more than a factor of two, implying a reduction of the ratio of pairs from correlated charm decays over prompt pairs by a factor of about five. This improved capability of the upgraded ITS is one of the key features of the ALICE upgrade to enable a measurement of thermal radiation at the LHC despite the large background from charm, as will be demonstrated below.

### Systematic uncertainties

The dominant sources of systematic uncertainties on the dilepton measurement arise from the large combinatorial and physical backgrounds.

The relative systematic uncertainty on the combinatorial background  $\Delta B/B$  propagates into the extracted inclusive dilepton signal error as  $\Delta S/S = \Delta B/B \cdot B/S$ . Therefore, the effect of the ITS PID on the  $S/B$  ratio has also a direct impact on the systematic uncertainty, as we will show in the next section. A conservative assumption  $\Delta B/B = 0.25\%$  was adopted, which corresponds to the uncertainty quoted by the PHENIX Collaboration for a similar analysis [78]. The systematic uncertainty on  $S$  is calculated bin-by-bin on the basis of the corresponding  $S/B$ .

A measurement of the thermal excess yield requires a precise subtraction of the had-

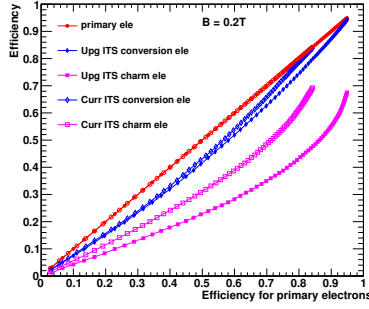


**Figure 8.23:** Efficiency for electrons from charm (magenta) and conversions (blue) as a function of the efficiency for prompt (primary) electrons, for current ITS (open symbols) and upgraded ITS (full symbols).

ronic cocktail and the contribution from charm from the inclusive dilepton yield. For the hadronic cocktail and the subtraction of the charm contribution, relative uncertainties of 10 % and 20 %, respectively, were assumed.

### 8.3.4 Results on physics performance

In the following, the results of the physics performance study are discussed.

The expected inclusive  $e^+e^-$  invariant mass spectrum (left-hand panel) and the excess spectrum (right-hand panel) are shown in Fig. 8.24 (without ITS PID) and in Fig. 8.25 (with ITS PID).

The left-hand panel of Fig. 8.26 shows the significance, normalized to one event, without ITS PID (solid green) and with ITS PID (dashed blue). The right-hand panel shows the ratio. The lack of PID information from the ITS implies a 10–20 % reduction of the significance.

Information on the early temperature of the system can be derived from the invariant-mass dependence of the dilepton yield at masses  $M_{ee} > 1.1 \text{ GeV}/c^2$  where the yield is completely dominated by the thermal radiation from the QGP. In order to quantify the sensitivity of the anticipated measurement, an exponential fit to the simulated spectra in the invariant mass region  $1.1 < M_{ee} < 2 \text{ GeV}/c^2$  was used. In particular, the fit function was  $dN_{ee}/dM_{ee} \propto M_{ee}^{3/2} \exp(-M_{ee}/T_{\text{fit}})$ . The fit parameter  $T_{\text{fit}}$  is compared to  $T_{\text{real}}$ , which is derived from the same fit to the thermal input spectrum. The ratio  $T_{\text{fit}}/T_{\text{real}}$  for Pb–Pb collisions in the 0–10 % centrality class is shown in Fig. 8.27. The temperature of the source emitting the thermal dileptons can be measured with a precision of 8 % if the ITS PID is used and 11 % if it is not used. This results from the deterioration by 15–20 % in the significance of the excess spectrum, shown in Fig. 8.26. The systematic uncertainty is estimated to be of about 20 %, independent of the usage of the ITS PID.

## 8.4 Hypernuclei

A hypernucleus [79, 80] is a nucleus that contains at least a strange baryon (hyperon) in addition to protons and neutrons. The lifetime of a hypernucleus depends on the strength of the hyperon–nucleon (YN) interaction. The study of this interaction is relevant for nuclear physics and nuclear astrophysics. For example, it plays a key role in understanding the

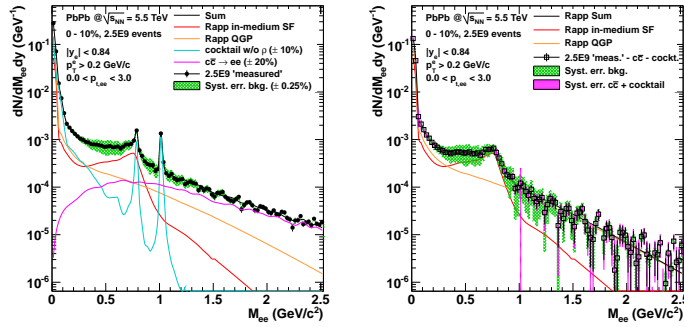


**Figure 8.24:** Inclusive  $e^+e^-$  invariant mass spectrum (left) and excess spectrum (right) for 0–10% most central Pb–Pb collisions at  $\sqrt{s_{NN}} = 5.5$  TeV,  $2.5 \times 10^9$  events. Tight  $d_0$  cut is applied. ITS PID is not applied. The green boxes show the systematic uncertainties from the combinatorial background subtraction, the magenta boxes indicate systematic uncertainties related to the subtraction of the cocktail and charm contribution.

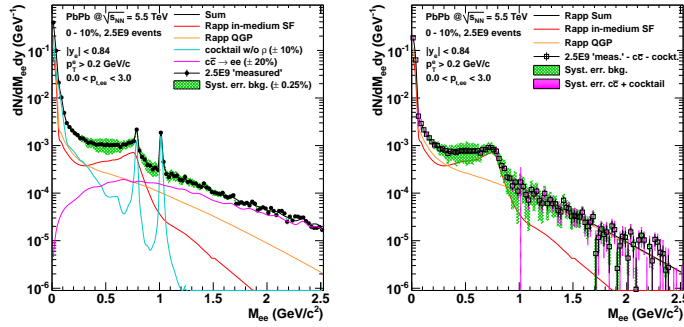


**Figure 8.25:** Inclusive  $e^+e^-$  invariant mass spectrum (left) and excess spectrum (right) for 0–10% most central Pb–Pb collisions at  $\sqrt{s_{NN}} = 5.5$  TeV,  $2.5 \times 10^9$  events. Tight  $d_0$  cut is applied. ITS PID is not applied. The green boxes show the systematic uncertainties from the combinatorial background subtraction, the magenta boxes indicate systematic uncertainties related to the subtraction of the cocktail and charm contribution.

structure of neutron stars. Depending on the strength of the YN interaction, the collapsed stellar core could consist of hyperons, strange quark matter, or a kaonic condensate.

The study of the production of  ${}^3_\Lambda\text{H}$ ,  ${}^4_\Lambda\text{H}$  and  ${}^4_\Lambda\text{He}$  via their mesonic weak decays is addressed here. In particular, the following decay channels (and charge conjugates) are considered:

$${}^3_\Lambda\text{H} \rightarrow {}^3\text{He} + \pi^-, \quad {}^4_\Lambda\text{H} \rightarrow {}^4\text{He} + \pi^-, \quad {}^3_\Lambda\text{He} \rightarrow {}^3\text{He} + \pi^- + p.$$

The Pb–Pb data set collected by ALICE in 2011 only allowed for the detection of the hypertriton  ${}^3_\Lambda\text{H}$  and anti-hypertriton  ${}^3_{\bar{\Lambda}}\text{H}$  with poor significance. The detection of heavier (anti)-hypernuclei is precluded with the present statistics.

Like for the heavy-flavour analyses, the benefit of the ALICE upgrade for the detection of heavy nuclear states will be two-fold. On one hand, the main advantage will originate from

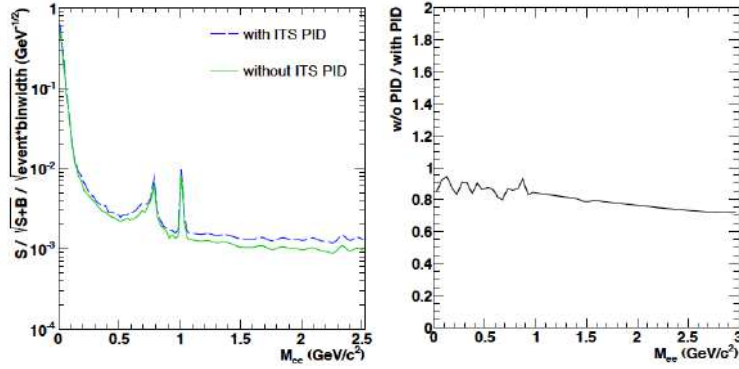


**Figure 8.26:** Significance versus pair invariant mass with no ITS PID and with ITS PID (left). Ratio of the significances without ITS PID / with ITS PID (right).

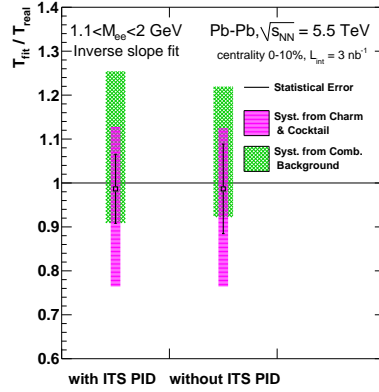


**Figure 8.27:** Expected relative uncertainty on the extraction of the  $T$  parameter from a fit to the invariant mass excess spectrum in  $1.1 < M_{ee} < 2 \text{ GeV}/c^2$  (see text). The results are shown for different scenarios, with tight  $d_0$  cuts, and for 0–10% event centrality. Error bars show the statistical uncertainties. The green boxes show the systematic uncertainties from the combinatorial background subtraction, the magenta boxes indicate systematic uncertainties related to the subtraction of the cocktail and charm contribution.

the very large statistics of minimum-bias Pb–Pb events that can be collected after LS2. On the other hand, the improved tracking resolution of the new ITS will determine a better separation of the reconstructed signal decays from the large combinatorial background of uncorrelated secondary tracks, thus increasing the statistical significance.

An estimation of the expected yields for hypernuclei with the upgraded ALICE detector was made for  $8 \times 10^9$  collisions in the 0–10% centrality class, corresponding to  $L_{\text{int}} = 10 \text{ nb}^{-1}$ . The  ${}^3_{\Lambda}\text{H}$ ,  ${}^4_{\Lambda}\text{H}$  and  ${}^4_{\Lambda}\text{He}$  yields per unit of rapidity at central rapidity ( $dN/dy$ ) predicted by the statistical hadronization model for central Pb–Pb collisions at  $\sqrt{s_{\text{NN}}} = 5.5 \text{ TeV}$  are reported in [81]. For the value of the chemical freeze-out temperature that

**Table 8.5:** Expected yields for three hypernuclear states (plus their antiparticles) for central Pb–Pb collisions (0–10 %) at  $\sqrt{s_{NN}} = 5.5$  TeV. From left to right: hypernuclear species, production yield from the thermal model [81], branching ratio of the considered hypernuclear mesonic weak decay, average acceptance-times-efficiency  $\langle \text{Acc} \times \varepsilon \rangle$  for  $p_T > 0$  and  $|y| < 1$ , and number of expected reconstructed decays for  $L_{\text{int}} = 10 \text{ nb}^{-1}$ .

State	$dN/dy$ [81]	B.R.	$\langle \text{Acc} \times \varepsilon \rangle$	Yield
${}^3_{\Lambda}\text{H}$	$1 \times 10^{-4}$	25 % [82]	11 %	44000
${}^4_{\Lambda}\text{H}$	$2 \times 10^{-7}$	50 % [82]	7 %	110
${}^4_{\Lambda}\text{He}$	$2 \times 10^{-7}$	32 % [83]	8 %	130

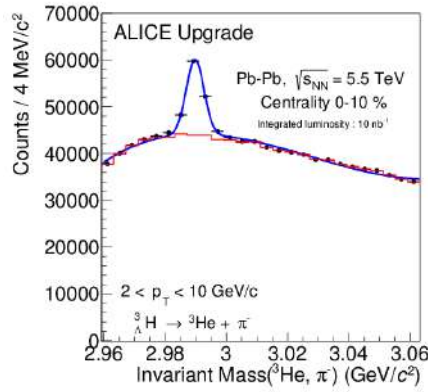


**Figure 8.28:** Expected invariant mass distribution for  ${}^3_{\Lambda}\text{H}$  (plus antiparticle) reconstruction in Pb–Pb collisions (0–10 % centrality class), corresponding to  $L_{\text{int}} = 10 \text{ nb}^{-1}$ .

currently best describes the LHC data ( $T_{\text{ch}} = 156 \text{ MeV}$ ), the expected hypertriton yield is  $dN/dy = 1 \times 10^{-4}$ . For the  ${}^4_{\Lambda}\text{H}$  a value  $dN/dy = 2 \times 10^{-7}$  is predicted, and it is reasonable to assume the same value for the  ${}^4_{\Lambda}\text{He}$ , which has a similar mass.

For the estimation of the number of reconstructed hypernuclei, the decay branching ratios (B.R.) and the acceptance and efficiency factors were taken into account. The latter were estimated using a simulation sample with a detailed description of the new ITS. The hypernuclei were generated with a flat transverse momentum distribution and  $|y| < 1$ . The average acceptance-times-efficiency for  $p_T > 0$  and  $|y| < 1$  was obtained by convoluting the simulation result with a blast-wave parametrization of the  $p_T$  distribution observed for  ${}^3_{\Lambda}\text{H}$  in Pb–Pb data. The B.R. were taken from [82] for  ${}^3_{\Lambda}\text{H}$  and  ${}^4_{\Lambda}\text{H}$  and from [83] for  ${}^4_{\Lambda}\text{He}$ . Table 8.5 shows the production yields ( $dN/dy$  for  $T = 156 \text{ MeV}$ ), the B.R., the average acceptance-times-efficiency and the expected number of reconstructed decays for Pb–Pb events in the 0–10 % centrality class.

An estimation of the expected background was carried out for the  ${}^3_{\Lambda}\text{H}$  state. A simulation sample generated with HIJING and including a detailed description of the new ITS was used to this purpose. The resulting background was scaled by the ratio of the background observed in data and in HIJING simulations with the current ITS, in order to account for



inaccuracies in the description of the physical backgrounds (primary and secondary  $^3\text{He}$ ) in the simulation. For  $p_T > 2 \text{ GeV}/c$ , the signal-to-background ratio and the significance are expected to be of about 0.1 and 60 (for  $L_{\text{int}} = 10 \text{ nb}^{-1}$ ), respectively. Figure 8.28 shows the corresponding invariant mass distribution for ( $^3\text{He}, \pi$ ) and charge conjugates.

## 8.5 Summary of the physics reach

The physics reach for various observables is summarised in Tab. 8.6 in terms of minimum accessible  $p_T$  and of statistical uncertainties. We consider a scenario with an integrated luminosity of  $10 \text{ nb}^{-1}$ , fully used for minimum-bias data collection, and a low-magnetic-field run with  $3 \text{ nb}^{-1}$  of integrated luminosity for the low-mass dielectron study. The case of the programme up to Long Shutdown 2 is shown for comparison. In this case a delivered luminosity of  $1 \text{ nb}^{-1}$  is assumed, out of which 10% is recorded with a minimum-bias trigger. Note that, in general, the systematic uncertainties are expected to be significantly reduced in the upgrade case.










**Table 8.6:** Summary of the physics reach: minimum accessible  $p_T$  and relative statistical uncertainty in Pb–Pb collisions for an integrated luminosity of  $10 \text{ nb}^{-1}$ . For heavy flavour, the statistical uncertainties are given at the maximum between  $p_T = 2 \text{ GeV}/c$  and  $p_T^{\text{min}}$ . For elliptic flow measurements, the value of  $v_2$  used to calculate the relative statistical uncertainty  $\sigma_{v_2}/v_2$  is given in parenthesis. The case of the programme up to Long Shutdown 2, with a luminosity of  $0.1 \text{ nb}^{-1}$  collected with minimum-bias trigger, is shown for comparison.

Observable	Current, 0.1 nb <sup>-1</sup>		Upgrade, 10 nb <sup>-1</sup>	
	$p_T^{\text{min}}$ (GeV/c)	statistical uncertainty	$p_T^{\text{min}}$ (GeV/c)	statistical uncertainty
Heavy Flavour				
D meson $R_{AA}$	1	10 %	0	0.3 %
D <sub>s</sub> meson $R_{AA}$	4	15 %	< 2	3 %
D meson from B $R_{AA}$	3	30 %	2	1 %
J/ψ from B $R_{AA}$	1.5	15 % <sub>(pT-int.)</sub>	1	5 %
B <sup>+</sup> yield	not accessible		2	10 %
Λ <sub>c</sub> $R_{AA}$	not accessible		2	15 %
Λ <sub>c</sub> /D <sup>0</sup> ratio	not accessible		2	15 %
Λ <sub>b</sub> yield	not accessible		7	20 %
D meson $v_2$ ( $v_2 = 0.2$ )	1	10 %	0	0.2 %
D <sub>s</sub> meson $v_2$ ( $v_2 = 0.2$ )	not accessible		< 2	8 %
D from B $v_2$ ( $v_2 = 0.05$ )	not accessible		2	8 %
J/ψ from B $v_2$ ( $v_2 = 0.05$ )	not accessible		1	60 %
Λ <sub>c</sub> $v_2$ ( $v_2 = 0.15$ )	not accessible		3	20 %
Dielectrons				
Temperature (intermediate mass)	not accessible			10 %
Elliptic flow ( $v_2 = 0.1$ ) [4]	not accessible			10 %
Low-mass spectral function [4]	not accessible		0.3	20 %
Hypernuclei				
<sup>3</sup> Λ yield	2	18 %	2	1.7 %










## A Explorer measurement summary

The following tables show a comprehensive summary of the results of the laboratory and test beam campaign for the Explorer-0 and Explorer-1 sensors. The measurements have been performed at different back bias voltages of  $-1\text{ V}$  and  $-6\text{ V}$  and before and after irradiation with  $1\text{ MeV n}_{\text{eq}}/\text{cm}^2$ . Results for the different pixels in all nine sectors for seed SNR, measured using a  $4\text{ GeV}/c$  electron beam, noise and cluster charge collection efficiencies are presented. Differences between the diode shapes of the pixels in each of the sectors are indicated in the left four columns of the tables.










**Table A.1:** Summary of Explorer-0 characteristics for different back-bias voltages of  $V_{\text{bias}} = -1$  V and  $-6$  V and with/without neutron irradiation.

Sector	Shape	Diameter [ $\mu\text{m}$ ]	Spacing [ $\mu\text{m}$ ]	Dose [1 MeV/nq]	Seed SNR				Noise [ $e^-$ ]				CCE [%]			
					$20 \times 20 \mu\text{m}^2$		$30 \times 30 \mu\text{m}^2$		$20 \times 20 \mu\text{m}^2$		$30 \times 30 \mu\text{m}^2$		$20 \times 20 \mu\text{m}^2$		$30 \times 30 \mu\text{m}^2$	
					$-1$ V	$-6$ V	$-1$ V	$-6$ V	$-1$ V	$-6$ V	$-1$ V	$-6$ V	$-1$ V	$-6$ V	$-1$ V	$-6$ V
1		2	0	$1 \times 10^{13}$	10.1	15.6	8.0	12.4	22.5	19.3	31.1	25.8	78.2	90.4	77.9	90.3
2		3	0	$1 \times 10^{13}$	11.6	19.9	8.4	13.9	29.1	26.5	41.1	33.4	81.2	97.7	74.3	91.0
3		4	0	$1 \times 10^{13}$	15.7	22.4	8.2	14.9	34.1	29.2	46.1	39.3	89.5	100.0	82.7	99.7
4		3	0	$1 \times 10^{13}$	13.9	21.8	9.4	16.9	33.1	26.9	42.3	33.4	95.9	97.5	96.1	96.7
5		3	0.6	$1 \times 10^{13}$	10.8	17.7	9.8	12.4	29.1	26.1	45.3	38.7	84.2	100.0	77.3	97.9
6		3	1.04	$1 \times 10^{13}$	16.9	28.2	12.3	19.5	28.2	24.3	35.8	30.3	97.3	97.5	95.1	97.1
7		2	1.54	$1 \times 10^{13}$	13.4	22.9	11.9	14.7	30.6	26.9	38.5	34.8	87.9	99.1	79.0	96.2
8		3	0	$1 \times 10^{13}$	15.8	23.9	12.2	17.0	28.5	26.1	36.2	33.3	89.1	100.0	83.1	97.9
9		3	1.04	$1 \times 10^{13}$	19.1	29.0	14.9	22.2	25.9	22.9	33.0	28.3	98.4	97.5	96.5	96.5
					15.8	23.9	12.2	17.0	28.5	26.1	36.2	33.3	89.1	100.0	83.1	97.9
					16.7	29.0	14.7	22.5	25.7	22.4	30.6	26.3	97.9	97.1	94.9	96.0
					14.9	23.1	11.9	16.0	29.2	25.5	34.5	31.6	87.8	100.0	77.7	96.2
					9.6	18.5	9.0	15.7	34.3	27.7	39.9	32.3	94.0	97.8	92.0	96.3
					8.8	17.6	7.8	11.0	35.8	29.8	42.7	36.1	78.4	99.7	68.6	91.0
					20.4	26.7	14.9	12.5	29.0	25.1	34.1	29.4	97.8	97.4	94.9	96.3
					13.7	18.6	9.5	12.5	31.7	27.9	37.5	34.4	89.1	100.0	80.7	98.3

**Table A.2:** Summary of Explorer-1, 18  $\mu\text{m}$ , 1 k $\Omega$  cm, characteristics for different back-bias voltages of  $V_{\text{bias}} = -1$  V and  $-6$  V and with/without neutron irradiation.

Sector	Shape	Diameter [ $\mu\text{m}$ ]	Spacing [ $\mu\text{m}$ ]	Dose [1 MeV neq]	Seed SNR				Noise [ $e^-$ ]				CBE [%]			
					$20 \times 20 \mu\text{m}^2$		$30 \times 30 \mu\text{m}^2$		$20 \times 20 \mu\text{m}^2$		$30 \times 30 \mu\text{m}^2$		$20 \times 20 \mu\text{m}^2$		$30 \times 30 \mu\text{m}^2$	
					$-1$ V	$-6$ V	$-1$ V	$-6$ V	$-1$ V	$-6$ V	$-1$ V	$-6$ V	$-1$ V	$-6$ V	$-1$ V	$-6$ V
1		1.13	3.035	$1 \times 10^{13}$	36.1	77.8	26.4	46.7	16.4	10.4	21.6	14.8	97.8	98.4	97.2	100.0
2		2	2.6	0	35.5	65.4	26.5	44.2	16.9	12.3	22.0	16.9	97.3	97.8	97.5	100.0
3		3	2.1	$1 \times 10^{13}$	34.6	55.6	25.1	37.5	17.7	14.6	23.3	20.0	97.7	97.0	97.3	99.3
4		1.13	3.035	0	33.7	67.1	26.6	48.7	17.0	11.4	20.0	14.5	97.7	100.0	96.3	100.0
5		2	2.6	$1 \times 10^{13}$	33.4	59.2	26.6	43.3	17.6	13.3	21.1	16.9	97.7	99.7	97.0	100.0
6		3	2.1	0	31.5	49.4	25.0	37.5	18.7	15.7	22.6	19.8	97.3	98.6	97.7	100.0
7		1.13	0.635 (top)	$1 \times 10^{13}$	28.0	62.4	23.7	48.3	21.4	12.8	23.5	14.7	97.3	100.0	96.7	100.0
8		1.13	0.635 (top)	0	28.6	63.5	24.6	48.9	19.8	12.1	21.7	13.8	96.9	100.0	96.7	100.0
9		2	2.6	$1 \times 10^{13}$	28.7	58.7	24.8	44.7	18.4	12.3	20.2	14.3	97.4	100.0	96.5	100.0

**Table A.3:** Summary of Explorer-1, 20  $\mu\text{m}$ , 6 kV cm, characteristics for different back-bias voltages of  $V_{\text{bias}} = -1\text{ V}$  and  $-6\text{ V}$  and with/without neutron irradiation.

Sector	Shape	Diameter [ $\mu\text{m}$ ]	Spacing [ $\mu\text{m}$ ]	Dose [1 MeV neq]	Seed SNR			Noise [ $\epsilon^-$ ]			CCE [%]		
					$20 \times 20 \mu\text{m}^2$ -1 V	$30 \times 30 \mu\text{m}^2$ -1 V	$20 \times 20 \mu\text{m}^2$ -6 V	$20 \times 20 \mu\text{m}^2$ -1 V	$30 \times 30 \mu\text{m}^2$ -1 V	$20 \times 20 \mu\text{m}^2$ -6 V	$20 \times 20 \mu\text{m}^2$ -1 V	$30 \times 30 \mu\text{m}^2$ -1 V	$20 \times 20 \mu\text{m}^2$ -6 V
1		1.13	3.035	$1 \times 10^{13}$	39.1	84.9	30.4	60.4	16.2	10.5	19.5	13.4	97.6
2		2	2.6	0	38.8	74.7	29.5	53.3	16.8	12.2	20.5	15.7	99.0
3		3	2.1	$1 \times 10^{13}$	37.3	59.9	28.2	45.4	17.6	14.7	21.5	18.6	98.3
4		1.13	3.035	0	35.2	76.7	29.8	57.8	16.3	11.1	18.7	13.2	98.3
5		2	2.6	$1 \times 10^{13}$	35.4	67.0	29.7	52.6	16.9	13.0	19.3	15.3	97.8
6		3	2.1	0	34.0	56.0	28.2	44.4	17.9	15.3	20.4	18.0	98.1
7		1.13	0.635 (top)	$1 \times 10^{13}$	31.5	75.5	27.2	57.7	20.3	11.9	21.4	13.5	99.2
8		1.13	0.635 (top)	0	31.7	75.0	27.5	58.7	18.5	11.2	20.0	12.6	98.3
9		2	2.6	$1 \times 10^{13}$	31.8	66.8	27.9	54.2	17.4	11.8	18.3	13.1	98.1

## B Alternative Stave implementation options

### B.1 Microchannel cooling systems

Two alternative cooling options to the Cold Plate with embedded pipes are being explored for the Inner Barrel Stave: they are based on a microchannel array fabricated either in a polyimide or a silicon substrate.

#### B.1.1 Polyimide microchannels

The polyimide microchannels structure is a system of parallel and rectangular cross-section microchannels manufactured in a polyimide substrate, which is directly glued to the Pixel Chips (Fig. B.1). The structure is a multilayer polyimide stack-up made of a layer of Pyralux LF110 at the bottom, a Photoimageable PC1020 layer in the middle and a Pyralux LF110 layer glued on the top. The rectangular pattern defining the channels is created with a photolithography process performed at 180 °C and the cover is made of a foil of LF7001, which is hot pressed on the top of the substrate where the channels are engraved. The full structure is then thermally cured at 180 °C for ten hours in order to achieve its ultimate end-use properties.

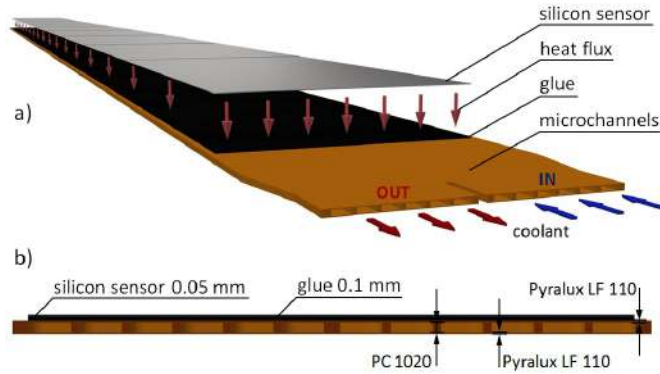


**Figure B.1:** a) Sketch of the polyimide cooling system interfacing silicon sensors; b) schematic view of the polyimide microchannels cross section.

A polyimide structure, with 16 microchannels of  $0.8 \text{ mm} \times 0.3 \text{ mm}$  cross section each, was glued to a wound truss carbon-fiber structure as shown in Fig. B.2. The prototype was equipped with nine blank silicon pieces, 0.5 mm thick, 15 mm wide and 30 mm long. Both thermal and mechanical behaviour of the microchannels were tested [84]. The thermo-fluid dynamic tests were performed starting with a simplified configuration where inlet and outlet were located at the opposite end. The performance of the final prototype with the inlet and outlet at the same end were studied at fixed width channel of 0.8 mm and by varying the height from 0.2 mm to 0.35 mm. Demineralized water was used as coolant

in single phase at about  $15^\circ\text{C}$  at the inlet and heat flux was varied from  $100\text{ mW cm}^{-2}$  to  $300\text{ mW cm}^{-2}$  by a Kapton heater glued on the microchannels surface. The temperature distribution above the heated surface was measured with a thermal infrared camera as shown in Fig. B.3.

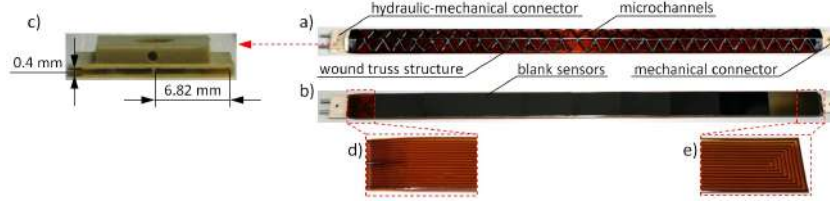


**Figure B.2:** a) Front view and b) back view of a dummy Module interfacing the polyimide microchannel structure; c) sketch of the hydraulic connector that is used also for the mechanical fixation; d) zoom of inlet/outlet and e) zoom of the reverse flow zone of the polyimide microchannel structure.

This on-detector cooling system has been demonstrated to be able to dissipate a power density ranging from  $100\text{ mW cm}^{-2}$  to  $300\text{ mW cm}^{-2}$  without exceeding  $30^\circ\text{C}$  in leakless mode [85]; the total pressure drop along the structure was measured to be 0.3 bar. The estimated material budget of such a structure is  $0.13\% X_0$ . Mechanical tests were performed to verify the leak tightness and pressure resistance. Neither leak nor delamination were observed up to a coolant pressure of 10 bar. The polyimide compatibility with water was successfully verified in a long term test in static and dynamic condition. Moreover, the fatigue behaviour of the thermal contact between heater and microchannels was tested by thermal and pressure cycles. Thermal contact efficiency did not show any worsening.

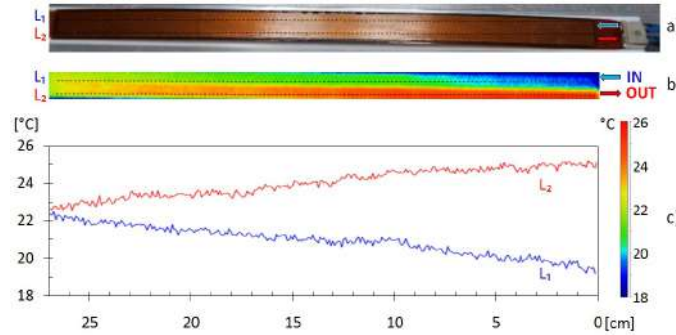


**Figure B.3:** The dummy Module under test with 16 microchannels  $0.8\text{ mm} \times 0.3\text{ mm}$  equipped with the heater glued on the surface: a) picture, b) thermographic image and c) temperature profiles. The test conditions are:  $300\text{ mW cm}^{-2}$  power density,  $1.41\text{ h}^{-1}$  water flow rate and  $14.9^\circ\text{C}$  water temperature at the inlet.

### B.1.2 Evaporative cooling with silicon microchannels

Silicon microchannel cooling has gained a huge attention over the last years for applications on computer chip cooling [86, 87]. The high heat transfer coefficient at the micro scale and the compact design achievable with microfabrication techniques favour the integration of silicon microchannels into the electronics during the packaging process. Recently, silicon microchannels started to be considered also for application on particle detectors cooling [88]. In the PH-DT group at CERN, several studies are on-going to investigate the application of silicon microchannels for on-detectors electronics cooling [89, 90].

For cooling the Inner Layers of the future ALICE ITS detector, special silicon frames with embedded microchannels are under study for flow boiling of perfluorobutane ( $C_4F_{10}$ ). The study is carried out in collaboration with the PH-DT group at CERN, the Two-phase Heat Transfer group at the University of Padova, the CMi and LTCM groups at EPFL (École Polytechnique Fédérale de Lausanne) and the Thai Micro Electronic Centre (TMEC) in Thailand.

For the minimization of the material budget contribution from the cooling system, a special device with a frame design (Fig. B.4) was realized: this design eliminates any material contribution in the inner region while keeping all the advantages linked to microchannel cooling.

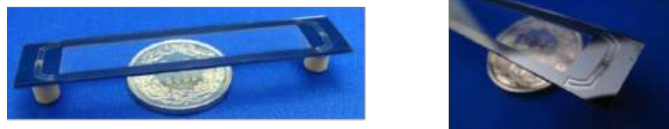


**Figure B.4:** The silicon frame with embedded microchannels (left) and a particular of the inlet manifold (right).

The first prototypes of silicon microchannels were fabricated at the class 100 clean-room of the Centre of MicroNano Technology at EPFL on 4 inch (100) 380  $\mu m$  thick Czochralski silicon wafers.

The thermal tests of the prototypes showed that the system is able to remove the power dissipated by the on-detector electronics, keeping the sensors within the operational constraints, as shown in Fig. B.5.

The size of the silicon prototypes is limited by the diameter of the silicon wafers; even using an 8" wafer, it would not be possible to reach the length of the Inner Barrel Staves. Preliminary tests executed with three cooling frames connected in parallel with an external mini-pipe have proved that a whole Stave can be efficiently cooled by an appropriate combination of shorter frames.

For this reason, a big effort was devoted to studying a reliable interconnection between several cooling devices in a full Stave prototype. As shown in Fig. B.6, each cooling device in the Stave will have its own inlet and outlet manifolds. Then, a distribution line running from the Stave inlet to the last device will provide the refrigerant distribution and a similar channel on the other side will recollect the vapor from the outlet manifold to the inlet of the Stave. This arrangement helps to keep the total pressure drop along the Stave low and places all the Stave hydraulic connections on one side only, as required.

The problem of the continuation of the distribution lines from one frame to the following is solved using a micro-fabricated fluidic bridge (Fig. B.7). The system, already successfully assembled and hydraulically tested, will be soon tested under nominal thermal load using microfabricated silicon dummy chips simulating the power dissipation of the pixel chips.



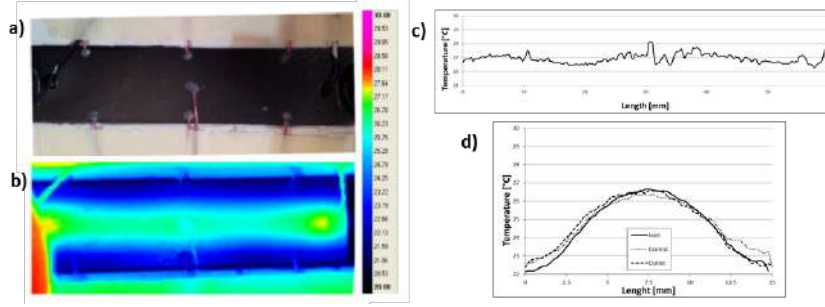


**Figure B.5:** The silicon dummy chip instrumented with thermocouples (a), IR image of the dummy chip at the nominal dissipation heat flux  $P_{\text{diss}} = 300 \text{ mW cm}^{-2}$  (b), the temperature profile along the microchannels (c) and radial temperature profiles at different longitudinal location (d).

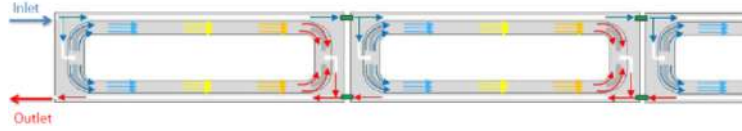


**Figure B.6:** Interconnection of silicon frames for the Stave cooling.

A new version of the silicon microchannel cooling prototype is under fabrication at the Thai Micro Electronic Centre (TMEC). The production will be carried out on 6" wafers, reducing to only two the number of frames needed to match the length of the Stave. This new prototype is designed with optimized silicon thickness in order to minimize the material budget contribution of the system.

Dummy prototypes with the same design are also under fabrication at the CMi clean room for mechanical tests: modal tests and thermal expansion tests will be performed.



**Figure B.7:** The continuation of the distribution line (left) is obtained with the installation of a micro-fabricated bridge (center). Pyrex-silicon bridge prototype installed at the intersection between two frames

In addition, optimal integration into the Low Mass Carbon Fibre structure developed for the ITS inner layers is presently under study (Figure B.8).

## B.2 Chips embedding in flex

A promising alternative to laser soldering consists in embedding the chips inside the FPC during the fabrication process. An overview of the process flow of this technology is given in Fig. B.9. The base material for the package is polyimide coated on a rigid carrier

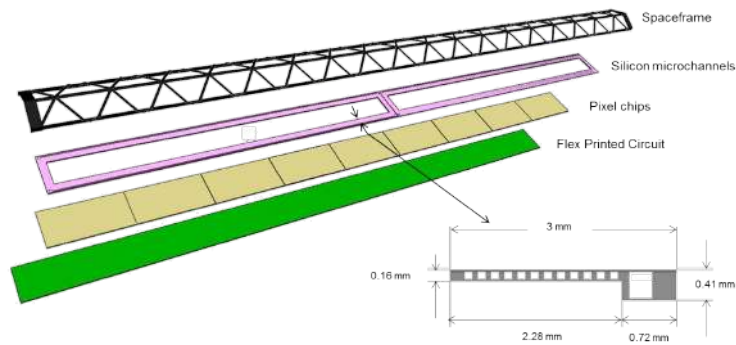


**Figure B.8:** Concept of the integration of the silicon micro-channel frames into the ITS IL stave.

(e.g. 1 mm thick Cu plate). The Pixel Chips are placed and glued face up on the polyimide layer using an epoxy resin by Krempel as adhesive material. After curing such as resin at 180 °C for two hours, a top polyimide layer is coated on top of the fixed dies. Finally, vias are opened by traditional lithography and metallised, thus generating the interconnection directly without any soldering. In this case, the rigid carrier is partially removed in the region where the chip-embedded FPC has to be glued and finally the external frame is cut away by precision laser cutting. A first dummy prototype of a full IB HIC with nine chips is shown in Fig. B.10

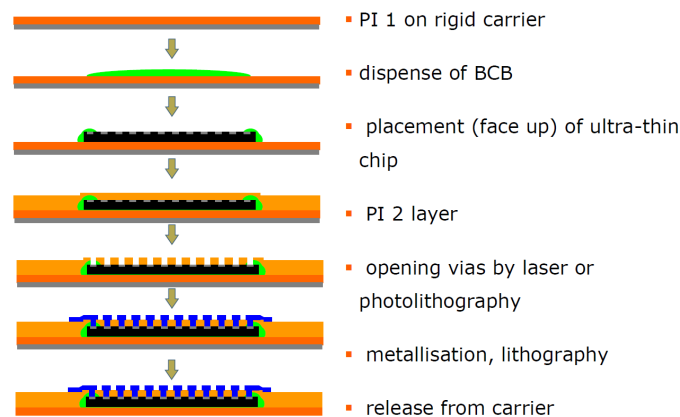


**Figure B.9:** Process flow of chip embedding in flex.

### B.3 Serial powering

Since the Power Bus for the Outer Barrel Staves represents a significant fraction of the material, especially in Layer 5 and Layer 6, an alternative powering scheme for reducing



**Figure B.10:** First dummy prototype of a full IB HIC with nine chips embedded inside the FPC (top) and a detail view of the edge (bottom).

the amount of aluminium needed, which is proportional to the current required by the Pixel Chips, is under study.

A way to reduce the current in the PB is by connecting in series the analogue and digital power of all Modules on a Stave. Such a serial powering scheme requires feeding each chain with a current source instead of a voltage source and a local shunt regulator for each Module. The PB can then be replaced by a common ground return bus of non-critical impedance. The development of a shunt regulator, which could be included in the final chip design or mounted separately on each Module, is currently under investigation. For Layers 5 and 6, this would reduce the current and amount of aluminium in the PB by a factor of seven. However, this solution would require the ground of one Module to be connected to the analogue and digital power plane of the next Module and the Module interconnection scheme could make the assembly procedure too costly. Also the signal distribution would have to be adapted since all signals would need to be translated from the local Module potential to the common potential of the read-out system.

## Bibliography

- [1] ALICE Collaboration, *ALICE: Physics Performance Report, Volume I*, J. Phys. **G30**, 1517–1763 (2004) (cit. on p. 1).
- [2] Directors of Research, *ALICE Memorandum of Understanding and related addenda*, CERN-ARCH-DIR-RES-02-1-1-03, ALICE RRB-D 00-41, 2000, (cit. on p. 1).
- [3] ALICE Collaboration, *The ALICE experiment at the CERN LHC*, JINST **3**, S08002 (2008) (cit. on pp. 1, 55, 76).
- [4] ALICE Collaboration, *Letter of Intent for the Upgrade of the ALICE Experiment*, CERN-LHCC-2012-012, LHCC-I-022, 2012, (cit. on pp. 1, 2, 110, 133, 143, 155, 156, 162).
- [5] ALICE Collaboration, *Addendum of the Letter Of Intent for the Upgrade of the ALICE Experiment: The Muon Forward Tracker*, CERN-LHCC-2013-014, LHCC-I-022-ADD-1, 2013, (cit. on pp. 2, 80).
- [6] STAR Collaboration, *The STAR Heavy Flavor Tracker, Conceptual Design Report*, submitted to DOE at CD1 review, 2009, (cit. on pp. 5, 46, 114).
- [7] H. Bichsel, *Straggling in thin silicon detectors*, Rev. Mod. Phys. **60**, 663–699 (1988) (cit. on p. 13).
- [8] Z. Xu et al., *A Heavy Flavor Tracker for STAR*, LBNL/PUB-5509, 2005 (cit. on p. 18).
- [9] L. Greiner et al., *A MAPS based vertex detector for the STAR experiment at RHIC*, NIM **A650**, 68–72 (2011) (cit. on pp. 18, 19).
- [10] I. Valin et al., *A reticle size CMOS pixel sensor dedicated to the STAR HFT*, JINST **7**, C01102 (2012) (cit. on pp. 18, 19).
- [11] Y. Degerli, *Design of fundamental building blocks for fast binary readout CMOS sensors used in high-energy physics experiments*, NIM **A602**, 461–466 (2009) (cit. on p. 18).
- [12] ALICE Collaboration, *Conceptual Design Report for the Upgrade of the ALICE ITS*, CERN-LHCC-2012-005, LHCC-G-159, 2012, (cit. on pp. 19, 27, 30, 110, 113, 122, 124, 125, 133, 135, 136, 138, 147, 149, 155, 156).
- [13] J. Baudot et al., *Optimisation of CMOS pixel sensors for high performance vertexing and tracking*, 2013, arXiv:1305.0531 [physics.ins-det] (cit. on pp. 29, 39).
- [14] SPiDeR Collaboration, *Advanced monolithic active pixel sensors for tracking, vertexing and calorimetry with full CMOS capability*, NIM **A650**, 178–183 (2011) (cit. on p. 30).
- [15] R. Doering and Y. Nishi, *Handbook of Semiconductor Manufacturing Technology* (CRC/Taylor & Francis, 2008) (cit. on pp. 43, 45).
- [16] S. Mattiazzo et al., *LePIX: First results from a novel monolithic pixel sensor*, in Proceedings of the 12th pisa meeting on advanced detectors, Vol. A718 (2013), pp. 288–291 (cit. on p. 44).
- [17] D. K. Schroder, *Semiconductor Material and Device Characterization* (John Wiley & Sons, 2006) (cit. on p. 45).

- [18] TenCate, *RS3 Technical Data Sheet*, RS-3\_DS.062612 (cit. on p. 59).
- [19] TenCate, *EX1515 Technical Data Sheet*, EX1515\_DS.120810 (cit. on p. 59).
- [20] M. Tavlet, A. Fontaine and H. Schönbacher, *Compilation of radiation damage test data, pt. 2*, CERN-98-01, 1998 (cit. on p. 59).
- [21] AMEC Thermasol, *Thermograph FGS003 Technical Data Sheet* (cit. on p. 60).
- [22] Mitsubishi Chemical, *k13D2U Technical Data Sheet* (cit. on p. 60).
- [23] Torayca Carbon Fibers America, Inc., *M60J Technical Data Sheet*, CFA-018 (cit. on p. 60).
- [24] Torayca Carbon Fibers America, Inc., *M55J Technical Data Sheet*, CFA-017 (cit. on p. 61).
- [25] Mitsubishi Chemical, *K13C2U Technical Data Sheet* (cit. on p. 61).
- [26] M. Santos and J. A. B. Direito, *ALICE SPD detector cooling system technical dossier. Hydraulic Part*, EDMS 1007785, 2009, (cit. on p. 61).
- [27] S. Ilie and M. Tavlet, *Qualification of coolants and cooling pipes for future high-energy-particle detectors*, NIM **B185**, 318–322 (2001) (cit. on p. 66).
- [28] ALICE Collaboration, *Upgrade of the ALICE Readout and Trigger System*, CERN-LHCC-2013-019, ALICE-TDR-015, 2013, (cit. on p. 80).
- [29] Airex Baltex, *AIREX R63 Tehcnical Data Sheet*, 07.2011 (cit. on p. 82).
- [30] G. Schneider, *Installation of the Beam Pipes in the Alice experiment*, LHC-VC2-IP-0001, EDMS 372648, 2003, (cit. on p. 87).
- [31] J. B. Jeanneret and R. Ostokic, *Geometrical Acceptance in LHC Version 5.0*, LHC-Project-Note-111, Geneva, Sept. 1997, (cit. on p. 88).
- [32] G. Dellacasa et al., *ALICE Time Projection Chamber: Technical Design Report*, CERN-OPEN-2000-183, ALICE-TDR-7, CERN-LHCC-2000-001, 2000, (cit. on p. 90).
- [33] F. Faccio et al., *TID and Displacement Damage Effects in Vertical and Lateral Power MOSFETs for Integrated DC-DC Converters*, IEEE Trans. Nucl. Sci. **57**, 1790–1797 (2010) (cit. on p. 108).
- [34] G. Schneider, *Installation of the central beryllium beam pipe in the alice experiment*, EDMS 1113439, 2011, (cit. on p. 109).
- [35] ALICE Collaboration, *Charged-Particle Multiplicity Density at Midrapidity in Central Pb–Pb Collisions at  $\sqrt{s_{NN}} = 2.76$  TeV*, Phys. Rev. Lett. **105**, 252301 (2010) (cit. on pp. 109, 134).
- [36] X. Wang and M. Gyulassy, *HIJING: A Monte Carlo model for multiple jet production in pp, pA and AA collisions*, Phys. Rev. **D44**, 3501–3516 (1991) (cit. on pp. 109, 127, 134, 137, 139, 144, 146, 149).
- [37] A. Alscher et al., *Multiple electromagnetic electron-positron pair production in relativistic heavy-ion collisions*, Phys. Rev. **A55**, 396–401 (1997) (cit. on p. 109).
- [38] K. Hencken, G. Baur and D. Trautmann, *Production of QED pairs at small impact parameter in relativistic heavy ion collisions*, Phys. Rev. **C69**, 054902 (2004) (cit. on p. 109).
- [39] K. Hencken, Y. Kharlov and S. Sadovsky, *Ultrapерipheral Trigger in ALICE*, ALICE-INT-2002-11, 2002, (cit. on p. 109).
- [40] S. Sadovsky, K. Hencken and Y. Kharlov, *Generator for  $e^+e^-$  pairs in PbPb collisions at LHC*, ALICE-INT-2002-27, 2002, (cit. on p. 109).

- [41] ALICE Collaboration, *Technical Design Report of the ALICE Computing*, CERN-LHCC-2005-018, ALICE-TDR-012, 2005, (cit. on pp. 109, 114).
- [42] O. S. Brüning et al., *LHC Design Report*, CERN-2004-003-V-1, 2004 (cit. on p. 110).
- [43] P. Billoir, *Track fitting with multiple scattering: A new method*, NIM **225**, 352–366 (1984) (cit. on pp. 114, 118).
- [44] R. Frühwirth, *Application of Kalman filtering to track and vertex fitting*, NIM **A262**, 444–450 (1987) (cit. on pp. 114, 118).
- [45] A. Mastroserio et al., *Simulation tools for the its upgrade*, ALICE Internal Note [http://aliceinfo.cern.ch/ITSUpgrade/sites/aliceinfo.cern.ch/ITSUpgrade/files/documents/Upgrade\\_IN.pdf](http://aliceinfo.cern.ch/ITSUpgrade/sites/aliceinfo.cern.ch/ITSUpgrade/files/documents/Upgrade_IN.pdf), 2012 (cit. on p. 114).
- [46] R. Brun, F. Carminati and S. Giani, *GEANT Detector Description and Simulation Tool*, CERN-W5013, CERN Program Library Long Writeup, 1994 (cit. on p. 114).
- [47] I. Abt et al., *CATS: A cellular automaton for tracking in silicon for the HERA-B vertex detector*, NIM **A489**, 389–405 (2002) (cit. on p. 120).
- [48] I. Kisel, *Event reconstruction in the CBM experiment*, NIM **A566**, 85–88 (2006) (cit. on p. 120).
- [49] G. Agakishiev et al., *A new robust fitting algorithm for vertex reconstruction in the CERES experiment*, NIM **A394**, 225–231 (1997) (cit. on p. 121).
- [50] V. Karimäki, *Effective Vertex Fitting*, CMS-NOTE-1997-051, 1997, (cit. on p. 121).
- [51] E. Bruna, E. Crescio and M. Masera, *Response functions for particle Identification in the Inner Tracking System*, ALICE-INT-2006-004, 2006, (cit. on p. 124).
- [52] PHOBOS Collaboration, *Identified hadron transverse momentum spectra in Au+Au collisions at  $\sqrt{s_{NN}} = 62.4$  GeV*, Phys. Rev. **C75**, 024910 (2007) (cit. on p. 125).
- [53] ALICE Collaboration, *Identified particles in pp and Pb–Pb collisions at LHC energies with the ALICE detector*, J. Phys. G **38**, 124025 (2011) (cit. on p. 126).
- [54] T. Sjöstrand, S. Mrenna and P. Skands, *PYTHIA 6.4 Physics and Manual*, JHEP **05**, 026 (2006) (cit. on pp. 134, 135, 137, 144).
- [55] ALICE Collaboration, *Measurement of charm production at central rapidity in proton-proton collisions at  $\sqrt{s} = 2.76$  TeV*, JHEP **1207**, 191 (2012) (cit. on pp. 135, 136).
- [56] ALICE Collaboration, *Measurement of electrons from beauty hadron decays in pp collisions at  $\sqrt{s} = 7$  TeV*, Phys. Lett. **B721**, 13–23 (2013) (cit. on pp. 135, 136).
- [57] Particle Data Group, *Review of particle physics*, Phys. Rev. **D86**, 010001 (2012) (cit. on pp. 136, 141, 142, 144, 146, 149).
- [58] M. Mangano, P. Nason and G. Ridolfi, *Heavy-quark correlations in hadron collisions at next-to-leading order*, Nucl. Phys. **B373**, 295–345 (1992) (cit. on p. 135).
- [59] K. Eskola, H. Paukkunen and C. Salgado, *EPS09 – A New Generation of NLO and LO Nuclear Parton Distribution Functions*, JHEP **0904**, 065 (2009) (cit. on p. 135).
- [60] M. Cacciari et al., *Theoretical predictions for charm and bottom production at the LHC*, JHEP **1210**, 137 (2012) (cit. on pp. 136, 137, 139, 144, 150, 154).
- [61] ALICE Collaboration, *Suppression of high transverse momentum D mesons in central Pb-Pb collisions at  $\sqrt{s_{NN}} = 2.76$  TeV*, JHEP **1209**, 112 (2012) (cit. on pp. 137–139, 153).
- [62] M. He, R. J. Fries and R. Rapp, *D<sub>s</sub>-Meson as Quantitative Probe of Diffusion and Hadronization in Nuclear Collisions*, 2012, arXiv:1204.4442 [nucl-th] (cit. on pp. 140, 152).

- [63] CDF Collaboration, *Measurement of the ratios of branching fractions  $B(B_s^0 \rightarrow D_s^- \pi^+)/B(B^0 \rightarrow D^- \pi^+)$  and  $B(B^+ \rightarrow \bar{D}^0 \pi^+)/B(B^0 \rightarrow D^- \pi^+)$* , Phys. Rev. Lett. **96**, 191801 (2006) (cit. on p. 141).
- [64] LHCb Collaboration, *Studies of b-hadron decays to charming final states at LHCb*, 2011, arXiv:1110.3249 [hep-ex] (cit. on p. 141).
- [65] ALICE Collaboration, *Measurement of prompt  $J/\psi$  and beauty hadron production cross sections at mid-rapidity in pp collisions at  $\sqrt{s} = 7$  TeV*, JHEP **1211**, 065 (2012) (cit. on p. 142).
- [66] F. Bossu et al., *Phenomenological interpolation of the inclusive  $J/\psi$  cross section to proton-proton collisions at 2.76 TeV and 5.5 TeV*, 2011, arXiv:1103.2394 [nucl-ex] (cit. on p. 142).
- [67] M. He, R. J. Fries and R. Rapp, *Non-perturbative Heavy-Flavor Transport at RHIC and LHC*, 2012, arXiv:1208.0256 [nucl-th] (cit. on p. 144).
- [68] ALICE Collaboration, *Strange and multi-strange particle production at the LHC energies with ALICE*, Acta Phys. Polon. **B43**, 645–654 (2012) (cit. on p. 146).
- [69] Y. Oh et al., *Ratios of heavy baryons to heavy mesons in relativistic nucleus-nucleus collisions*, Phys. Rev. **C79**, 044905 (2009) (cit. on p. 152).
- [70] ALICE Collaboration, *D meson elliptic flow in non-central Pb–Pb collisions at  $\sqrt{s_{NN}} = 2.76$  TeV*, Phys. Rev. Lett. **111**, 102301 (2013) (cit. on p. 153).
- [71] J. Uphoff et al., *Open heavy flavor in Pb + Pb collisions at  $\sqrt{s} = 2.76$  TeV within a transport model*, Physics Letters **B717**, 430–435 (2012) (cit. on p. 153).
- [72] J. Huang, Z.-B. Kang and I. Vitev, *Inclusive b-jet production in heavy ion collisions at the LHC*, 2013, arXiv:1306.0909 [hep-ph] (cit. on p. 154).
- [73] ALICE Collaboration, *Measurement of the inclusive differential jet cross section in pp collisions at  $\sqrt{s} = 2.76$  TeV*, Phys. Lett. **B722**, 262–272 (2013) (cit. on p. 154).
- [74] T. Sjostrand, S. Mrenna and P. Z. Skands, *A Brief Introduction to PYTHIA 8.1*, Comput. Phys. Commun. **178**, 852–867 (2008) (cit. on p. 154).
- [75] A. Hocker and V. Kartvelishvili, *SVD approach to data unfolding*, NIM **A372**, 469–481 (1996) (cit. on p. 155).
- [76] R. Rapp and J. Wambach, *Low-mass dileptons at the CERN-SpS: evidence for chiral restoration?*, Eur. Phys. J. **A6**, 415–420 (1999) (cit. on p. 156).
- [77] H. van Hees and R. Rapp, *Dilepton Radiation at the CERN Super Proton Synchrotron*, Nucl. Phys. **A806**, 339–387 (2008) (cit. on p. 156).
- [78] PHENIX Collaboration, *Detailed measurement of the  $e^+e^-$  pair continuum in p + p and Au + Au collisions at  $\sqrt{s_{NN}} = 200$  GeV and implications for direct photon production*, Phys. Rev. **C81**, 034911 (2010) (cit. on p. 157).
- [79] M. Danysz and J. Pniewski, *Delayed Disintegration of a Heavy Nuclear Fragment*, Phil. Mag. **44**, 348–350 (1953) (cit. on p. 158).
- [80] W. Alberico and G. Garbarino, *Weak decay of  $\Lambda$ -hypernuclei*, Phys. Rep. **369**, 1–109 (2002) (cit. on p. 158).
- [81] A. Andronic, P. Braun-Munzinger and J. Stachel, *Hadron production in central nucleus–nucleus collisions at chemical freeze-out*, Nucl. Phys. **A772**, 167–199 (2006) (cit. on pp. 160, 161).
- [82] T. A. Armstrong et al., *Production of  ${}^3_\Lambda\text{H}$  and  ${}^4_\Lambda\text{H}$  in central 11.5 GeV/c Au + Pt heavy ion collisions*, Phys. Rev. **C70**, 024902 (2004) (cit. on p. 161).

- [83] H. Outa et al., *Mesonic and non-mesonic decay widths of  ${}^4_{\Lambda}\text{H}$  and  ${}^4_{\Lambda}\text{He}$* , Nucl. Phys. **A639**, 251c–260c (1998) (cit. on p. 161).
- [84] G. Fiorenza et al., *An innovative polyimide microchannels cooling system for the pixel sensor of the upgraded ALICE inner tracker*, in 5th IEEE International Workshop on Advances in Sensors and Interfaces (IWASI) (2013), pp. 81–85 (cit. on p. 167).
- [85] M. Bosteels, *Système a pression hydrostatique inverse*, (1985) (cit. on p. 168).
- [86] B. Agostini et al., *State of the Art of High Heat Flux Cooling Technologies*, Heat Transfer Eng. **28**, 258–281 (2007) (cit. on p. 169).
- [87] F. Alfieri et al., *3D Integrated Water Cooling of a Composite Multilayer Stack of Chips*, J. Heat Transfer **132**, 121402 (2010) (cit. on p. 169).
- [88] J. R. Thome, J. A. Olivier and J. E. Park, *Two-Phase Cooling of Targets and Electronics for Particle Physics Experiments*, in Topical workshop on electronics for particle physics (2009), pp. 366–376, <https://cds.cern.ch/record/1235840> (cit. on p. 169).
- [89] A. Mapelli et al., *Low material budget microfabricated cooling devices for particle detectors and front-end electronics*, Nucl. Phys. **B215**, 349–352 (2011) (cit. on p. 169).
- [90] A. Francescon et al., *Application of micro-channel cooling to the local thermal management of detectors electronics for particle physics*, Microelectr. J. **44**, 612–618 (2013) (cit. on p. 169).





## Glossary

ADC	Analogue-to-Digital Converter.
AGND	Analogue Ground.
ASIC	Application Specific Integrated Circuit.
AVDD	Analogue Positive Supply Voltage.
BER	Bit Error Rate.
CA	Cellular Automaton.
CCE	Charge Collection Efficiency.
CCSS	Cylindrical and Conical Structural Shells.
CDF	Cumulative Distribution Function.
CDR	Conceptual Design Report.
CDS	Correlated Double Sampling.
CFRP	Carbon Fibre Reinforced Plastic.
CMM	Control Measuring Machine.
CMOS	Complementary Metal-Oxide-Semiconductor.
COSS	Conical Structural Shells.
COTS	Commercial Off-The-Shelf.
CRU	Common Read-out Unit.
CTE	Coefficient of Thermal Expansion.
CTLE	Constant Time Linear Equalisation.
CVD	Chemical Vapour Deposition.
CYSS	Cylindrical Structural Shell.
CZ	Czochralski-grown.
DAC	Digital-to-Analogue Converter.
DAQ	Data Acquisition.
DBG	Dice Before Grind.
DC	Direct Current.
DCA	Distance of Closest Approach.
DCS	Detector Control System.
DGND	Digital Ground.
DPL	Deputy Project Leader.
DVDD	Digital Positive Supply Voltage.
EMCAL	Electromagnetic Calorimeter.
EMI	Electromagnetic Interference.
ENC	Equivalent Noise Charge.
EP	Event Plane.
ESD	Event Summary Data.
FDR	Flexible Data Routing.
FET	Fast Estimation Tool.
FIFO	First In, First Out.

FIT	Fast Interaction Trigger.
FMCT	Fast Monte Carlo Tool.
FMD	Forward Multiplicity Detectors.
FPC	Flexible Printed Circuit.
FPGA	Field Programmable Gate Array.
FPN	Fixed Pattern Noise.
FSBB	Full-Scale Building Block.
FWHM	Full Width at Half Maximum.
GDSII	Graphic Database System II.
GEM	Gas Electron Multiplier.
HFT	Heavy Flavor Tracker.
HIC	Hybrid Integrated Circuit.
HL-LHC	High-Luminosity LHC.
HLT	High Level Trigger.
HSO	High Speed Output.
HV	High Voltage.
IB	Inner Barrel.
ILC	International Linear Collider.
IP	Intellectual Property.
ITS	Inner Tracking System.
LED	Light-Emitting Diode.
LHCC	LHC Experiments Committee.
LOI	Letter of Intent.
LS	Long Shutdown.
LV	Low Voltage.
MAPS	Monolithic Active Pixel Sensor.
MC	Monte Carlo.
MFT	Muon Forward Telescope.
MIP	Minimum Ionising Particle.
MOSFET	Metal-Oxide Semiconductor Field-Effect Transistor.
MPV	Most Probable Value.
MPW	Multi-Project Wafer.
NEG	Non-Evaporable Getter.
NIEL	Non-Ionising Energy Loss.
NLO	Next-to-Leading Order.
NMOS	n-channel MOSFET.
OB	Outer Barrel.
PB	Power Bus.
PCB	Printed Circuit Board.
PE	Pre-Emphasis.
PID	Particle Identification.
PL	Project Leader.
PMOS	p-channel MOSFET.

pQCD	perturbative QCD.
PTC	Photon Transfer Curve.
QCD	Quantum Chromodynamics.
QED	Quantum Electrodynamics.
QGP	Quark-Gluon Plasma.
RAM	Random-Access Memory.
RMS	Root Mean Square.
RTS	Random Telegraph Signal.
RU	Read-out Unit.
SDD	Silicon Drift Detector.
SEL	Single Event Latchup.
SEM	Scanning Electron Microscope.
SEU	Single Event Upset.
SF	Space Frame.
SNR	Signal-to-Noise Ratio.
SPD	Silicon Pixel Detector.
SPS	Super Proton Synchrotron.
SpTAB	Single point Tape Automated Bonding.
SRAM	Static RAM.
SRP	Spreading Resistance Profiling.
SSD	Silicon Strip Detector.
TC	Technical Coordinator.
TDR	Technical Design Report.
TID	Total Ionising Dose.
TMEC	Thai Micro Electronic Centre.
TN	Temporal Noise.
TOF	Time of Flight.
TPC	Time Projection Chamber.
TRD	Transition Radiation Detector.
UHV	Ultra-High Vacuum.